INFORMATION TO USERS

This manuscript has been reproduced from the microfilm master. UMI films the text directly from the original or copy submitted. Thus, some thesis and dissertation copies are in typewriter face, while others may be from any type of computer printer.

The quality of this reproduction is dependent upon the quality of the copy submitted. Broken or indistinct print, colored or poor quality illustrations and photographs, print bleedthrough, substandard margins, and improper alignment can adversely affect reproduction.

In the unlikely event that the author did not send UMI a complete manuscript and there are missing pages, these will be noted. Also, if unauthorized copyright material had to be removed, a note will indicate the deletion.

Oversize materials (e.g., maps, drawings, charts) are reproduced by sectioning the original, beginning at the upper left-hand corner and continuing from left to right in equal sections with small overlaps.

ProQuest Information and Learning
300 North Zeeb Road, Ann Arbor, MI 48106-1346 USA
800-521-0600

Copyright

by

Carolyn Elizabeth Schmit

2001

The Dissertation Committee for Carolyn Elizabeth Schmit certifies that this is the approved version of the following dissertation:

EVALUATION OF X-RAY IMAGING TO

INVESTIGATE HYDRAULIC PERFORMANCE

OF VAPOR-LIQUID CONTACTORS

Committee:

R. Bruce Eldridge, Co-Supervisor

Roger T. Bonnecaze, Co-Supervisor

James R. Fair

Jack S. Watson

Richard A. Ketcham

David T. Allen

EVALUATION OF X-RAY IMAGING TO INVESTIGATE HYDRAULIC PERFORMANCE OF VAPOR-LIQUID CONTACTORS

by

Carolyn Elizabeth Schmit, M.S.E., B.S.

Dissertation

Presented to the Faculty of the Graduate School of

The University of Texas at Austin

in Partial Fulfillment

of the Requirements

for the Degree of

Doctor of Philosophy

The University of Texas at Austin

December 2001

UMI Number: 3055243

Copyright 2001 by
Schmit, Carolyn Elizabeth

All rights reserved.

UMI Microform 3055243
Copyright 2002 by ProQuest Information and Learning Company.
All rights reserved. This microform edition is protected against
unauthorized copying under Title 17, United States Code.

ProQuest Information and Learning Company
300 North Zeeb Road
P.O. Box 1346
Ann Arbor, MI 48106-1346

To my family and friends,

especially Geoffrey,

for their support, encouragement,

and understanding.

ACKNOWLEDGEMENTS

Where do I begin? While neither he, nor I, could tell you how many times I asked that question, Dr. Bruce Eldridge provided helpful answers during my years of graduate study. His direction at the times when I was unsure of where to head and his encouragement along the way were invaluable. Bruce, we definitely saw more than an elephant along the journey.

I would like to express my appreciation to all members of my dissertation committee for their assistance. I thank Dr. Roger Bonnecaze for presenting me with challenges and allowing me to explore and discover without boundaries. With the guidance of Dr. Jack Watson, Dr. Rich Ketcham, Dr. David Allen, and Dr. James Fair, many questions were answered, and issues solved.

I am grateful for the opportunities I had to benefit from the wisdom of Dr. James Fair. His technical knowledge is unsurpassed; however, his wisdom is broader than one can imagine.

I also must thank the people who assisted with this research project over the years. I enjoyed, and greatly appreciated, the collaboration with Dwight Cartmel at the start of this project. Those who assisted with equipment selection, design, and assembly include: Robert Montgomery, Steve Orwick, and Steve Briggs (Separations Research Program), Mitch Goss (APW Systems), and Mark Smith (Chemical Engineering Machine Shop). The personnel at 3DID, including Joe Llamas, Ed Strickland, Glenn Myers, and Chris McKim were all responsive to my often unique imaging requests. Jessica Perkins assisted with the computer simulations. De Vu was part of many discussions about writing a dissertation in general, and graduate school requirements in particular, that aided in the completion of this work.

Without the financial support I received from the NSF Graduate Research Fellowship Program, the College of Engineering at UT, and the Separations Research

Program this work would not have been feasible. In addition, I appreciate funding from Koch-Glitsch, Inc., Oak Ridge National Laboratory, and Sulzer ChemTech.

Throughout the many places I have lived, and endeavors I have pursued, I have always been able to count upon my family for support. Mom, Dad, Tom, and Dan, you have all been there from the start and I appreciate the silent vote of confidence that you each have given me. To my late Grandma Schnipp, I think of you often and hope you are aware that you continue to influence me. Geoffrey, there is little more that I can say, except thank you. Grant, although it took a while for you to speak to me, I can only hope that you have benefitted from our friendship as much as I have. George and Sharon, I appreciate the active interest you have had in my pursuits. Aunt Bobbie and George, I could not ask for a more fun couple to be part of my life.

Although I did not realize it at the time, the chemical engineering education that I obtained at Case Western Reserve University was a reflection of the excellent teachers. Specifically, I would like to thank Dr. Donald Feke, Dr. Nelson Gardner, Dr. Coleman Brosilow, and Dr. Philip Morrison.

Over the years, many people have had a significant influence in my life. I would like to recognize the following people, who were and are important in influencing who I am: Lisa Goldberg; Jen McFadden; Mom, Dad, and Heather O'Brien; Anne Irwin; Sarah McKittrick; Clay Flannigan; Mr. Barry Crossman; Mr. Thomas LaRochelle; Mrs. ~~Chris~~ Veeder; Mrs. Jamie Cucinotta; Mr. Robert Czirr; Ajay Chawan; Joy Masters; Joy Manstream; Noe Kidder; Miss Ruth Ragonese; Juan Martinez; Kim Shaw; Nancy Moon Tofil; Jen Redman; Ed Rozak; Meg Fernando; Nancy and Greg Whitlock; Kelly Belz; Tammie Rupnik; Josh Widick; Barb Calvert; Nicole Pauly; Mandy Whaley; Shilpa Damle; and Tony Lanagan.

EVALUATION OF X-RAY IMAGING TO

INVESTIGATE HYDRAULIC PERFORMANCE

OF VAPOR-LIQUID CONTACTORS

Publication No. _____

Carolyn Elizabeth Schmit, Ph.D.

The University of Texas at Austin, 2001

Supervisors: R. Bruce Eldridge, Roger T. Bonnecaze

Vapor-liquid contacting applications, such as distillation, absorption, and stripping, require contact between the two phases to accomplish the desired separation. The current models to predict the efficiency of the operation of columns rely upon measurements representative of the column average, and thus, do not predict detrimental behavior caused by variations in properties throughout the column. In this work, x-ray imaging techniques are investigated to determine the feasibility of measuring vapor-liquid contacting behavior at a local scale within packed columns. X-ray computed tomography (CT) was used to obtain images of three experimental systems, and x-ray transmission measurements were used to quantify and measure the variability of the liquid present.

The experimental studies were focused on characterizing the materials present in an air-water contactor, measuring the thickness of a liquid film on a steel surface, and observing the hydraulic behavior of an air-water contactor containing structured

packing. Two x-ray CT scanners, capable of distinct spatial and temporal resolutions, were compared. Imaging studies of test objects indicated that to distinguish between air and water, the noise level associated with the transmission measurements is a critical parameter that is related to the spatial resolution and time of a scan. Films of water with a thickness of 0.24–0.37 mm were successfully measured and identified in CT images. Images of the operating air-water contactor containing Mellapak 500Y indicated that liquid accumulation occurs between two elements of packing at low flow rates, below the loading point. Although image artifacts obscured identification of the liquid in the images of the air-water contactor, the variation in flow along fixed paths was measured with the use of x-ray transmission measurements. With the use of computer simulations, the artifacts were attributed to the combination of the dynamics of the flows and the scan procedure. In general, the local liquid holdup was calculated from the transmission data with less than 10% error.

TABLE OF CONTENTS

Acknowledgements v

Table of Contents ix

List of Tables xii

List of Figures xiv

Nomenclature xxvi

Chapter 1. Introduction 1

1.1. Vapor-Liquid Contactors 1
1.2. Process Tomography 8
1.3. Project Scope 10

Chapter 2. Literature Review 11

2.1. Packed Column Models 11
2.1.1. Semi-Empirical Performance Models 11
2.1.2. Simplified Modeling Approaches 18
2.1.3. Rigorous Modeling Approaches 19
2.1.4. Modeling Limitations 20
2.2. Process Tomography 23
2.2.1. Process Measurements Using Gamma Rays 25
2.2.2. Process Measurement Using X Rays 26
2.2.3. Applications of Gamma-Ray CT to Fluidized Beds 28
2.2.4. Applications of Gamma-ray CT at Washington University 31
2.2.5. Applications of Gamma-Ray CT to Packed Columns 34
2.2.6. Applications of X-Ray CT to Fluidized Beds 35
2.2.7. Applications of X-Ray CT to Packed Columns 40
2.2.8. Applications of ECT to Packed Columns 48
2.2.9. Applications of MRI to Packed Beds 51
2.3. Summary 52

Chapter 3. Experimental Equipment and Procedures 54

3.1. Principles of X-Ray CT 54
3.2. Measurement Equipment for X-Ray CT 57
3.3. Image Reconstruction for X-Ray CT 63
3.4. Description of the X-Ray CT Scanners Used 67

3.4.1. X-Ray CT Scanner Specifications 69
3.4.2. Standard Scanning Startup Procedure 73
3.5. Imaging Techniques Implemented 74
3.5.1. Radiogram 74
3.5.2. CT Scan 76
3.5.3. Stationary Transmission Measurements 78
3.6. Calculation of Liquid Holdup from Transmission Data 81
3.6.1. Local Liquid Holdup 84
3.6.2. Section-Averaged Liquid Holdup 85
3.7. Experimental Systems Imaged 87
3.7.1. Phantoms for Characterizing a Static System 88
3.7.2. Film-Flow System 96
3.7.3. Air-Water Contactor 105
3.8. Measurement of Column-Average Liquid Holdup 112

Chapter 4. Experimental Results 113

4.1. Imaging of Phantoms 113
4.1.1. Radiograms 113
4.1.2. CT Images 115
4.1.3. Histogram Evaluation 130
4.1.4. Profiles Along Selected Lines 146
4.1.5. Calculation of Percent Water Using Sinograms 155
4.2. Film-Flow Imaging Experiments 161
4.2.1. Accuracy of the Metering Pump 161
4.2.2. Radiograms 161
4.2.3. CT Images 165
4.2.4. Histograms and Line Profiles 169
4.2.5. Film-Thickness Calculations 172
4.2.6. Sinogram Analysis 179
4.3. Air-Water Contactor with Structured Packing 187
4.3.1. Radiograms 187
4.3.2. CT Images 189
4.3.3. Image Histogram 200
4.3.4. Determination of Liquid Holdup 200
4.3.5. Stationary Transmission Measurements 205
4.4. Summary 214

Chapter 5. Simulation of X-Ray CT 216

5.1. Computer Simulation Procedures 216
5.2. Simulation Scenarios Studied 221

5.2.1. Method Validation 221
5.2.2. Object Position Dependent Upon View 225
5.2.3. Measurement Error at a Detector 228
5.2.4. Object Position Dependent Upon Subposition – One Circle 230
5.2.5. Object Position Dependent Upon Subposition – Two Circles 239
5.2.6. Comparison of Scanners Requiring and Not Requiring Subpositions 249
5.3. Summary 253

Chapter 6. Discussion of Results 254

6.1. Evaluation of X-Ray Imaging 255
6.1.1. Requirements for CT Images 256
6.1.2. Use of Sinograms 260
6.2. Evaluation of the Air-Water Contactor 263
6.2.1. Investigation of Image Artifacts 263
6.2.2. Variability of Liquid Flow 266
6.2.3. Observation of Liquid Flow Patterns 268
6.3. Requirements for the Imaging System 269

Chapter 7. Conclusions and Recommendations 273

7.1. Summary of Conclusions 273
7.2. Recommendations for Future Study 276
7.2.1. Studies With the Scanner at 3DID 276
7.2.2. Studies That Require the Use of an Alternate Scanner 277

Appendix A. Geometry of Phantoms and Calculation of Percent Water 278

A.1. Geometry of Phantoms 278
A.2. Calculation of Expected Water for 101B+ Scans 281
A.2.1. Calculation of Void Volume at 101B+ Scan Elevations 282
A.2.2. Calculation of Percent Water Present 283
A.3. Calculation of Expected Water for Alliant Scans 285
A.3.1. Calculation of Void Volume at Each Elevation 286
A.3.2. Calculation of Percent Water at Each Elevation 290

Appendix B. Derivation of Expected Film Thickness 294

Appendix C. Variables Specified for Computer Simulations of X-Ray CT 299

Bibliography 307

Vita 314

LIST OF TABLES

Table 3-1. X-Ray CT Scanner Characteristics 67

Table 3-2. CT Scanning Parameters Used for Imaging the Phantoms with the 101B+ Scanner.. 92

Table 3-3. CT Scanning Parameters Used for Imaging the Phantoms with the Alliant Scanner 92

Table 3-4. Parameters for X-Ray CT Scanning of the Film-Flow Apparatus 100

Table 3-5. Water Flow Rates for Film-Flow Experiments and Film Thicknesses Predicted from Theory 101

Table 3-6. CT Scanning Parameters for the Air-Water Contactor Studies..... 110

Table 3-7. X-Ray Scanner Parameters for Stationary Measurements 111

Table 4-1. Ranges of Grayscale Associated with Pixels for the CT Images Obtained at High Resolution with the 101B+ Scanner..... 132

Table 4-2. Characterization of Pixels in Ranges of Grayscale for the CT Images Obtained at High Resolution with the 101B+ Scanner..... 132

Table 4-3. Ranges of Grayscale Associated with Pixels for the CT Images Obtained at Low Resolution with the 101B+ Scanner..... 138

Table 4-4. Characterization of Pixels in Ranges of Grayscale for the CT Images Obtained at Low Resolution with the 101B+ Scanner. 139

Table 4-5. Ranges of Grayscale Associated with Pixels for the CT Images Obtained with the Alliant Scanner.. 143

Table 4-6. Characterization of Pixels in Ranges of Grayscale for the CT Images Obtained with the Alliant Scanner..... 144

Table 4-7. Sequential Order of Material Along the Specified Lines Through Images of the Phantoms Obtained with the 101B+ Scanner. 148

Table 4-8. Sequential Order of Material Along the Lines Through the Images of the Phantoms Obtained with the Alliant Scanner. 151

Table 4-9. Measured Flow Rates of the Metering Pump 162

Table 5-1. Parameters Used for Computer Simulations 222

Table 5-2. Summary of Simulation Scenarios Studied..... 223

Table A-1: Length and Area of the Acrylic Walls of the Phantoms. 278
Table A-2: Void Areas of the Phantoms Calculated for the 101B+ Scans. 284
Table A-3: Volume of Water Calculated at Scan Elevations of 101B+ Scans. 286
Table A-4: Void Area Calculated for Scan Elevations of the Alliant Scans 287
Table A-5: Volume of Water in the Scan Plane for Each Set of Scans 293
Table C-1. Parameters Specified for the Simulations of a Revolving Circle 299
Table C-2. Parameters Specified for the Simulations of Motion Along a Line 299
Table C-3. Parameters Specified for the Simulations of Flipping Object Position . 300
Table C-4. Parameters Specified for the Simulations of a Bad Detector 300
Table C-5. Simulations with One Circle Per Subposition, Two Fixed Positions . . . 301
Table C-6. Simulations with One Circle Per Subposition, Motion Centered 302
Table C-7. Positions of Two Circles Per Subposition, Cases S2.1–S2.4 303
Table C-8. Positions of Two Circles Per Subposition, Cases S2.5–S2.7 304
Table C-9. Positions of Two Circles on a Rectangular Grid, Cases S2.8–S2.10 . . . 305
Table C-10. Positions of Two Circles, Cases C.1–C.4 306

LIST OF FIGURES

Figure 1-1. Typical process flow diagram for distillation in a packed column..... 2

Figure 1-2. Common types of random and structured packing used for distillation: (a) 5/8" plastic ballast ring, (b) 5/8" metal ballast ring, (c) plastic #0A Cascade Mini-Ring (CMR), and (d) plastic #1A CMR..... 3

Figure 1-3. A Mellapak 500Y structured packing element, with diameter of 6 inches and height of 8 inches..... 4

Figure 1-4. Cross section of a column with structured packing representing typical flow patterns. The black lines represent packing surface. Gray regions represent fluid. (a) Packing only. (b) Completely wetting film flow on packing surface. (c) Rivulet flow on packing surface..... 5

Figure 1-5. Typical dependence of efficiency (HETP) on gas and liquid velocity expected for packed columns..... 6

Figure 1-6. Basics of the x-ray CT imaging technique..... 9

Figure 2-1. Concentration profiles at an interface as described by the two-resistance theory..... 15

Figure 2-2. Illustration of the dependency of the Rocha-Bravo-Fair model on the effective interfacial area term..... 21

Figure 2-3. Depiction of a gamma scan of a column. The source and detector are moved simultaneously in fixed increments. A measurement of gamma-ray intensity is obtained at each elevation..... 26

Figure 2-4. The view of the cross section of a column, with the four gamma-ray paths used in a grid scan depicted..... 27

Figure 2-5. (a)(b) Two examples of vertical scan planes located along the diameter of a column..... 36

Figure 3-1. Graphical representation of the attenuation of a beam of x rays. (a) A monoenergetic x-ray beam passes through an object with uniform linear attenuation coefficient and the intensity of the beam changes with position. (b) The intensity of the x ray is decreased exponentially with distance through the uniform object..... 55

Figure 3-2. Adjustment of the aperture of the detectors effectively changes the size of the detectors and is used to vary the thickness of the slice plane. (a) Physical size of detector is the black square region. (b) The height of the detector has been effectively decreased. (c) Both the height and width of the detector have been decreased. 58

Figure 3-3. First-generation scanning configuration that employs parallel-beam geometry. Ray paths for measurements obtained using a source and single detector for eight translational positions at each of three rotational positions are depicted..... 59

Figure 3-4. Fan-beam geometry scanners. (a) Ray paths for three rotational positions for a third-generation geometry. (b) Ray paths for three rotational positions for a fourth-generation geometry..... 60

Figure 3-5. Definition of geometry used for parallel-beam x-ray CT..... 61

Figure 3-6. Definition of geometry used for equiangular fan-beam x-ray CT. 62

Figure 3-7. Illustration of the transformation of one parallel projection into the Fourier domain, as described by the Fourier slice theorem. (a) Space-domain coordinates of object. (b) Frequency-domain values. 64

Figure 3-8. Process of reconstructing an image from a set of projection data..... 66

Figure 3-9. (a) Standard third-generation CT scanner in which one rotation is required to acquire the transmission data. (b) Pseudo-third-generation CT scanner used for imaging experiments in which translation of the object, as depicted by the three circles, is required to acquire the transmission data..... 68

Figure 3-10. X-ray source for the 101B+ scanner used for imaging experiments. (a) Philips industrial x-ray tube. (b) Collimator. (c) Camera to view scan plane (non-essential to x-ray source)..... 69

Figure 3-11. Detector system of the 101B+ Scanner. The arrow indicates the location of the collimator leading to the array of 125 scintillation detectors. . 70

Figure 3-12. X-ray source of the Alliant scanner used for x-ray CT..... 71

Figure 3-13. Detector system of the Alliant CT Scanner, which contains an array of 88 individual detectors each with 1.0 x 1.0 mm^2 aperture, is seen on the right side of the scanner as indicated by the arrow..... 72

Figure 3-14. (a) Section of an image of dry structured packing for which the incorrect shift value was used. (b) Same section for which the correct shift measurement was determined..... 74

Figure 3-15. Acquisition of a radiogram requires translation of the object in two directions to obtain an image, as shown in (a) and (b). (c) Resulting radiogram is a two-dimensional representation of the attenuation of the x rays through the object. 75

Figure 3-16. Flow chart describing the steps involved in acquiring a series of CT scans using a 3DID scanner. 77

Figure 3-17. Rotation and translation of the object during a pseudo-third-generation CT scan (a) Rotation to acquire data at radial positions. (b) Counter-rotation required for a flow system. (c) Translation required for subpositions. (d) Translation to select elevation of the scan plane. 79

Figure 3-18. Formation of a sinogram image for a pseudo-third-generation scanning geometry in which two subpositions, three views, and four detectors are used. (a) Geometry of views and subpositions. (b) Array representing the sinogram indicating view, detector (D), and subposition (S) corresponding to each pixel. (c) The sequence in which the sinogram values are acquired. Dark pixels indicate values that have been measured. 80

Figure 3-19. Ray paths of the x rays measured during a set of stationary transmission measurements. 81

Figure 3-20. Cross section of two columns containing structured packing and the same liquid holdup. (a) well-distributed liquid leads to good performance. (b) maldistribution of liquid leads to poor performance. 85

Figure 3-21. Major components of the 6-inch-diameter column used for imaging studies. (a) 3 1/2-inch-tall aluminum base, (b) 6-inch-tall acrylic section, (c) 18-inch-tall acrylic section, and (d) 24-inch-tall acrylic section. 87

Figure 3-22. Photograph of the main sections of the 6-inch diameter column. (back, l-r) 24-inch acrylic section containing structured packing, 18-inch acrylic section, and 6-inch acrylic section. (front) aluminum base section including fluid connections. 89

Figure 3-23. Phantoms used to characterize regions and interfaces of importance in a vapor-liquid contactor. 91

Figure 3-24. Definition of slice planes for scans in which the vertical aperture, and thus slice thickness, was at 0.3 mm and at 1.0 mm. 93

Figure 3-25. An example of an image histogram. 94

Figure 3-26. The wetted-wall film-flow apparatus used to determine feasibility of measuring the thickness of a thin fluid film. The 18" acrylic section has been removed from around the top segment. 97

Figure 3-27. Film-flow apparatus for measuring film thickness on a curved vertical surface of stainless steel. 98

Figure 3-28. Flow diagram for the film-flow apparatus. 99

Figure 3-29. Depiction of the observed linear attenuation coefficient for a feature that is not fully-resolved for a case with no measurement or reconstruction errors. 103

Figure 3-30. Area defined as void for the film-flow scans. 104

Figure 3-31. Schematic of the 6-inch-diameter air-water contactor used for x-ray imaging experiments. 106

Figure 3-32. Flow diagram for air-water contactor. 107

Figure 3-33. The air-water contactor used for flow experiments that contains a mist eliminator, a liquid distributor, two elements of Mellapak 500Y structured packing, and an air distributor. 108

Figure 4-1. Radiogram of the phantoms obtained with the 101B+ x-ray CT scanner with scan elevations identified. 114

Figure 4-2. Radiograms of the phantoms obtained with the Alliant x-ray CT scanner with scan elevations identified. The two radiograms were obtained from orthogonal directions. 115

Figure 4-3. Typical features of the CT images obtained of the phantoms: (1) column wall, (2) metal surfaces, (3) horizontal metal surface, (4) air regions, (5) water regions, and (6) phantom walls. 116

Figure 4-4. Positions of the four phantoms for images obtained with (a) the 101B+ scanner and (b) the Alliant scanner. 118

Figure 4-5. CT images of the phantoms obtained with the 101B+ scanner and high-resolution scan parameters at an elevation of 144.5 mm. 119

Figure 4-6. CT images of the phantoms obtained with the low-resolution scan parameters for the 101B+ scanner at an elevation of 142.7 mm. (a) Dry phantoms. (b) Partially-filled phantoms. (c) Completely submerged phantoms. 121

Figure 4-7. CT images of the phantoms at an elevation of 146.0 mm obtained with the Alliant scanner. (a) Phantoms at minimum-water condition. (b) Phantom 3 filled with water. (c) Phantoms 3 and 4 filled with water. (d) Phantoms 2, 3, and 4 filled with water. (e) Phantoms at maximum-water condition.. 121

Figure 4-8. Difference image of the phantoms with the 101B+ scanner indicating the shift in position between the partial- and maximum- water scans at an elevation of 144.5 mm. 122

Figure 4-9. Difference image of the phantoms with the Alliant scanner indicating that the phantoms did not shift position. 123

Figure 4-10. A series of CT images obtained of the phantoms with the 101B+ scanner at the high resolution parameters. (a)–(h) Images start at an elevation of 124.9 mm and increment by 0.3 mm until a final elevation of 127.0 mm. (3x) 123

Figure 4-11. A series of CT images obtained of the phantoms with the 101B+ Scanner at the high resolution parameters. (a)–(o) Images start at an elevation of 140.3 mm and increment by 0.3 mm until the final elevation of 144.5 mm. (3x) 125

Figure 4-12. A series of CT images of the phantoms obtained at the low resolution parameters for the 101B+ scanner. (a)–(h) Images begin at an elevation of 124.9 mm and increment by 0.3 mm until the final elevation of 127.0 mm. 126

Figure 4-13. A series of CT images obtained of the phantoms with the 101B+ scanner at the low resolution parameters. (a)–(o) Images start at an elevation of 140.3 mm and increment by 0.3 mm to an elevation of 144.5 mm.. 127

Figure 4-14. CT images of the phantoms, with Phantoms 3 and 4 filled with water, obtained with the Alliant scanner. (a)–(f) Images begin at an elevation of 127.0 mm and increment by 0.5 mm until a final elevation of 129.5 mm. 128

Figure 4-15. CT images of the phantoms, with Phantoms 3 and 4 filled with water, obtained with the Alliant scanner. (a)–(l) Images at increments of 0.5 mm, from 142.0 mm to 147.5 mm. 129

Figure 4-16. Histograms of the high-resolution images obtained with the 101B+ scanner shown in Figure 4-5. 131

Figure 4-17. Location of pixels with values within the specified range for a high-resolution image obtained with the 101B+ scanner.. 133

Figure 4-18. Histograms for three selected low-resolution images obtained with the 101B+ scanner. 138

Figure 4-19. Image of the phantoms containing partial water obtained with the 101B+ scanner with the low-resolution parameters. (a) Original image. (b)–(i) Images indicating pixels in various ranges of the grayscale. 140

Figure 4-20. Histograms for images obtained with the Alliant scanner of the phantoms with minimum, partial, and maximum water present. 143

Figure 4-21. Image of the phantoms containing partial water obtained with the Alliant scanner. (a) Original image. (b)–(h) Images indicating pixels in various ranges of the grayscale. 145

Figure 4-22. Lines specified through the high-resolution images of the phantoms and the values of grayscale along each line. 147

Figure 4-23. Low-resolution image of the phantoms with a line specified through each and plots of the values of grayscale along each of the lines. 149

Figure 4-24. Line profile through Phantom 2 in the images at an elevation of 127.0 mm obtained with the Alliant scanner. 150

Figure 4-25. Line profile through Phantom 1 in the images at an elevation of 129.0 mm obtained with the Alliant scanner. 152

Figure 4-26. Line profile through Phantom 3 in the images at an elevation of 143.5 mm obtained with the Alliant scanner. 153

Figure 4-27. Line profile through Phantom 4 in the images at an elevation of 145.5 mm obtained with the Alliant scanner. 154

Figure 4-28. Sinograms corresponding to high-resolution CT scans of the phantoms with the 101B+ scanner at an elevation of 142.7 mm for (a) dry, (b) partially-filled, and (c) flooded conditions. 156

Figure 4-29. Sinograms corresponding to low-resolution CT scans of the phantoms with the 101B+ at an elevation of 140.9 mm for (a) dry, (b) partially-filled, and (c) flooded conditions. 157

Figure 4-30. Sinograms corresponding to CT scans of the phantoms with the Alliant scanner at an elevation of 146.0 mm for (a) column and phantoms dry, (b) Phantom 4 filled, (c) Phantoms 2,3, and 4 filled, (d) entire column filled. 158

Figure 4-31. Parity plot of the expected vs. calculated percent water present in the phantoms, as determined using the sinogram data from the scans with the 101B+ scanner. 159

Figure 4-32. Parity plot of the expected vs. calculated percent water present in the phantoms. Calculations were performed using the sinogram data from the Alliant scans. 160

Figure 4-33. Relationship between volumetric flow rate of water at ambient conditions and the pump drive setting. 162

Figure 4-34. Radiogram of the film apparatus showing the 6-inch acrylic section and the stainless-steel wetted-wall surface. The elevation of the CT scans is indicated. 163

Figure 4-35. Radiogram of the top of the film apparatus from the standard perspective. (a) Entire column in view. (b) Magnified regions near the edges of the pipe with the top of the apparatus marked. 164

Figure 4-36. Radiogram of the top of the film apparatus from the standard perspective after adjustments. (a) Entire column in view (b) Magnified regions near the edges of the pipe. 164

Figure 4-37. Radiogram of the film apparatus after adjustment of the levelness and a 90° rotation. (a) Entire width of the column. (b) Magnified sections of the radiogram. 165

Figure 4-38. CT images of the film-flow apparatus. (a) Dry. (b) Stainless-steel pipe filled with water. (c) Thin film flowing on stainless-steel surface. (d) Entire column filled with water. 166

Figure 4-39. Images of the difference between flow images at various film thickness and the image with the pipe full of water. Flow rates (gpm): (a) 0.19 (b) 0.28 (c) 0.60 (d) 0.73 167

Figure 4-40. Images of the average film thickness, after processing in polar coordinates, corresponding to the images shown in Figure 4-39. Flow rates (gpm): (a) 0.19 (b) 0.28 (c) 0.60 (d) 0.73 168

Figure 4-41. Histogram of the column region of the images of the film apparatus without water, with the pipe full of water, and with the column full of water. 170

Figure 4-42. Values of grayscale along selected line through the images of the film apparatus. (a)–(c) Dry, pipe-full, and column-full images with lines drawn. (d) Line profile through each image 171

Figure 4-43. Line profiles through the polar-averaged images that represent average film thickness. Sample line along which profiles were obtained and line profiles. 172

Figure 4-44. Parity plot for calculation of the film thickness with the maximum-value method compared with the theory-predicted values. 174

Figure 4-45. Parity plots for the integration method of calculating film thickness: (a) Definition 1, (b) Definition 2, (c) Definition 3 175

Figure 4-46. Angular variation in film thickness at a flow rate of 0.37 gpm. (a) Average values for 5° increments and the entire circumference are shown. (b)-(c) Location of angular variation is indicated for both images. 177

Figure 4-47. Angular variation in film thickness at a flow rate of 0.73 gpm. (a) Average values for 5° increments and the entire circumference are shown. (b)-(c) Location of angular variation is indicated for both images. 178

Figure 4-48. Sinograms for film-flow apparatus corresponding to the CT images shown in Figure 4-38. (a) No water present. (b) Stainless-steel pipe filled with water. (c) Thin film of water flowing on stainless-steel surface. (d) Entire column filled with water. 180

Figure 4-49. Parity plot of theory-predicted film thickness versus film thickness calculated using the entire region of the sinograms. 181

Figure 4-50. Variation with time in the air region of the sinogram for the film-flow experiments. 183

Figure 4-51. Parity plot of theory-predicted film thickness versus that calculated from the sinograms, after correcting for the scanner drift. 184

Figure 4-52. Parity plot of theory-predicted film thickness versus the scaled film thickness calculated from the sinograms. 185

Figure 4-53. Variation with time in the air mean for the phantom scans with the Alliant scanner. 186

Figure 4-54. Percent water adjusted for the phantoms 187

Figure 4-55. Radiogram of the air-water contactor containing structured packing with the scan elevations labeled. 188

Figure 4-56. Image of dry structured packing with features of interest identified. . 190

Figure 4-57. Four conditions at 348.7 mm represented: (a) almost dry, (b) static holdup only, (c) flow, and (d) flooded. (2x) 191

Figure 4-58. Ring-like artifacts observed in the flow images. (a) Region of magnification is identified. (2x) (b) Region of image with flow artifacts. (1/2x) (c) Region of corresponding static-holdup image. (1/2x) ... 192

Figure 4-59. Images of the air-water contactor containing static holdup. The images in (a) and (b) were acquired sequentially. (c) Difference image. (d)–(g) Magnified regions indicate the presence of limited artifacts near regions of water. ... 193

Figure 4-60. Image of structured packing without flows. (a) No overlap correction. (b) With overlap correction ... 195

Figure 4-61. Flow image reconstructed (a) without the overlap correction and (b) with the overlap correction. ... 196

Figure 4-63. Images at different elevations. (2x) ... 197

Figure 4-62. Image of a flow condition at low resolution ... 197

Figure 4-64. A series of CT images at the joint between elements of structured packing. The elevation change between images is 0.3 mm. Water flow=10.5 gpm/ft^2, F-factor=0.20 (ft/sec)(lb$^{0.5}$/ft$^{1.5}$). (2x) ... 199

Figure 4-65. Histogram of four images representing different conditions for the structured packing. ... 201

Figure 4-66. Sinograms for four conditions at 348.7 mm: (a) almost dry, (b) static holdup only, (c) flow, and (d) flooded. ... 202

Figure 4-67. Scanner drift measured for the scans of the air-water contactor at an elevation of 348.7 mm. ... 203

Figure 4-68. Comparison of the two experimental methods: sinogram vs. traditional method. ... 204

Figure 4-69. Parity plot comparing experimental methods of determining holdup with the model-predicted values. ... 205

Figure 4-70. Sinogram with the row and columns that correspond to the paths of the stationary measurements marked. ... 206

Figure 4-71. (a) Mean value and range of attenuation measured over a five-minute period for a water flow rate of 10.5 gpm/ft^2 and air flow rate of F-factor = 0.20 (ft/sec)(lb$^{0.5}$/ft$^{1.5}$). Maximum-water condition determined from the sinogram. (b) Standard deviation of attenuation at each detector. ... 207

Figure 4-72. Mean attenuation values for three flow conditions ... 208

Figure 4-73. Standard deviation of attenuation values for the three flow conditions shown in Figure 4-72. 209

Figure 4-74. Variation in attenuation at detector: (a) 31, (b) 36, and (c) 57. 211

Figure 4-75. Variation in attenuation measured for a no-flow condition. 213

Figure 5-1. Comparison of the data acquisition and image reconstruction procedures for (a) experiments and (b) simulations. 217

Figure 5-2. CT simulation process steps in the code for the IDL demonstration. . . 218

Figure 5-3. Two scenarios depicting variations in rivulet flow above the scan plane that affect the cross-sectional image. (a) The rivulet is in a different position in the scan plane. (b) The rivulet is no longer in the scan plane. . . . 219

Figure 5-4. (a) Original array containing a circle. (b) Image representing the original array reconstructed from the computer simulation of x-ray CT. . . . 221

Figure 5-5. (a) Sinogram obtained for simulation Case R.1. (b)-(d) Path of revolution of the circle and the reconstructed images for each of the three simulation cases. The circle labelled '1' represents the original position, the gray arc represents the continuous motion, and the circle labelled '2' represents the final position. 224

Figure 5-6. Motion of the circle along a line in the object array and the reconstructed image. 226

Figure 5-7. (a) The two object positions, as indicated by the white and gray circles. (b) Sinogram for Case F.2. Reconstructed images for flip cycles of (c) 128 (d) 32 and (e) 8. 228

Figure 5-8. Reconstructed images representing measurement error during one subposition. 229

Figure 5-9. Process to simulate four subpositions by reconstructing an image from a composite sinogram created from sinograms calculated for four object arrays. 231

Figure 5-10. Two fixed positions of the object for simulations involving subpositions, Cases S1.1–4. 232

Figure 5-11. Sinogram calculated for Case S1.1. 232

Figure 5-12. Simulation results of a scenario in which the position and value of the circle was dependent upon subposition, two fixed positions. (a)–(d) Cases S1.1–4. 233

Figure 5-13. Positions of the circle for the simulations in which one circle was present for each subposition, Cases S1.5–8. 236

Figure 5-14. Simulation results of a scenario in which the position of the circle was dependent upon subposition. (a)-(d) Cases S1.5–8. 237

Figure 5-15. Positions of the circles for the simulations in which two circles were present for each subposition. Circle 1 positions are represented by white circles, and Circle 2 positions by gray circles. Cases S2.1–4. 240

Figure 5-16. Sinogram calculated for Case S2.3. 240

Figure 5-17. Simulation results of a scenario in which the position of two circles was dependent upon subposition. (a)-(d) Cases S2.1–4. 241

Figure 5-18. Positions of the circles for the simulations in which two circles were present for each subposition. Circle 1 positions are represented by white circles, and Circle 2 positions by gray circles. Cases S2.5–7. 243

Figure 5-19. Simulation results of a scenario in which the position of two circles was dependent upon subposition. (a)-(c) Cases S2.5–7. 245

Figure 5-20. Rectangular grids on which circles are located for simulations of subposition. (a) Case S2.8. (b) Case S2.9. (c) Case S2.10. 246

Figure 5-21. Simulation results of a scenario in which the position of two circles was dependent upon subposition. (a)-(c) Cases S2.8–10. 247

Figure 5-22. Position of two circles for simulations comparing cases with subpositions to cases without subpositions. Circle 1 positions are represented by white circles, and Circle 2 positions by gray circles. Cases C.1–4. . 250

Figure 5-23. Simulation results of scenarios to compare a scanner that requires subpositions, (a) and (c), with one that does not, (b) and (d). 251

Figure 6-1. Three common definitions of neighbor pixels: (a) four, (b) four diagonal, and (c) eight. 258

Figure A-1. Actual dimensions of the phantoms. 279

Figure A-2. Top view of the phantoms indicating the layout of the acrylic walls with dimensions labelled. (a) walls for Phantoms 2, 3, 4. (b) walls for Phantom 1. 281

Figure A-3. Regions of the 101B+ scans that did not contain water. Section of the image obtained at 140.3 mm elevation is shown. 283

Figure A-4. Geometry of the region of Phantom 1 that does not contain water with elevations defined for the 101B+ scans. 284

Figure A-5. Geometry used to calculate the region of water present in Phantom 1 at some elevations. 285

Figure A-6. Region of CT image at 142.5 mm elevation depicting the regions of Phantoms 1 and 4 that never contain water. 288

Figure A-7. Geometry of the region of Phantom 1 at elevations 142.0, 142.5, and 143.0 that is always dry. 289

Figure A-8. Regions of Phantoms 1 and 4 at the lower elevations that always contain air. CT scan at 127 mm is shown. 290

Figure A-9. Geometry defining length of the rectangular region of Phantom 1. . . . 291

Figure A-10. Geometry defining segment of the elliptical region of Phantom 4. . . 292

Figure B-1. Coordinate system for film apparatus 294

NOMENCLATURE

Chapter 2

a, a_p	specific packing surface area (m^{-1})
a_e	effective interfacial area (m^{-1})
c	exponent in Equation 2-7 (dimensionless)
C_{pk}	packing characteristic in Equation 2-9 (dimensionless)
d_p	particle diameter; $d_p \equiv 6(1-\varepsilon)/a$ (m)
d_p'	particle diameter including surface liquid (m)
D_L	diffusion coefficient, liquid phase (m^2/s)
D_v	diffusion coefficient, vapor phase (m^2/s)
$F\text{-}factor$	measure of gas flow rate, $F\text{-}factor = U_g\sqrt{\rho_g}$ ($m/s\ (kg/m^3)^{0.5}$)
F_{SE}	factor for surface enhancement (dimensionless)
f_o	friction factor for flow past a single particle (dimensionless)
f_o'	friction factor for flow past a single wetted particle (dimensionless)
F_t	correction factor for total holdup due to effective wetted area (dimensionless)
Fr_L	liquid Froude number (dimensionless); $Fr_L = U_L^2/Sg$
g	gravitational constant; 9.81 m/s^2
g_c	gravitation conversion factor; 1 kg m/s^2 N^{-1}
g_{eff}	effective gravity (m/s^2)
h	liquid holdup ($m^3\ m^{-3}$)
h_0	liquid holdup below the loading point ($m^3\ m^{-3}$)
h_t	total liquid holdup ($m^3\ m^{-3}$)
H_{OG}	height of an overall transfer unit, gas-phase basis (m)
$HETP$	height equivalent to a theoretical plate (m)
k_g	mass-transfer coefficient, gas phase (m/s)

k_L	mass-transfer coefficient, liquid phase (m/s)
K_2	correlation constant in Equation 2-3 (dimensionless)
L	molar liquid flow (kmol/s)
M_L	molecuiar weight of liquid (kg/kmol)
M_v	molecular weight of vapor (kg/kmol)
ΔP	pressure drop (Pa)
ΔP_d	pressure drop through a dry bed (Pa)
ΔP_{irr}	pressure drop through an irrigated bed (Pa)
Re_L	liquid Reynolds number; $Re = (U_L S \rho_L)/\mu_L$
S	side dimension of corrugation (m)
u_v	vapor velocity (m/s)
U_g	superficial gas velocity through a packed bed (m/s)
U_{gs}	superficial gas velocity (m/s)
U_{LS}	superficial liquid velocity (m/s)
V	molar vapor flow (kmol/s)
We_L	liquid Weber number; $We_L = (U_L^2 \rho_L S)/(\sigma g_c)$
Z	total height of packing (m)
ΔZ	incremental height (m)

Greek Symbols

γ	contact angle between solid and liquid film (degrees)
ε	void fraction of packing (dimensionless)
ε'	void fraction of wetted packing (dimensionless)
θ	angle with horizontal for falling film or corrugation channel (degrees)
λ	ratio of slopes, operating line to equilibrium line (dimensionless)
μ_L	liquid viscosity (kg/(m s)
μ	viscosity ratio, $\mu_L : \mu_L$ for water at 70°F (dimensionless)
π	3.14159...
ρ_L	liquid density (kg/m^3)

ρ_v	vapor density (kg/m^3)
ρ_g	gas density (kg/m^3)
σ	surface tension (N/m)

Chapter 3

A	area
a	multiplicative factor indicating the increase in radius due to the film of fluid
a_p	specific packing surface area (m^{-1})
d_i	attenuation of the x-ray beam along a specific path
dI	differential intensity
dL	differential length
ds	differential length along the x-ray beam path
dt	differential in the direction perpendicular to parallel-beam x rays
dw	differential in the w-direction
dx	differential in the x-direction
dy	differential in the y-direction
e	2.71828...
$f(x, y)$	generic function of two variables, x and y, to be determined by image reconstruction
$F(u, v)$	Fourier transform of the function $f(x, y)$
$F(w, \theta)$	Fourier transform of the function $f(x, y)$, represented in polar coordinates
g_z	component of gravitational acceleration in the z-direction
h_t	liquid holdup
I	intensity of the x-ray beam
I_0	initial intensity of the x-ray beam
j	imaginary number, $\sqrt{-1}$
L	path length
N	total number of ray paths

$P_\theta(t)$, $P(\theta, t)$	set of x-ray transmission data for parallel-beam geometry; parallel-beam projection data
Q	volumetric flow rate of the fluid
$Q_\theta(t)$	filtered projection data
R	radius of the tube on which the film flows
$R(\beta, \gamma)$, $R_\beta(\gamma)$	set of x-ray transmission data for fan-beam geometry; fan-beam projection data
s	position along the path of the x-ray beam
$S_\theta(w)$	Fourier transform of the parallel-beam projection data
t	perpendicular distance of the ray from the origin for parallel-beam geometry
u	Cartesian coordinate in the frequency domain
v	Cartesian coordinate in the frequency domain
w	polar coordinate in the frequency domain, representing the distance from the origin to the point of interest
x	coordinate in the object space
y	coordinate in the object space
	Greek Symbols
β	angle that the central ray of the fan beam makes with the axes of the object space
γ	angle between the ray path and the central ray path for fan-beam geometry
δ	film thickness of fluid
ε	void fraction of packing (dimensionless)
θ	angle the x-rays make with the axes of the object space for parallel-beam geometry; polar coordinate in the frequency domain
$d\theta$	differential angle
μ	linear attenuation coefficient
μ_L	viscosity of the fluid
$\mu(s)$	function of linear attenuation coefficient along the path of the x-ray beam
$\mu(x, y)$	function representing the distribution of the linear attenuation coefficient

π	3.14159...
ρ_L	density of the fluid

Subscripts and Superscripts

a	air
film	film region
i	ray path
max	maximum-water condition
min	minimum-water condition
p	plastic
s	stainless steel
tot	total
v	void
w	water

Chapter 6

d_i	attenuation of the x-ray beam along a specific path
h_t	liquid holdup

Greek Symbols

ε	void fraction of packing (dimensionless)

Subscripts and Superscripts

a	air
empty	empty column, no water or packing
full	full column, with water, no packing
i	ray path
min	minimum-water condition
max	maximum-water condition
p	plastic
s	stainless steel
v	void
w	water

Appendix A

A	area
a	dimension of the phantoms
b	dimension of the phantoms
c	dimension of the phantoms
h	dimension of the phantoms
L_c	length within circle
W	width of phantom
x	dimension of the phantoms
x'	dimension of the phantoms
z	elevation of the scan (mm)
z'	modified elevation of the scan (in)
z_c	elevation of center of the circle

Greek Symbols

π	3.14159...

Appendix B

a	multiplicative factor indicating the increase in radius due to the film of fluid
C_1	constant of integration
C_2	constant of integration
dr	differential distance in the r-direction
dv_z	differential velocity in the z-direction
$\frac{d}{dr}$	derivative with respect to r
$\frac{Dv}{Dt}$	substantial time derivative of velocity
g	gravitational acceleration constant
g_z	component of gravitational acceleration in the z-direction
p	pressure
Q	volumetric flow rate of the fluid

r	coordinate in the radial direction
R	radius of the tube on which the film flows
v	velocity field
v_z	component of velocity in the z-direction

Greek Symbols

δ	film thickness of fluid
θ	coordinate in the azimuthal direction
$d\theta$	differential in the θ-direction
μ	viscosity of the fluid
π	3.14159...
ρ	density of the fluid
τ_{rz}	shear stress exerted in the z-direction on a fluid surface of constant r in the direction of lesser r

Operators

∇	gradient operator
∇^2	Laplacian operator

CHAPTER 1: INTRODUCTION

1.1. Vapor-Liquid Contactors

Vapor-liquid contacting is a fundamental physical phenomenon in distillation, absorption, and stripping. In each of these unit operations, mass transfer occurs between liquid and gas phases. The feed stream is separated into two enriched product streams as a result of the mass transfer. The properties of the contacting behavior are important in determining the separation that is achieved in the distillation column, absorber, or stripper. This study is focused on imaging the local vapor-liquid contacting patterns within a vapor-liquid contactor.

The distillation process involves separating a multi-component feed stream into two or more product streams. A typical flow diagram for the distillation process is shown in Figure 1-1. Within a distillation column, vapor and liquid flow counter-currently. The vapor is generated by the addition of heat in the reboiler at the bottom of the column. In fact, the energy required to operate distillation processes accounts for approximately 40% of the total energy consumed by the chemical processing industries [53]. The vapor is condensed after exiting the top of the column, and the liquid is fed back into the column. Throughout the column, the more volatile component is vaporized, while the less volatile component is condensed. The degree to which separation is achieved depends upon the process conditions and the contact between the vapor and liquid phases throughout the column.

Absorption and stripping are related unit operations. Absorption is the process by which a component is transferred from the gas phase into the liquid phase. Stripping is the reverse process; a component is transferred from the liquid phase to the gas phase. Heat is often not added to the system to produce the vapor phase for

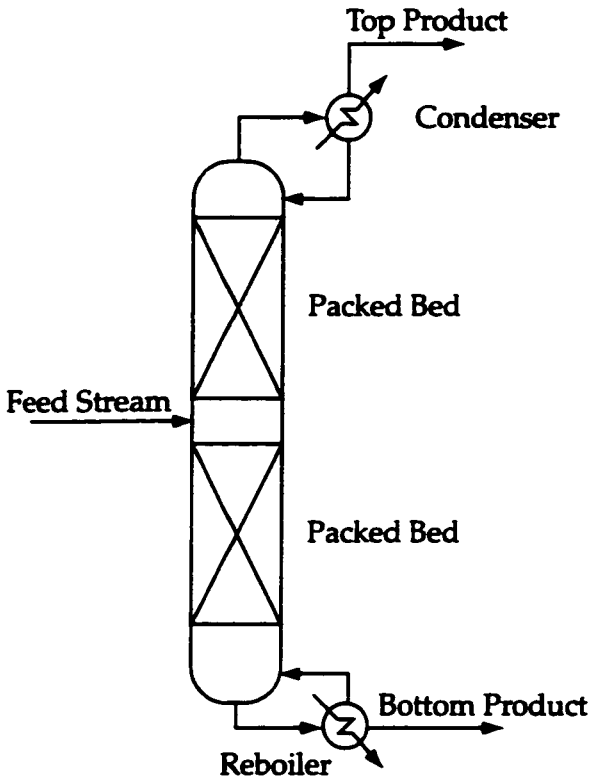

Figure 1-1. Typical process flow diagram for distillation in a packed column.

either of these processes. A vapor feed enters the column near the bottom of the column, and a liquid feed enters the column near the top. As with distillation, the separation achieved depends upon the contact between the liquid and vapor phases and phase-equilibrium limitations at all locations in the column.

The two main types of vapor-liquid contactors that are used for distillation, absorption, and stripping are trayed (plate) columns and packed columns. Both types of columns are intended to increase the amount and quality of contact between the vapor and liquid streams. The trays of a column incorporate evenly spaced openings

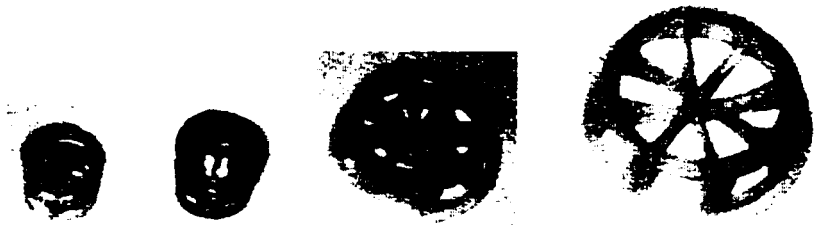

(a) (b) (c) (d)

Figure 1-2. Common types of random and structured packing used for distillation: (a) 5/8" plastic ballast ring, (b) 5/8" metal ballast ring, (c) plastic #0A Cascade Mini-Ring (CMR), and (d) plastic #1A CMR.

to allow vapor to flow upward. Specific types of trays, as described by the type of opening, include sieve trays, bubble-cap trays, and valve trays. The packed column contains packing, which is of the random or structured type. The random packings are also termed dumped packings, which describes the method that is typically used to fill the column with the packing. Structured packing is an ordered packing that consists of corrugated sheets of metal, ceramic, or plastic. The sheets comprising structured packing are typically perforated and have various surface treatments. Several types of random packing are shown in Figure 1-2. An example of structured packing is pictured in Figure 1-3. Liquid is initially distributed at the top of each section containing packing. The liquid flows downward on the solid surfaces in the column. The vapor flows upward, contacting the downward-flowing liquid. Typical flow patterns on the packing are depicted in Figure 1-4.

Historically, models developed to predict the performance of distillation, absorption, and stripping columns are semi-empirical. Such models are valuable in evaluating the operation of existing columns and in designing new columns. However, models that are developed with an improved understanding of the flow behavior will allow columns to be operated more efficiently and designed more

Figure 1-3. A Mellapak 500Y structured packing element, with diameter of 6 inches and height of 8 inches.

optimally. New column designs based upon this understanding will be more precise and thus will have greater capacity or reduced column size.

The predominant capacity limitation of a packed column is flooding. Flooding is the phenomenon that occurs when liquid accumulation in the packed section of the column leads to unstable column operation. The point at which flooding occurs depends upon the packing type as well as the flow velocities of both the liquid and gas. The mass-transfer efficiency decreases significantly as a result of poor contacting between the vapor and liquid phases. Figure 1-5 represents the typical dependence of efficiency on the gas and liquid velocities. Flooding occurs at flow rates higher than

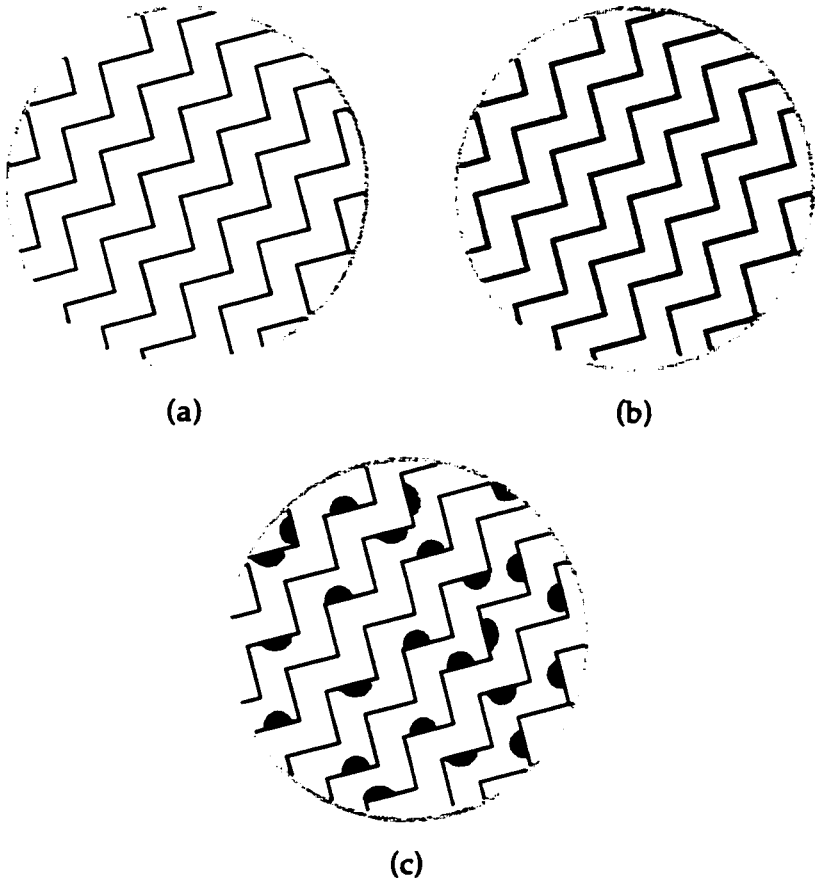

Figure 1-4. Cross section of a column with structured packing representing typical flow patterns. The black lines represent packing surface. Gray regions represent fluid. (a) Packing only. (b) Completely wetting film flow on packing surface. (c) Rivulet flow on packing surface.

the ideal operating point, and the increase in the height equivalent to a theoretical plate (HETP), which indicates a decrease in efficiency, occurs. As seen in Figure 1-5, the typical operating range is at flow velocities lower than the ideal operating point. This is often a result of not understanding the column behavior. The column is operated in

a safe region, rather than at the optimal efficiency, to avoid flood upsets. Less efficient operation from a mass-transfer perspective is also less efficient from an energy-use perspective.

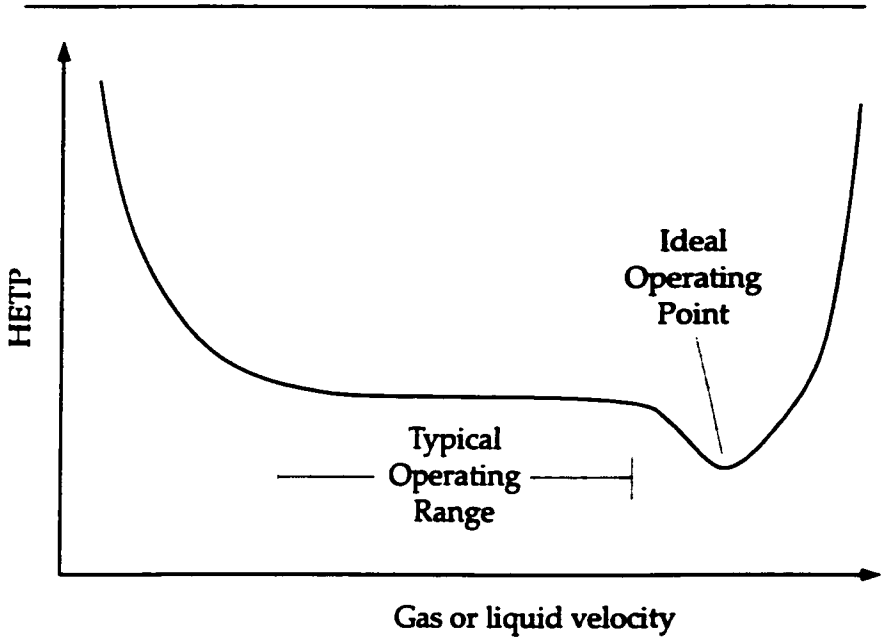

Figure 1-5. Typical dependence of efficiency (HETP) on gas and liquid velocity expected for packed columns.

Another detrimental behavior that occurs in packed columns is poor distribution of liquid. When the initial liquid distribution is poor, the liquid distributor can be adjusted or redesigned. The difficulty arises when the distribution of liquid within the packed bed is poor. The separating capacity of the column decreases as a result of the poor contact between liquid and vapor. Unfortunately, the cause of the deterioration of the liquid distribution is often not identified. Improved understanding of the flow behavior in the packed bed will lead to a greater understanding of

maldistribution of liquid in columns. Current practice is to limit the height of a packed bed to twenty feet to avoid excessive maldistribution. A liquid distributor is required for each packed bed section in a column. New packing designs that incorporate features to encourage good distribution and reduce maldistribution will result in more efficient separation and perhaps increased packed bed height. Increased bed heights will also lead to reduced capital and installation costs by eliminating the number of liquid distributors throughout the column.

Distillation columns are important in the processing industries, with a total of approximately 40,000 in operation in the United States alone [21]. Increased knowledge of the local flow characteristics within such vapor-liquid contactors has the potential to improve separation efficiency. An increase in efficiency will result in a reduction in the energy used by existing columns or in increased throughput. New distillation columns will be designed with smaller height and diameter, thus reducing capital investment, to achieve the same separation.

Significant gains in the understanding of the operation of vapor-liquid contactors will occur when the phenomena that lead to flooding, maldistribution, and other detrimental process conditions are measured and identified. The current methods of measuring process conditions involve a measurement at a single location within the column. Imaging techniques, which provide a measure of a property throughout a given cross section, have the potential to obtain measurements that indicate the pattern of flow in a column. Measuring, and subsequently understanding, the phenomena that are detrimental to performance will lead to improved designs and more efficient operation. The area of imaging that is focused on measuring local properties within a process vessel is process tomography.

1.2. Process Tomography

Process tomography is a non-invasive, non-intrusive method of measuring properties of the materials within a process vessel. It involves determining the spatial distribution of the property of interest from data measured without affecting the operation. Methods of process tomography include transmission tomography (x-ray or gamma-ray), electrical capacitance tomography, magnetic resonance imaging (MRI), ultrasonic tomography, electrical resistance tomography, and electrical inductance tomography. The basic tomography system, regardless of type, consists of sensors to measure the property and a computer with an appropriate image reconstruction algorithm to produce an image from the measurements. The imaging technique used in this study is x-ray computed tomography (CT).

X-ray CT involves directing a beam of x rays at the object and measuring the intensity of the beam after it passes to a set of detectors. A reconstructed image represents the linear attenuation coefficient of the object at each location. The linear attenuation coefficient is equivalent to the product of the mass density of the material and the mass attenuation coefficient. Figure 1-6 represents the process of obtaining an image using x-ray CT. The x rays pass through a thin horizontal slice of the object. The image obtained after the measurement data are reconstructed represents a finite slice of the object. While an image represents one thin segment of the object, a series of images can be combined to provide a three-dimensional representation of the object.

X-ray CT was selected for use in this study because of the technical maturity of the tomography technique and the compatibility with a vapor-liquid contacting system. Gamma-ray imaging, including CT, has been applied to distillation columns for more than 40 years. The principles of gamma-ray CT are the same as those of x-ray CT. However, the spatial resolution attainable with the use of the current x-ray technology is much better than that attainable with gamma rays. Images produced

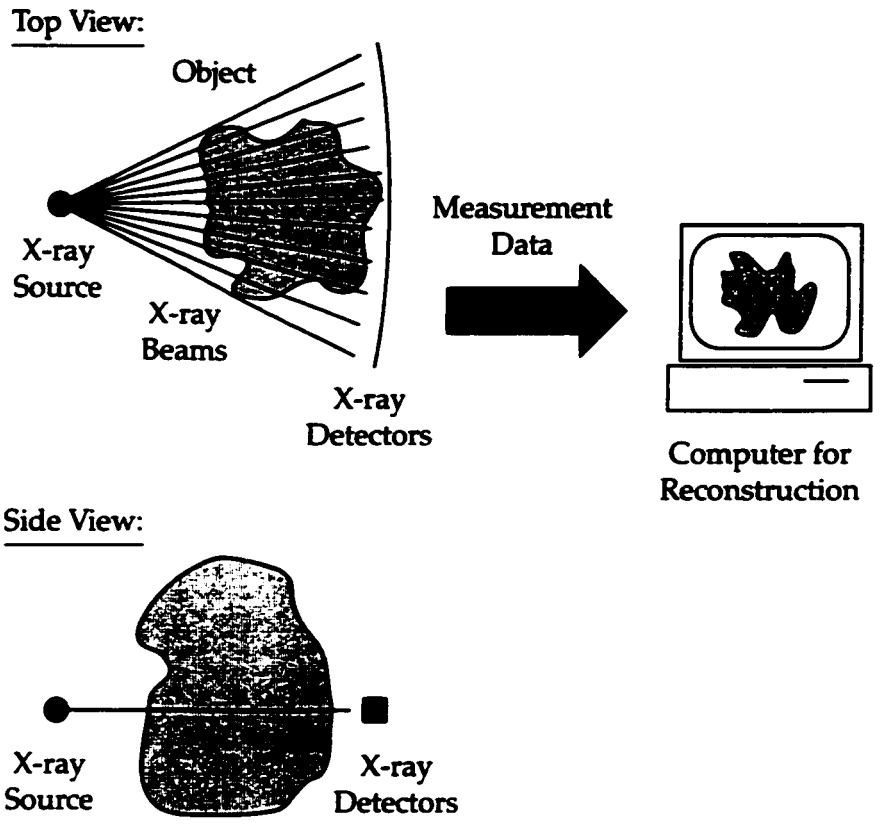

Figure 1-6. Basics of the x-ray CT imaging technique.

using x-ray CT have high resolution, which allows features of packing in a vapor-liquid contactor to be observed. In contrast, electrical tomography techniques result in images with resolution that is not sufficient to observe the detail of packing used for distillation. The physics of x-ray transmission are well understood and standard reconstruction algorithms have been developed and applied for many years. Many of the random and structured packings in use in distillation columns are constructed of stainless steel which is incompatible with MRI due to the iron content. While the temporal resolution attainable with x-ray CT is limited, compared with other imaging

techniques, the spatial resolution and material compatibility of x-ray CT make it the most promising technique for imaging vapor-liquid contactors.

1.3. Project Scope

Distillation, absorption, and stripping are described as mature technologies. However, the development and availability of advanced imaging systems offer the potential to further the knowledge of the vapor-liquid contacting behavior that is fundamental to the performance of packed columns. The imaging work that has been published, which is discussed in Chapter 2, has provided several examples of the use of transmission tomography to image packed columns. However, the measurement techniques have not successfully been used to measure all of the variables typically used to model the hydraulics within a packed column.

The objective of this work was to obtain a more fundamental understanding of the vapor-liquid contacting behavior in packed columns and to determine the feasibility of using x-ray CT to image such columns. This involves:

1. Evaluating the use of x-ray CT for vapor-liquid contactors, including
    - characterizing the features of a static system
    - measuring the capability to identify thin films
    - comparing image resolution capabilities
2. Evaluating the hydraulic performance of an operating vapor-liquid contactor, including
    - observing flow patterns
    - measuring the variation of flow with time
    - determining the liquid holdup
3. Investigating the imaging results with the use of computer simulations of the x-ray CT process.

CHAPTER 2: LITERATURE REVIEW

2.1. Packed Column Models

The current standard method for modeling packed-column performance is to develop a fundamental model which incorporates experimentally-determined correlation constants. There are several emerging approaches for modeling packed column operation of varying complexity. There are models appearing that are highly complex, such as those that incorporate computational fluid dynamics. However, there are also predictive models that are based upon simplifications to existing models and those that use complex data-fitting approaches, such as neural networks.

The objective of modeling packed columns is two-fold. The hydraulic limitation of a column, based upon flow rates, fluid properties, and type of packing, must be determined to specify the diameter. In addition, the mass-transfer efficiency of the column must be determined in order to specify the height. The type of packing will influence the separation efficiency of a column. A primary factor in determining mass-transfer performance is the area of contact between the vapor and liquid phases. Coupled with the mass-transfer area are the mass-transfer coefficients and concentration driving forces. The height equivalent to a theoretical plate (HETP) is the typical measure of packed-column mass-transfer performance.

2.1.1. Semi-Empirical Performance Models[*]

Typical models for determining hydraulic characteristics of packed columns include those of Stichlmair et al. [58] for random packing and Rocha et al. [41] for

[*] Part of this section is reproduced with permission from Schmit, C.E., D. Cartmel, and R.B. Eldridge, Ind. Eng. Chem. Res. 2000, 39, 1546-1553. Copyright 2000 American Chemical Society.

structured packing. Models to predict mass-transfer performance include those of Wagner et al. [64] for random packing and Rocha et al. [42] for structured packing. These models are semi-empirical and do not rigorously represent the underlying momentum-, heat-, and mass- transfer processes. The measurements used in the development of such models are representative of the entire column, such as inlet and outlet compositions and column pressure drop.

Hydraulic models developed for packed columns can be described as either channel models or particle models. The channel models are those that describe the gas as flowing generally upward in numerous channels. The downward-flowing liquid is characterized as flowing on the walls of these channels, reducing the area that is available to the gas, which results in an increased pressure drop. The model presented by Rocha et al. [41] is an example of this type of approach. The other approach, which produces the particle models, involves attributing the pressure drop to the drag of a particle. The Stichlmair et al. model [58] follows this approach.

The Rocha-Bravo-Fair hydraulic model [41] is based upon a mechanistic approach and is used to predict pressure drop and maximum flow capacity (the flood point) in columns containing structured packing. The cross sections of the channels are described as being diamond-shaped with equal-length sides on which the liquid flows. The model is limited to structured packing of the corrugated sheet geometry. The first step in developing this model was to determine the total liquid holdup for the column. The total holdup is comprised of the static holdup and the operating holdup. Static holdup is the amount of liquid that remains in the packed bed after operation ceases. The operating holdup is that attributed to operation and is equivalent to the difference between total and static holdup. The effective gravity acting on the liquid film flowing on the packing surface was determined using a force balance. The forces included were gravity, liquid buoyancy, vapor pressure drop, and drag on the liquid caused by the vapor. The static holdup for the structured packing was neglected to

simplify the model. This was justified because the holdup correlation fits the data well both with and without the static holdup contribution. The expression for total holdup is shown in Equation 2-1. The correction factor for total holdup due to effective area, F_t, incorporates the correlation of Shi and Mersmann [55] described by Equation 2-2, which accounts for the interfacial area available for mass transfer.

[2-1] $$h_t = \left(4\frac{F_t}{S}\right)^{2/3}\left(\frac{3\mu_L U_{LS}}{\rho_L(\sin\theta)\varepsilon g_{eff}}\right)^{1/3}$$

[2-2] $$\frac{a_e}{a_p} = F_{SE}\,\frac{29.12(We_L\,Fr_L)^{0.15}S^{0.359}}{Re_L^{0.2}\varepsilon^{0.6}(1-0.93\cos\gamma)(\sin\theta)^{0.3}}$$

The pressure drop correlation is then determined using this channel model. The dry pressure drop required in the model is calculated with the use of a friction factor equation. The dry pressure drop prediction is independent of the liquid behavior. The irrigated pressure drop expression, shown in Equation 2-3, was correlated using experimental data. The irrigated pressure drop is predicted based upon the dry pressure drop. With the expressions for dry pressure drop and liquid holdup fixed, the correlation constant, K_2, was found to have a linear dependence on packing size. The use of this model to predict pressure drop and flooding point requires iterative calculations.

[2-3] $$\frac{\Delta P}{\Delta Z} = \frac{\Delta P_d}{\Delta Z}\left(\frac{1}{1-K_2\,h_t}\right)^5$$

A general model for prediction of pressure drop primarily in random packed columns was developed by Stichlmair et al. [58]. The approach used to describe the hydrodynamics is the particle-based model. The dry pressure drop is determined based upon the drag of an individual element of random packing. This expression is

shown by Equation 2-4. As expected, the dry pressure drop is dependent upon the specific packing type. Values of the constants used to calculate the friction factor, f_o, are given by Stichlmair et al. [58] for a variety of packing types, including some structured packings.

[2-4] $$\frac{\Delta P}{Z} = \frac{3}{4} f_o \left(\frac{1-\varepsilon}{\varepsilon^{4.65}} \right) \frac{\rho_g U_g^2}{d_p}$$

Introduction of the liquid phase to the column increases the pressure drop as a result of the liquid holdup. The liquid reduces the void fraction of the bed as it effectively increases the particle diameter. In addition, the friction factor for the wet particle is different than that for the dry particle. Again, this is related to the increase in the particle diameter. The pressure drop of the column with liquid flows is expressed by Equation 2-5.

[2-5] $$\frac{\Delta P_{irr}}{Z} = \frac{3}{4} f_o' \left(\frac{1-\varepsilon'}{\varepsilon'^{4.65}} \right) \frac{\rho_g U_g^2}{d_p'}$$

The ratio of irrigated pressure drop to dry pressure drop can then be expressed in terms of the void of the packing, the liquid holdup, and the packing-specific constants. An empirical relation for liquid holdup, as shown by Equation 2-6, is presented for use with the model. In the region below what is termed the loading point, the liquid holdup does not depend upon the gas velocity. Above the loading point, the relationship in the Stichlmair-model indicates the liquid holdup depends upon the pressure drop and the liquid density. The accuracy of this model relies upon the accuracy of the determination of liquid holdup below the loading point. The ratio of dry to irrigated pressure drop is expressed by Equation 2-7, and requires iterative calculations. This model has been validated for many types of random packing, as well as for some structured packing.

[2-6] $$h = h_0\left[1 + 20\left(\frac{\Delta P_{irr}}{Z\rho_L g}\right)^2\right]$$

[2-7] $$\frac{\Delta P_{irr}}{\Delta P} = \left(\frac{1-\varepsilon[1-(h/\varepsilon)]}{1-\varepsilon}\right)^{(2+c)/3}\left(\frac{1}{1-(h/\varepsilon)}\right)^{4.65}$$

The two-resistance theory of mass transfer describes interphase transfer in terms of the properties of two thin films, as shown in Figure 2-1 [20][51]. In this theory, the vapor and liquid are in equilibrium at the interface. There is a concentration gradient across a thin film in each phase, but the bulk concentrations are constant. For steady-state mass transfer, the flux through each phase must be constant. This leads to the possibility of describing the mass flux by any number of mass transfer coefficients provided the appropriate driving force is used.

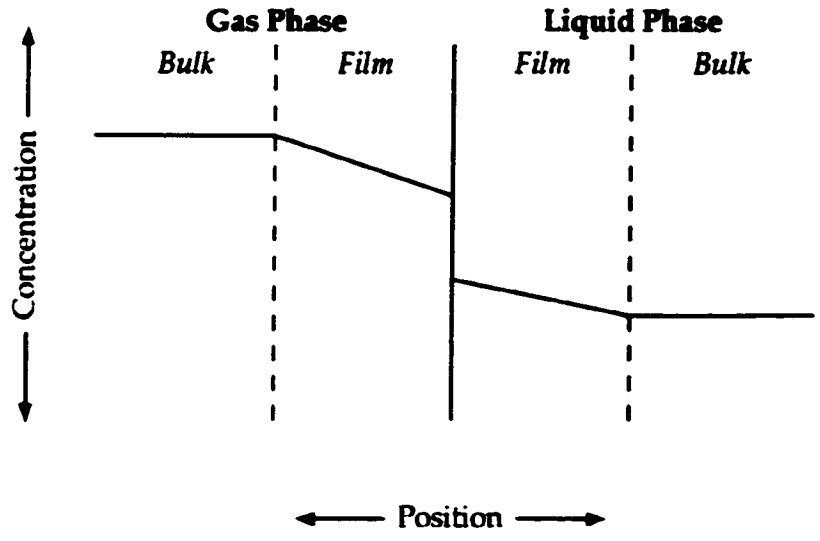

Figure 2-1. Concentration profiles at an interface as described by the two-resistance theory.

Penetration theory may be used to describe mass transfer across a gas-liquid interface [14][20]. The theory presents a time-averaged mass-transfer coefficient which is proportional to the square root of the liquid diffusion coefficient and inversely proportional to the contact time to the one-half power. The flow pattern that leads to this behavior has been described in two manners. The first is that small elements of liquid contact the gas phase for an average exposure time before being replaced by another element from the bulk. The second description involves a laminar flow along a surface, with liquid-mixing occurring after the contact time. The theory is mainly applicable to determine the liquid-phase mass-transfer coefficient.

The mass-transfer model of Rocha et al. [42] is based upon the two-resistance theory, with the assumption of equilibrium at the phase interface. The main parameters are the individual phase mass-transfer coefficients and the effective interfacial area. The gas-phase coefficient was determined based on earlier wetted-wall column studies and involves correlation of dimensionless groups; three parameters were determined to best fit the database. The liquid-phase mass-transfer coefficient was based on penetration theory. The exposure time was based on liquid flow across one corrugated face of the packing. The semi-empirical equation developed by Shi and Mersmann [55] was applied to determine effective area for sheet metal structured packings. The expression for calculating effective area is shown above by Equation 2-2. For gauze packing surfaces, a correlation based on packing area, packing dimensions, and liquid flow rate was applied to determine effective area.

The three parameters of gas-phase mass-transfer coefficient, liquid-phase mass-transfer coefficient, and effective interfacial area, were used to calculate height equivalent to a theoretical plate (HETP), according to Equation 2-8.

[2-8] $$HETP = H_{OG}\frac{\ln\lambda}{\lambda-1} = \left(\frac{U_{gs}}{k_g a_e} + \lambda\frac{U_{Ls}}{k_L a_e}\right)\frac{\ln\lambda}{\lambda-1}$$

For columns containing random packings, Wagner et al. [64] developed a predictive mass-transfer model. The model incorporated the hydraulic model of Stichlmair et al. [58] described above. Mass-transfer coefficients for both the liquid and vapor phases were described by penetration theory. The effective area for mass transfer is derived from the hydraulic model and is related to the area of the packing, the void fraction, and the liquid holdup. An additional term accounts for the area that is ineffective for mass transfer. In the development of the model, there is a packing-specific parameter that is required to evaluate the characteristic length for contact. Other required parameters to predict HETP are based upon the bed characteristics, flow rates, and properties of the fluids (diffusion coefficients, molecular weight, and density). The final expression for predicting HETP is:

[2-9]
$$HETP = \frac{\frac{C_{pk}}{a_p}\left(\frac{Z}{\pi\,(\varepsilon - h)\,u_v}\right)^{0.5}\left(\frac{4D_v}{\pi\,(\varepsilon - h)\,u_v}\right)^{0.5}\left[1 + \left(\frac{hD_vM_L\rho_v}{(\varepsilon - h)D_LM_v\rho_L}\right)^{0.5}\left(\frac{V}{L}\right)^{0.5}\right]}{\left(\frac{1 - \varepsilon + h}{1 - \varepsilon}\right)^{2/3} - 1}$$

As the description of both the Rocha-Bravo-Fair model [42] and the Wagner et al. model [64] indicates, the prediction of mass-transfer performance is highly dependent on the ability to predict accurately the hydrodynamics of the column. Both of these models use the liquid holdup to determine the effective mass-transfer area. As was mentioned by Fair et al. [15] more reliable mass-transfer efficiency models require a more accurate method for predicting interfacial area. Non-invasive imaging techniques, such as x-ray tomography, were mentioned as having potential to provide the required experimental data.

2.1.2. Simplified Modeling Approaches

Recent models to predict HETP for columns containing structured packing have been developed to simplify the semi-empirical approach described above. These models include that of Lockett [30] which is based upon the Rocha-Bravo-Fair model [42] and those of Whaley et al. [65] and Pollock and Eldridge [36] which use a neural network methodology.

The goal of Lockett [30] was to develop a short-cut method to predict HETP. The model was based upon what he determined to be the best of the rigorous models published for predicting the performance of columns with structured packing. The observation that formed the basis of the model occurred when plotting HETP versus F-factor. He noted that the data points at 80% of flood fell along a straight line. The general form for the correlation to determine mass-transfer efficiency is represented by Equation 2-10, and depends upon the physical properties of the system and the surface area of the packing. As was noted by Lockett, the short-cut method developed is limited to small-diameter columns with good radial mixing, relatively short bed lengths, and good liquid distribution.

[2-10]
$$HETP = \frac{1.54 g^{0.5} (\rho_L - \rho_g)^{0.5} \mu^{-0.06}}{a\left[1 + 0.78 \exp(0.00058a)\left(\frac{\rho_g}{\rho_L}\right)^{0.25}\right]^2}$$

The neural network approach to predict HETP for structured packing was examined by Whaley et al. [65]. The multi-layer perceptron (MLP) model initially incorporated the same fifteen inputs as the Rocha-Bravo-Fair model [41][42]. The data set consisted of 240 values of HETP and pressure drop for four different types of structured packing and four operating pressures. The MLP model predicted HETP more accurately than the semi-empirical approach of Rocha et al. [41][42]. Whaley and coworkers simplified the neural network model by evaluating the sensitivity of the

HETP prediction to the various inputs. The simplified model requires determination of fewer physical properties and does not include those that do not have a significant impact on performance. The corrugation angle was determined to have the greatest impact on the HETP for the data sets used. A separate MLP model was developed to predict pressure drop, which also performed well in comparison with the Rocha-Bravo-Fair model. In contrast, the semi-empirical approach uses the results of the pressure drop prediction from the hydraulic model as input to the mass-transfer model.

Application of a neural network to predict mass-transfer performance of packed columns with structured packing was extended by Pollock and Eldridge [36]. The same fifteen input variables were initially in the neural network model to predict HETP. Thus, the network was essentially a curve fit in fifteen dimensions. The number of types of structured packing was increased to nine. The packings were from three different manufacturers. The prediction of HETP with the neural network model was determined to be dependent on the roughness of the packing, which was classified as either rough or smooth. The input parameters were ranked in order of their relative importance; however the sensitivity of the network with respect to each variable was difficult to interpret for the larger data set. When compared to the Rocha-Bravo-Fair model, the neural network approach performed substantially better. Because the neural network modeling approach is empirical, the resulting model is only valid for systems with similar properties.

2.1.3. Rigorous Modeling Approaches

More rigorous models being developed include computational fluid dynamics (CFD) models. The work of Yin et al. [67] describes one such approach to predicting mass-transfer performance in randomly-packed distillation columns. The potential benefit of CFD models in predicting column performance is the ability to predict, and account for, local variations in flow throughout the column. CFD models require the

use of closure models to describe the transport phenomena on a small scale within the column. Equations are averaged on a volume-basis to describe the performance on the column scale. The closure models used by Yin and coworkers were based upon empirical correlations that were available in the published literature. The models were used to describe variables such as pressure drop and mass-transfer coefficients. The CFD model was able to predict HETP of a packed column containing Pall rings better than traditional models. The variation in HETP was reported as a function of packed bed height by Yin and coworkers, demonstrating the potential of CFD models to make predictions on a local-scale within the packed column.

Yin and coworkers noted that better experimental techniques to measure flow and concentration distributions will lead to further refinement in the closure models. Improvements in the closure models incorporated into CFD models will result in a more accurate, more rigorous prediction of column performance. Additionally, improved measurement techniques will allow the more rigorous CFD models to be validated on scales smaller than the column level.

2.1.4. Modeling Limitations

The performance models currently available were all validated using measurements that were representative of the entire column behavior. The simplified models are only valid for ideal column conditions or for columns that are not much different from those used to create the models. These models are not reliable when predicting the performance of a column operated at a different set of conditions. The semi-empirical and CFD modeling approaches aim to include the fundamentals of momentum-, heat-, and mass- transfer. However, the models are limited due to the limited data available for validation. The measured data are currently available at the overall column level, thus prediction is limited to explaining phenomena occurring at this level.

The prediction of the hydraulic and mass-transfer performance using the Rocha-Bravo-Fair models depends strongly upon the Shi-Mersmann expression for determining effective interfacial area. Figure 2-2 shows where this term; which is based upon the packing void fraction, packing geometry, superficial liquid velocity, contact angle, and physical properties of the liquid; appears in the hydraulic and mass-transfer models. As a result of these dependencies, inaccuracies in the theory to develop effective interfacial area directly and indirectly affect the accuracy of the mass-transfer model.

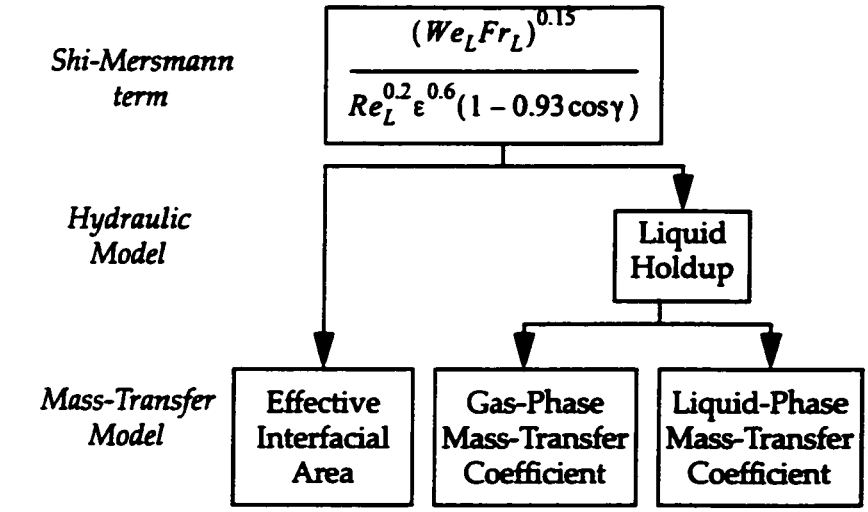

Figure 2-2. Illustration of the dependency of the Rocha-Bravo-Fair model on the effective interfacial area term.

Another limitation of the semi-empirical performance models is the assumption of uniform vapor and liquid distribution throughout the column. Variations in performance result from maldistribution in both the radial and the axial directions. Incorporation of the effects of the liquid distribution into the column performance models would lead to an increase in predictive accuracy. Although the

more rigorous CFD models are able to incorporate radial and axial variations, they still depend upon correlations to describe the transport behavior in a packed column.

The empirical neural-network-based modeling approach has shown promise. However, it will always be limited because it does not provide a fundamental description of the transport phenomena. In the two models discussed above, parameters used to describe the packing were identified as having significant influence on the mass-transfer performance. The features of the packing are believed to be important in predicting performance. However, the effect is not expected to be as large as has been indicated by the neural network models. It is possible that another parameter, that was not included in the model, has similar affects on performance. While larger data sets may reduce the likelihood of incorrectly attributing performance changes to the wrong model input, it must be remembered that the neural network models are empirical.

The need for local-scale measurements within packed columns has been identified by authors of both the semi-empirical models and the CFD models. The semi-empirical models are valuable for predicting performance when hydrodynamic and mass-transfer parameters are constant throughout the column. However, the models are of diminishing value when significant changes are present in the radial or axial direction. While CFD models are able to determine affects of local variations, these models still rely on the empirical or semi-empirical models to describe the small-scale phenomena in the column.

Both the hydraulic and mass-transfer behaviors depend upon the distribution of the liquid and vapor phases in the column. Poor performance, exhibited by poor separation or limited flow capacity, is often attributed to phenomena within the column that influence distribution. When liquid and vapor do not come into contact with each other, the mass transfer between phases does not occur. A reduction of contact in one region within the column results in a decrease in separation efficiency.

The onset of flooding within a column is often at one location within the column, rather than a column-wide phenomenon. However, the adverse effect influences neighboring regions and eventually the entire column.

This study is aimed at identifying and evaluating an imaging technique that can be used to make local measurements that will reveal the underlying causes of poor performance as related to the distribution of the liquid phase. The current performance models rely heavily upon prediction of both liquid holdup and interfacial area. Validation of the prediction of both variables at local positions within a vapor-liquid contactor will lead to improved models. In addition, correlation of the liquid flow patterns with the location of the packing surfaces will provide an indication of how effective the solid surfaces are in promoting contact between vapor and liquid. In general, the characteristics required of a new measurement technique include both the ability to measure small-scale phenomena and the ability to measure the variation in such parameters throughout the column.

2.2. Process Tomography

Process tomography is a non-invasive, non-intrusive method of imaging a cross section of a process vessel. Tomography involves measuring a property from various positions around the vessel and subsequently reconstructing an image based upon the measurements. The tomography technique used determines the property that is represented in the resulting image. Process tomography techniques that have been applied include gamma-ray tomography, x-ray tomography, ultrasonic tomography, electrical capacitance tomography (ECT), electrical resistance tomography (ERT), electrical inductance tomography (EIT), and nuclear magnetic resonance imaging (MRI). Many of these techniques were originally developed for medical applications. Subsequently, some of the techniques were used for non-destructive evaluation. The

application of these techniques to image process vessels began developing approximately 20 years ago. A review of non-invasive tomography techniques for multi-phase flows was published by Chaouki et al. [9].

The main objective for process tomography is to identify process characteristics without influencing or changing the nature of the process. Selection of a tomography technique depends upon the characteristics of the process. The time required to obtain an image (temporal resolution) and the features that can be seen in an image (spatial resolution) vary for each of the methods. Also important when selecting a technique is the compatibility with the process. The tomography techniques must be capable of distinguishing between the regions or phases of interest. For example, when using ECT to monitor the mixing of two fluids in a vessel, it is important that the fluids are of different permittivities.

Although the technique used was invasive, the studies of Potthoff [37] were important in understanding liquid distribution in packed beds. Temperature measurements were made throughout the cross section of a packed column to evaluate liquid distribution for both random and structured packing. The fluids used for the studies were hot liquid, which was either water or methanol, and dry air. The studies indicated that the tendency to generate maldistribution in a packed bed depends upon the type of packing. In addition, different packings respond differently to an initial maldistribution of liquid.

X-ray computed tomography (CT) is the technique that was selected for this study. The spatial resolution attainable and the existence of commercial scanners capable of imaging vertical columns of the desired size were primary factors in the selection. The details of x-ray CT, including measurement and image reconstruction, will be discussed in Chapter 3. The quantification of liquid holdup, liquid distribution, and effective mass-transfer area at locations throughout the column is the impetus for

using x-ray CT to image vapor-liquid contactors. More accurate measurements of these parameters will lead to improved models to predict column performance.

Many recent applications of tomography to make process measurements are described below to illustrate the scope of research that has occurred. The applications discussed include tomography applied to multi-phase columns on laboratory-, pilot-, and industrial- scale equipment. The focus is on applications involving x rays, gamma rays, and packed beds. Some of the measurement techniques are not specifically tomography; however, they involve non-invasive, spatially-dependent measurements in process vessels.

2.2.1. Process Measurements Using Gamma Rays

The use of gamma rays for industrial process measurements dates back to at least 1962, when a radiation scan was performed at DuPont [54]. The initial method of scanning involved lowering the radiation source, a 60-milliCurie Cesium-137 source, and a scintillation detector simultaneously down a 42-inch diameter column, with the use of chain hoists. Measurements of radiation intensity were taken at 2-inch increments and the intensities were recorded. The average density at the various elevations was calculated, and a plot of the axial density in the column was made. Gamma scans, as these measurements are commonly called, continue to be made on process vessels today. Figure 2-3 illustrates the process of performing a gamma scan. Gamma scans are a useful industrial process diagnostic tool. A gamma scan can be used to diagnose mechanical problems, such as tray damage, or process-related problems, such as flooding of a column.

A type of scan using gamma rays in industrial measurements that is more applicable to packed columns is the grid scan. A grid scan consists of four sequential standard gamma scans performed along perpendicular paths of equal length through the column. The paths for a typical grid scan are shown in Figure 2-4. A grid scan

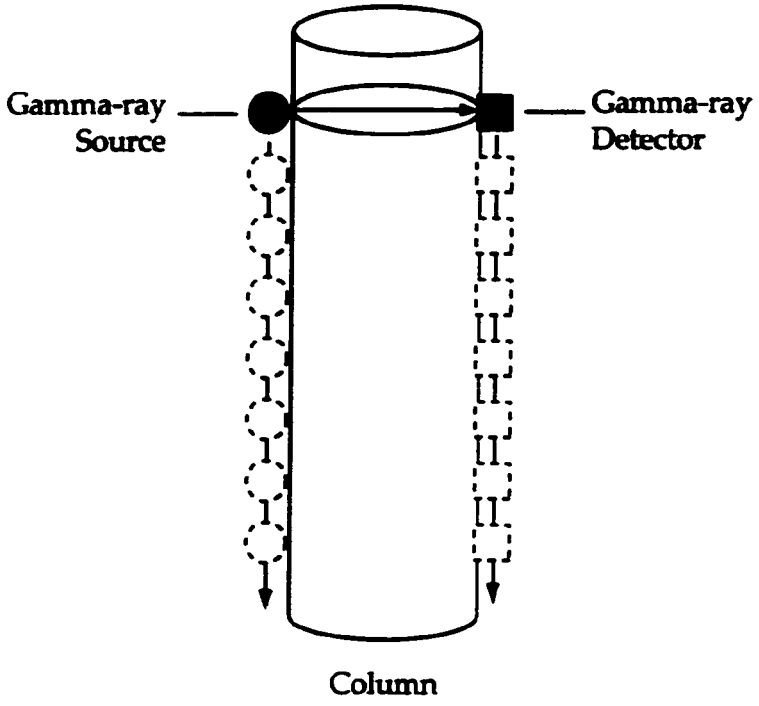

Figure 2-3. Depiction of a gamma scan of a column. The source and detector are moved simultaneously in fixed increments. A measurement of gamma-ray intensity is obtained at each elevation.

provides information about the average density along these four paths. A comparison of the density along each path provides an indication of the uniformity of the packing and process fluids within the vessel. Industrial grid scans and examples of uses were described by Bowman [6][7].

2.2.2. Process Measurement Using X Rays

Smith and coworkers [56] studied the hydrodynamic properties of slurry bubble columns and three-phase fluidized beds using an x-ray imaging technique. In particular they measured the bubble sizes, velocities, and hold-up within columns non-

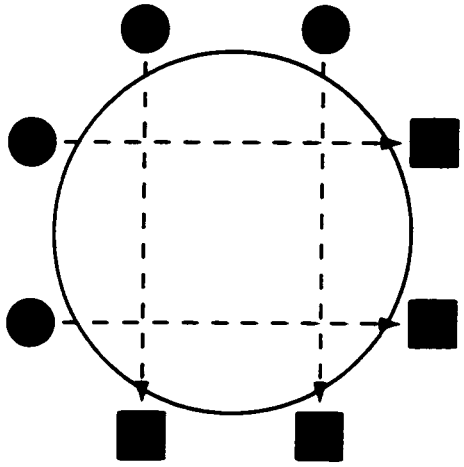

Figure 2-4. The view of the cross section of a column, with the four gamma-ray paths used in a grid scan depicted.

intrusively. The technique was a radiographic approach, in which x-ray pulses were passed through a reactor, amplified by a cesium-iodide image intensifier, and then captured on a video camera. The video camera was operated at 50 frames per second and was synchronized with the x-ray pulses. Bubbles with diameters as small as one millimeter were resolved with the equipment used for this technique. The images produced were analyzed frame by frame.

The radiographic technique was used to study three reactors. The reactors were each 2 meters in length and had diameters of 50 mm, 127 mm, and 178 mm. The reactors were fabricated from aluminum to allow penetration of the x rays. A grade-C sintered-brass distributor plate was used in all the reactors. A perforated-plate distributor, with 37 holes of 3-mm diameter arranged on a triangular pitch, was used in the 127-mm reactor for comparison. The solid phase in the reactors was zirconia of diameter 38 μm or 67 μm. The liquids used were water and water-glycerol mixtures. The fluidizing gas was typically nitrogen, although helium was used for some of the high-pressure experiments. The superficial gas velocity ranged up to 17 cm/sec, while

the pressure was in the range of 1 to 8 bar. The x-ray images were recorded 50 cm from the grid plate, below the surface of the bed. At this level, the bubble sizes had coalesced and reached their maximum. The experiments in which the viscosity of the liquid was varied did not identify any differences in the hydrodynamic properties for these systems.

2.2.3. Applications of Gamma-Ray CT to Fluidized Beds[*]

Bartholomew and Casagrande [5] reported an early, often-referenced application of gamma-ray tomography. The experimental work was performed on both pilot-plant and commercial units with dense- and dispersed-phase fluidization. The data reported were obtained on a 20.4-inch inside diameter vertical catalyst riser in a fluid catalytic cracking unit. The gamma-ray transmission data were obtained using an encapsulated, uncollimated 5-milliCurie Cobalt-60 source and an uncollimated Victoreen 1B85 Geiger-Müller tube as the detector. Measurements were taken along eighteen scan lines across the riser, over a period of approximately one hour. During the time required for data acquisition, the riser operation was held as steady as possible. The gas velocity in the line was approximately 40 feet per second for the measurements. The gamma-ray source was located at four locations and the detector was located at eleven locations around the circumference of the riser; measurements were not taken at all source and detector combinations.

Density contour maps were obtained from the gamma-ray transmission data using two methods of image reconstruction. The first reconstruction method was an analytical approach. The density function was assumed to be of polynomial form. Coefficients were determined using the method of least squares to best fit the experimental data. The second method was a graphical approach. Initial densities

---

[*] Part of this section is reproduced with permission from Schmit, C.E., D. Cartmel, and R.B. Eldridge, Ind. Eng. Chem. Res. 2000, 39, 1546-1553. Copyright 2000 American Chemical Society.

were assumed for points of intersection of scan lines based upon the average density of the intersecting scan lines. Additional intersections were included in the calculation until there was satisfactory agreement for all paths. The resulting density contours were similar to each other. Both contours were asymmetrical and contained a region of high density in the same region. At the time the work was performed, the analytical method required substantial machine computation time.

Gamma-ray CT was used to determine the distribution of fluidized solids under simulated conditions and in industrial applications by Azzi et al. [3]. The applications included a spent catalyst pipe on a fluidized catalyst cracking (FCC) unit, a cold-flow simulation of an FCC riser, and an industrial FCC riser. The gamma-ray source was a 57-milliCurie Cesium-137 (0.66MeV) source for the first and third experiments and Americium-241 (35 keV) for the second experiment. The detector was a collimated scintillation detector, with a 30-mm diameter opening, that was surrounded with lead. The spent catalyst standpipe had an internal diameter of 0.609 m through which 278 kg/s of catalyst was flowing. The cold-flow simulation of an FCC vertical riser had an inner diameter of 0.19 m. The FCC industrial riser had a 0.7-m inner diameter, through which 1080 kg/(m^2s) of catalyst was flowing with a superficial velocity of 21 m/s.

The reconstruction technique used to obtain the density map requires the use of what Azzi and coworkers term natural pixels. In essence these are small elements of the circular cross section; such as hexagons, triangles, or pieces near the edge; which correspond to the intersection of the scan lines. A quasi-Newtonian algorithm was used to compute the density map. The scan lines used were parallel and were in three directions. For the first system, five measurements were taken in each direction, while seven were taken for the other two systems. Data were obtained for an empty pipe and under operating conditions in order to apply the reconstruction technique. The density maps resulting from the reconstruction technique consisted of constant density regions

with triangular or hexagonal shapes. There were a total of 97 regions to represent the entire cross section. As a result, the resolution is limited; however, the technique is suitable for diagnostic purposes such as identifying severe maldistribution.

A commercial industrial gamma-ray CT technique for reactor risers and packed beds has been developed by Tru-Tec Services, Inc. (LaPorte, Texas). The technique is an extension of one-dimensional gamma-ray measurements. The scan line orientations consist of either 7 or 13 source and detector locations, spaced evenly around the column circumference [7]. The number of data points limits the resolution of the resulting density map. The industrial limitations include the accessibility of the vessel from all the desired source and detector locations. The gamma-ray CT technique was applied to a packed bed column to determine the density contour map. The results showed variations in the density of the packed-bed cross section. A region of low density indicated that the vapor flow was biased toward that section of the column. The maldistribution was also identified with a grid scan, which, as described previously, consists of transmission measurements along four perpendicular, equal-length paths. The advantage of the CT approach was to quantify the pattern of maldistribution. Some forms of maldistribution, such as concentric annular flow would not be identified by the simpler method, but would be identified and quantified with the use of CT.

Tru-Tec Services, Inc. applied the gamma-ray CT technique to an industrial flexicracker riser as reported by Anderson et al. [2]. CT images were reconstructed using gamma-ray absorption data before and after a revamp of the process. A numerical analysis of the image data indicated that the standard deviation from the mean density dropped from 4.2 lbs/ft^3 to 1.2 lbs/ft^3 as a result of the process revamp. This is indicative of a reduction in the maldistribution within the riser. Prior to the revamp, the regions near the walls were much less dense than those in the center of the

riser. The density map produced by this technique is limited to identifying large-scale density fluctuations.

2.2.4. Applications of Gamma-ray CT at Washington University

Kumar and Dudukovic [27] used gamma-ray CT to obtain void fraction distribution in bubble columns. The CT scanner was a third-generation configuration, in which the source and detectors were rotated around the object to be imaged. The detectors consisted of an array of eleven 2" x 2" NaI scintillation detectors. A collimator was used to effectively increase the number of detectors. However, the increased spatial resolution required additional scan time. The source was an encapsulated 100-milliCurie Cesium-137 isotope, which provided a fan beam of gamma rays with an angle of 40 degrees. The maximum rotational speed of the entire scanning assembly is one revolution per minute, which limits the speed of a scan. The scanning assembly can be moved up and down, with respect to the object to be imaged. Five different diameter bubble columns were used: 0.10, 0.14, 0.19, 0.26, and 0.30 m. The fluids used were air and tap water. Superficial gas velocities of 0.02, 0.05, 0.08, and 0.12 m/s were used in order to cover all of the flow regimes, from bubble to churn-turbulent. There was no liquid flow. A static liquid height to diameter ratio of at least five was used for all experiments. A perforated-plate distributor was primarily used for gas distribution. A simple cone distributor and a single bubble cap riser distributor were also evaluated.

Gamma-ray CT images of a bubble column were obtained by Kumar et al. [28] to observe the effects of initial gas maldistribution. The column used had an internal diameter of 26.0 cm and the perforated-plate distributor had holes in only one half of the plate. The fluids were air and water. The superficial gas velocity was 5.0 cm/s. Images were obtained at elevations 17.0, 27.0, 83.0, and 121.0 cm above the distributor. It was observed that the density in one region of the column was much

higher at the lowest elevation, thus the air was not distributed well, as expected. Throughout the column the maldistribution was corrected, as evidenced by the more uniform density distribution at higher elevations in the bed. In addition to qualitatively illustrating maldistribution within the bubble column, a 13.9-cm-inner-diameter column was imaged under a common set of flow conditions with the intent to compare the results obtained. The void fraction measured with the CT method deviated from the expected. The void fraction, which compared well at high and low gas velocities, was lower than expected for the intermediate velocities. The void fraction measurements based upon the CT scanning were on the right order, as confirmed by the column void fraction determined by the expansion of the liquid phase in the column.

Additional studies of gas-holdup measurements in bubble columns using the gamma-ray CT system were reported by Kumar et al. [29]. The effects of various operating parameters on gas holdup and gas distribution were investigated. The operating variables altered included column diameter, distributor type, distance from the distributor, gas velocity, and physical properties of the liquid. Experiments were also performed on successive days, at the same operating conditions, to determine the reproducibility of the measurement technique. The gas holdup computed from the CT images was compared to values obtained from a pressure-drop method and from a bed-expansion method. There was variation in gas holdup near the center of the column from one day to the next. This was attributed to the fact that flow characteristics in a given bubble column often change, in spite of operating at the same conditions. The studies incorporating various liquid physical properties involved deionized water and a equal-volume mixture of isopropanol and water. The bubbles observed in the isopropanol-water system were smaller than those in the tap-water system, as expected due to the decreased surface tension. In addition, the gas holdup

was increased significantly for this system. The opposite results were observed in the deionized-water system.

The use of the gamma-ray computed tomography system used by Kumar and coworkers was extended by Chen et al. [10] to image air-drakeoil systems. The resolution of the images produced for these experiments was 0.35 cm in the horizontal direction and 1.0 cm in the vertical direction. The first bubble column used was 44 cm in diameter and 240 cm in height and was made of Plexiglas. The distributor was a perforated plate with a hole diameter of 0.77 mm and an open area of 0.076%. The static liquid height was 160 cm and superficial gas velocities of 2, 5, and 10 cm/s were used. CT scans were performed at heights above the distributor of 51, 89, 132, and 170 cm. The second bubble column was an air-water system in a 10-cm-diameter column. A perforated-plate distributor with 0.5-mm-diameter holes and 0.23% open area was used. The superficial air flow rates were 2.0, 5.0 and 10.0 cm/s and the static water height was 120 cm. The images at a superficial gas velocity of 10 cm/s indicated nearly symmetric gas holdup distribution for both fluid systems, with a higher holdup in the center of the column. At the lowest gas velocity (2 cm/s) the gas holdup distribution was not symmetric. The radial gas-holdup profiles obtained from the images are similar in shape for different axial locations. The comparison of the holdup within the columns of different diameters indicated that there was a lower holdup in the larger diameter column. This was attributed to the larger holes and lower open area in the distributor used for the larger diameter column.

Liquid-solid circulating fluidized beds were the focus of studies using gamma-ray CT reported by Roy et al. [44]. The tomography system was again the same used by Kumar and coworkers. The fluidized bed was a lab-scale cold-flow model constructed of Plexiglas. The column height was 210 cm and the diameter was 15 cm. The solids were 2.5-mm-diameter glass beads. Tap water was used to fluidize the bed in the riser section and was then recirculated. The column was scanned at four axial

locations at various water flow rates in the range 12-23 cm/s. The results reported were at 20 cm/s and were typical of all flow rates. It was observed that the solids holdup varies with both axial and radial position. The holdup was higher at the center of the column, which is opposite the trend observed for gas-solid systems. In addition, a region that was part of a mixing zone, near the entrance to the column, was identified by the low solids holdup.

2.2.5. Applications of Gamma-Ray CT to Packed Columns[*]

An application of gamma-ray computed tomography, in which liquid distribution and liquid holdup were quantified for an industrial-sized packed column, was reported by Xu and Kennedy [66]. Density maps were produced based upon gamma-ray absorption measurements in a 3-foot-diameter Plexiglas column that contained five feet of random packing. The column operated with water as the liquid flow, but with no vapor flow. During the gamma-ray measurements, the liquid distribution was measured by collecting the amount of exiting liquid in a segmented collector. The gamma-ray source was located at nine locations evenly spaced around the column, six inches above the bottom of the bed. For each source location, nine detectors were used to measure gamma-ray intensity. A fourth-order equation with x and y representing position in the column was regressed to determine the density map, based upon the method described by Bartholomew and Casagrande [5]. The liquid distribution based upon this expression compared favorably to the experimental values. Liquid volume fraction for any specific area was obtained by integrating the difference between the operating bed density distribution and the dry bed density distribution. Gamma-ray CT was successfully used to represent the large-scale phenomena within an industrial column. However, this technique does not have the

---

[*] Reproduced with permission from Schmit, C.E., D. Cartmel, and R.B. Eldridge, Ind. Eng. Chem. Res. 2000, 39, 1546-1553. Copyright 2000 American Chemical Society.

image resolution required for yielding data to use in the development of a rigorous hydraulic model. The technique does have value for validating such a model on industrial columns.

2.2.6. Applications of X-Ray CT to Fluidized Beds[*]

Banholzer et al. [4] used a medical x-ray CT scanner to image a 43-mm-diameter 150-mm-tall fluidized bed. The scanner was a General Electric 8800 Series whole body medical scanner. The x-ray source was a rotating anode x-ray tube capable of producing a 30° fan beam of x rays with energies between 20 and 120 keV. A total of 517 gas-filled x-ray detectors were used. The images produced were vertical slices with a spatial resolution of 0.24 x 0.24 mm^2 with a thickness of 1.5 mm. A scan, which consisted of 576 views, was completed in 9 seconds with this system. The solid selected for the studies was subbituminous coal, because it contained the same elements (carbon, hydrogen, oxygen) for which the medical scanner was calibrated. The coal was fluidized with air at room temperature that was distributed using two crossed layers of nylon mesh containing openings of 34 μm. The bed was imaged under static conditions, near minimum fluidization, and in the bubbling regime.

The images presented were vertical slices obtained along a diameter of the fluidized bed, as depicted in Figure 2-5. In addition, the density along selected lines in the image was shown to quantitatively present the image data. The void fraction at regions within the bed was calculated from the image data. In the static bed, a vertical gradient in void fraction was observed, which was explained by the compression of the bed due to the weight of the bed. The images of the fluidized bed showed that the change in density from top to bottom of the bed was at a steeper gradient than that of

---

[*] Part of this section is reproduced with permission from Schmit, C.E., D. Cartmel, and R.B. Eldridge, Ind. Eng. Chem. Res. 2000, 39, 1546-1553. Copyright 2000 American Chemical Society.

the static bed. In the bubbling regime, a central bypass region was observed as indicated by significantly lower density (higher void fraction).

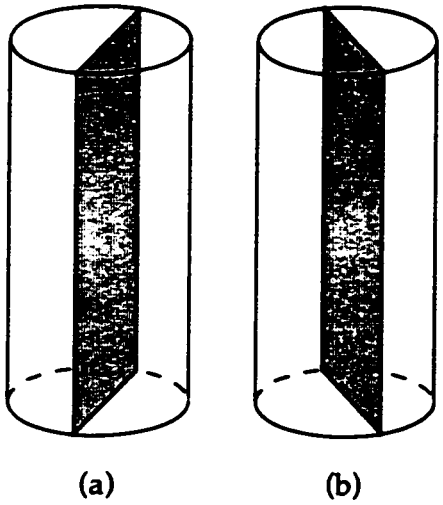

Figure 2-5. (a)(b) Two examples of vertical scan planes located along the diameter of a column.

A modified medical x-ray CT scanner was used by Kantzas [24] to determine the holdup in fluidized and trickle beds. The scanner, an EMI 7070 fourth-generation x-ray CT scanner, was capable of imaging objects of up to 32-cm diameter that were oriented either horizontally or vertically. The energy of the CT system could be varied between 100 and 140 kVp. During a scan, components of the scanner rotate around the object. The duration of a scan is 3 sec, which is longer than the dynamics of the flows. As a result, the images are time-averaged representations of the flow.

The trickle-bed column imaged was 4.5 cm in diameter and 0.45 m in height and was constructed of Plexiglas. The bed contained glass beads of size 0.4-0.6 mm. Water flowed downward at a rate of 1.57 cm^3/s. A total of 150 scans were performed to obtain images with resolution of 0.4 mm x 0.4 mm x 3.0 mm. The fluid holdup in

the column was found to be non-uniform, in spite of the uniform packing. The range for the water holdup fraction was between 0.74 and 0.91.

The fluidized bed that was imaged was 15 cm in height, within a 10-cm-diameter, 100-cm-tall column. The bed contained either 20-30-mesh glass beads or 0.4-cm polyethylene particles (926 kg/m^3 density). Nitrogen was distributed at the bottom of the bed using a distributor plate with a long orifice in the center. A sequence of images was obtained to represent the entire fluidized bed at a constant nitrogen feed pressure. Additional images were obtained below and above the orifice at three nitrogen feed rates. The holdup was calculated for each 0.4 x 0.4 x 5.0 mm^3 volume element in the images. A plot of the average gas holdup as a function of bed elevation indicated there was a relatively constant holdup throughout the column. However, there was considerable radial variation in these values. Kantzas concluded that a one-dimensional description of the holdup behavior would be an oversimplification. An additional study of the time-varying holdup was performed, by imaging one slice of the bed continuously for 30 minutes. The holdup values calculated for this series of images were all within a 0.04 range. Spatial variation of the density was observed across the cross section.

The imaging studies of Kantzas described above illustrate how the use of tomography can lead to a better understanding of the flow characteristics than could be determined from macroscopic column measurements. In addition, it was shown that even though the flow dynamics were not captured, changes in the time-averaged representations are measurable.

Further studies were performed after soaking some of the polyethylene particles in NaI solution in order to increase the absorption of x rays, thus causing the tagged particles to appear denser. The mixing in the fluidized bed was studied by placing tagged polyethylene particles in the bottom of the column and filling the rest with untagged polyethylene. After incorporation of the tagged polyethylene particles,

mixing was observed to occur in the center of the column as indicated by the location of the tagged particles. There were regions in which no mixing occurred, as indicated by the lack of movement of the tagged particles.

Imaging studies of gas-phase fluidized beds containing commercially available polyolefin resins using the EMI 7070 scanner were reported by Kantzas and Kalogerakis [25] and Kantzas et al. [26]. The column used for the experiments was 10 cm in diameter and 1 m tall. The bed height was varied with height to diameter ratios of one, two, and three. The bed consisted of either high density polyethylene (HDPE), linear low density polyethylene (LLDPE) or impact polypropylene resin. The particle-size distribution and fluidization velocity also varied. The flow of air or nitrogen through the column was at ambient conditions. Hundreds of images with resolution 0.4 x 0.4 x 3.0 mm^3 were obtained for each set of studies. The issue of channelling was addressed in the studies, as the beds were not of uniform void fraction even at low velocities. It was again noted that although the void fraction is often constant from one horizontal slice to the next, there is significant radial variation.

Zarabi and Kantzas [68] used the same modified medical x-ray CT scanner to do further evaluation of the characteristics of fluidized beds. The experimental system contained either HDPE or LLDPE. The resin particles had mean particles sizes of 1.50 or 0.75 mm and had a very-narrow particle-size distribution. The density of the LLDPE was 0.917 g/mL, while the density of the HDPE was 0.942 for the 1.50 mm particles and 0.943 for the 0.75 mm particles. The time required to obtain an image of one slice of the column was three seconds; however, approximately 40 seconds was required to process the data before scanning the next slice. The image resolution was 0.4 x 0.4 mm^2 and the slice thickness was 3 mm. The entire column was scanned at a given flow condition. The parameters varied during the experiments were the fluidization number, Froude number, and Archimedes number. To analyze the CT results, a method for determining two threshold values for distinguishing the dense

phase, emulsion phase, and gas phase was developed. The size of bubbles in the column was measured and compared to several correlation methods. In addition, the number of bubbles present within a given cross section was determined. The phase distribution was evaluated and the effects of gas velocity, particle morphology, and elevation were studied.

Characterization of solids concentration in a circulating fluidized bed was the focus of studies performed by Grassler and Wirth [18]. The x-ray CT system used consisted of a 60-keV fan-beam source and an array of 1024 detectors. The source and detectors were mounted on a stainless-steel support and rotated around the fluidized-bed column during scans. Two fluidized beds constructed of Plexiglas were used in the studies. The riser, in which gas flowed upward, was 0.19 m in diameter and was 14-m tall. The downflow section of the fluidized bed was 0.15 m in diameter and was 8.5-m tall. Both beds contained glass beads between 50 and 70 μm in diameter. The superficial velocities through the column ranged from 2 to 7 m/s.

The data collected to reconstruct an image consisted of 128 sets of data from different angular positions. The images of the fluidized beds were 256x256 pixels with a resolution of 0.8 mm. The time required to obtain a cross-sectional image of the bed was between 20 and 40 minutes. The energy of the x-ray source was varied to measure different ranges of solids concentration.

The images of solids concentration that were obtained of the fluidized beds indicated that the solids distribution had a parabolic shape with the maximum close to the wall. The average solids fraction measured ranged from approximately 2 vol% up to 20 vol%. This parabolic shape was observed at various superficial velocities and different circulating mass fluxes.

2.2.7. Applications of X-Ray CT to Packed Columns[*]

Liquid distribution in trickle beds was the focus of studies by Lutran and coworkers [32] that used a medical x-ray CT system. The objective of the work was to achieve three-dimensional flow visualization within a packed column. A 30.48-cm-tall Plexiglas column with a square cross section was used. The inside width was 6.03 cm, while the outside width was 7.30 cm. The column contained a 19-cm-tall bed of either 3-mm- or 6-mm-diameter glass spheres, supported by wire gauze. Water, with barium bromide added to increase the absorption index for better contrast with the glass spheres, was distributed using a plate in which 25 holes were drilled in a 5x5 square pattern. The effect of surface tension on flow pattern was investigated with the use of a water-ethanol mixture. A square tank was located at the bottom of the column, where the liquid was collected before it was recycled. Liquid flow rates of 11.5 mL/s (11386 kg/m^2hr), 23 mL/s (22752 kg/m^2hr), and 33 mL/s (32672 kg/m^2hr) were used. Gas flow was not incorporated. The uniformity of the liquid distribution was measured in the empty column by collecting liquid in 16 equal-sized square zones at the exit.

As a result of the medical scanner geometry, the images obtained were vertical slices through the column. The column and recycle pump were placed on the conveyor belt and moved through the imaging plane. Vertical scans, which required 26 seconds to complete, were taken at 3-mm increments. Images of the dry column were obtained. Images were obtained at each flow rate in an increasing order. To determine the effect of prewetting on flow distribution, images were also obtained while decreasing the flow rate. For these experiments, the spatial resolution was approximately 0.5 mm, determined because 1-mm objects could be resolved according to Lutran and coworkers.

---

[*] Part of this section is reproduced with permission from Schmit, C.E., D. Cartmel, and R.B. Eldridge, Ind. Eng. Chem. Res. 2000, 39, 1546-1553. Copyright 2000 American Chemical Society.

The flow images were analyzed to qualitatively characterize the flow patterns. The liquid was observed to travel as tortuous filaments down the column packed with 3-mm spheres. As the flow rate was increased, the filaments were observed to branch into a few new filaments. At the high flow rate (33 mL/s) the column was observed to flood. The images obtained after the bed was prewetted were quite different. In these images, the liquid was scattered throughout the bed, with liquid pockets forming. When the bed was prewetted, it was discovered that the liquid flow rate did not have as much influence on the flow pattern. When the column contained the 6-mm spheres, changes were noted in the flow patterns. After switching from the low flow rate to the medium flow rate, new filaments appeared, as opposed to the branches that were identified for the 3-mm spheres.

The liquid distributor was modified to determine the contribution of each individual inlet to the flow pattern. The two distribution patterns used were: (1) one row of five holes down the middle of the column and (2) one inlet hole at the center of the distributor. For these configurations the liquid flow rate per inlet hole was unchanged. The liquid flowed down the column primarily as films. With the one-inlet-hole configuration, prewetting the bed reduced the liquid maldistribution in the column. The water-ethanol mixture used for determining surface tension effects had a surface tension of 49.7 dyne/cm and a viscosity of 1.6 cP. The column was packed with the 3-mm spheres and the line-distribution scheme was used. The liquid flow rate was 4.6 mL/s, corresponding to the medium water flow rate with uniform distribution. With the reduced surface tension, the flow filaments seemed less tortuous, because the flow paths remained in the center of the column near the distribution line. Lutran and coworkers assumed the effect of viscosity was small enough to neglect.

Significant observations were made regarding the flow of the liquid in the square column, using a medical CT scanner. Similar measurements, using column internals used for distillation, would provide needed insight into the flow patterns.

The studies of Lutran and coworkers show that the effects of initial liquid distribution can be identified. Therefore, the effects of packing features on flow patterns in a column should also be identifiable.

X-ray computed tomography was applied to trickling filters by Toye and coworkers [60]. A trickling filter is distinguished from a trickle bed by the lack of co-current vapor-phase flow. The application of the trickling filters was in the treatment of wastewater, where the local packing properties and liquid distribution are important in determining the area on which a biofilm can form. In addition, it is important to know the distribution of the three phases (gas, liquid, and solid) in the filter to develop an accurate model for performance. X-ray computed tomography was selected because it offered a true non-invasive technique, spatial resolution of 1-2 mm with a 2.5-min measurement time, and the ability to provide information on local packing morphology and local liquid flow.

The x-ray CT system used was built from available components. It is capable of scanning objects up to 0.8 m in diameter and 2-m tall. The x-ray source produces a 40° fan beam of x rays with energy between 0 and 160 kV. The detector is a linear array of 1024 photodiodes. The motion of the source and detectors around the object is synchronized in the axial and radial directions.

The trickling filter imaged was constructed of polyethylene and was 2-m tall with a 0.6-m inner diameter. The fixed bed consisted of random polypropylene packing, Etapak 210 (diameter 0.05 m, void fraction of 0.95, specific area 220 m^2/m^3). Water was distributed at the top of the column by a multiple point distributor.

Images were obtained of dry packing and under flow conditions. The geometry of the individual packing elements could be seen clearly in the images of dry packing. Also evident was the non-uniform distribution of the packing elements across the cross section at a given elevation. The void fraction was calculated using the images for the dry packing; the value matched the 0.95 claimed by the

manufacturer. For the flow conditions, an image representing the liquid only was obtained by subtracting the drained-column raw data from the irrigated-system raw data prior to image reconstruction. The values calculated for liquid holdup compared favorably with holdup determined by a tracer technique.

Further experiments by Toye and coworkers [61] with the same column and x-ray system were used to identify characteristics of the flow regime. The water was distributed at the top of the column by a four-point distributor. Experiments were performed in order of increasing liquid flow rate, from 0 to 10^5 L/hr (0 to 14.5 gpm/ ft^2). As before, the projection signals from the drained column were subtracted from those of the irrigated column. The image, representing the local dynamic liquid holdup, indicated that the liquid flow was comprised of rivulets on the surface of the packing elements. Therefore, the liquid flow distribution should be correlated with the solid phase distribution. A conclusion reached by the authors was that in trickling filters, the packing heterogeneity is one of the essential causes for liquid flow maldistribution.

Toye and coworkers [62] evaluated the liquid distribution in a packed column containing polypropylene #1A Cascade Mini-Ring (CMR) packing (diameter 0.044 m, height 0.016 m, specific surface area 185 m^2/m^3, void fraction 0.92). The same x-ray computed tomography system was used. Tomographic images were obtained at two elevations of the column, with and without flow. Again, subtraction of the projection data was performed before reconstruction of the images to obtain images representing the dynamic liquid holdup only. The local holdup values were obtained by averaging a six-by-six pixel region of the image. A stochastic partial-wetting model was used to compare the computed holdup values with a predicted value. It was reported by Toye et al. [63] that the water flowed mainly in films and rivulets on the surface of the #1A CMR packing elements.

Additional results of the x-ray imaging of #1A CMR polypropylene packing were reported by Marchot et al. [33]. The 2-m-tall, 0.6-m-diameter column was filled with the packing. The column was fed by three types of liquid distributors providing different drip-point densities. The resolution of the images was around 0.1 mm. The liquid flow rate was varied from 1000 to 6000 L/hr (1.5 to 8.7 gpm/ft^2), with images at different elevations obtained at each rate. There was no gas flow during the experiments. Local dynamic liquid holdup was again calculated by averaging the values of a six-by-six pixel region. Also calculated were radial dispersion coefficients and maldistribution factors to characterize the flow through the column.

The results obtained from the various experiments by Toye and coworkers [33][60][61][62][63] are indicative of the capabilities of x-ray tomography. Quantification of the area on which a film forms, which was mentioned as a goal for wastewater treatment applications, has not yet been reported. Successful measurement of the liquid holdup and of the distribution of the liquid in the column has been shown. Classification of the liquid flow as rivulet flow is important in determining the approach to take for model development. Although the scan time of this work was significantly longer (2.5 minutes vs. 3 seconds) than the work of Kantzas [24], the time-averaged images were still valuable for evaluating flow characteristics.

A medical CT scanner was used by Deshusses et al. [13] to obtain images of a biotrickling filter that was nearly clogged. The reactor was constructed of 15.2-cm-inner-diameter clear PVC tubing. It was filled with 2.5-cm polypropylene Pall rings to a height of 1.3 m. The biotrickling filter was operated in a downflow model and with degraded toluene as a model pollutant. During operation, a biomass had grown to a content of approximately 70%, thus nearly clogging the reactor. Prior to scanning, the biotrickling filter was allowed to drain for over three hours. The scanner used for the

studies was a General Electric clinical scanner. The slice between sections imaged was 3 mm, and the resolution of an image was 0.3 mm.

In the cross-sectional images obtained of the bioreactor, the biofilm was observed to be covering the Pall rings. Regions existed in which the entire Pall ring was covered by biomass. The features of some Pall rings were still identifiable, as they were only covered with a thin layer of biomass. While these images were obtained of a non-operational biotrickling filter, the distribution of the biomass was indicative of the flows that occurred during operation. The biofilm formed in a heterogeneous manner. The location of the channels of biomass indicated that significant wall effect occurred in the bioreactor imaged. The interfacial area that resulted from these large channels was calculated from the images.

Schmitz and coworkers [49][50] evaluated the liquid phase distribution for random and structured packing with the use of x-ray CT. The x-ray scanner consisted of a fixed x-ray-tube source and an array of 15 detectors. The x-ray source was set to 360 keV and a current of 4 mA. The source provided a fan beam of collimated x rays, with 40° aperture and 2-mm thickness. A filter consisting of 2-mm aluminum and 3-mm copper was attached to the front of the x-ray tube to reduce beam-hardening effects. The spatial resolution of the scanner was set to 0.4 x 0.4 mm^2 which resulted in a time of 15 minutes per image. The 200-mm-diameter column was constructed of 5-mm-thick acrylic glass and was 250-mm tall. The random packing was 10-mm-diameter ceramic spheres and the structured packing was Mellapak 250Y from Sulzer. Mellapak 250Y is a folded metal structured packing with 0.1-mm thickness. Water was distributed at the top of the column with the use of a perforated-plate distributor. The distributor contained 177 holes of 1-mm diameter each. The maximum water flow rate was 30 m^3/m^2h (12.3 gpm/ft^2).

Images were obtained of both dry and wetted packing. Images of dry packing were subtracted from the images of wetted packing to obtain the liquid distribution.

Liquid holdup was calculated for both types of packing. For the ceramic spheres, water was distributed irregularly with the water flowing mainly in regions with a high density of ceramic spheres. Schmitz and coworkers attributed this to the high attraction of the spheres for water. In some regions, there was no water. Axially, there was a significant change in the distribution of the liquid after a 2-mm displacement. The authors concluded that liquid distribution measurements made at the outlet of the column are not representative of the distribution throughout the column. For the structured metal packing, a film of water was found over all packing surfaces. The thickness of the water varied with the position of the metal elements. Films on upward-facing surfaces were three to four times thicker than films on the underside of the packing. The actual film thickness was not reported. Water was found to accumulate where the metal sheets of packing were close to each other. The variation in the axial direction was not observed for the structured packing. The holdup compared favorably with Suess and Spiegel [59]. Schmitz and coworkers [50] noted that maldistribution was reduced when a gas phase was introduced through the packing in counter-current flow. A three-dimensional representation of the x-ray measurements obtained during these experiments was presented by Reinecke et al. [40].

Flows on the OPTIFLOW structured packing from Sulzer ChemTech were imaged in an air-water system by Schmitz et al. [48]. The x-ray CT system used for the experiments is the same as described above for use by Schmitz and coworkers. The column was 200 mm in diameter and 700-mm tall. It contained three elements of the structured packing. The water contained barium chloride to enhance the attenuation. In some experiments, surfactants were added to the water to reduce the surface tension from 0.06 N/m to 0.032 N/m. The liquid distributor was a perforated plate containing 177 1.2-mm-diameter holes. There was no gas flow for the experiments reported.

Forty scans, spaced 1.2 mm apart axially, were obtained at a liquid flow rate of 10 m/h (4.1 gpm/ft^2). These scans were all in the lowest of the three packing elements. Each scan required 15 minutes. Images representing water only were obtained by subtracting the trickle-flow images from the dry images. It was observed that the water accumulates at the intersections of the metal sheets. For this packing, there were elevations where the liquid was only located at these intersections, resulting in evenly-spaced pockets of liquid. At other elevations, the thin films of liquid appeared to follow the structure of the folded metal sheets. The liquid holdup was presented as a function of the axial distance for these 40 scans. The calculated values varied from 1 to 8%, with a mean of 3.05%.

The surface tension of the liquid was varied in the studies of Schmitz and coworkers. Mean liquid holdup was reported at five liquid flow rates ranging from 2 to 26 m/h (0.82 to 10.7 gpm/ft^2) for both of the liquids. A slightly higher liquid holdup was reported for the reduced-surface-tension fluid. The holdup values for both liquid systems were in the range predicted by three models used for comparison.

These applications of tomography advanced the understanding of the flow characteristics in both structured and random packing. Imaging of structured packing constructed of metal, within a column of 200-mm diameter, was feasible with the 360-keV x-ray source. The method of holdup calculation differed from the method used by Toye and coworkers [60][61][62]. The reconstructed images were subtracted, rather than the projection data. The successful identification of film thickness on structured packing is a step toward quantifying interfacial area.

X-ray CT was used to image packed columns by Cartmel [8]. The scanner used for the studies was comprised of a 420-kV x-ray source and a linear array of 125 detectors. The object was rotated during a scan, which required approximately five minutes. The slice thickness for the images was either 0.2 or 0.3 mm. A 2-foot-tall, 6-inch-diameter dry packed column containing five types of packing was initially

imaged. The types of packing included 5/8-inch metal ballast rings, #0A CMR, #1A CMR, 5/8-inch plastic ballast rings, and Sulzer BX metal structured packing. The void fraction calculated from the image of each type of packing compared favorably to that published by the manufacturer.

Additional studies by Cartmel involved an air-water contactor. The contactor had a total height of 48 in, with a bed height of 16.6 in. The 6-inch-diameter column was filled with 5/8-inch metal ballast rings. Water was fed to the top of the column with a 4-point liquid distributor. Air was introduced to the bottom of the column with a ring-type distributor. A total of 98 scans at various liquid flow rates, water flow rates, and column elevations were obtained. Several of these images comprised a 4.2-mm-thick three-dimensional image of the column with flows. Liquid holdup was calculated for each of the scans using two methods. The first method involved direct calculation from the CT images. The second method involved calculation of holdup from the transmission data used to reconstruct the CT images. These values were compared with measurements of the bulk holdup obtained with a non-tomographic technique. The results of the imaging studies were discussed further by Schmit et al. [47].

2.2.8. Applications of ECT to Packed Columns

Electrical capacitance tomography has been used to image two-phase flows in packed beds. The technique relies upon measurements of capacitance between sets of two electrodes. Each measured capacitance is dependent upon the permittivity field of the entire measurement plane. The reconstruction of this permittivity field is quite complicated in comparison to x-ray CT because of the non-linearity of the measurement. While the data required for an image can be acquired in a period of 0.015 sec, the images produced using this technique have a resolution no better than approximately 5-10% of the column diameter. Thus, a major limitation of ECT for

visualization of flows in packed beds is that the features of the packing surfaces can not be resolved. In spite of this, some studies have been performed using ECT to determine the fluid distribution in a packed column.

ECT was applied to a trickle-bed reactor by Reinecke and Mewes [38]. The imaging system consisted of three planes of electrodes each segmented into 16 electrodes. The set of measurement electrodes is 30-mm tall. The two sets of guard electrodes are each 100-mm tall. The electrodes can be moved axially to image different planes. The imaging frequency is 100 Hz, with a total of 104 capacitance measurements required per image. In the reconstructed image, the column area is represented by 32-by-32 pixels. The column used was constructed of acrylic and was 120 mm in diameter. The packed section contained two meters of 10-mm-diameter ceramic spheres. Air and water flowed co-currently downward through the column at ambient pressure during the studies.

The results of the ECT imaging of a trickle-bed included images representing the flow in the column over time. Pulse flow was observed at various liquid and gas rates. At high liquid flow rate, the periodic structure seen at lower rates was no longer observed and the gaseous regions were seen to decrease in size. Wall effects were seen in this 120-mm-diameter vessel.

Two-phase flow in trickle beds was the focus of additional studies by Reinecke and Mewes [39]. The ECT equipment described was the same as that used for the previous studies. The column was also the same, and experiments were performed with three sizes of ceramic spheres. Air and deionized water flowed through the column co-currently. The focus of the work was on highly transient flow regimes imaged at the bottom of the column. The results presented included 98 images of the cross section at 0.015-second intervals and images representing data along one line at this same interval. The changes in liquid holdup with time were reported for two sizes of ceramic spheres. Additional images of flow in a co-current trickle-bed using ECT

work were presented by Reinecke et al. [40]. The slices displayed were taken at an interval of 3 ms. The images showed the changes occurring in the phase distribution and identified liquid plugs.

ECT was used to image flows through ceramic monoliths by Mewes et al. [34]. The ECT system described by Reinecke and coworkers was used. A 120-mm-diameter reactor contained a large number of co-current injection nozzles at the top to feed air and deionized water. The liquid flow rate was varied, while keeping the gas rate zero. At the low flow rates, maldistribution was observed with over 80% of the column containing no liquid. As the liquid flow rate was increased, the maldistribution decreased and a liquid layer was observed at the top of the monolith. The size of the channels in the monolith was not reported, thus can not be compared to the size of the pixels in the images presented.

The same ECT system described above was used by Loser et al. [31] to image countercurrent flow in structured packings. The column was 120 mm in diameter and had a bed height of 1.5 m. The two types of polypropylene packing used were Mellapak 250Y and Sulzer BX. For each packing type, four elements of packing were used with each rotated 90° with respect to the previous one. Deionized water and air were the fluids in the system. The liquid was distributed at the top of the column by a distributor containing 36 injection nozzles, and the air was fed at the bottom of the column. Images were obtained at a rate of 54 per second.

The images obtained of the packed bed containing structured packing consisted of 32-by-32 pixels. The images represented the liquid only, not the packing surfaces, because the calibrations were performed with the packing in the column. The non-linear relationship between measured capacitance and liquid holdup necessitated calibration of the ECT system using values of liquid holdup predicted by the models in the literature. The average liquid holdup was calculated from the images and presented as a function of time. There was a higher holdup and more variation in

holdup at higher gas rates, with a constant liquid rate. The quality of distribution in the column was represented by a maldistribution factor which was also presented as a function of time. For a specific gas rate and liquid load, Loser and coworkers concluded that the liquid holdup and maldistribution changed at a small scale and thus could be considered quasi-stationary. The maldistribution observed using the ECT system was attributed to the orientation of the packing and the resulting flow to and from the walls.

2.2.9. Applications of MRI to Packed Beds

Nuclear magnetic resonance imaging has been used to image packed beds containing glass spheres [16][52][23]. A major limitation of this technique is the inability to study ferromagnetic materials. Metal packings used in vapor-liquid contactors, such as ballast rings and structured packings, mentioned above, could thus not be used for imaging studies. However, as the work of Gladden and Alexander [16], Sederman et al. [52], and Johns et al. [23] has demonstrated, the technique is valuable for studying flow in pores. The three sets of MRI flow experiments used the same imaging system, a Bruker Spectrospin DMX 200 NMR spectrometer with a 4.77 T, 15-cm-bore vertical magnet.

Gladden and Alexander [16] focused on characterizing the pore spaces in a packed bed of particles. A 4.5-cm-inner-diameter glass column containing 6-mm glass spheres and water was imaged. A three-dimensional data set was acquired that was used to identify the pores. From this information, the pore size distribution and the pore volume as a function of pore surface area were calculated.

The work of Sederman et al. [52] incorporated short (4.5 cm) and tall (70 cm) packed beds. Five-millimeter-diameter glass spheres were used in both. The flow in the tall column was expected to be free from end effects. The columns were filled with deionized water, all air bubbles removed, and a seal was formed to prevent air

from entering the system during imaging. A constant flow rate of water passed through the column as the images were obtained. The focus of this study was to obtain velocity images. The flow velocity was then correlated with the structure of the bed to visualize the flow around individual glass spheres.

The same techniques were used by Johns et al. [23] to image flows of a glucose solution and water in a packed bed consisting of 5-mm spheres. Three flow rates were used for each of the solutions to determine the effect of Reynolds number on the flow patterns. Large regions of stagnant fluid were found to exist within the columns at various flow rates. In addition, it was observed that the flow patterns are repeated after stopping the flow and restarting it.

2.3. Summary

Current state-of-the-art performance models for vapor-liquid contactors serve the chemical processing industry relatively well. However, these models are limited in scope to applications and conditions that are similar to those for which the model was validated. Experimentally-determined correlation coefficients are included in the predictive models, which limits the use to types of packing used in the development of the model. The more rigorous predictive models that have recently been introduced are limited by the use of correlations to describe the transport processes in the contactor.

The development of any new model must rely upon experimental validation. For most existing performance models, this validation occurred with column-level measurements, such as column pressure drop and inlet and outlet concentrations. As modeling approaches become more rigorous, and capable of predicting column behavior at a smaller scale, measurement techniques must also advance to aid in the modeling effort. Models based upon computational fluid dynamics are being

developed; measurements based upon tomographic techniques are emerging. X-ray CT has been proven as a valid technique for identifying liquid within an operating packed column.

The focus of this study is to evaluate x-ray CT for use in measuring the liquid flow patterns in a counter-current vapor-liquid contactor. Limitations of and requirements for imaging systems will be investigated. Systems that operate at different spatial and temporal resolutions will be directly compared to evaluate the trade-off between the two resolutions. Experiments will be performed to characterize features present in images of a flow system, and calculation methods to obtain quantitative values for liquid holdup will be analyzed. In experiments previously reported, thin films on packing surfaces have been compared, but not quantitatively measured. This study will provide a quantitative measure of the thickness of the smallest identifiable water film on a steel surface using x-ray CT, which will indicate a limitation of the tomographic technique. An operating air-water contactor containing structured packing will be imaged, with particular attention given to the region between packing elements. New packing designs have begun to focus on increasing capacity by altering the redistribution of liquid in this region. The imaging studies will provide insights into the pattern of flow. Finally, computer simulations of the x-ray CT technique will be used to investigate the effects the dynamic nature of the flows in a vapor-liquid contactor have on a reconstructed CT image.

CHAPTER 3: EXPERIMENTAL EQUIPMENT AND PROCEDURES

3.1. Principles of X-Ray CT

X-ray CT is a tomographic technique that is used to obtain a cross-sectional image of an object. The technique is non-invasive, i.e. no sensors are placed within the object, and non-intrusive, i.e. the object is not altered by the imaging technique. The imaging technique can be applied to view the internal structure of opaque objects non-destructively. X-ray CT involves the measurement of the transmission of x rays through the object and the mathematical reconstruction of a detailed image representing a horizontal or vertical thin section of the object. A three-dimensional representation of an object can be obtained by imaging multiple adjacent sections.

The transmission of x rays through an object is measured in x-ray CT. The intensity of an x-ray beam that is measured depends upon the material through which the beam passed. As an x ray passes through a small length of an object, dL, the attenuation of the intensity, dI, is described by Equation 3-1. This expression defines the linear attenuation coefficient, μ. This coefficient characterizes the local rate at which x rays are removed from the incident beam. For a uniform material of length L, if the initial intensity of the monoenergetic beam is I_0, the final intensity of the beam is described by Equation 3-2. The attenuation of the beam through the uniform object is depicted in Figure 3-1.

[3-1] $$\frac{dI}{I} = -\mu dL$$

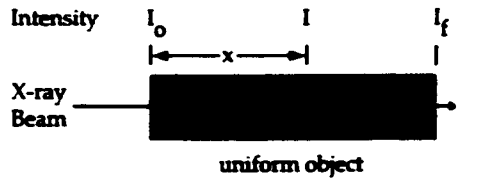

(a)

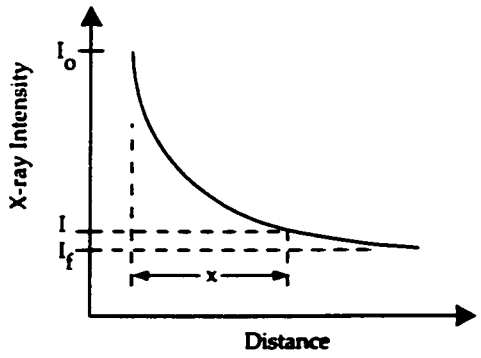

(b)

Figure 3-1. Graphical representation of the attenuation of a beam of x rays. (a) A monoenergetic x-ray beam passes through an object with uniform linear attenuation coefficient and the intensity of the beam changes with position. (b) The intensity of the x ray is decreased exponentially with distance through the uniform object.

[3-2] $$I = I_0 \ e^{-\mu L}$$

For a non-homogenous material, the attenuation of the x ray beam is expressed in the more general form as shown in Equation 3-3. The attenuation is a function of the values of the linear attenuation coefficient along the entire ray path which are no longer constant.

[3-3] $$I = I_0 \, e^{-\int \mu(s) ds}$$

The linear attenuation coefficient is proportional to the density of the material [1]. In fact, the value of the coefficient increases with the atomic number of the material and the density [12]. However, the coefficient is dependent upon both the material and the energy of the x-ray beam. Typically, the attenuation is greater at lower energies [19]. Therefore, when a polyenergetic x-ray beam is used, the energy spectrum of the beam changes as it passes through a homogeneous object. The low-energy x rays are attenuated preferentially, which results in a beam with a higher average energy. This effect can be reduced by experimental techniques, such as using opaque objects to pre-harden the beam. For some scanning situations, the beam-hardening effect is significant and results in artifacts in the reconstructed images. In general, artifacts are features in a reconstructed image that do not represent the physical reality of the object. Whether artifacts are present or not, it is a simplification to assume that a CT image quantitatively represents the density at each location when a polyenergetic beam is used.

The mathematical foundation of x-ray CT is the inverse Radon transform, which states that a function of two variables, $f(x, y)$, can uniquely be determined from an infinite set of line integrals of $f(x, y)$. In x-ray CT, the line integrals are the measured values of x-ray transmission. The function that is desired is $\mu(x, y)$, the distribution of the linear attenuation coefficient. If Equation 3-3 is rewritten as shown in Equation 3-4, the similarity between the measured data and the line integrals is more apparent. The transmission measurements are discrete and are finite in number. Image reconstruction algorithms, to approximate the inverse Radon transform, are applied to this measurement data to produce an image representing the linear attenuation coefficient at each point.

$$[3\text{-}4] \qquad -\ln\left(\frac{I}{I_0}\right) = \int_{ray} \mu(s)ds$$

3.2. Measurement Equipment for X-Ray CT

The measurement system of an x-ray CT scanner consists of an x-ray source and x-ray detectors. The source and detectors are located on opposite sides of the object to measure the transmission of x rays through the object. To obtain measurements from various radial positions, either the object, or the source and detectors, must be rotated. For medical systems, the source and detectors are typically rotated. However, for many industrial CT scanners, the object is rotated.

Several types of radiation sources are used in industrial CT systems. The common x-ray sources are industrial x-ray tubes, linear accelerators, and isotope sources. The x-ray tubes produce x rays that are of lower energy than those produced by linear accelerators. The high-energy x rays produced by the linear accelerator sources are required to penetrate very large objects or objects constructed of highly absorbing materials. Both of these types of sources produce polyenergetic x ray beams. In contrast, isotope sources of radiation produce a beam that is of one, or sometimes two, distinct energy levels. Unfortunately, one of the drawbacks to using isotope sources is that the flux of x rays is typically much less than that produced by either of the electronic methods.

The detectors used for x-ray CT are typically either ionization detectors or scintillation detectors [1][12]. The ionization detectors contain a Noble element that is most often in the gas phase. The incoming x ray gives up energy which results in the generation of a measurable current. The scintillation detectors rely on the use of fluorescent materials that produce visible radiation when exposed to x rays. The light

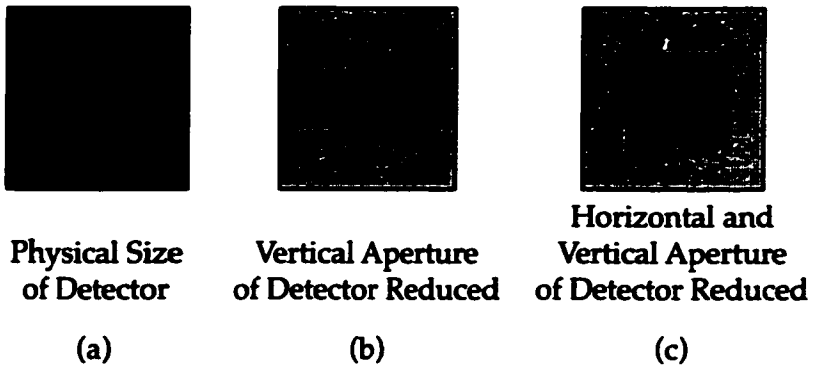

Figure 3-2. Adjustment of the aperture of the detectors effectively changes the size of the detectors and is used to vary the thickness of the slice plane. (a) Physical size of detector is the black square region. (b) The height of the detector has been effectively decreased. (c) Both the height and width of the detector have been decreased.

emitted is then converted to an electrical signal with the use of a photodiode or a photomultiplier tube. Either type of detector can be arranged in a linear array that is comprised of hundreds or thousands of individual detectors. The effective size of the detectors can be varied by adjusting the aperture of the detector, as is shown in Figure 3-2. The aperture perpendicular to the scan plane defines the thickness of the scan plane.

There are many methods that can be used to collect the transmission data used to reconstruct an image of the cross section of the object [1]. Parallel-beam geometry is typically referred to as a first-generation system. This scanning configuration often incorporates an x-ray source and a single detector. As shown in Figure 3-3, the source and detector are translated simultaneously to obtain transmission measurements along parallel ray paths. The source and detectors are then rotated and measurements are obtained from another radial position. This process is continued until a complete set

of data from 180° is measured. A second-generation system still requires translation and rotation of the source and detector; however, a fan-beam source is used which allows for simultaneous measurement of transmission along more than one path. Figure 3-4 depicts both the third- and fourth-generation systems. The third-generation system is a rotate-only system and again makes use of a fan-beam geometry. A complete rotation of 360° is required to acquire data for the reconstruction. However, unlike the first- and second- generation systems, no translation is required. A fourth-generation system contains a fan-beam source and a set of detectors that comprises a complete circle. For the fourth-generation systems, movement of the source only is required.

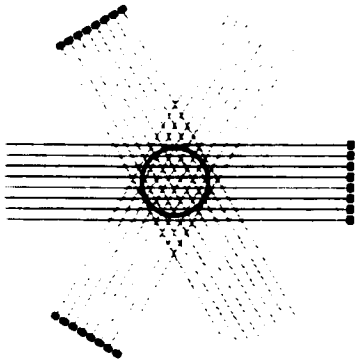

Figure 3-3. First-generation scanning configuration that employs parallel-beam geometry. Ray paths for measurements obtained using a source and single detector for eight translational positions at each of three rotational positions are depicted.

Further advancements in x-ray CT scanning systems are in various stages of development. The improvements include investigation of the use of more than one source in a single scanner. Area detectors and a cone-beam geometry are implemented in some scanners, which allows transmission measurements to be obtained

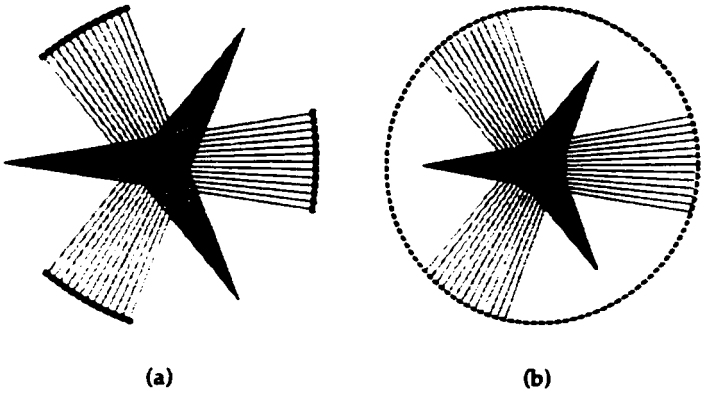

Figure 3-4. Fan-beam geometry scanners. (a) Ray paths for three rotational positions for a third-generation geometry. (b) Ray paths for three rotational positions for a fourth-generation geometry.

simultaneously for more than one elevation. Some of the advancements that have been made in the medical imaging field include spiral scans, in which the object is translated continuously during rotation. New developments in scanning methodology are typically accompanied by modification of existing, or development of new, reconstruction algorithms. As the method of data collection changes, the reconstruction algorithm must be modified to account for any changes in the format of the data. For significant changes, such as the introduction of cone-beam geometry, new algorithms must be developed and tested to accurately reconstruct an image representative of the object.

Another important component of the scanning systems is the mechanical assembly. Rotation of the object, or the source and detectors, must be precisely controlled. For first- and second-generation systems, the translation must also be controlled with the mechanical handling equipment. In addition, most systems allow for multiple scan planes to be imaged which requires additional translation. The accuracy of this equipment is important, as it will affect the quality of the final images.

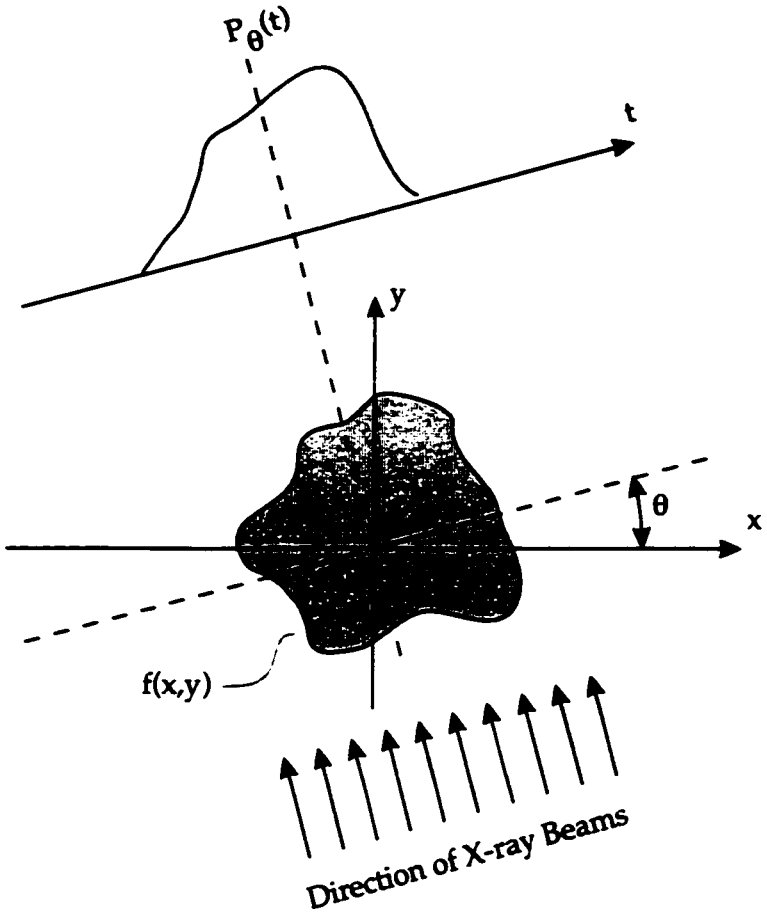

Figure 3-5. Definition of geometry used for parallel-beam x-ray CT.

Regardless of the geometry of the scanner, measurement data are collected from various locations around the object. The transmission data obtained from the scanner represent the measurements of line integrals of the attenuation coefficient, as was described by Equation 3-4. The methods for measuring transmission data lead to two general forms of representing the set of data. For parallel-beam geometry, the set of projection data is a function of the angle the rays make with the axes of the object space, θ, and of the distance the ray path is from the center of rotation, t. These

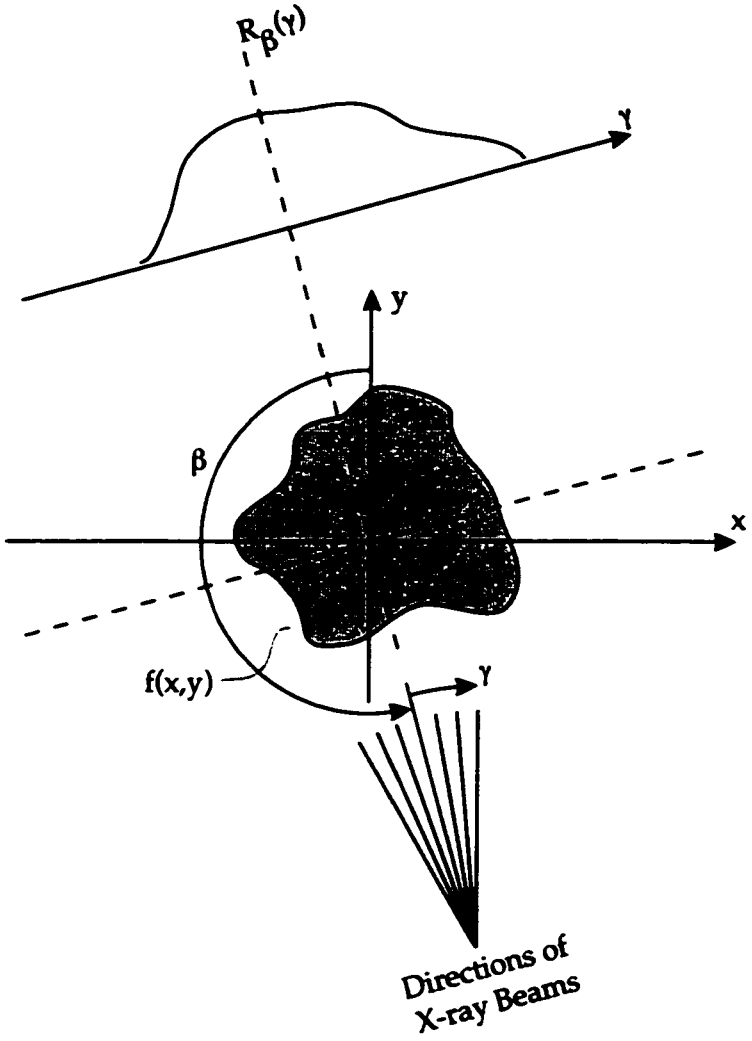

Figure 3-6. Definition of geometry used for equiangular fan-beam x-ray CT.

parameters are depicted in Figure 3-5. Mathematically, the transmission data for this type of system are referred to as $P(\theta, t)$ or $P_\theta(t)$. One possible geometry for a fan-beam system is depicted in Figure 3-6. The angle that the central ray of the fan beam

makes with the axes of the object space, β, is again a parameter used to describe the projection data. The angle between the ray path and the central ray path, γ, is the second parameter for the equiangular case that is depicted. For this geometry, the transmission data are mathematically referred to as $R(\beta, \gamma)$ or $R_\beta(\gamma)$. Another possible fan-beam geometry is to have equally-spaced detectors along a straight line.

When displayed as an image, the entire set of measurement data is referred to as a sinogram. The axes of the image are the parameters of the measurement data, i.e. θ and t or β and γ. The terminology is derived from the sinusoidal pattern that results when tracing the location of a particular feature of the object.

3.3. Image Reconstruction for X-Ray CT

Standard algorithms for image reconstruction have been described in detail by Herman [19] and Rosenfeld and Kak [43]. The two algorithms most often employed for transmission tomography applied to process applications are the filtered backprojection technique and the algebraic reconstruction technique.

The algebraic reconstruction technique can be classified as a finite series-expansion algorithm [1]. The technique can be valuable for reconstructing images when a limited set of transmission measurements exists. Basically, an iterative approach is taken to alter the image matrix to determine a best match with the transmission data. This reconstruction approach was used in the gamma-ray CT work at Washington University [10][27][28][29][44].

The most commonly used algorithm for image reconstruction from x-ray CT data is the filtered backprojection algorithm, which is used in this work. The algorithm was also used in the x-ray CT work at the University of Liege [33][60][61][62][63] and at the University of Hannover [40][48][49][50]. This is also the algorithm used by most medical CT scanners. The Fourier slice theorem is the

mathematical basis for this reconstruction algorithm. The theorem states that the one-dimensional Fourier transform of each of the parallel projections of an object correspond to values on radial lines in the frequency domain, as depicted in Figure 3-7.

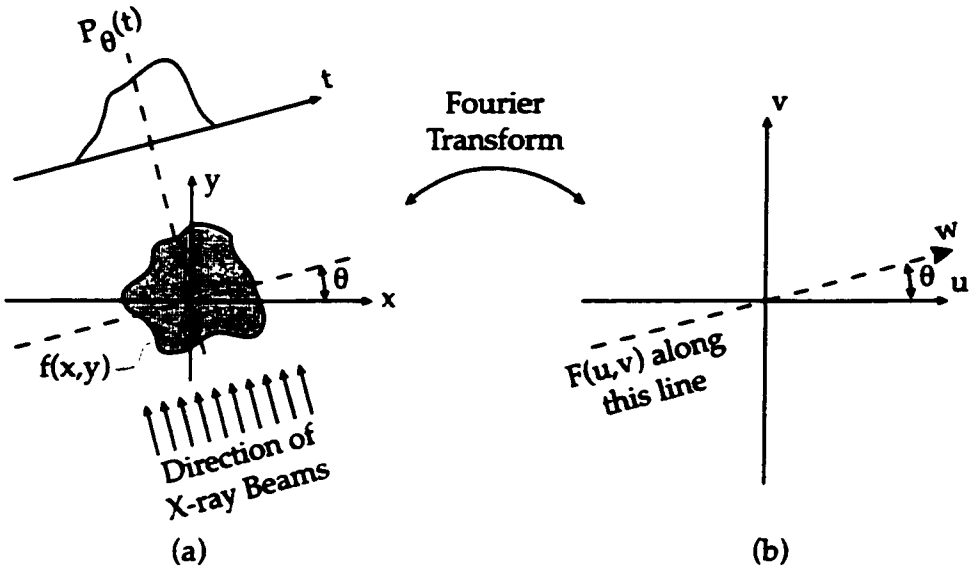

Figure 3-7. Illustration of the transformation of one parallel projection into the Fourier domain, as described by the Fourier slice theorem. (a) Space-domain coordinates of object. (b) Frequency-domain values.

If the original function is $f(x, y)$, then the Fourier transform of this function, $F(u, v)$, is defined as shown by Equation 3-5. It was shown by Rosenfeld and Kak [43] that the Fourier transform of the projection $P_\theta(t)$ is also equivalent to the Fourier transform of the original function $f(x, y)$. This is expressed in polar coordinates in the frequency domain, where $u = w\cos\theta$ and $v = w\sin\theta$, in Equation 3-6. If an

infinite number of projections could be obtained, the original function, $f(x, y)$, could be obtained by using the inverse Fourier transform. However, for x-ray CT, a finite number of projections are measured.

[3-5] $$F(u, v) = \int_{-\infty}^{\infty}\int_{-\infty}^{\infty} f(x, y)e^{-j2\pi(ux + vy)}dxdy$$

[3-6] $$F(w, \theta) = F(u, v) = \int_{-\infty}^{\infty} P_\theta(t)e^{-j2\pi wt}dt = S_\theta(w)$$

The filtered-backprojection algorithm is an accurate and fast method to reconstruct an image function from projection data. The process of transforming projection data into a reconstructed image is depicted in Figure 3-8. There are four main steps involved in transforming the projection data into a reconstructed image. As shown in Equation 3-6 for parallel-beam projection data, $S_\theta(w)$ represents the Fourier transform of the projection data. The filtered projection, $Q_\theta(t)$, is calculated as shown in Equation 3-7 by applying a mathematical filter to approximate $|w|$ and then performing the inverse Fourier transform. Mathematical filters that have been used in x-ray CT include Ram-Lak, Shepp-Logan, Low-pass cosine, and Generalized Hamming [22]. The form of the filter will influence the sharpness of the image and the amount of noise in the image. The final step in the reconstruction is backprojection, as expressed by Equation 3-8, which involves calculating the contribution of each filtered projection to each pixel within the image. For fan-beam data, the calculation is similar. Typically, the fan-beam data are either converted to parallel-beam data or a set of equations derived for the fan-beam geometry is applied.

[3-7] $$Q_\theta(t) = \int_{-\infty}^{\infty} S_\theta(w)|w|e^{j2\pi wt}dw$$

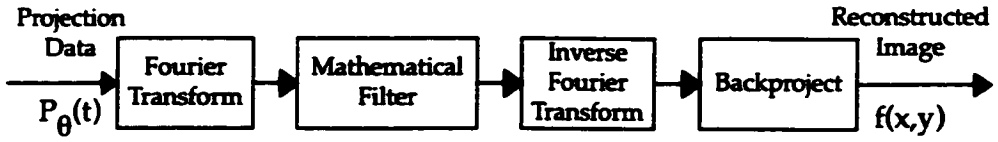

Figure 3-8. Process of reconstructing an image from a set of projection data.

[3-8] $$f(x,y) = \int_0^{\pi} Q_\theta(t)d\theta = \int_0^{\pi} Q_\theta(x\cos\theta + y\sin\theta)d\theta$$

The result produced by the reconstruction algorithm is a digital image. As compared to an object viewed with the human eye, which can be described as a two-dimensional analog signal, an image is comprised of discrete values. An image consists of picture elements, or pixels, that represent the value of a function in a particular region. Pixels are typically square. Often in CT, the term voxel, which refers to volume element is also used because the image element represents a section of the object that has a finite thickness. An image can also be described as an array of intensities. The images obtained from x-ray CT are often 8-bit or 12-bit images, which means that the value of a pixel can have integer values from 0 to 255 (2^8-1) or 4095 ($2^{12}-1$). For an n-bit image, the value of zero corresponds to black, while the value (2^n-1) corresponds to white. The values in between correspond linearly to various brightness levels of gray. A commonly used image format for grayscale images is TIFF (tagged image file format), which retains all pixel information.

3.4. Description of the X-Ray CT Scanners Used

The x-ray CT systems used for the imaging experiments are owned and operated by 3D Imaging & Development, Inc. [3DID; formerly Scientific Measurement Systems (SMS)] in Austin, Texas. Each of the two imaging systems used, referred to as the 101B+ and the Alliant scanners, consists of a measurement system to obtain the projection data and reconstruction software to produce an image from the data. The scanners use the same software even though the source and detectors are not identical. Both systems can be described as pseudo-third-generation scanners. The details of the x-ray CT scanners are summarized in Table 3-1.

Table 3-1. X-Ray CT Scanner Characteristics

Model	101 B+	Alliant
X-ray source maximum energy (kV)	420	320
Detector type	scintillator	scintillator
Number of Detectors	125	88
Detector Aperture	0.2 – 1.0 mm	1.0 mm
Maximum Object Weight	50 lbs	~150 lbs
Maximum Object Diameter	10 in	8 in
Maximum Scan Height	30 in	32 in
Maximum Object Height	6 ft	6 ft

The geometry of the scanners is described in Figure 3-9. Unlike a true-third-generation scanner, the detectors are positioned with a distance of 2.5 or 3.5 mm between each of the detectors in the array. While the fan beam of x rays is wide enough to include the entire object space, translation is required to get a complete set of data because of this physical space between detectors. As a result, more than one rotation is required to obtain a complete set of projection data. Following each

rotation, a small translation perpendicular to the x-ray path is performed before acquiring projection data for the next rotation. Each translational position is termed a subposition. As the aperture is opened in the horizontal direction, the number of subpositions required to obtain a complete set of projection data is decreased. The use of subpositions and a variable detector aperture with the pseudo-third-generation geometry allows variation in the image resolution and thus scan time. In contrast, this capability does not exist for a third-generation scanner. With the 3DID scanners, the object, rather than the source and detectors, is rotated and translated during a scan.

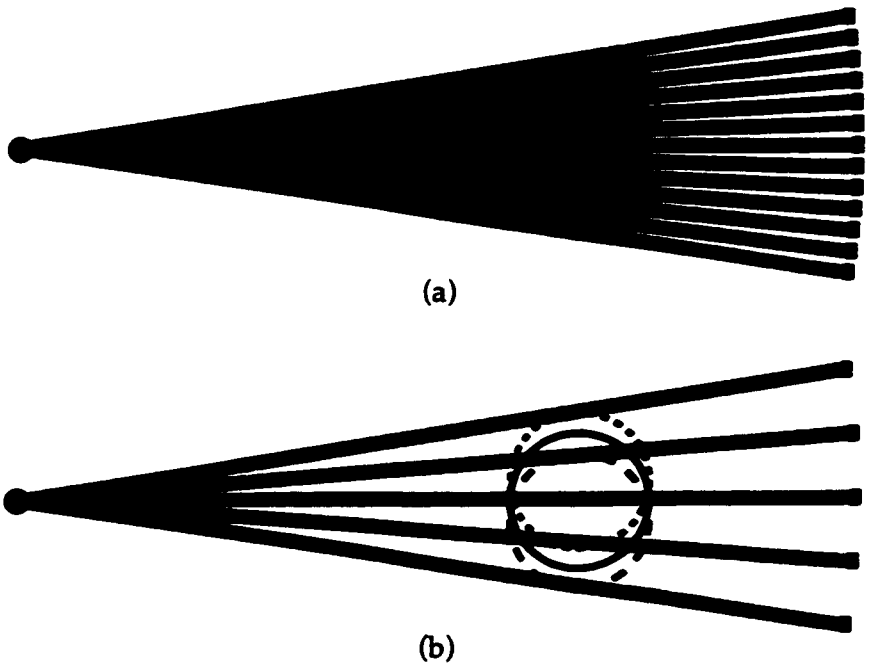

Figure 3-9. (a) Standard third-generation CT scanner in which one rotation is required to acquire the transmission data. (b) Pseudo-third-generation CT scanner used for imaging experiments in which translation of the object, as depicted by the three circles, is required to acquire the transmission data.

3.4.1. X-Ray CT Scanner Specifications

The 101B+ scanner contains a 420-kV Philips industrial x-ray tube as the source. The spot size of the source is 1.5 mm. A fan beam of x rays is produced with a maximum energy that can be varied in the range 120 – 420 kV. The x-ray energy for the studies reported here was 420kV, with a corresponding current of 3mA. The x-ray beam is collimated to eliminate x rays that are not travelling in the direction of the detectors. The source and collimation device are shown in Figure 3-10. Filters, consisting of thin plates of various metals, can be placed at the exit of the collimator to harden the x-ray beam.

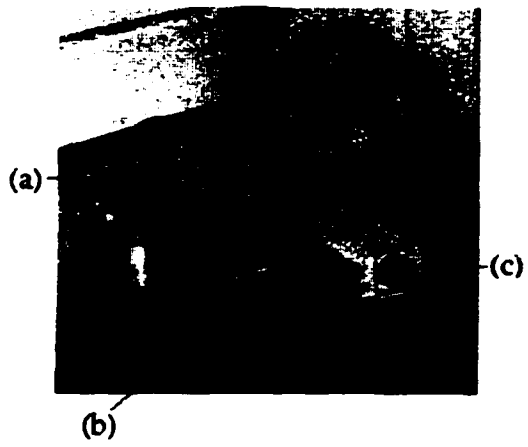

Figure 3-10. X-ray source for the 101B+ scanner used for imaging experiments. (a) Philips industrial x-ray tube. (b) Collimator. (c) Camera to view scan plane (non-essential to x-ray source).

The scanner uses a linear array of 125 scintillation detectors positioned on an arc with equal-angle spacing. Each detector is attached to a photomultiplier tube. The detector system of the 101B+ is shown in Figure 3-11. Prior to the detectors, the x-ray beam is again collimated, which restricts the detectors to measuring only those x rays

that travelled through the scan plane. The measurement of x rays that are incident on each detector is recorded by the computer system. The aperture of the detectors can be varied between 0.2 and 1.0 mm and is not required to be square. The aperture in the horizontal direction defines the best spatial resolution attainable from the scan data. The scan thickness, as defined by the vertical aperture, can be adjusted independent of the spatial resolution of the image, as was shown in Figure 3-2.

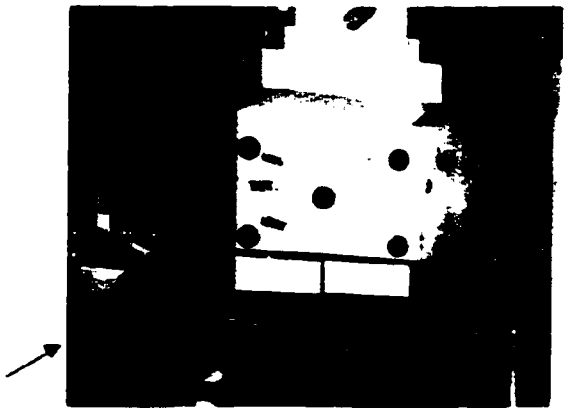

Figure 3-11. Detector system of the 101B+ Scanner. The arrow indicates the location of the collimator leading to the array of 125 scintillation detectors.

The x-ray source for the Alliant scanner at 3DID is a 320-kV Comet industrial x-ray tube which has a 1.8-mm spot size. The maximum energy attainable with the scanner is 320 kV although the energy can be varied. For the imaging performed in this work, the x-ray energy was 305 kV, with a current of 5.2 mA. The x-ray beam is collimated and filters can be used to harden the x-ray beam. The x-ray tube and collimator are shown in Figure 3-12.

A total of 88 detectors are spaced at equal angles in the detector array. Each detector is connected to a photomultiplier tube and a collimator is used to ensure that

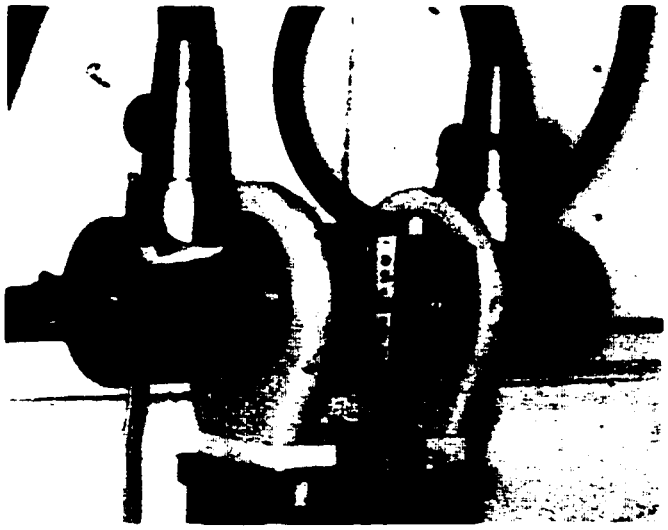

Figure 3-12. X-ray source of the Alliant scanner used for x-ray CT.

the measured x rays travelled through the scan plane. The aperture of each detector is fixed at 1.0 x 1.0 mm^2, which sets the slice thickness and the image resolution. The set of detectors is shown in Figure 3-13.

The mechanical components of both scanners are used to perform the rotations and translations. The object is placed on the turntable of the scanner for a scan. The turntable for the Alliant scanner is shown in the center of Figure 3-13. Drive motors are used to move the object and spatial encoders are used to determine the exact position of the object. The translation of the object occurs in three orthogonal directions. The elevation of the object is varied which defines the scan plane. The distance the object is located from the detectors influences the maximum diameter of the object to be scanned. The third translational motion is required for the pseudo-third-generation geometry.

The computer system is a Sun workstation. The computer is used to control the motion of the system, to acquire and record the data, and to perform the

Figure 3-13. Detector system of the Alliant CT Scanner, which contains an array of 88 individual detectors each with 1.0 x 1.0 mm^2 aperture, is seen on the right side of the scanner as indicated by the arrow.

reconstruction algorithm. The software written for the scanning system is proprietary to the SMS-constructed scanners. Images are output as 8-bit grayscale TIFF images or an array of 32-bit floating point numbers. When TIFF images are created, the data are scaled between a minimum and maximum value.

The image reconstruction algorithm used by 3DID is filtered backprojection. The mathematical filter function incorporated is the Shepp-Logan filter. The fan-beam transmission data are converted to parallel-beam data which are then reconstructed. In addition, an overlap correction is typically included prior to reconstructing the image.

This correction accounts for some of the difference measured by adjacent detectors along the same ray path.

3.4.2. Standard Scanning Startup Procedure

The scanning procedure used at 3DID begins with calibration measurements. The first calibration involves attenuation measurements for two conditions. A set of dark measurements is recorded with the x-ray source off, i.e. with no production of x rays. This measurement is also referred to as an offset measurement and is used to correct for variations between the detectors. With the x-ray source on, but no object between the source and detectors, a set of air measurements is obtained. These values, after being corrected with the dark measurements, are used to determine the initial intensity of the x-ray beam. As discussed previously, this initial intensity of the x-ray beam, I_0, is required to determine the attenuation of the beam through an object. The second calibration measurement required for the 3DID scanners is determination of the shift. The shift is a measure of the location of the center of rotation of the object, which is critical for the reconstruction algorithm. A series of images are acquired with the object shifted horizontally, perpendicular to the central ray path. Based upon the sharpness of the images, the shift is determined. Typically, the shift is determined for the range of elevations at which images will be obtained. Examples of images with correctly and incorrectly adjusted shift values are shown in Figure 3-14. These calibration measurements are acquired at the start of a series of scans, after the detector aperture is adjusted, or after the x-ray source energy is adjusted.

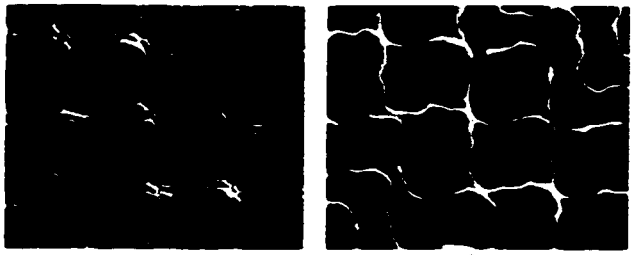

Figure 3-14. (a) Section of an image of dry structured packing for which the incorrect shift value was used. (b) Same section for which the correct shift measurement was determined.

3.5. Imaging Techniques Implemented

3.5.1. Radiogram

A radiogram is a two-dimensional projection of x-ray attenuation that is analogous to traditional x-ray film images. The acquisition of a radiogram of an object is described by Figure 3-15. The radiogram represents the shadow an object makes when x rays are transmitted through the object. During acquisition of a radiogram, the object is translated, but not rotated, such that all attenuation measurements are taken from the same direction. The height of the object is varied by translating the object in the vertical direction to obtain the two-dimensional projection, as shown in (a). For the pseudo-third-generation scanner configuration used by 3DID, additional horizontal translation to the required number of subpositions occurs, as shown in (b). The radiogram is typically used in CT imaging to define scan planes of interest. A radiogram can be used to determine the plane in which features are present, but not the spatial position of those features within the plane.

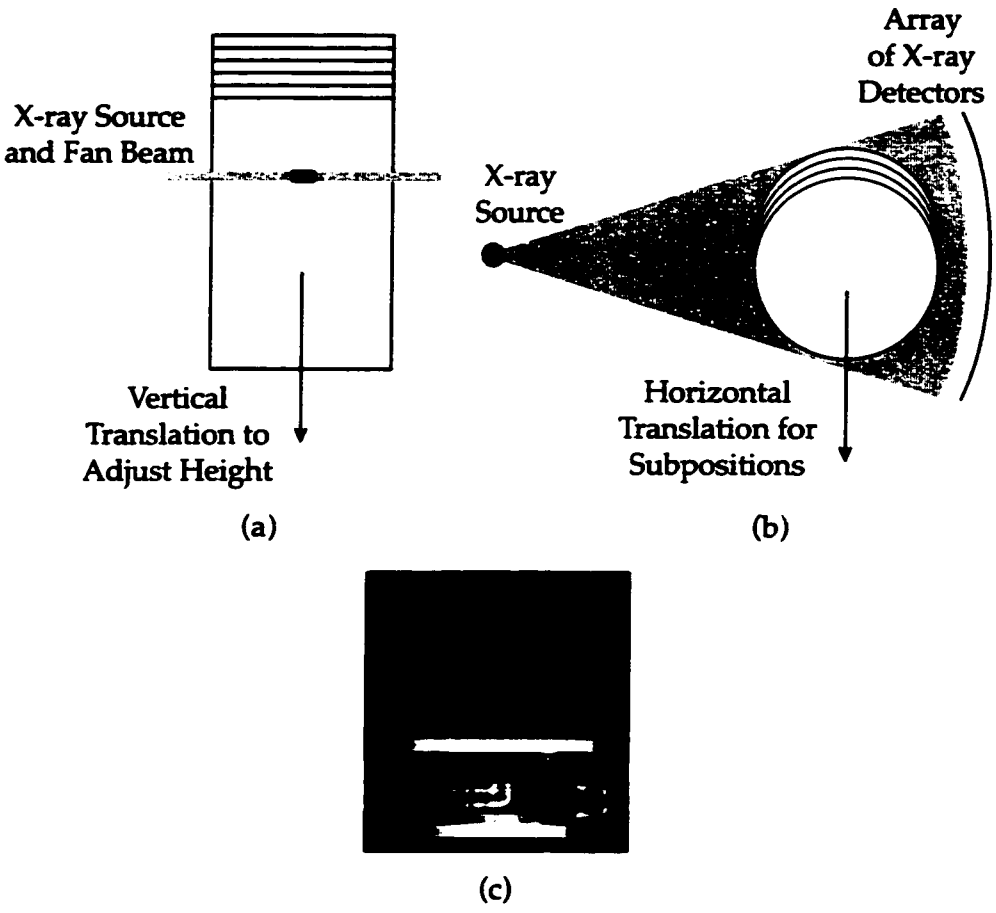

Figure 3-15. Acquisition of a radiogram requires translation of the object in two directions to obtain an image, as shown in (a) and (b). (c) Resulting radiogram is a two-dimensional representation of the attenuation of the x rays through the object.

The radiogram represents the transmission measurements, without image reconstruction required. The dark and air measurements are incorporated and the natural logarithm is calculated, as expressed previously in Equation 3-4, so that the

radiogram represents the integral of the attenuation coefficients along the path of the x ray.

3.5.2. CT Scan

A CT scan, which produces a cross-sectional image of an object, requires transmission data measured from various rotational positions of the object. The geometry of the 3DID scanner is pseudo-third-generation. Both rotation and translation of the object are required to obtain a complete set of transmission measurements as required by the reconstruction algorithm. The process of acquiring a scan with the 3DID scanners is outlined in Figure 3-16.

The parameters required to specify the scan sequence at 3DID include the number of views, the number of subpositions, the snapshot time, and the scan elevations. The number of views specifies the rotational positions at which data will be obtained. The total rotation of 360° is divided by the number of views to determine the degrees of rotation between collection of transmission data. The snapshot time specifies the duration of each measurement. The number of subpositions represents the number of translations required. For each translation, the object is rotated and data are measured. A single scan elevation or a series of scan elevations can be specified. The scan elevation defines the vertical location of the object that corresponds to the center of the slice plane.

The motions of the object during a scan are depicted in Figure 3-17. The object is first rotated, with measurements acquired by each detector at equally spaced rotational positions. The number of views at which data are obtained is typically 600 – 900 for the two 3DID scanners, which corresponds to rotational increments of 0.4° – 0.6°. In Figure 3-16 at the location marked A, an additional step is incorporated for scans of flow systems. A rotation in the opposite direction is required to keep the tubing in which the fluids flow from becoming twisted over time. As indicated, if the

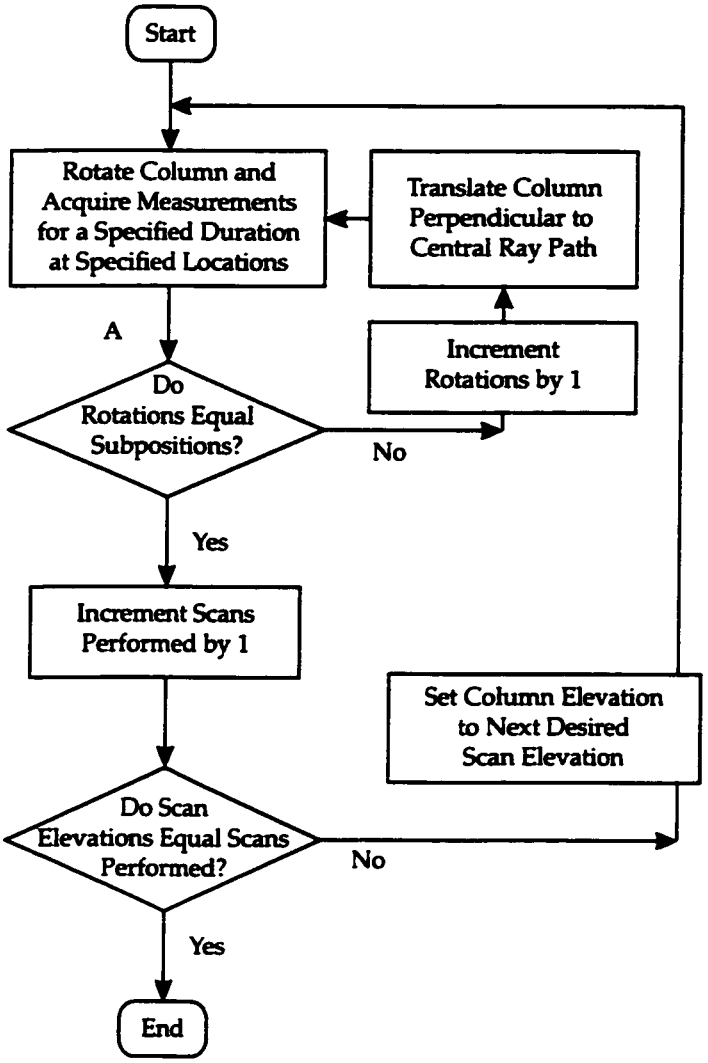

Figure 3-16. Flow chart describing the steps involved in acquiring a series of CT scans using a 3DID scanner.

total number of subpositions has not been reached, a small translation as depicted in Figure 3-17(c) is performed prior to acquisition of transmission data during another rotation. This translate-rotate sequence is continued until all subpositions are

complete. The time required to obtain data for one image with the 3DID systems is approximately 1-5 minutes, depending upon the scanning parameters. For a sequence of scans, the object is moved to the new elevation as shown in Figure 3-17(d) when data acquisition for one scan is complete. The process of acquiring scan data is then repeated at the new elevation.

For each x-ray CT scan performed, a set of transmission measurements referred to as a sinogram is obtained. This set of data is used to reconstruct the cross-sectional image. The equi-angular fan-beam geometry of the scanner, as was depicted in Figure 3-6, indicates that the axes of the sinogram represent β and γ. One set of simultaneously acquired data does not correspond to a complete row or column for the pseudo-third-generation scanner. The acquisition process and the corresponding values in a sinogram are depicted in Figure 3-18 for a simple case. Data acquired simultaneously at each of the detectors are contained within one row. However, a number of spaces, equal to one less than the number of subpositions, is located between the simultaneously acquired values. A row of the sinogram does contain all of the data acquired from one particular view, or rotational position, of the object.

3.5.3. Stationary Transmission Measurements

The acquisition of stationary transmission measurement data is not a standard x-ray CT technique. The measurements are of x-ray attenuation, as with both the radiogram and the CT scan. However, the object of interest remains in one position during the entire scan period. Measurements are acquired for a number of ray paths that is equal to the number of detectors, as shown in Figure 3-19. For the case depicted, measurements are made at each of seven detectors. Adjustment of the aperture of the detectors, as was depicted in Figure 3-2, alters the region of the object through which the ray path passes. A larger aperture corresponds to a wider or taller ray over which attenuation is measured. The stationary transmission measurements

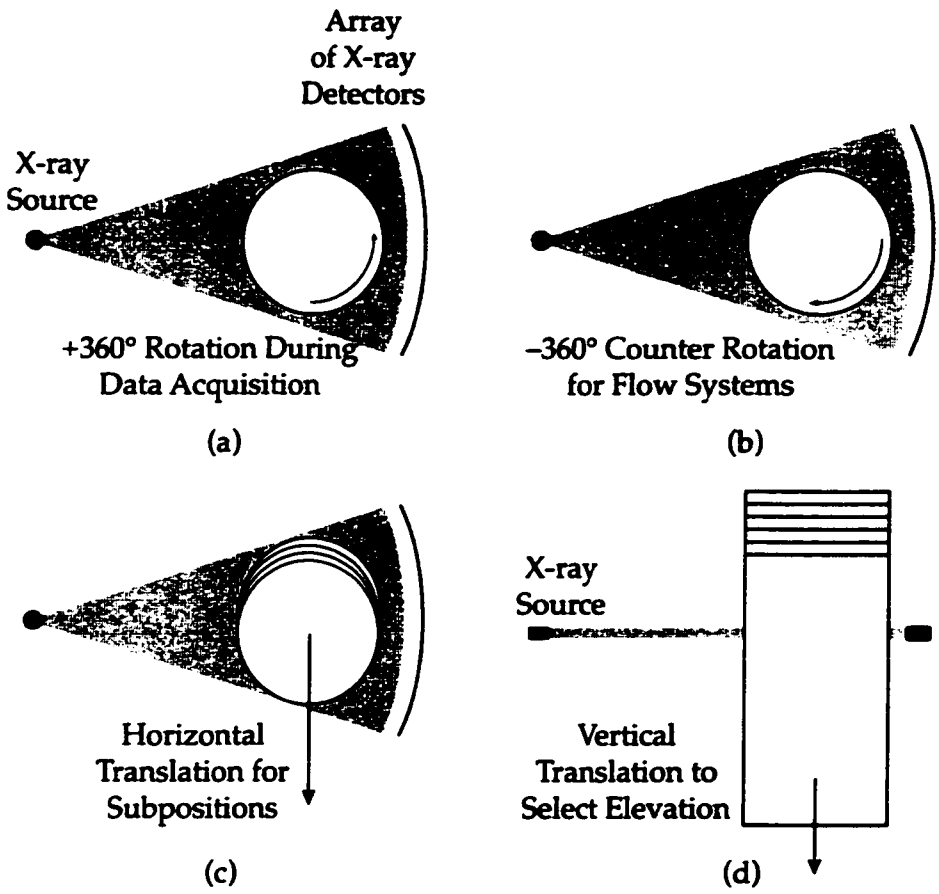

Figure 3-17. Rotation and translation of the object during a pseudo-third-generation CT scan (a) Rotation to acquire data at radial positions. (b) Counter-rotation required for a flow system. (c) Translation required for subpositions. (d) Translation to select elevation of the scan plane.

are obtained simultaneously by each detector over a fixed period of time. The snapshot time is the parameter that specifies the length of the period for each individual measurement.

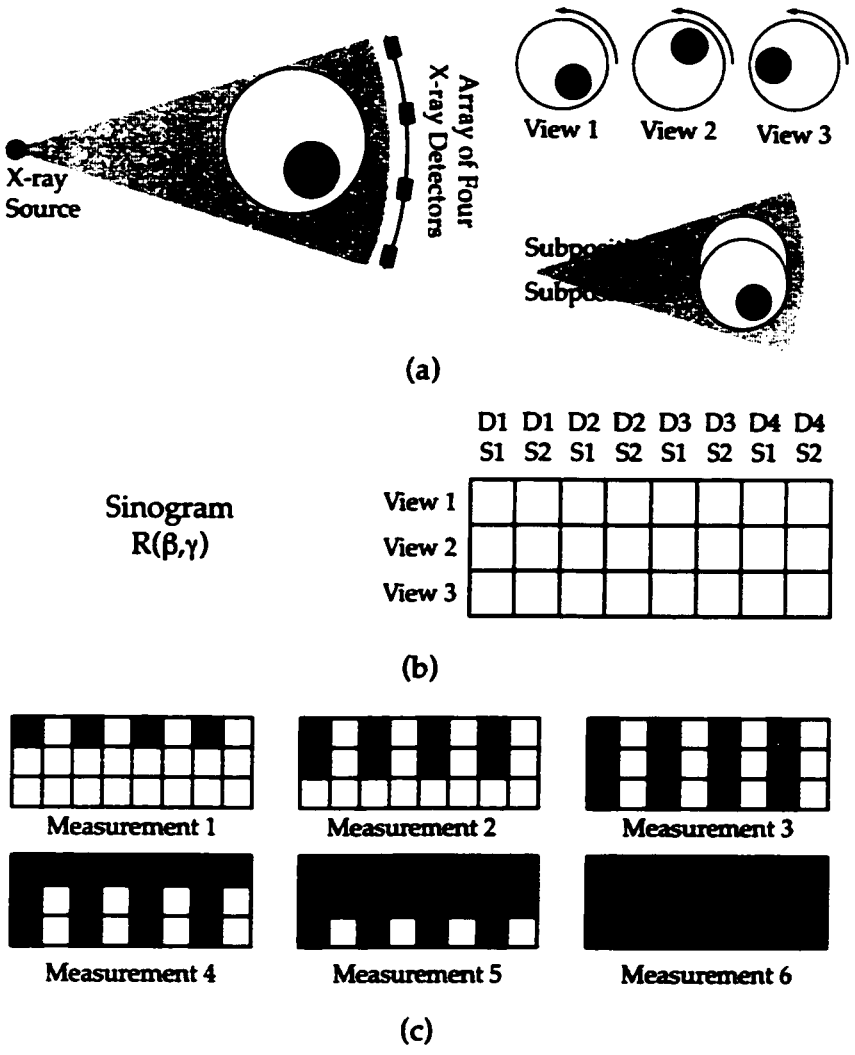

Figure 3-18. Formation of a sinogram image for a pseudo-third-generation scanning geometry in which two subpositions, three views, and four detectors are used. (a) Geometry of views and subpositions. (b) Array representing the sinogram indicating view, detector (D), and subposition (S) corresponding to each pixel. (c) The sequence in which the sinogram values are acquired. Dark pixels indicate values that have been measured.

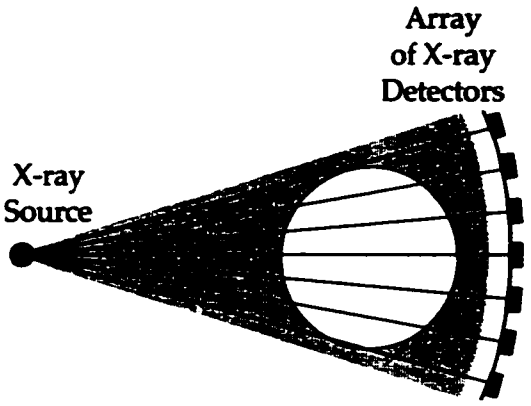

Figure 3-19. Ray paths of the x rays measured during a set of stationary transmission measurements.

3.6. Calculation of Liquid Holdup from Transmission Data

The measurements of x-ray transmission that are instrumental in all of the above described imaging techniques are all of the form described by Equation 3-4. The amount of liquid present in the object space at a given instant in time can be calculated from these measurements, if objects required to determine an appropriate scaling are imaged. An advantage to using the transmission measurements to determine the amount of water present in the column is that the measurement is not dependent upon identification of small regions of liquid in the reconstructed image.

For all of the experimental systems used for this work, there were four materials present: air, water, plastic, and stainless steel. The attenuation of each x-ray beam that passes through the object is represented by d_i, as shown by Equation 3-9. The subscript, i, refers to the path along which the attenuation occurred. The integral on the right side of the equation can be replaced by the product of the attenuation coefficient for each material and the total length through that material along the specific path. If the attenuation coefficient for each material is constant, the

attenuation of the beam can then be represented as shown in Equation 3-10. The total attenuation depends upon the total length of each material and the attenuation coefficient for each material. As previously mentioned, the initial x-ray intensity is obtained by measuring the transmission through the object space, with no object in place. This measurement is valid because the linear attenuation coefficient of air can be approximated as zero. As a result, the equation describing each transmission measurement is simplified as shown in Equation 3-11.

[3-9] $$d_i = \ln\left(\frac{I_0}{I}\right)_i = \int_{\text{ray } i} \mu(s)ds$$

[3-10] $$d_i = \mu_a L_i^a + \mu_w L_i^w + \mu_p L_i^p + \mu_s L_i^s$$

[3-11] $$d_i = \mu_w L_i^w + \mu_p L_i^p + \mu_s L_i^s$$

For the objects used in this work, the total length of each path through the object can be described as the sum of the paths through air, water, plastic, and steel, as shown by Equation 3-12. The length through air includes only the air within the object, not the lengths between the source and the object and the object and the detectors. The void length through the object is defined as the length through air and water, or that not through plastic and steel, as described by Equation 3-13.

[3-12] $$L_i^{tot} = L_i^a + L_i^w + L_i^p + L_i^s$$

[3-13] $$L_i^v = L_i^a + L_i^w = L_i^{tot} - L_i^p - L_i^s$$

Acquisition of x-ray transmission measurements through the object under three sets of conditions is required to calculate the percent of void space comprised of water. The first two measurements are used to determine the scaling, by defining a maximum and minimum amount of water that will be present. The first measurement required

represents the minimum-water condition and is that of the object with no water present, i.e. with the entire void space comprised of air. The second measurement required is that of the object with no air present, i.e. with the void space filled with water. This measurement represents the condition of maximum water. The final measurement obtained is that of the object for which the percent water will be calculated. For these studies, this measurement is of the phantoms with water in select regions, the operating film-flow apparatus, or the operating air-water contactor. Portions of the void space contain air, and portions contain water. The attenuation measured for the condition with maximum water is expressed by Equation 3-14. The subscript i again specifies the measurement along a particular path. The entire set of transmission measurements acquired is comprised of measurements along many paths. Similarly, Equation 3-15 represents the attenuation for the minimum-water condition. The partial-water condition is represented by Equation 3-11, the equation representing the measurement of attenuation through the object. This condition represents the object of interest, and not a condition used for scaling.

[3-14] $$d_i^{max} = \mu_w L_i^w + \mu_p L_i^p + \mu_s L_i^s = \mu_w L_i^v + \mu_p L_i^p + \mu_s L_i^s$$

[3-15] $$d_i^{min} = \mu_a L_i^a + \mu_p L_i^p + \mu_s L_i^s = \mu_p L_i^p + \mu_s L_i^s$$

Each measurement technique involves the measurement of the transmission of x rays along many paths, each of a different length through the object and each comprised of different lengths of each material. The percent water present along each path can be calculated, and the average percent water over the entire set of measurements can be calculated, without specifying these lengths. Both of these calculations are discussed below. The mean of the local percent water calculations is not equivalent to the average percent water.

For vapor-liquid contacting applications, liquid holdup is defined as the volume of liquid per volume of the packed bed. The calculations outlined above to

determine the percent of the void space that is filled with water can be extended to any liquid. To convert from percent liquid to liquid holdup, the void fraction of the packed bed, or other object of interest, must be determined. The relationship between liquid holdup (h_t), void fraction (ε), and percent liquid is described by Equation 3-16, with percent liquid defined as the volume of liquid per volume of void.

[3-16] $$h_t = (\%\ \text{liquid})(\varepsilon)$$

3.6.1. Local Liquid Holdup

The local liquid holdup is of interest in a vapor-liquid contactor, as it provides a measure of the distribution of the liquid. One advantage x-ray imaging has over non-tomographic imaging techniques is the ability to distinguish between cases that contain equal amounts of liquid distributed in significantly different patterns. As depicted in Figure 3-20, two scenarios of flow on structured packing may contain the same amount of liquid. However, due to the maldistribution of the liquid, the mass-transfer performance of the column in (b) will be much worse. The local values of liquid holdup can be determined from the sinogram, i.e. the transmission data.

The percent of void space that is filled with water can be calculated with the use of the three sets of measurements described above. For calculating percent water, it is important that the orientation of the object is the same for all of the measurements. The expression for local percent water along path i is shown by Equation 3-17. The fraction of water is equal to the total length of water along a path divided by the total length of void along the same path. The expression was derived by combining Equation 3-11, Equation 3-14, and Equation 3-15. Calculation of a local value of percent water is accomplished with the use of the values in the same row and column of the sinograms of the three required conditions.

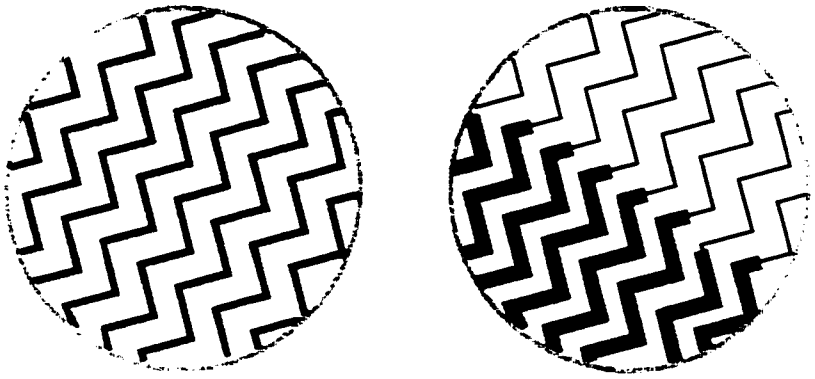

Figure 3-20. Cross section of two columns containing structured packing and the same liquid holdup. (a) well-distributed liquid leads to good performance. (b) maldistribution of liquid leads to poor performance.

[3-17] $$\% \text{ water} = \frac{L_i^w}{L_i^v} = \frac{d_i - d_i^{min}}{d_i^{max} - d_i^{min}}$$

3.6.2. Section-Averaged Liquid Holdup

The section-averaged liquid holdup can also be determined from the x-ray transmission values along each path. The value that is desired is the total amount of water present in the column, as indicated by the sum of the length along each path. To determine the percent of void that is filled with water, the sum of the void length must also be calculated. The ratio of the total length of the water along all N ray paths through the column to the total length of void along all paths, as expressed in Equation 3-18, represents the average percent water for the section. To accomplish this calculation, it is not required to determine the path length through each material for each ray path. The difference between Equation 3-11 and Equation 3-15 is shown, and

subsequently simplified, in Equation 3-19. The variables $\bar{d}_i$ and $\overline{d_i^{min}}$ represent the average measured attenuation over all ray paths for the partial- and minimum- water conditions. Similarly, the difference between Equation 3-14 and Equation 3-15 is shown in Equation 3-20, with $\overline{d_i^{max}}$ representing the average of the attenuation along all ray paths for the maximum-water condition. The ratio of these two differences is equivalent to the average percent water for the section, as described by Equation 3-18.

[3-18] $$\overline{\%\ \text{water}} = \sum_{i=1}^{N} L_i^w \Big/ \sum_{i=1}^{N} L_i^v$$

[3-19] $$\mu_w \sum_{i=1}^{N} L_i^w = \sum_{i=1}^{N} (d_i - d_i^{min}) = \sum_{i=1}^{N} d_i - \sum_{i=1}^{N} d_i^{min} = N(\bar{d}_i - \overline{d_i^{min}})$$

[3-20] $$\mu_w \sum_{i=1}^{N} L_i^v = \sum_{i=1}^{N} (d_i^{max} - d_i^{min}) = \sum_{i=1}^{N} d_i^{max} - \sum_{i=1}^{N} d_i^{min} = N(\overline{d_i^{max}} - \overline{d_i^{min}})$$

The average liquid holdup for a region of interest is calculated using Equation 3-21. This expression is not equivalent to the average of the expression shown in Equation 3-17.

[3-21] $$\overline{\%\ \text{water}} = \frac{\sum_{i=1}^{N} L_i^w}{\sum_{i=1}^{N} L_i^v} = \frac{\bar{d}_i - \overline{d_i^{min}}}{\overline{d_i^{max}} - \overline{d_i^{min}}}$$

These calculations can be performed with the transmission measurements collected for the three scenarios described above. The mean of all values in each of the three sinograms is first calculated and then the ratio of the difference between these means is calculated. Alternatively, if the path length corresponding to each

measurement was known, the local values of holdup described in the previous section could simply be weighted by the length and then averaged.

3.7. Experimental Systems Imaged

The column used for the imaging studies was constructed of acrylic, with an aluminum base. The column contains four sections that are each six inches in diameter and are depicted in Figure 3-21. The aluminum base, the 18-inch section, and the 24-inch section were originally used in the studies by Cartmel [8]. The column contained different internals for the various imaging experiments which are described in the following sections.

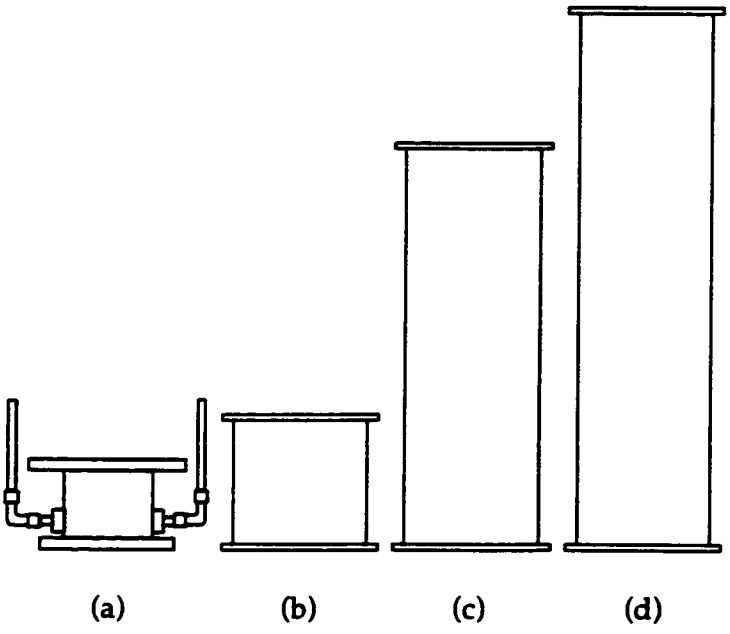

Figure 3-21. Major components of the 6-inch-diameter column used for imaging studies. (a) 3 1/2-inch-tall aluminum base, (b) 6-inch-tall acrylic section, (c) 18-inch-tall acrylic section, and (d) 24-inch-tall acrylic section.

The aluminum base section is three and a half inches tall, contains two 3/4-inch NPT flow connections, and has holes for attaching to the turntable of the scanner. This section is shown in Figure 3-22. The inlet line passes through one of the 3/4-inch NPT connections of the column using a bore-through fitting. Inside the column, the inlet line ends with a 1/2-inch Swagelock male thread. The water outlet line is attached to the second 3/4-inch NPT connection. Externally, the lines connecting to the contactor are 3/4-inch OD (1/2-inch ID) flexible vinyl tubing. For flow experiments, the water is pumped from the contactor using a 1/12 horsepower pump. Four holes at the bottom of the base section match the bolting pattern on the turntable of the scanner. The column is secured to the scanner by bolting through these holes. The other four holes are threaded and are used to attach stainless steel supporting rods.

The remainder of the column is comprised of three sections constructed of clear acrylic of 1/8-inch wall thickness, as shown in Figure 3-22. Each acrylic section has a flange attached to each end. The sections are six-, 18-, and 24-inches tall. The 6-inch-tall section contains grooves at each flange in which o-rings are placed. The 18-inch- and 24-inch-tall sections contain these grooves and o-rings at the bottom only.

A water-tight seal is obtained by bolting the sections together with an o-ring in between. Stainless-steel supporting rods that extend the length of the column are used to provide added stability. The rods pass through the flanges of the two taller acrylic sections and are bolted into the base section.

3.7.1. Phantoms for Characterizing a Static System

In CT imaging, a phantom is defined as a test object containing features of known size, spacing, and contrast, which can be scanned to determine spatial or density resolution [1]. A set of phantoms was designed to determine characteristics

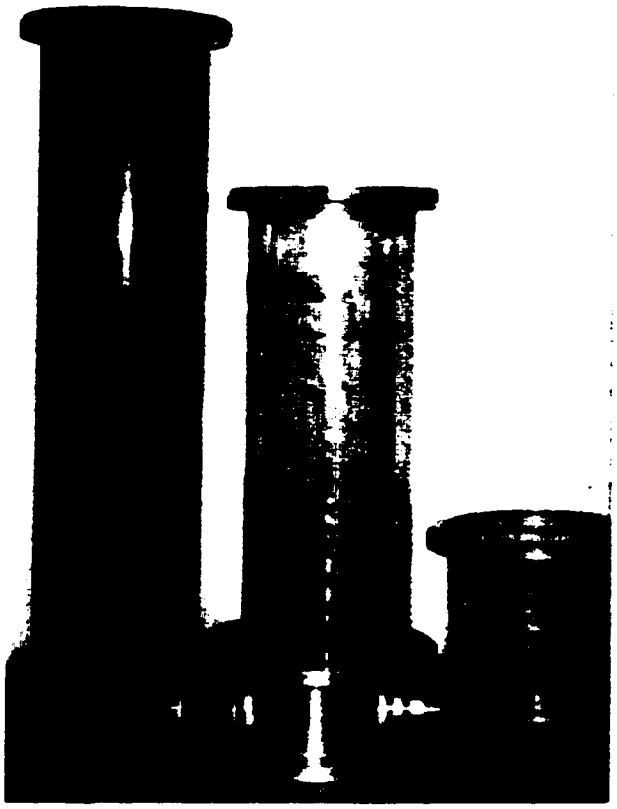

Figure 3-22. Photograph of the main sections of the 6-inch diameter column. (back, l-r) 24-inch acrylic section containing structured packing, 18-inch acrylic section, and 6-inch acrylic section. (front) aluminum base section including fluid connections.

that are important in applying x-ray CT to a vapor-liquid system containing stainless-steel packing.

Four phantoms were designed to incorporate static interfaces between three materials: air, water, and stainless steel. Flat and curved surfaces were constructed of 302 stainless steel. The thickness of the metal was 0.015 inches (0.38 mm). The curved surfaces all had a radius of curvature of 5/16 of an inch. The metal surfaces

were placed at five different angles to the horizontal: 0°, 30°, 45°, 60°, and 90°. Regions of air and water were included to form air/metal/air, air/metal/water, and water/metal/water interfaces at each of the angles. To include all interface combinations, fifteen interfaces were incorporated with a flat metal surface and fifteen with a curved metal surface. These interfaces were divided between four phantoms that are each 0.625 inches wide and 2.5 inches tall. The length of each is between 2.25 and 3.25 inches. Each phantom was constructed between 0.12-inch-thick walls of acrylic. The set of four phantoms was placed upon an acrylic platform of 5.625-inch diameter. A photograph of the phantoms on this platform is shown in Figure 3-23. The phantoms and platform were then placed inside of the air-water contactor, just above the aluminum base, for the scanning experiments.

Both the 101B+ scanner and the Alliant scanner at 3DID were used for the imaging experiments. With the phantoms inside, the air-water contactor was bolted to the turntable of the scanner. A radiogram of the phantoms was acquired to determine the scan elevations desired. CT scans were performed with the 101B+ scanner using the two sets of scanning parameters listed in Table 3-2. The images obtained represent horizontal cross-sectional slices through the phantoms. Images were obtained at various elevations to capture each of the thirty interface combinations. Similar horizontal cross-sectional images were obtained with the Alliant scanner. The amount of water present in the phantoms was varied for scans on the Alliant scanner. The parameters for these scans are shown in Table 3-3.

The scan elevation is defined by the vertical position of the center of the detectors. The vertical-step size between slices is specified independently of the detector aperture. For the sequences of images obtained with the 101B+ scanner, the difference between scan elevations was set to 0.15 mm for both the high- and low-resolution images. At the high-resolution scanning parameters, the step size is half the thickness of the slice. Therefore, two consecutive slices have half of the slice in

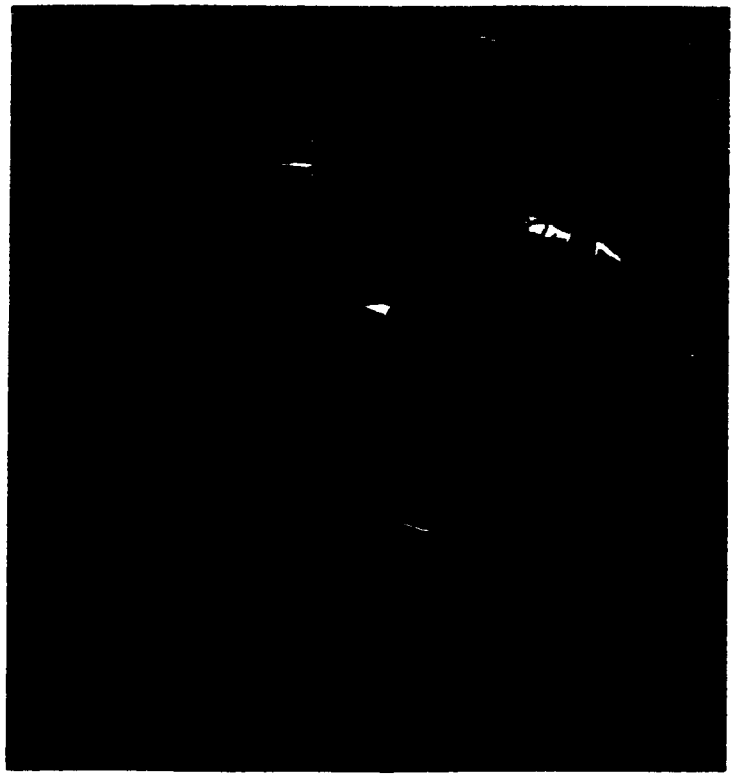

Figure 3-23. Phantoms used to characterize regions and interfaces of importance in a vapor-liquid contactor.

common at the high resolution. At the low resolution, two consecutive slices have more than half of the slice in common. The relative location of slices for the two sets of scanning parameters is illustrated in Figure 3-24.

A total of 120 images of the phantoms were obtained with the 101B+ scanner. The images included a total of 44 elevations. In addition to scans of the phantoms with the desired interfaces, scans were performed with no water and with the phantoms completely submersed. The phantoms with desired regions of air, water, and steel were scanned at each elevation for both sets of operating parameters (88

Table 3-2. CT Scanning Parameters Used for Imaging the Phantoms with the 101B+ Scanner.

Parameter	High Resolution	Low Resolution
Detector aperture	0.3 x 0.3 mm^2	1.0 x 1.0 mm^2
Views	900	600
Subpositions	13	4
X-ray filter	0.040 lead	0.040 lead
Snapshot time	0.015 sec	0.015 sec
Slice scan time	4 min	1 min
Image pixel size	0.15 mm	0.4 mm

Table 3-3. CT Scanning Parameters Used for Imaging the Phantoms with the Alliant Scanner

Parameter	Value
Detector aperture	1.0 x 1.0 mm^2
Views	750
Subpositions	7
X-ray filter	0.018 lead
Snapshot time	0.007 sec
Slice scan time	1.7 min
Image pixel size	0.34 mm

images). The dry and flooded scans were done at eight selected elevations for both sets of scanning parameters (32 images).

The Alliant scanner was used to obtain 108 images of the phantoms. The scans were obtained at a total of 18 elevations, with a 0.5 mm increment between adjacent

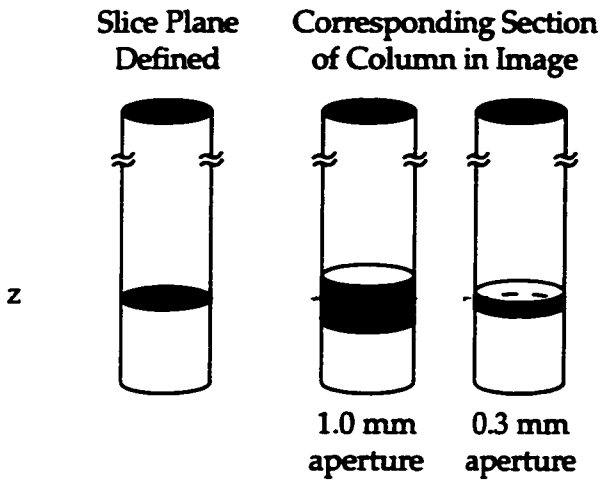

Figure 3-24. Definition of slice planes for scans in which the vertical aperture, and thus slice thickness, was at 0.3 mm and at 1.0 mm.

slices. Initial scans were obtained of the phantoms with no water present in the column. Each of the four phantoms was subsequently filled with water and four sets of images were obtained. The final set of scans was obtained with the phantoms submersed in water.

The CT images of the phantoms were analyzed to characterize the materials present. The four materials that are of interest in an operating air-water contactor are air, water, stainless steel (or plastic), and acrylic. The phantoms were designed to incorporate these materials with a known distribution. The images were analyzed using three main methods. The first method involved obtaining the image histogram to obtain the total count of the number of pixels at each value of grayscale in the image. The second method of analysis was performed to identify the spatial position of pixels at particular values of grayscale. The correspondence between particular features and regions with a range of grayscale was thus determined. The final method

involved obtaining the values of the attenuation coefficient along select lines through features, particularly interfaces between phases, in the images.

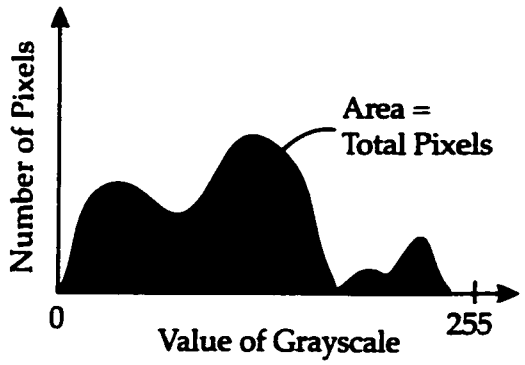

Figure 3-25. An example of an image histogram.

An image histogram is a plot of the frequency of each value of grayscale in the image. A generic histogram is shown in Figure 3-25. For the CT images in these studies, there are 256 distinct values of grayscale in the range from 0 to 255. The abscissa of a histogram plot is the grayscale, while the ordinate is the count of pixels at each value. The total area under the histogram curve is equal to the number of pixels in the image. A histogram can also be obtained for a region of interest of the image, in which case the area under the curve is equal to the number of pixels in the region. A homogeneous region within a CT image is expected to have a normal (Gaussian) distribution due to the nature of the noise in CT imaging [1]. If there are two homogeneous regions in an image, the histogram will be bimodal. When there is a small difference in the mean value of each region, the two Gaussian peaks will overlap between the means along the grayscale. A pixel that has a value of grayscale in this overlap has a non-zero probability of being part of either region.

For the CT images of the phantoms, the region of interest selected was the area inside the acrylic column wall. For the dry, partially-filled, and submerged images of

the phantoms, histograms were determined using a program written in the LabVIEW 5.1 application from National Instruments Corporation (Austin, Texas).

The spatial location of values in small ranges of the grayscale was investigated further with the use of another program written for LabVIEW. An image and range of grayscale was selected. Pixels in the range specified were set to white and all other pixels were set to black. The location of pixels in the original image in each range of grayscale was evaluated. The result was a specification of what features a pixel of a given value may represent. In addition, the range of values that each feature of interest may have was also specified.

Line profiles were evaluated for selected lines through the phantoms. Lines were identified through each of the four phantoms, along which the values of grayscale profile were determined. The lines passed through the stainless-steel features of interest, including curved and flat surfaces at the various angles. In addition, regions of air and water were along the paths of the lines. A program written for LabVIEW was used to perform the calculations. The coordinates of the lines of interest are required input to the program, and the outputs of the program include a file that contains the values of grayscale along the lines and an image with the lines marked. These profiles were obtained to characterize and illustrate the interfaces through which the line passed.

In addition to characterizing the materials and interfaces present in the phantoms, the method of calculation of the percent water from the sinogram was evaluated. The expected percent water in a given cross section of the phantoms was calculated from the known geometry of the phantoms. The position of the metal surfaces was determined after the phantoms were constructed. The actual dimensions are shown in Appendix A. Based upon the known geometry of the phantoms, the expected percent water was calculated for each of the scan elevations. The details of these calculations are presented in Appendix A. The mean percent water was

calculated using the entire set of 32-bit transmission data, as described by Equation 3-21. The expected water was compared to the percent water calculated from the transmission data, also referred to as the sinogram. A program was written using LabVIEW to calculate the mean of each 32-bit sinogram. These calculations were performed for the scan elevations at which scans of the maximum and minimum water conditions were obtained.

3.7.2. Film-Flow System

A film-flow apparatus was designed and constructed to evaluate the feasibility of measuring the thickness of a thin film of fluid on a steel surface with x-ray CT. The apparatus is a wetted-wall system in which the fluid flows up the center of a vertical pipe and forms a film on the outside of the curved surface. The steel surface was a standard nominal-3-inch schedule-10S stainless-steel pipe, with the exterior surface electropolished. The actual outside diameter of the pipe is three and a half inches with a wall thickness of 0.12 inches. The pipe was welded to a flat 6.5-inch-diameter stainless steel plate in an off-center position. Two 1-inch-diameter drainage holes were drilled in the steel plate. A tube of 0.5-inch diameter was welded through the center of the large pipe for the inlet flow. A photograph of the system is shown in Figure 3-26.

As depicted in Figure 3-27, the film-flow apparatus was designed to be contained within the 6-inch-diameter column. The steel plate was bolted between the 6-inch and 18-inch sections of the column, with o-rings on both the upper and the lower surfaces to ensure a tight seal. A section of 1/2-inch stainless-steel tubing was connected to the 1/2-inch Swagelock fitting inside of the aluminum base section. Vinyl tubing of 3/4-inch OD (1/2-inch ID) was used to connect the feed line to the 1/2-inch-diameter tube of the film-flow apparatus. As shown in the flow diagram in Figure 3-28, liquid is fed to the column from a six-gallon tank and is recycled back to

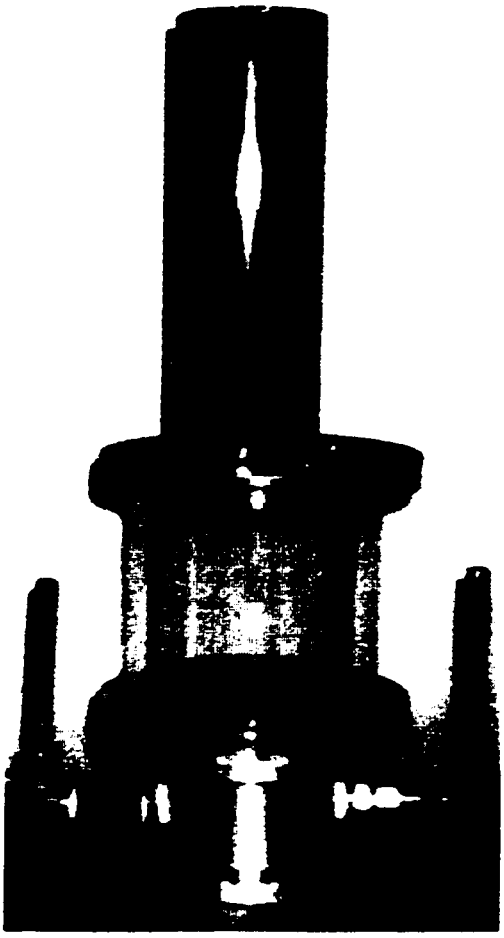

Figure 3-26. The wetted-wall film-flow apparatus used to determine feasibility of measuring the thickness of a thin fluid film. The 18" acrylic section has been removed from around the top segment.

the tank from the column. Water from the house supply is pumped from the tank to the column using a Ismatec compact drive with a Micropump cavity-style pumphead. The pump flow range is 32-3200 mL/min. Water was removed from the column through the second fluid connection in the aluminum section using the 1/12-horsepower pump.

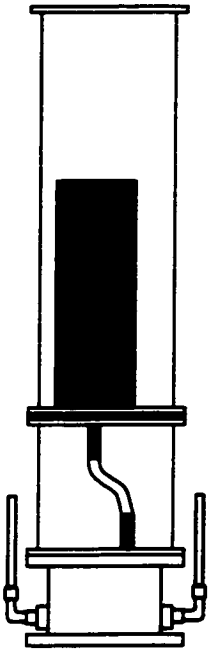

Figure 3-27. Film-flow apparatus for measuring film thickness on a curved vertical surface of stainless steel.

The actual flow rates and the accuracy of the metering pump were measured experimentally. Water was collected and measured using a graduated cylinder for flows in the range desired. Repetition of the measurement was performed for each rate, with all measurements occurring in a random order. The pump accuracy was verified by repeating measurements on a total of four days over a 5-month period.

The column containing the film-flow apparatus was bolted to the turntable of the CT scanner during experiments. The inlet and outlet tubing was suspended from above the scanner, and the counter-rotation step was implemented to avoid entanglement of the tubing. Radiograms of the column were obtained from two orthogonal directions to determine the levelness of the top of the film-flow apparatus. Adjustments were made by placing 0.041-inch-thick shims under two corners of the column. The scan elevation was determined from the radiograms.

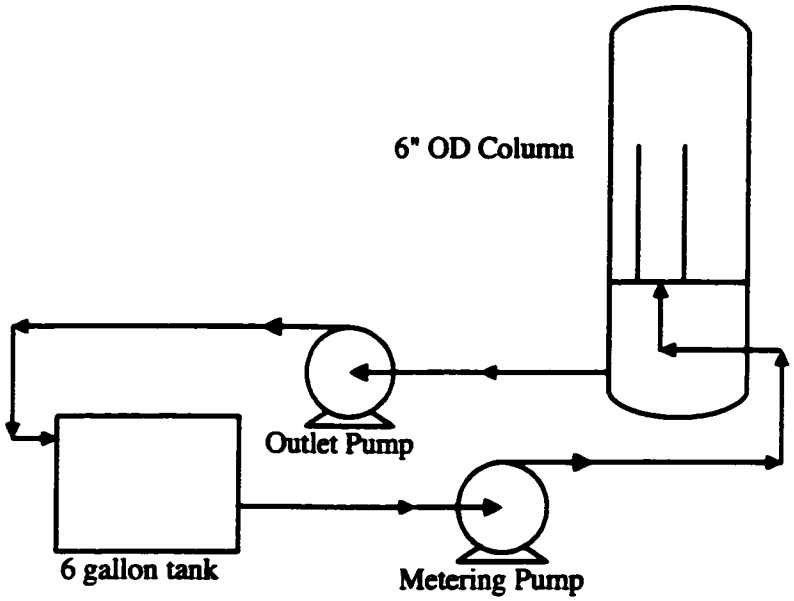

Figure 3-28. Flow diagram for the film-flow apparatus.

The film-flow apparatus was operated at six flow rates and 38 CT images were obtained using the Alliant scanner of 3DID. The set of scanner parameters used for the imaging is listed in Table 3-4. Prior to introducing water to the apparatus, a set of dry scans was acquired. Scans of the column with the 3.5-inch-diameter pipe filled with water were obtained. In addition, scans were obtained with the entire column filled with water. A total of 26 CT images were obtained for water flow rates in the range 0.19-0.73 gal/min. Analysis of the images was performed to measure the average film thickness for each flow case. The calculated values for film thickness were then compared with the film thickness predicted from theory for each flow rate.

Experimentally, the film thickness depended upon the flow rate of the water to the column. The relationship between the volumetric flow rate and expected film thickness was derived from the Navier-Stokes equation. A detailed derivation is presented in Appendix B. Equation 3-22 and Equation 3-23 express the relationship

Table 3-4. Parameters for X-Ray CT Scanning of the Film-Flow Apparatus

Parameter	Value
Model	Alliant
Detector aperture	1.0x1.0 mm
Views	750
Subpositions	7
X-ray filter	0.018" lead
Snapshot time	0.007 sec
Slice scan time	2.3 min
Image pixel size	0.34 mm

which must be solved iteratively to calculate the film thickness for a given flow rate. The flow rates used for experiments, and the corresponding expected film thickness are presented in Table 3-5.

[3-22] $$Q = \frac{\pi \rho_L g_z R^4}{2\mu_L}\left(-\frac{3a^4}{4} + a^2 - \frac{1}{4} + a^4 \ln a\right)$$

[3-23] $$\delta = R(a-1)$$

The expected thickness of the film of water is approximately the same as the pixel size specified for the imaging experiments. The smallest film has a thickness that is 70 percent of the pixel size, while the largest is only eight percent larger than the width of a pixel. At these sizes, the film is not expected to be fully resolved; i.e., if two films of this size were located with a gap of equal size between the films, the individual films would not be distinguishable. A feature of an object, that is smaller than what can be fully resolved with an x-ray CT imaging system, can still be identified in an image. However, the linear attenuation coefficient of the feature in the

Table 3-5. Water Flow Rates for Film-Flow Experiments and Film Thicknesses Predicted from Theory

Water Flow Rate (gal/min)	Film Thickness (mm)	Film Thickness ($x10^{-3}$ in)
0.19	0.236	9.29
0.28	0.268	10.6
0.37	0.294	11.6
0.46	0.317	12.5
0.59	0.344	13.5
0.73	0.368	14.5

image will be less than the true attenuation coefficient. In addition, the apparent thickness of the feature will be larger than the actual thickness. However, the total attenuation of the x-ray beam due to the feature is still consistent with the thickness of the material that is present.

The objective of image analysis was to measure the film thickness from the CT image for each of the flow conditions. Prior to measuring the film thickness, the image histograms were calculated for inside the column region to provide quantitative comparisons of the images. In addition, the line profiles were obtained along select paths perpendicular to the metal surface. The LabVIEW programs used for these calculations were the same as for the comparable calculations using the phantom images. Two methods of image analysis were then applied to obtain quantitative measures of the film thickness. The first calculation method produced an average film thickness along the entire surface. The second method of calculating film thickness produced average values for each 5° section of the film, which were averaged to produce the mean along the entire circumference. Both methods of calculation using the CT images involved first subtracting the pipe-full image from the flow image. In

addition to the analysis of the CT images, the sinograms were used to calculate the percent of water in the column due to the flow of the film. The details of each calculation method follow.

The two methods of image analysis have several steps of analysis in common. A difference image between the flow image and the image of the film-flow apparatus with the pipe full of water was calculated. The resulting difference image, which represents water outside of the metal pipe, was then converted into polar coordinates. The center of the polar coordinate system was defined as the center of the metal pipe. The location of the center of the pipe in the original image was calculated using a proprietary image analysis algorithm developed by SMS to outline an object with a circular cross section. The conversion to polar coordinates involved bilinear interpolation to determine values that do not fall directly on a point in the Cartesian system.

The first method of image analysis, which will be described as the maximum-value method, continued with the objective of determining an average film thickness along the entire film surface. In polar coordinates, the average of each column was calculated, which is analogous to calculating a radial average in Cartesian coordinates. The average images were then converted back into Cartesian coordinates, using bilinear interpolation. As mentioned previously, the film of water is not fully resolved in the images. Thus, in the image, the film will be wider and less bright than if fully resolved, as depicted in Figure 3-29. The difference in the attenuation is anticipated to be observed by a variation in brightness of the film in the difference images. The maximum value in the film region of the polar-averaged difference image, μ_{film}, will be determined. As the film becomes thinner, this value will decrease. The attenuation coefficient for a fully-resolved region of water, μ_{water}, can be used to subsequently calculate a film thickness from this calculated attenuation coefficient. The film thickness is calculated according to Equation 3-24 for the maximum-value method.

Alternatively, known values of film thickness can be used to scale the thickness calculated with the maximum-value method.

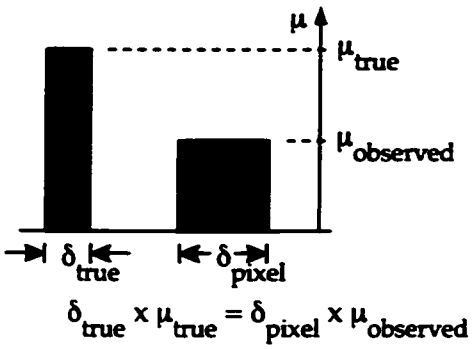

Figure 3-29. Depiction of the observed linear attenuation coefficient for a feature that is not fully-resolved for a case with no measurement or reconstruction errors.

$$[3\text{-}24] \qquad \delta = \frac{\mu_{film} \times \text{pixel size}}{\mu_{water}}$$

The second method for calculating film thickness involved integration of the attenuation of the x-ray beam due to the water film. These calculations, which will be termed the integration method, were performed to measure the average film thickness and to quantify the variation in film thickness around the steel pipe. The analysis was again performed on the difference image after transformation into polar coordinates. The region of integration to determine the film thickness was defined by three methods. These values resulting from the three definitions were compared to evaluate the accuracy in predicting the film thickness. Initially, the edges of the region of integration were defined by the center of the pipe and a circle outside of the film. The second definition used specified the edges of the average water film as the region of integration. The final definition further limited the region of integration. The edges

were specified by determining the location at which the attenuation value of the average water film equaled half of the attenuation attributed to water. This definition was set to reduce the amount of noise in the calculation, and was expected to calculate a film thickness less than the actual thickness. However, further scaling could be applied to get a more accurate calculation. For each definition of the range of integration, an average value of film thickness was determined for each 5° section of the column, to provide a total of 72 values for each image. To determine each value, the integrated attenuation was divided by the attenuation coefficient determined for water to yield the integration length.

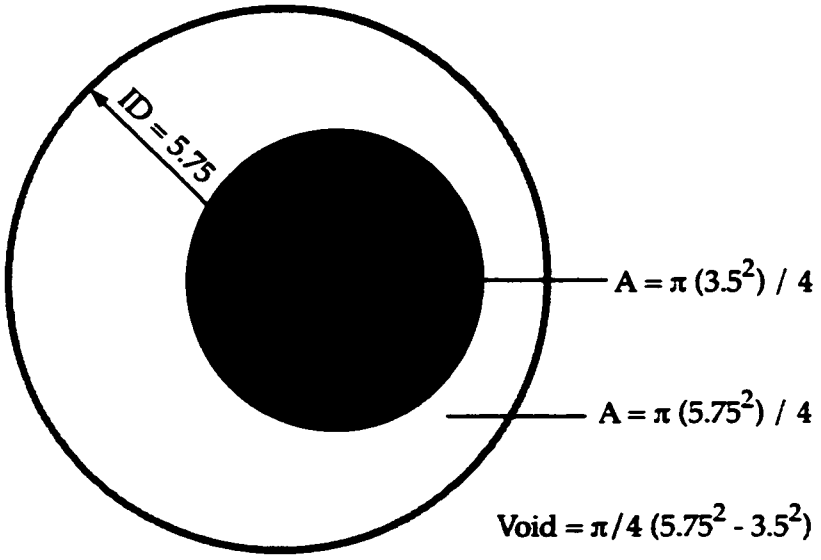

Figure 3-30. Area defined as void for the film-flow scans.

The sinogram was used to calculate the percent water during a scan, and subsequently the average film thickness. The procedure outlined in Section 3.6.2 was applied to calculate an experimental value of percent water using sinograms from

three conditions, according to Equation 3-21. The minimum-water condition was specified as that with water in the inner region of the stainless steel pipe. The maximum-water condition was the scan in which the entire column contained water. The total void area is the region between the steel pipe and the column wall, as shown in Figure 3-30. The percent water in this region depends upon the film thickness, δ, as described by Equation 3-25. The same relationship is described by Equation 3-26, in which the film thickness is calculated from the predicted percent water. For the range of flow rates used for the film imaging studies, the maximum theory-predicted percent water is 0.5%.

$$[3\text{-}25] \qquad \%\ \text{water} = \frac{(3.5+\delta)^2 - (3.5)^2}{(5.75)^2 - (3.5)^2}$$

$$[3\text{-}26] \qquad \delta = \sqrt{(\%\ \text{water})[(5.75)^2 - (3.5)^2] + (3.5)^2} - 3.5$$

3.7.3. Air-Water Contactor

An air-water contactor was designed to image counter-current fluid flow through a packed bed. The contactor consists of three main sections: the base section, the packed section, and a top section. A schematic of the air-water contactor is shown in Figure 3-31.

The top section of the contactor contains the liquid distributor and the mist eliminator. The liquid is fed to the liquid distributor at the top of the column through 3/4-inch-OD vinyl tubing. The riser-type liquid distributor was designed and constructed by Koch-Glitsch, Inc. It uses four drip points to provide a drip point density of 22.2 points/ft^2. A York plastic mesh mist eliminator is located above the liquid distributor to remove entrained water from the exit air.

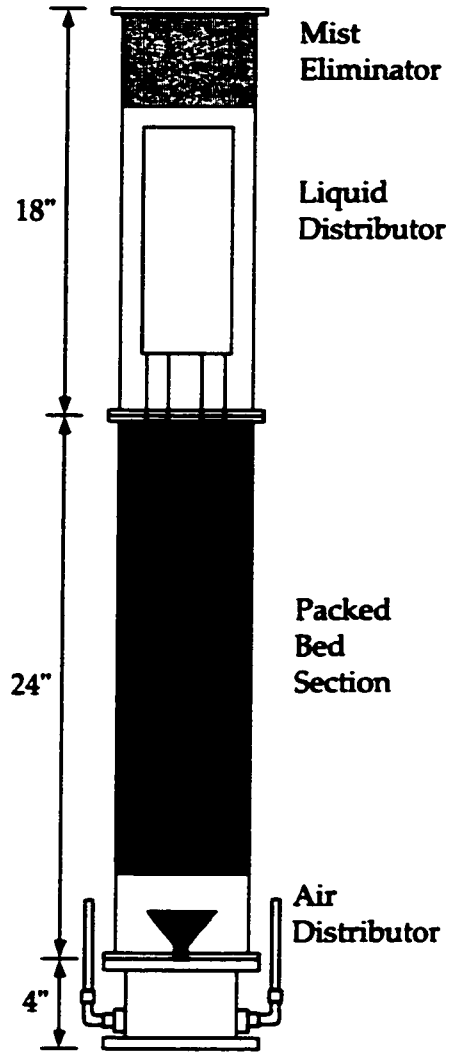

Figure 3-31. Schematic of the 6-inch-diameter air-water contactor used for x-ray imaging experiments.

The packed section contains the air distributor and the packed bed. A cone-type air distributor is used. The base of the inverted cone is four-and-a-half inches in diameter and is covered with a perforated plate. The cone tapers to a 1/2-inch

stainless-steel-tubing connection that is connected to the 1/2-inch Swagelock fitting inside the base of the column. The packed bed for these experiments consisted of two 8-inch tall elements of Mellapak 500Y stainless-steel structured packing (a_p = 507 m^2/m^3, ε = 0.975 [35]). Wiper bands were located at the top and bottom of each element. The elements were rotated 90° with respect to each other when installed.

The base section provides flow connections at the bottom of the contactor. The air inlet line passes through one of the 3/4-inch NPT connections using a bore-through fitting. The water outlet line is attached to the other 3/4-inch NPT connection. The water is pumped from the contactor using a 1/12-horsepower pump. The base section is used to bolt the contactor to the turntable and to secure the end of the support rods. In Figure 3-33, the column is shown with the air-water contactor internals.

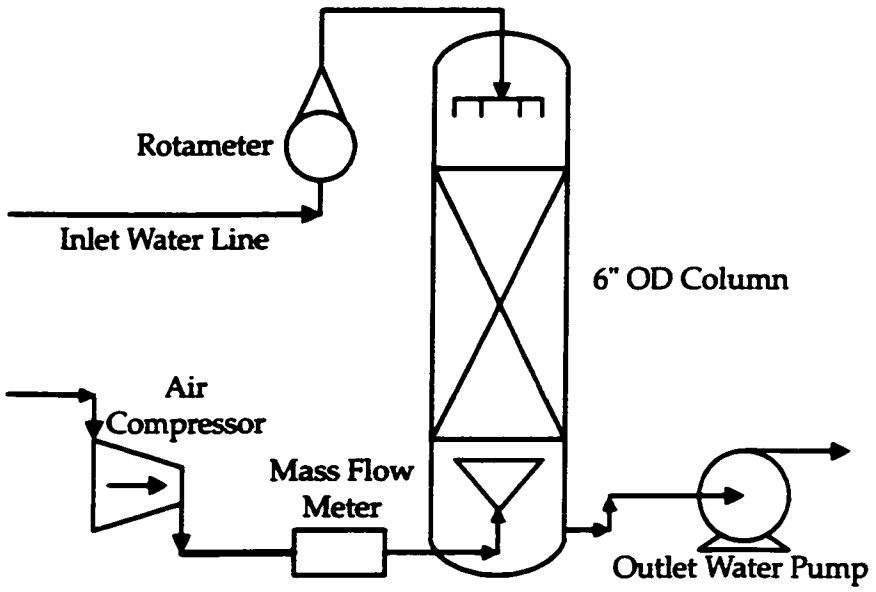

Figure 3-32. Flow diagram for air-water contactor.

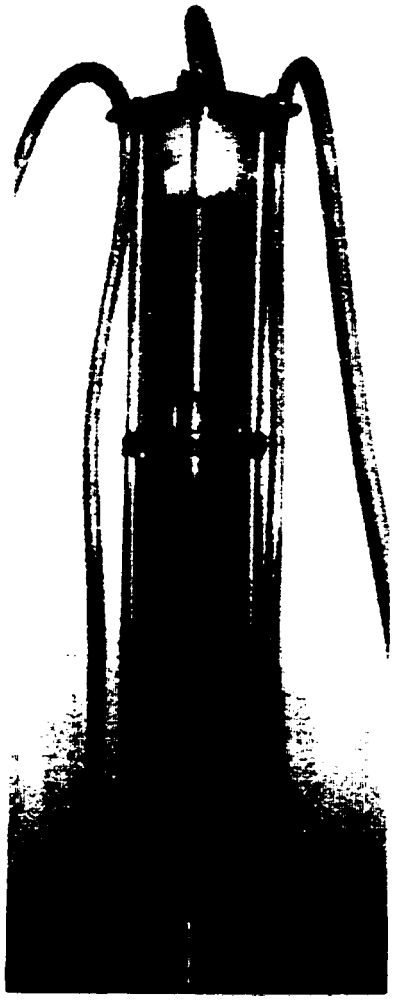

Figure 3-33. The air-water contactor used for flow experiments that contains a mist eliminator, a liquid distributor, two elements of Mellapak 500Y structured packing, and an air distributor.

A flow diagram for the air-water contactor is shown in Figure 3-32. The fluids used for the experiments were water and air. The water is provided from the house water supply. The flow rate of the water is measured using a rotameter. The air was

provided from a Sullivan Industries D130Q6 air compressor. This is a single stage, oil flooded rotary screw compressor with a maximum air flow rate of 130 cfm. A separator is used to remove the condensed water from the air stream. The air flow rate is measured using a MicroMotion Basis F050 mass flow meter. The signal from the mass flow meter is read using a DAQCard-700 and the LabVIEW software from National Instruments Corporation. Dial temperature and pressure gauges are used to measure the properties of the air feed stream. The lines connecting to the contactor are 3/4-inch OD (1/2-inch ID) flexible vinyl tubing. Those associated with the air flow rate and water flow rate measurement systems are 3/4-inch OD stainless steel tubing. The water feed line leading to the flow meter is 5/8-inch OD. The line connecting the air compressor to the air flow rate measurement system is 3/4-inch air hose.

The air-water contactor with structured packing was scanned using the 101B+ scanner at 3DID. Three methods of acquiring imaging data were used: radiograms, CT scans, and stationary transmission measurements. The adjustable experimental variables were water flow rate, air flow rate, and scan elevation.

Initially, a radiogram was obtained of the column without flow. The radiogram was used to identify the elevations of interest. Based upon the radiogram, three regions were selected for the remainder of the scanning. The first elevation was approximately two inches from the bottom of the packed bed. The second elevation selected was in the upper element of structured packing approximately two inches from the top of the packed bed. The third region was selected to capture flow behavior at the joint between the two packing elements.

A total of 93 CT scans were performed. Two sets of imaging parameters, as indicated in Table 3-6, were used to obtain images with high and low resolution. Images of the dry column and of the water-full column were obtained at an elevation of 348.7 mm. The water flow rates for the imaging experiments were: 0.0, 2.2, 10.5, and 20.0 gpm/ft^2. The air flow rates for the experiments were: 0.0, 0.4, 0.6, and 0.8 lb/

min (F-factor of 0.00, 0.14, 0.20, and 0.27 (ft/sec)($lb^{0.5}/ft^{1.5}$)). Entrainment of liquid in the exit stream limited the air flow rate to this range.

Table 3-6. CT Scanning Parameters for the Air-Water Contactor Studies

Parameter	High Resolution	Low Resolution
Model	101B+	101B+
Detector aperture	0.3 x 0.3 mm	1.0 x 1.0 mm
Views	900	600
Subpositions	13	4
X-ray filter	0.040" lead	0.040" lead
Snapshot time	0.015 sec	0.015 sec
Slice scan time	4.8 min	1.4 min
Image pixel size	0.15 mm	0.4 mm

The CT images were evaluated using techniques similar to those used for the phantom and film-flow systems. The image histograms for the reconstructed CT images were calculated for the cases with and without flows. In addition, the distribution of liquid in the region near the joint between packing elements was evaluated.

The liquid holdup value was calculated using each sinogram. The mean for each sinogram was first calculated using the same LabVIEW program that was used to evaluate the previous sinograms. The sinogram means were then scaled based upon the means of the full-water sinogram and the static holdup sinogram, as described by Equation 3-21. The resulting values represent the percent of the void space filled with water during the flow scan. The liquid holdup was calculated using the value of void fraction provided by the packing manufacturer. The liquid holdup was calculated at

the lowest scan elevation. The weight limit of the scanner restricted water-full scans, and thus measurement of the scaling factors, to this elevation.

Stationary transmission measurements were obtained for several flow conditions in the same range of flow rates as the CT scans. A set of data was collected over a one-minute period, with five consecutive data sets collected for a set of air and water operating conditions. A total of 86 stationary transmission measurement data sets were acquired at different elevations and operating conditions. As with the CT scans, measurements were obtained at two sets of imaging parameters. Table 3-7 summarizes the scanner parameters for the measurements.

Table 3-7. X-Ray Scanner Parameters for Stationary Measurements

Parameter	High Resolution	Low Resolution
Model	101B+	101B+
Detector aperture	0.3 x 0.3 mm	1.0 x 1.0 mm
X-ray filter	0.040" lead	0.040" lead
Data set acquisition time	60 sec	60 sec

The stationary transmission measurements were grouped into 19 data sets for analysis. Each data set was comprised of sequential measurements at constant operating condition and elevation. The mean, standard deviation, minimum, and maximum were calculated for each column in the data sets, which corresponds to each of the 117 physical detectors used for the measurements. To determine which 117 values in the sinogram correspond to the stationary measurements, the linear correlation coefficient for the two sets of data was calculated. The variability in the amount of water over the period of time that the data were collected was determined for the various paths and operating conditions.

3.8. Measurement of Column-Average Liquid Holdup

The liquid holdup within the packed section of the air-water contactor was measured experimentally without the x-ray imaging equipment. The measurement technique is widely used for air-water systems. All fluid flows to and from the column are simultaneously stopped and the volume of liquid that subsequently drains from the packed bed is measured. This method determines the column-average holdup, rather than the holdup at a specific cross section.

The column-average liquid holdup was measured for the air-water contactor containing the Mellapak 500Y structured packing. The ranges of air and water flow rates were the same as used for the x-ray imaging experiments. The column was operated at steady-state conditions, prior to shutting flows to and from the column. The volume of water drained from the column was measured; the liquid holdup volume of the distributor was subtracted. The average liquid holdup was calculated using Equation 3-27.

$$[3\text{-}27] \qquad \text{Holdup} = \frac{(\text{Water Drained}) - (\text{Distributor Volume})}{\text{Volume of Packed Bed}}$$

CHAPTER 4: EXPERIMENTAL RESULTS

Three experimental systems were imaged with the intent to determine the capabilities and limitations of the CT scanners, to evaluate image analysis approaches, and to gain insights into the operation of an air-water contactor. The imaging experiments using the phantoms were performed with three sets of scanning parameters and the two CT scanners. The various materials present in an operating air-water contactor were included, and features were analyzed using several image analysis approaches. The focus of the film-flow studies was to identify and measure a thin film of water flowing on a stainless-steel surface for a controlled situation. Several analysis approaches were applied to both the reconstructed CT images and to the sinograms. The third experimental system used was an air-water contactor. Both CT scans and stationary transmission measurements were used to measure operating characteristics of the column at various flow conditions. The reconstructed images and the sinograms were evaluated from these studies, with the objective of identifying the water present. The results from these three experimental studies will be presented in the following sections.

4.1. Imaging of Phantoms

4.1.1. Radiograms

The phantoms were imaged with both the 101B+ scanner (420 kV) and the Alliant scanner (320 kV) at 3DID. The radiograms obtained with the two scanners are shown in Figure 4-1 and Figure 4-2, respectively. On each of the radiograms, the scan

elevations are indicated in the right margin. The scan elevation is relative to a fixed point on each scanner, and an elevation on one machine does not necessarily correspond to the same elevation on the other scanner. A larger scan elevation corresponds to a scan plane that is physically higher. The scan elevations indicated are in two clusters to capture the various interfaces of interest. Two radiograms from the Alliant scanner are shown in Figure 4-2. The radiograms are obtained at rotational positions 90° apart from each other. The radiogram shown in (a) provides an end view of the phantoms, whereas a side view of the phantoms is shown in (b).

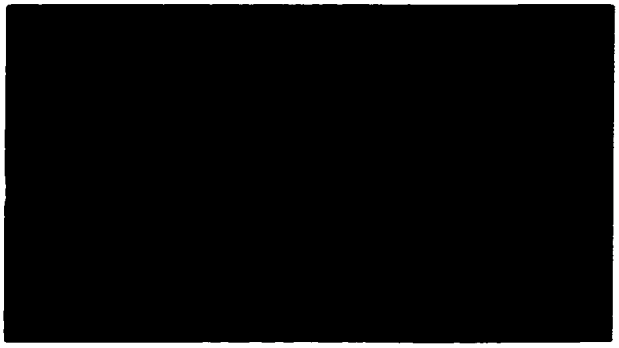

Figure 4-1. Radiogram of the phantoms obtained with the 101B+ x-ray CT scanner with scan elevations identified.

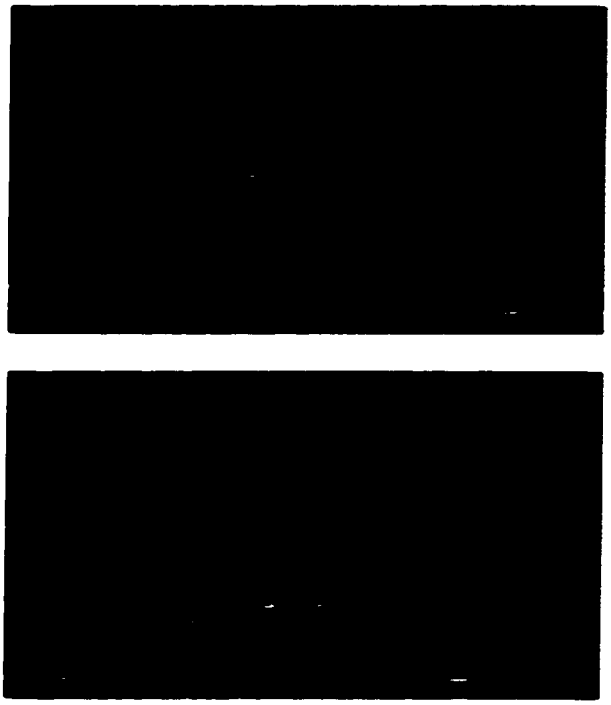

(a)

(b)

Figure 4-2. Radiograms of the phantoms obtained with the Alliant x-ray CT scanner with scan elevations identified. The two radiograms were obtained from orthogonal directions.

4.1.2. CT Images

Images of the phantoms were obtained with three sets of scan parameters. The images presented are 8-bit-grayscale TIFF (tagged image file format) images. The value of each pixel in the image is an integer in the range 0 – 255, with zero at the black end of the scale. The reconstructed image is scaled by 3DID to this range by specifying the values that correspond to the maximum and minimum of the range. The size of each image depends upon the pixel size that was specified prior to reconstruction. The column wall has an outside diameter of six inches (152.4 mm). Thus, the column will be represented by a circle with a diameter of 381 pixels in an

image with a pixel size of 0.4 mm, but a diameter of 1016 pixels when the pixel size is 0.15 mm. Most images in this section are presented at a fixed number of pixels per inch; however, the size of some images is increased or decreased to represent the features of interest. A number located in parenthesis in the figure caption indicates the magnification, when this occurs. For example, in Figure 4-10, a portion of the caption, "(3x)", indicates that there are three times as many pixels per inch. As shown, the image is decreased by a factor of three from the size the image would be with standard presentation. When comparing images with two different pixel sizes, that are displayed at the same number of pixels per inch, an image in which a pixel represents 0.15 mm will be 2 2/3 times the size of an image in which a pixel represents 0.4 mm.

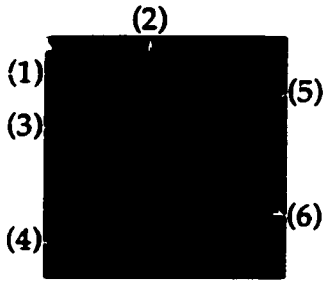

Figure 4-3. Typical features of the CT images obtained of the phantoms: (1) column wall, (2) metal surfaces, (3) horizontal metal surface, (4) air regions, (5) water regions, and (6) phantom walls.

The features that are present in the images of the phantoms are labeled in Figure 4-3. The column wall is visible as a gray circle, marked (1), and is present in each of the images. The more opaque materials, such as stainless steel, are brighter, or closer to white, in the images. The thin bright lines, as shown by (2), that are curved and straight represent the stainless-steel surfaces. When the metal surface is parallel to the scan plane, the white region within the image is larger, such as that shown by (3). The stainless-steel surface represented by this feature is flat and at a slight angle

relative to the scan plane. Less opaque materials, such as air, are toward the black end of the grayscale. Air regions, denoted by (4), are inside and outside of the column walls. Slightly more opaque than the air regions are the plastic and water regions. The gray regions that represent water, such as those labeled (5), are all bounded by the column wall, the phantom walls, or stainless-steel surfaces. The three gray rectangles and two thick parallel gray lines indicated by (6) represent the acrylic walls of the four phantoms. The orientation and location of the phantoms were different for the two scanners used. The location of each of the phantoms is identified for the 101B+ scans and the Alliant scans in Figure 4-4. The numbering of the phantoms is based upon the numbering set during design and is not indicative of the position in the column.

The first three sets of CT images are of the phantoms with varying amounts of water present at one elevation. The images represent dry, partially-filled, and flooded phantoms at the three sets of scan parameters. The images shown in Figure 4-5 and Figure 4-6 were obtained using the 101B+ scanner at high- and low- resolution parameters, respectively. In the images, the bright object in the upper left corner of the image, outside of the column, represents a hose clamp. The other features present are described in Figure 4-3. All of the phantoms, except for Phantom 2, contained some water for the scans of the partially-filled condition. However, at the scan elevations shown, Phantom 1 does not contain water at the elevation of the high-resolution image. In the low-resolution image representing the partial-water condition, only a small meniscus of water is present in Phantom 1. The images of the phantoms obtained with the Alliant scanner are of five different conditions, as shown in Figure 4-7. In the first image, (a), there is no water present. Water was added to the region of Phantom 3 for the first image containing water, shown in (b). In the two subsequent images, (c) and (d), the regions of first Phantom 4, and then Phantom 2, were filled with water. For the final image of the set, the entire column was filled with water. Some streak artifacts are noticeable in the water region of Phantom 4. The dark lines

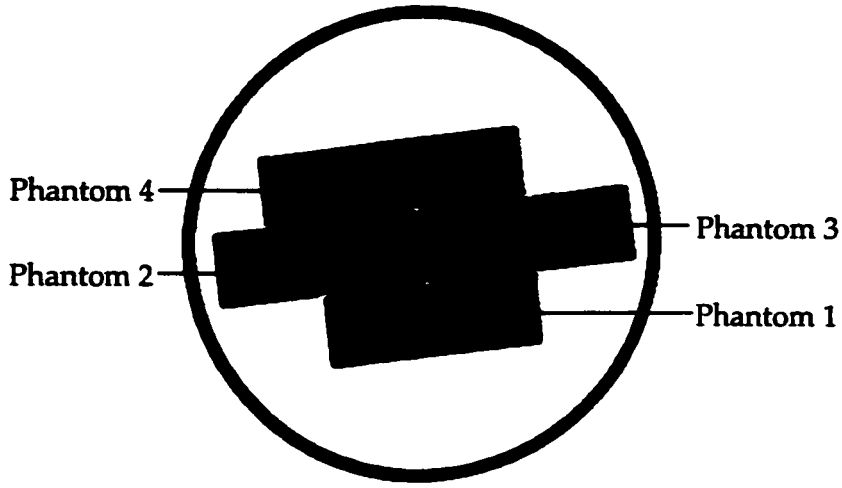

(a)

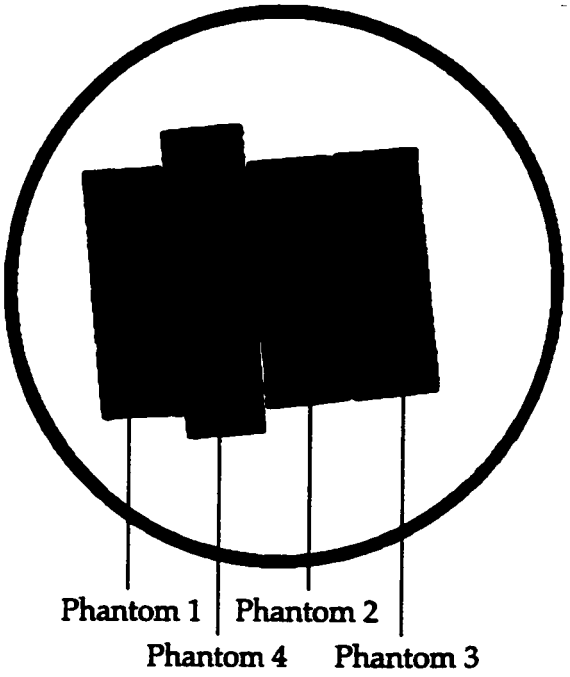

(b)

Figure 4-4. Positions of the four phantoms for images obtained with (a) the 101B+ scanner and (b) the Alliant scanner.

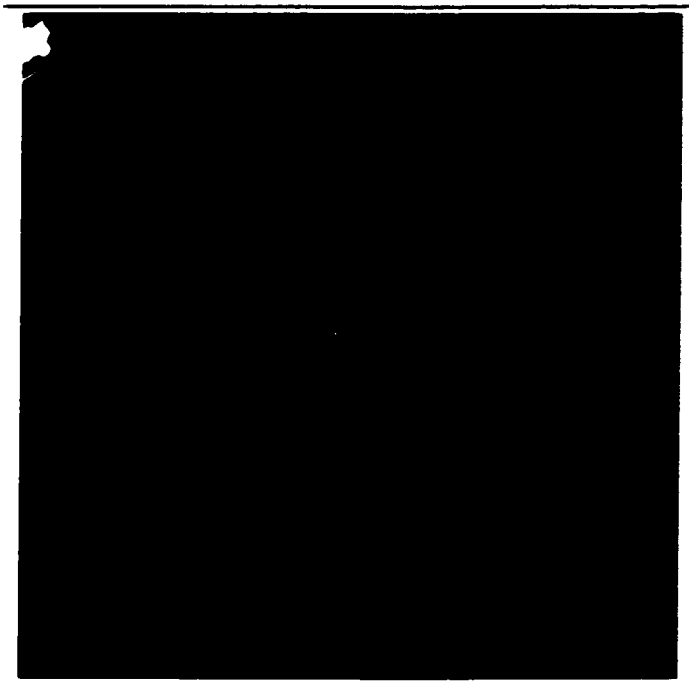

(a) Dry phantoms.

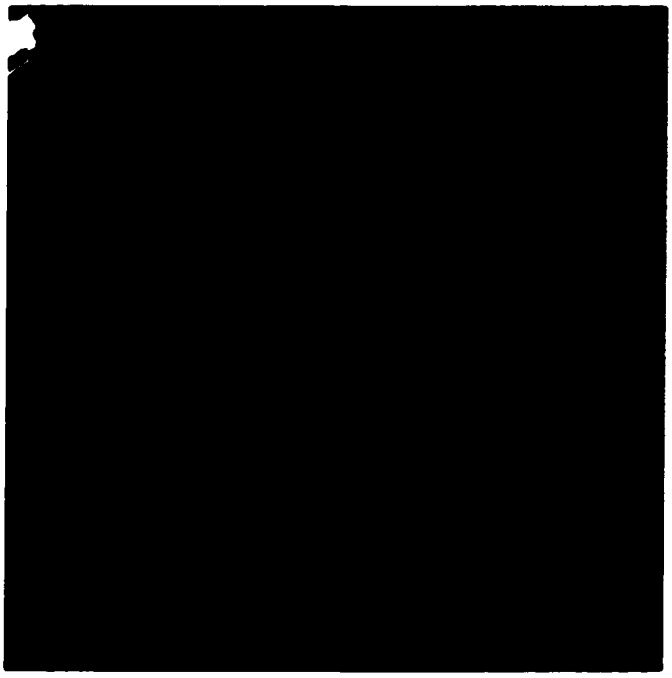

(b) Phantoms filled partially with water.

Figure 4-5. CT images of the phantoms obtained with the 101B+ scanner and high-resolution scan parameters at an elevation of 144.5 mm.

(c) Phantoms and column filled completely with water.

Figure 4-5 (cont.) CT images of the phantoms obtained with the 101B+ scanner and high-resolution scan parameters at an elevation of 144.5 mm.

extending from the two parallel stainless-steel surfaces are a result of the hardening of the x-ray beam as it passed through long regions of metal. Similarly, streak artifacts are noticeable in the region to the left of Phantom 1.

An image that represents the difference between two images is valuable in determining whether the position of objects changed. A difference image between the flooded and partial-water cases shown in Figure 4-5 is shown in Figure 4-8. Although not apparent in the images representing the two conditions, it is obvious from the difference image that there was a shift in the position of the phantoms. The gray pixels, such as those outside the column wall, signify regions of no change. Pixels that are lighter indicate that a more opaque region was present at the location during the flooded scan, while darker pixels indicate the opposite. The shift in position of the phantoms was noticed when the column was filled with water. As an air bubble

(a) (b) (c)

Figure 4-6. CT images of the phantoms obtained with the low-resolution scan parameters for the 101B+ scanner at an elevation of 142.7 mm. (a) Dry phantoms. (b) Partially-filled phantoms. (c) Completely submerged phantoms.

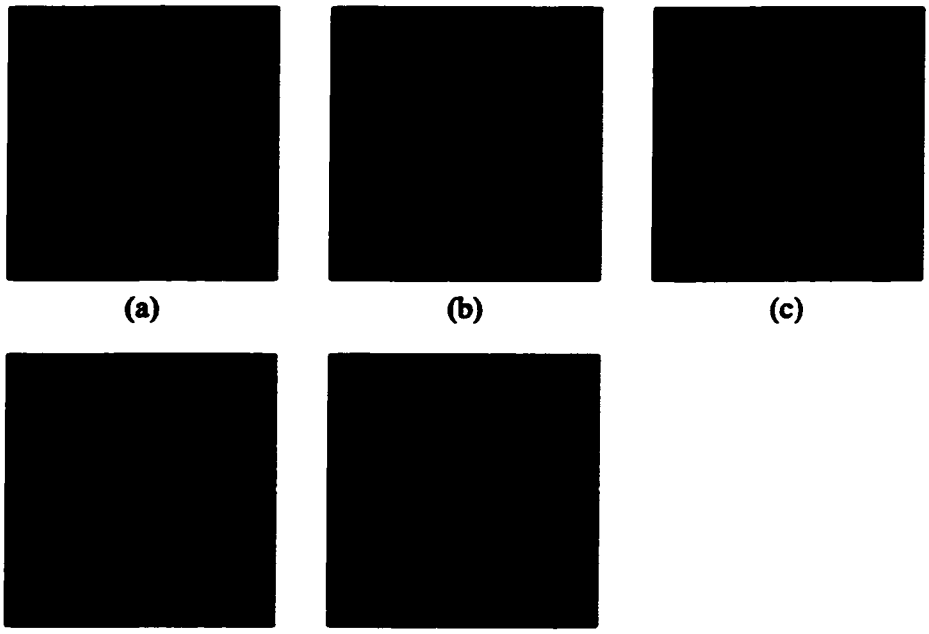

(a) (b) (c)

(d) (e)

Figure 4-7. CT images of the phantoms at an elevation of 146.0 mm obtained with the Alliant scanner. (a) Phantoms at minimum-water condition. (b) Phantom 3 filled with water. (c) Phantoms 3 and 4 filled with water. (d) Phantoms 2, 3, and 4 filled with water. (e) Phantoms at maximum-water condition.

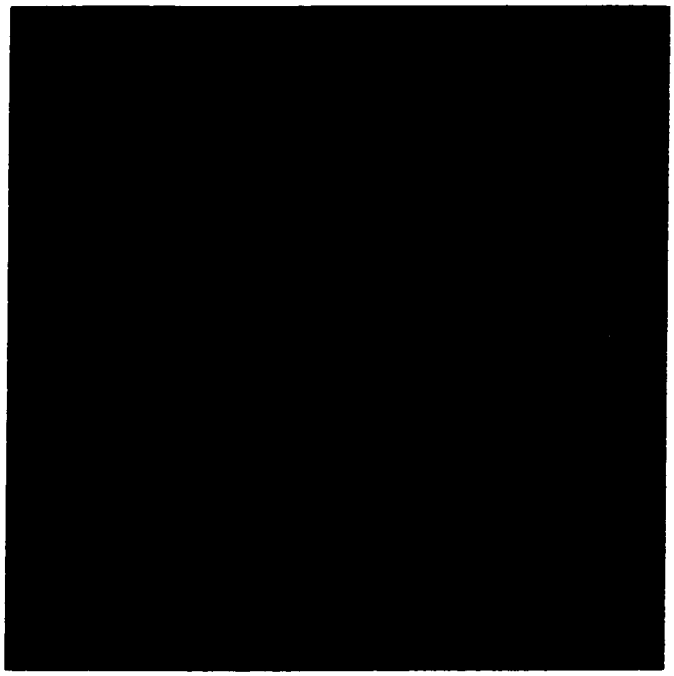

Figure 4-8. Difference image of the phantoms with the 101B+ scanner indicating the shift in position between the partial- and maximum- water scans at an elevation of 144.5 mm.

escaped from below the platform on which the phantoms were placed, the platform rotated. The shift in position was the same for the low-resolution images with the 101B+ scanner. A difference image for the Alliant scans between the dry and flooded case indicates that the position of the phantoms did not shift, as shown in Figure 4-9.

A set of adjacent high-resolution images that was obtained with a change in elevation of 0.3 mm between slices is shown in Figure 4-10. At the high-resolution scan parameters, the slice thickness is 0.3 mm, as determined by the vertical aperture of the detectors. Thus, the top of one image corresponds to the bottom of the adjacent image. The images are displayed from the lowest elevation, or toward the bottom of the phantoms, to the highest elevation. The radiogram, shown in Figure 4-1, indicates

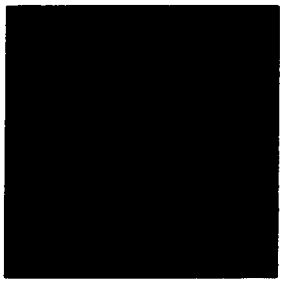

Figure 4-9. Difference image of the phantoms with the Alliant scanner indicating that the phantoms did not shift position.

(a) 124.9 mm (b) 125.2 mm (c) 125.5 mm (d) 125.8 mm

(e) 126.1 mm (f) 126.4 mm (g) 126.7 mm (h) 127.0 mm

Figure 4-10. A series of CT images obtained of the phantoms with the 101B+ scanner at the high resolution parameters. (a)–(h) Images start at an elevation of 124.9 mm and increment by 0.3 mm until a final elevation of 127.0 mm. (3x)

the locations of the elevations of the scan planes. Throughout the series of images, the features that are visible change. For instance, in Phantom 1, a curved surface that is horizontal begins to emerge in image (c). The surface is present in image (d), but has

begun to divide into the two segments of the curve in image (e). By the end of the sequence, in image (h), the surface is difficult to differentiate from flat metal surfaces in the images.

A second set of adjacent slices is depicted in Figure 4-11. The starting elevation for this series is 140.3 mm, and the increment between images is 0.3 mm. The upper region of the horizontal curved surface in Phantom 1 is captured in this range of elevations. The surface is contained within the scan plane at an elevation of 141.8 mm, as shown in image (f). On the right side of Phantom 4, the air region at the lower elevations is replaced by a horizontal flat metal surface in images (e) and (f), which is then is replaced by a water region at higher elevations. Thin features, such as the horizontal metal surfaces that are 0.38 mm thick, are expected to be present in two or three adjacent 0.3-mm-thick slices, depending upon how the surface aligns with the scan planes. The horizontal surface in Phantom 4 is aligned such that it is present in only two slices, shown in (e) and (f). The other horizontal surface that is captured within this elevation range is at an angle with respect to the scan plane. As seen in image (k), the flat surface in Phantom 2 first appears as a triangular region. The progression of the surface, in images (l) through (o), is indicative of the angle at which the surface is positioned. The top of the region of water in Phantom 1 was at an elevation of approximately 143 mm. Just above this level; in images (k), (l), and (m); a meniscus of water can be seen near the edges of this same region.

The series of images obtained at the same elevations with the low-resolution scan parameters are displayed in Figure 4-12 and Figure 4-13. The slice thickness represented by these images is 1.0 mm, rather than 0.3 mm. As a result, each image represents material that is present in slightly more than three adjacent slices obtained at the high-resolution parameters. The center of each slice is at the same position as the center of the corresponding high-resolution slice, as was described in Figure 3-24. In the low-resolution images, the horizontal metal surfaces are expected to be present

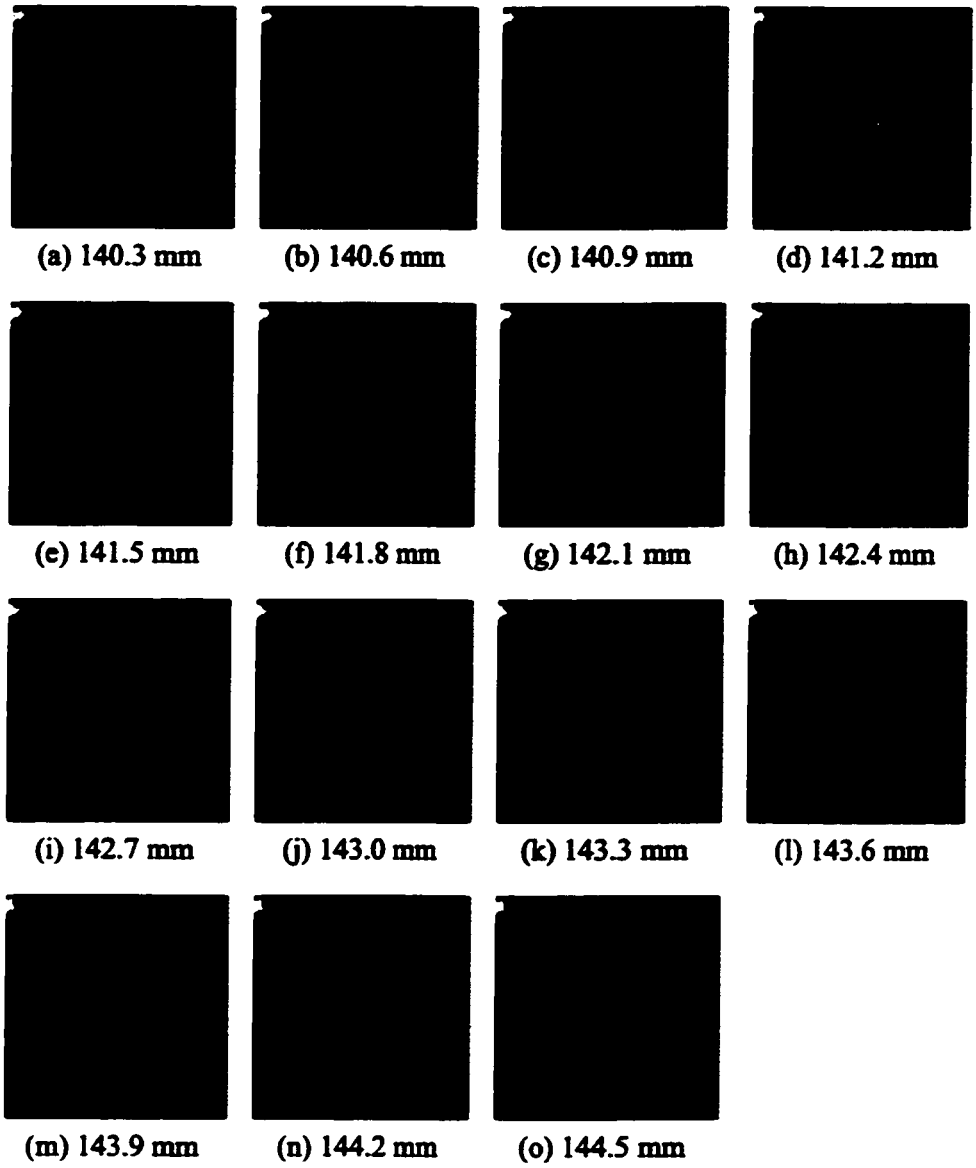

Figure 4-11. A series of CT images obtained of the phantoms with the 101B+ Scanner at the high resolution parameters. (a)–(o) Images start at an elevation of 140.3 mm and increment by 0.3 mm until the final elevation of 144.5 mm. (3x)

(a) 124.9 mm (b) 125.2 mm (c) 125.5 mm (d) 125.8 mm

(e) 126.1 mm (f) 126.4 mm (g) 126.7 mm (h) 127.0 mm

Figure 4-12. A series of CT images of the phantoms obtained at the low resolution parameters for the 101B+ scanner. (a)–(h) Images begin at an elevation of 124.9 mm and increment by 0.3 mm until the final elevation of 127.0 mm.

in two more images than in the high-resolution series. As seen in images (d), (e), (f), and (g), the horizontal surface is visible in four images. In the first and last images, the surface comprises a much smaller fraction of the slice than in the middle two images, thus appears less bright in the images.

Comparison of the low-resolution and high-resolution images results in the identification of differences. The metal features in the low-resolution images appear less sharp than in the high-resolution images, which can be explained by the larger pixel size. The features of the object are smaller than the pixel size of the low-resolution images. However, the smallest size at which the features can be represented is one pixel. Therefore, the attenuation of the x-ray beam due to the metal is spread over the entire pixel. As a result, the brightness of the pixel is reduced, and the feature does in fact appear to be present in a larger region. Another difference noted was the

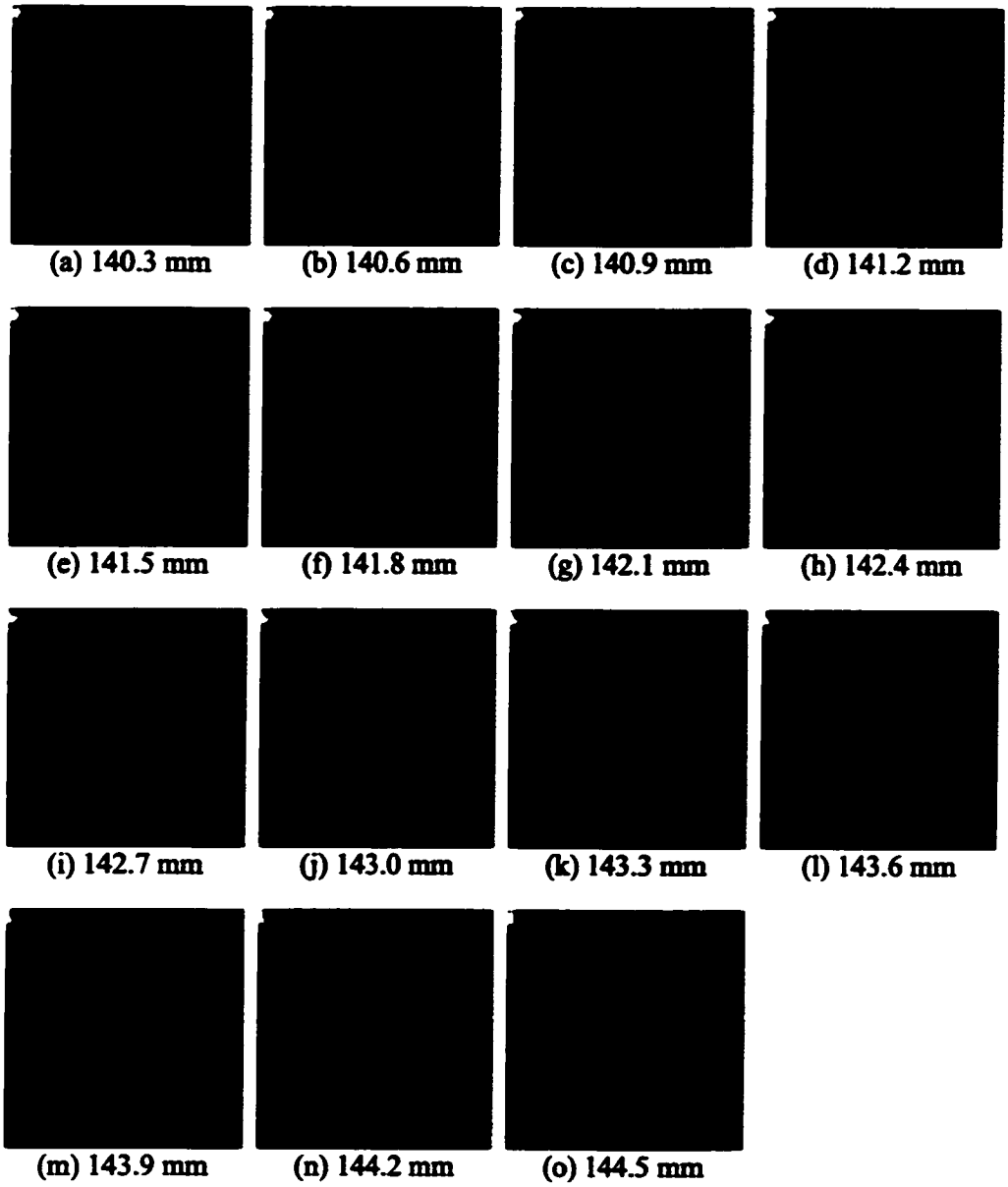

Figure 4-13. A series of CT images obtained of the phantoms with the 101B+ scanner at the low resolution parameters. (a)–(o) Images start at an elevation of 140.3 mm and increment by 0.3 mm to an elevation of 144.5 mm.

level of the water within Phantom 1. For the scans at the high-resolution parameters, the water level was higher than for the scans at the low-resolution parameters. This difference was physically observable in the phantoms at the time of the scans. The difference is also apparent when comparing the images. The top of the water in Phantom 1 is observed in image (d) of the low-resolution series, which corresponds to an elevation of 141.2 mm. Above this elevation, water is visible, but appears more along the edges in the form of a meniscus. As previously noted, the top of the water in the high-resolution images was observed at an elevation of 143 mm.

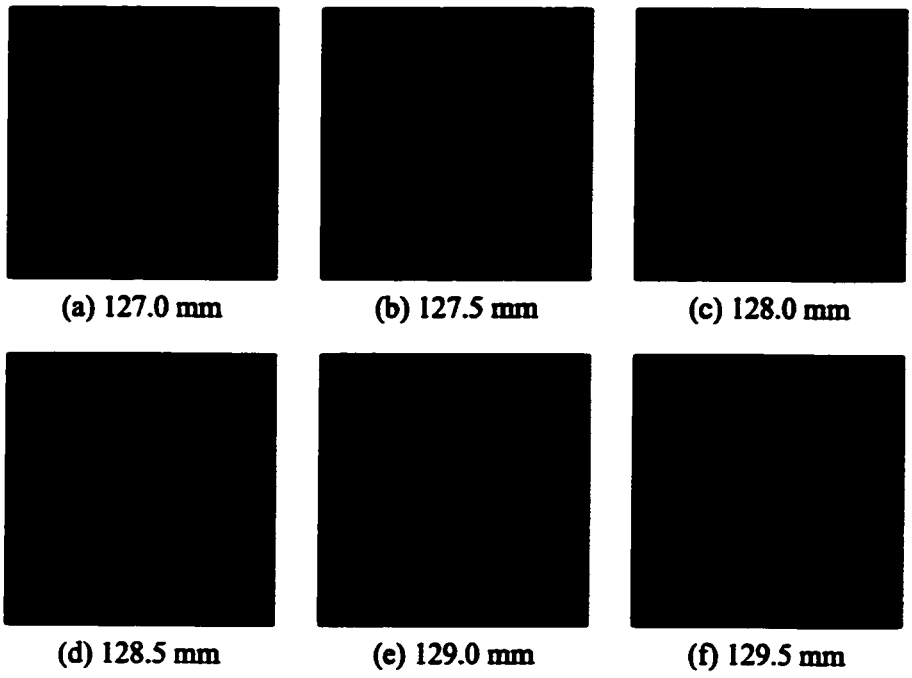

Figure 4-14. CT images of the phantoms, with Phantoms 3 and 4 filled with water, obtained with the Alliant scanner. (a)–(f) Images begin at an elevation of 127.0 mm and increment by 0.5 mm until a final elevation of 129.5 mm.

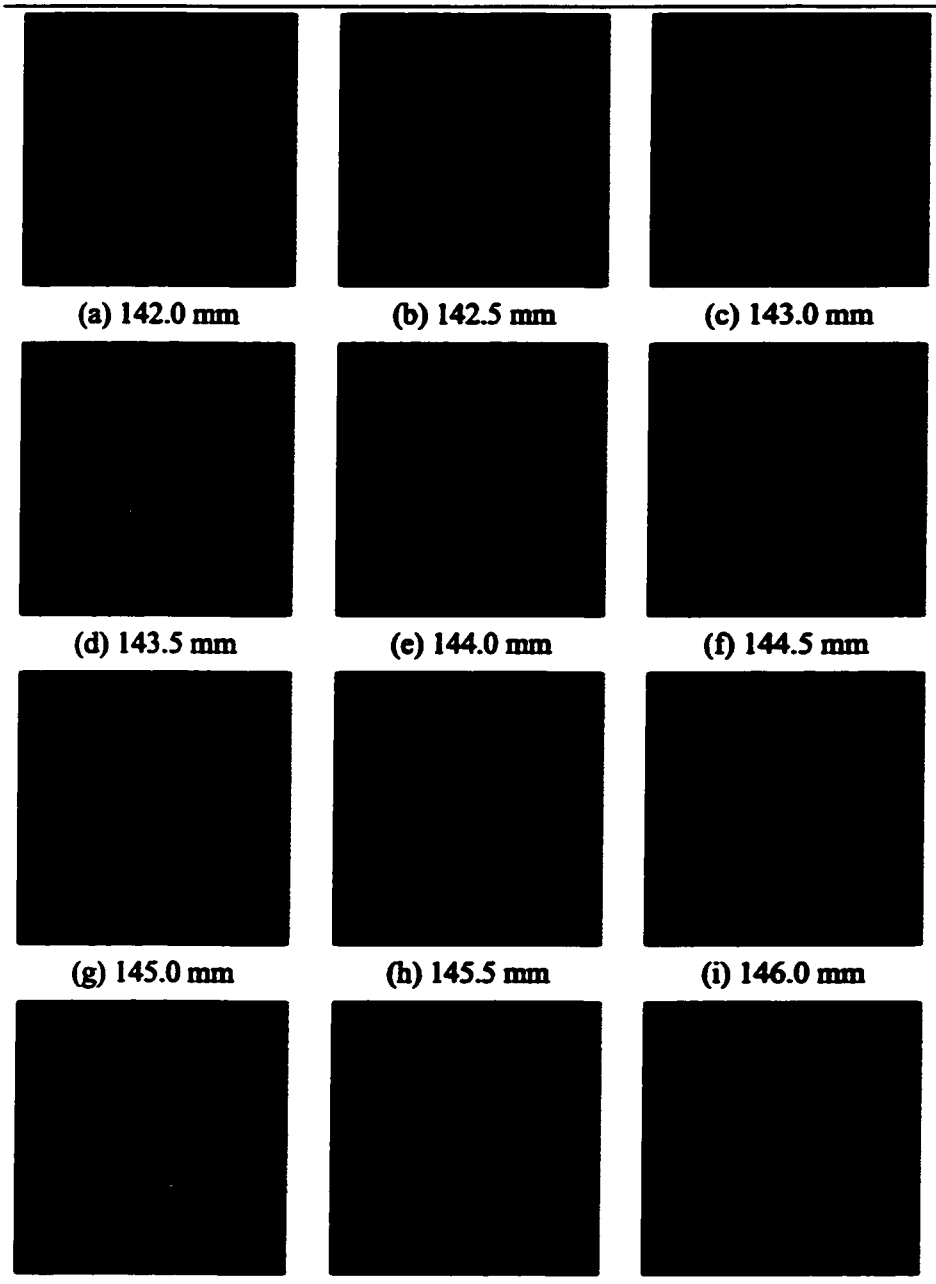

(a) 142.0 mm (b) 142.5 mm (c) 143.0 mm

(d) 143.5 mm (e) 144.0 mm (f) 144.5 mm

(g) 145.0 mm (h) 145.5 mm (i) 146.0 mm

(j) 146.5 mm (k) 147.0 mm (l) 147.5 mm

Figure 4-15. CT images of the phantoms, with Phantoms 3 and 4 filled with water, obtained with the Alliant scanner. (a)–(l) Images at increments of 0.5 mm, from 142.0 mm to 147.5 mm.

Two series of CT images were obtained with the Alliant scanner. The images in Figure 4-14 and Figure 4-15 each represent a slice that is 1.0 mm thick. The images presented were obtained at 0.5 mm increments. Thus, the top of one slice corresponds to the center of the next image in the series and the bottom of the slice corresponds to the center of the previous image in the series. Qualitatively, the features observed in the images obtained using the Alliant scanner are similar to the appearance of the features in the images from the 101B+ scanner.

4.1.3. Histogram Evaluation

An image histogram represents the number of pixels in the image that are of each value of grayscale. The histogram does not contain spatial information about the location of the pixels at a particular grayscale, but does provide general information about the distribution of values of grayscale in the image. Image histograms were calculated for the images obtained from the CT scans. The region of interest of the images for all of the histograms was the circular region within the column walls.

In Figure 4-16, the histograms for three high-resolution images obtained with the 101B+ scanner are shown. The images for which the histograms were calculated are shown in Figure 4-5. In the histogram plot, there are two distinct peaks centered at values of approximately 30 and 60. In general, these peaks represent the pixels representing air and water in the images, respectively. The peak at the upper value is much larger for the image of the maximum-water condition. The peak at the lower value is smaller for the image of the partial-water condition, and is nearly non-existent for the maximum-water condition. The total amount of metal present in the image is small and is comprised mainly of pixels that are at the boundary with another material. As a result, there is no distinct peak to represent the stainless steel. The range of values of grayscale that represent the stainless steel is large, and the number of pixels at each value is small.

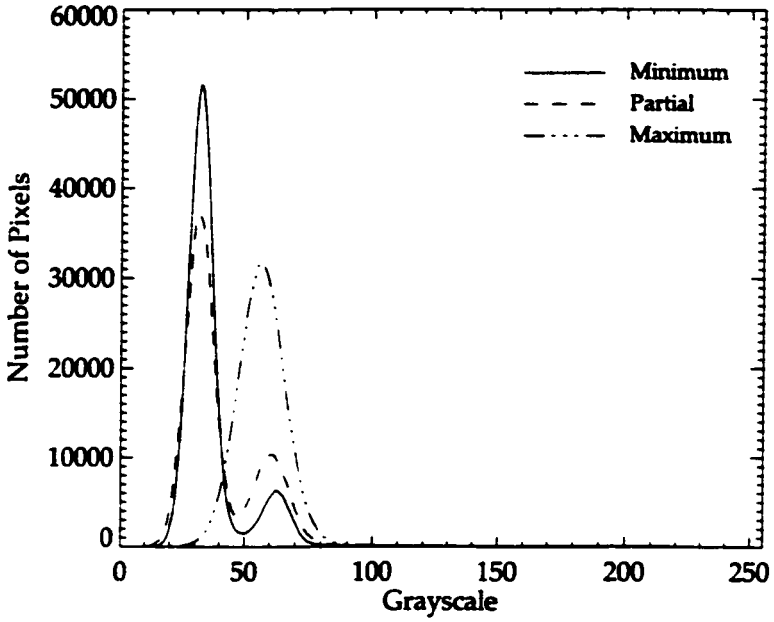

Figure 4-16. Histograms of the high-resolution images obtained with the 101B+ scanner shown in Figure 4-5.

To further investigate the distribution of materials represented by the histograms, the range of grayscale was evaluated in two manners. First, the range of grayscale for each material present in the image was determined. For the high-resolution scans, this classification is presented in Table 4-1. The range of values overlaps for the various materials, therefore, each range of grayscale was also characterized by the possible materials that a pixel with a particular value represents. As indicated in Table 4-2, for a high-resolution image of the phantoms, the range between 48 and 51 can represent any one of the four materials. As a result of this overlap, simple image calculations such as thresholding will not be accurate in identifying the phases present.

Table 4-1. Ranges of Grayscale Associated with Pixels for the CT Images Obtained at High Resolution with the 101B+ Scanner.

Description of Pixels	Range of Grayscale
Air Region	0 – 51
Water Region	24 – 95
Plastic Region (including edges)	24 – 95
Metal Edges	48 – 99
Metal	100 +

Table 4-2. Characterization of Pixels in Ranges of Grayscale for the CT Images Obtained at High Resolution with the 101B+ Scanner.

Range of Grayscale	Description of Pixels in Range
0 – 23	Air region
24 – 47	Air region, water region, plastic region
48 – 51	Air region, water region, plastic region, metal edges
52 – 95	Water region, plastic region, metal edges
96 – 99	Metal edges
100 +	Metal

Neither a histogram, nor the tables that classify the values of grayscale, present spatial information about the values in an image. A series of images are presented in Figure 4-17 to illustrate the evaluation of the histogram. The images represent the location of pixels that are within particular ranges of grayscale. The pixels that are white indicate that the value of the pixel was within the specified range. A pixel assigned a value of black indicates that it is outside of the range specified for that particular image. The original image is presented in (a). The pixels within the range

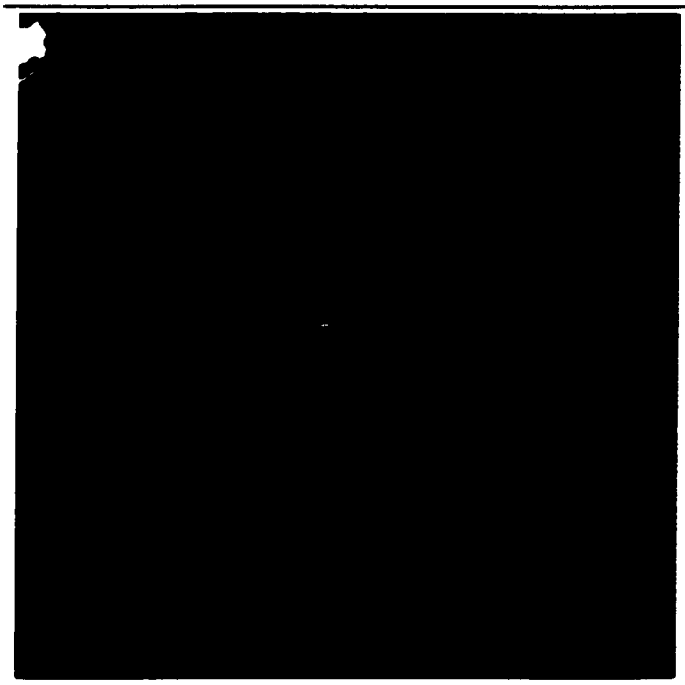

(a) Original image at an elevation of 144.5 mm.

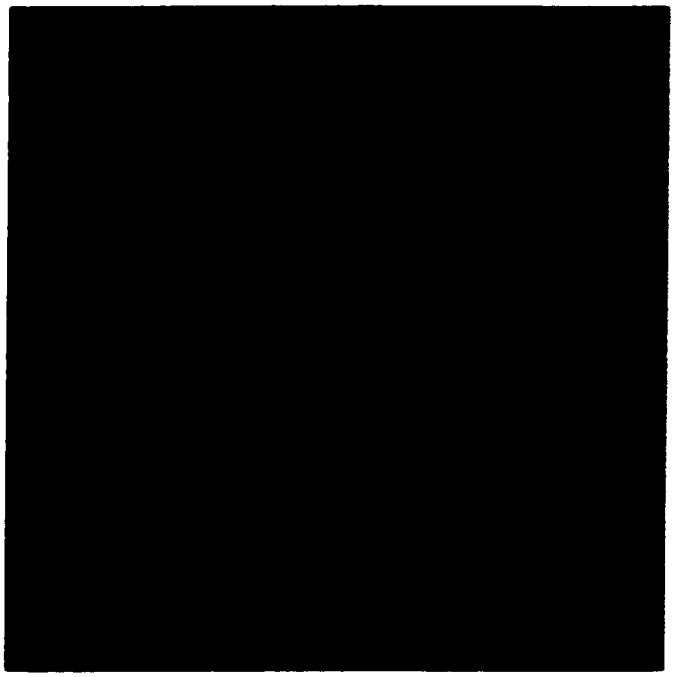

(b) Grayscale: 0 – 23

Figure 4-17. Location of pixels with values within the specified range for a high-resolution image obtained with the 101B+ scanner.

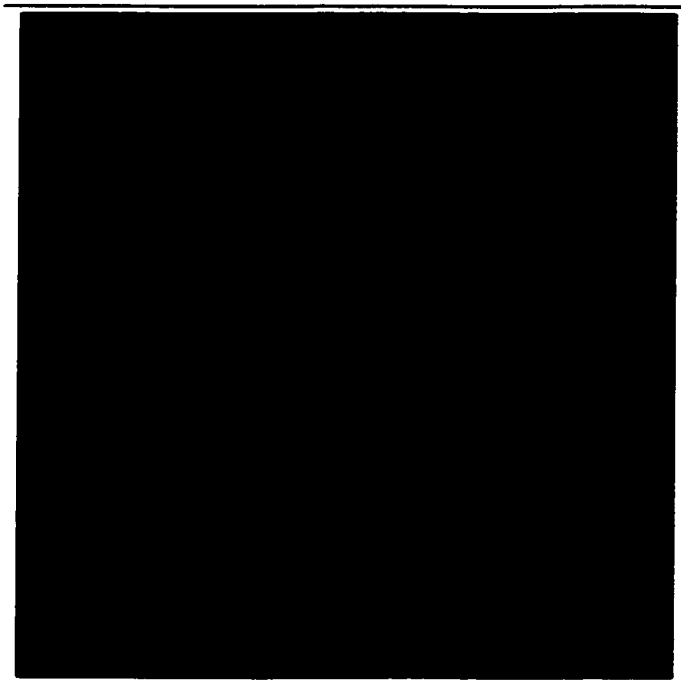

(c) Grayscale: 48 – 51

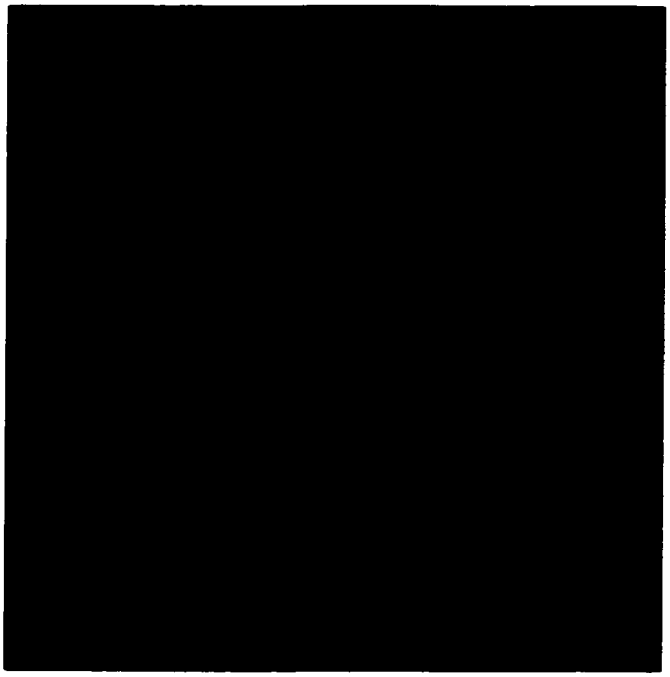

(d) Grayscale: 76 – 83

Figure 4-17 (cont.) Location of pixels with values within the specified range for a high-resolution image obtained with the 101B+ scanner.

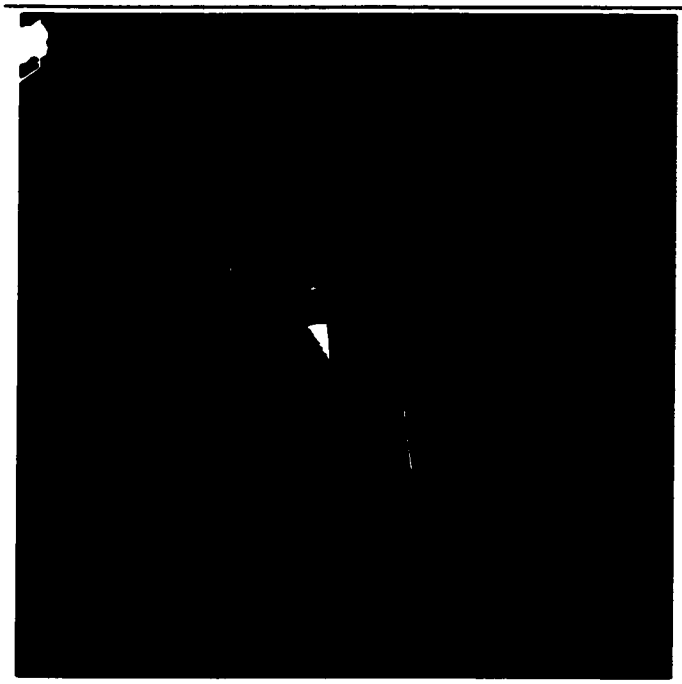

(e) Grayscale: 100 +

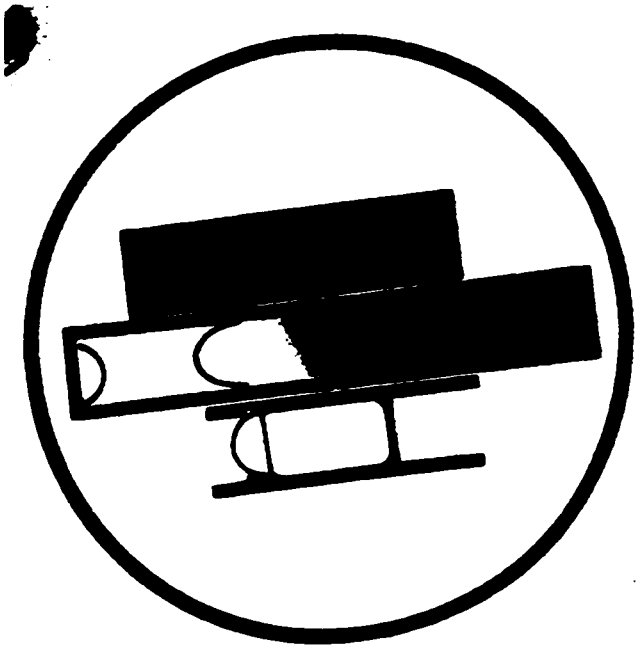

(f) Grayscale: 0 – 51

Figure 4-17 (cont.) Location of pixels with values within the specified range for a high-resolution image obtained with the 101B+ scanner.

(g) Grayscale: 24 – 95

Figure 4-17 (cont.) Location of pixels with values within the specified range for a high-resolution image obtained with the 101B+ scanner.

of zero to 23 are given a value of 255, or white, in the image shown in (b). As indicated in Table 4-2, all of these pixels are located in the region of air. However, there are still black pixels in the air region, indicating that not all of the air pixels are captured. The pixels represented in image (c) are representative of air, water, plastic, and metal regions. The positions of the column walls and phantom walls are apparent, and the outline of the stainless-steel surfaces are visible within the phantoms. Although the water region spans values from 24 to 95, the water region is well-defined by only the values in the range from 48 to 51, as shown. Even though the region represented by the white pixels in image (d) represents the same materials as those in (c), there are noticeable differences. The pixels in (d) are in the range from 76 to 83 and represent the plastic region, rather than the plastic edges. In addition, the positions of the stainless steel are more apparent. There are some isolated pixels in the

water region. Above a value of 100, the pixels represent metal regions, as seen in image (e). However, as the metal edges were previously observed in images of other ranges, this image does not represent all of the metal. At the end of this series of images there are ranges of grayscale represented to capture all of the pixels of one particular material. As seen in image (f), all of the air pixels are represented by the range from zero to 51. However, many pixels within the plastic and water regions are also included. When compared with image (c), which is a subset of image (f), it is apparent that there are metal edges included. The final image, (g), represents the region that includes all of the plastic and water pixels. There are pixels that are within the air region included in this range.

An analogous analysis of the histograms for images of the phantoms at low resolution was performed. The histogram is represented in Figure 4-18, with the image classifications in Table 4-3 and Table 4-4. The series of images representing various ranges of grayscale is shown in Figure 4-19.

The histogram for the low-resolution images contains peaks that are more well defined than those in the high-resolution images. The region of the histogram from 40 to 90 is shown magnified in the inset. The same two peaks for air and water exist. However, the range for plastic appears to be slightly different than that for water. In the histogram of the image of the partial-water condition, there is a distinct shoulder on the water peak, in the same region as the peak for the minimum-water case. In contrast with the histogram of the high-resolution images, the peak of the histogram of the maximum-water case trails off before the region representative of the air is reached. The air peak is lower for the partial-water case than it is for the minimum-water condition, as expected. In a similar trend, the ranges of pixels defined in the tables are much narrower. The air region does not extend to as high of a value as in the high-resolution case.

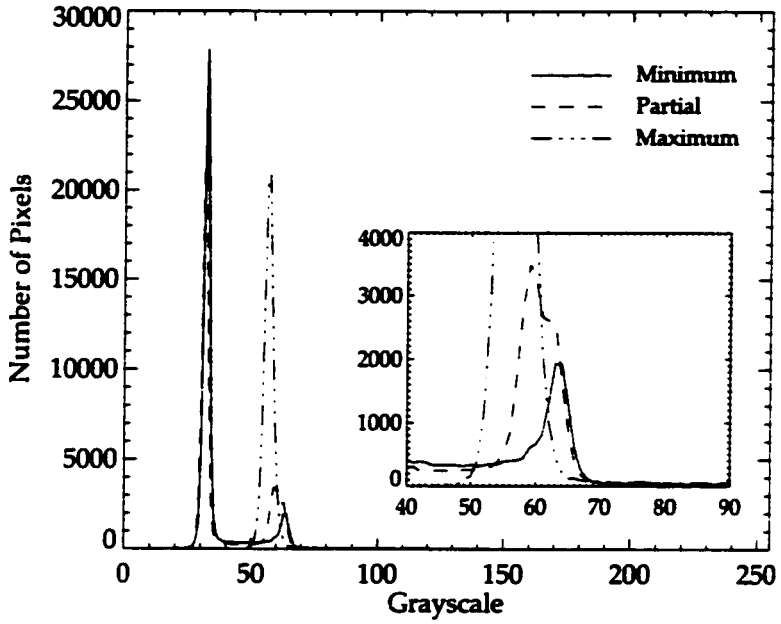

Figure 4-18. Histograms for three selected low-resolution images obtained with the 101B+ scanner.

Table 4-3. Ranges of Grayscale Associated with Pixels for the CT Images Obtained at Low Resolution with the 101B+ Scanner.

Description of Pixels	Range of Grayscale
Air Region	16 – 39
Water Region	48 – 63
Plastic Edges	32 – 59
Plastic Region	60 – 67
Metal Edges	36 – 115
Metal	116 +

Table 4-4. Characterization of Pixels in Ranges of Grayscale for the CT Images Obtained at Low Resolution with the 101B+ Scanner.

Range of Grayscale	Description of Pixels in Range
0 – 31	Air Region
32 – 35	Air Region, plastic edges
36 – 39	Air Region, plastic edges, metal edges
40 – 47	Plastic edges, metal edges
48 – 59	Water Region, plastic edges, metal edges
60 – 63	Water Region, plastic region, metal edges
64 – 67	Plastic region, metal edges
68 – 115	Metal edges
116 +	Metal

The location of the pixels for various ranges of grayscale is presented in the images in Figure 4-19. The original image is presented as image (a). The pixels that are in the range from zero to 31 are shown in image (b). These pixels are all representing regions of air; however, all of the air region is not represented. In this image, there were no pixels in this image below a value of 16, as the histogram indicates. The region of grayscale needs to be extended to an upper value of only 39, as shown in image (h), to capture the entire air region. However, by extending the range of values, some pixels that represent plastic or metal edges are also included. In fact, some of these pixels are show in image (c). In addition to representing air regions, the pixels in the limited region of grayscale from 36 to 39 represent the edges of plastic, as the outline of both the column wall and the phantom walls indicate, and the edges of metal as seen within Phantoms 1 and 2. The metal edges that are represented are primarily those that are bounded by air and not those that are located adjacent to water; the same trend holds for the plastic edges. Image (d) represents

(a) Original Image (b) Grayscale: 0 – 31 (c) Grayscale: 36 – 39

(d) Grayscale: 48 – 59 (e) Grayscale: 60 – 63 (f) Grayscale: 64 – 67

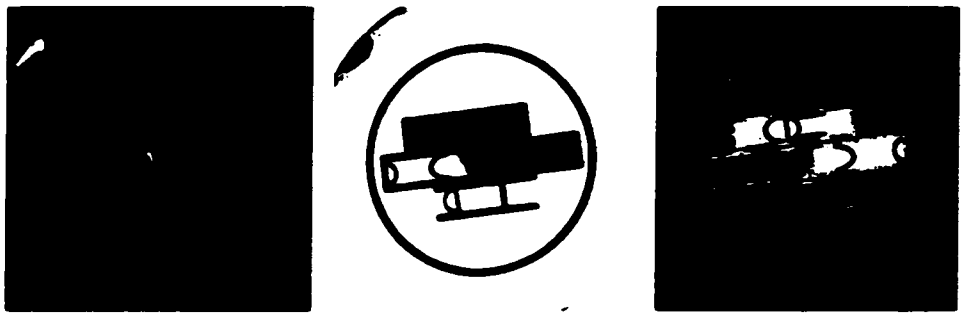

(g) Grayscale: 116 + (h) Grayscale: 16 – 39 (i) Grayscale: 48 – 63

Figure 4-19. Image of the phantoms containing partial water obtained with the 101B+ scanner with the low-resolution parameters. (a) Original image. (b)–(i) Images indicating pixels in various ranges of the grayscale.

pixel locations that have a value within the range from 48 to 59. These pixels represent water, plastic edges, or metal edges. For this set of images, the regions of

water and air do not overlap. The plastic and metal edges are present with the ranges of both air and water, however. The region of water continues into the range from 60 to 63, shown in (e), at which point the plastic regions are also represented. The combination of these two ranges is shown in image (i). In the range from 48 to 63, the entire water region is represented. As the range of grayscale is increased to 64 to 67 for image (f), the regions represented by the pixels shift to the plastic region and the metal edges. At the top end of the scale, as shown in image (g), the metal regions are represented.

The primary difference between the shape of the histograms for the high- and low- resolution images is the width of the peaks. The width of a peak representing a particular material is indicative of the amount of noise within the region for that material. Thus, the level of noise was much higher for the images obtained with the high-resolution scan parameters. The higher level of noise can be explained with use of the values for the detector aperture and the snapshot time. The snapshot time represents the amount of time for which x-ray beams are measured at one position. The aperture of the detectors represents the total area over which x rays are measured. Between the two sets of scan parameters on the 101B+ scanner, the snapshot time was kept constant and the detector aperture was varied. The total number of x rays measured decreases as the aperture of the detectors is decreased. In x-ray CT, the measurement noise is inversely proportional to the square root of the number of measurements, as random effects partially cancel each other [1]. Therefore, the level of noise is expected to be higher for the high-resolution (small-aperture) case, in which fewer x rays are measured. The width of the histograms for the two sets of scan parameters indicates that the noise is higher for the high-resolution images.

The histograms of the high- and low- resolution images are expected to be different in the region between the air and water peaks. As the pixel size in the images increases, a greater portion of the pixels represent more than one material. One effect

of this, which is seen in the histogram of the low-resolution images, is that the histogram does not tend to decrease to zero between peaks for two distinct regions. For the histogram of the high-resolution images, the overlap of the two peaks obscures any behavior due to pixels that contain more than one material.

The images obtained from the Alliant scanner were analyzed using the same method of histogram evaluation as was used for the images from the 101B+ scanner. The histograms for three conditions are presented in Figure 4-20. The histograms are most similar to the images obtained at low resolution on the 101B+ scanner. The peaks are well defined without the degree of overlap observed for the high-resolution images. The range of the grayscale is different than that seen in the histograms from the 101B+ scanner, because the export of the reconstructed image to TIFF format was performed with different values specified for the maximum and minimum. Therefore, a value of grayscale does not correspond to the same calculated linear attenuation coefficient for images presented from the two scanners. Table 4-5 and Table 4-6 summarize the characterization of pixels for ranges of grayscale.

Regions of grayscale for an image obtained with the Alliant scanner are depicted in black and white images in Figure 4-21. Again, the white pixels represent the pixels within the range specified, while the black pixels represent pixels outside of the range. The original image is shown in (a) for comparison. All of the pixels that are white in image (b) represent the air region; all of the air pixels, and some edge pixels, are white in (f). The region of the grayscale depicted in image (c) includes the upper end of the air range as well as the pixels along the edges of both plastic and metal. As with the low-resolution images from the 101B+ scanner, the edges in this range are primarily bounding regions of air, not water. The range of grayscale that includes the most amount of materials is depicted in image (d). All materials except air regions are included in the pixels that are white. As shown in image (e), the upper range of the grayscale represents metal surfaces. However, the pixels along the edges of metal are

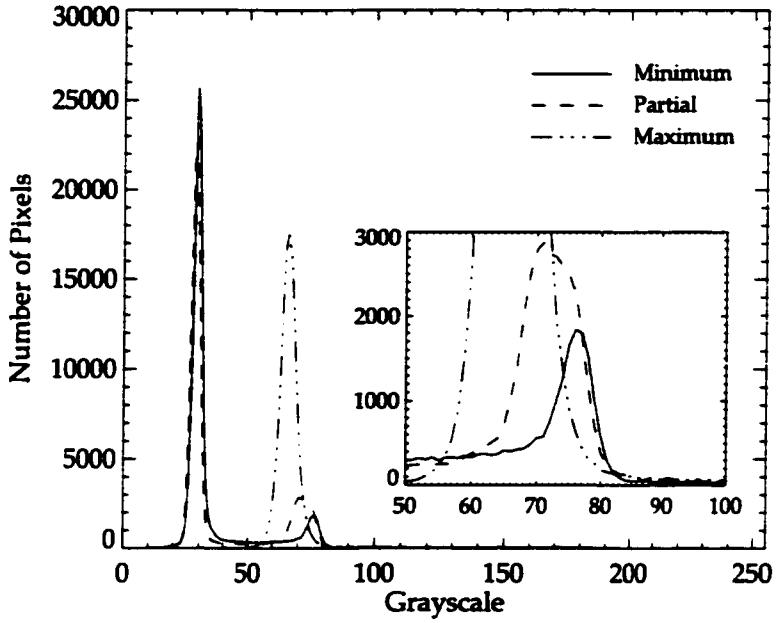

Figure 4-20. Histograms for images obtained with the Alliant scanner of the phantoms with minimum, partial, and maximum water present.

Table 4-5. Ranges of Grayscale Associated with Pixels for the CT Images Obtained with the Alliant Scanner.

Description of Pixels	Range of Grayscale
Air Region	0 – 39
Water Region	64 – 83
Plastic Edges	32 – 63
Plastic Region	64 – 83
Metal Edges	36 – 131
Metal	132 +

Table 4-6. Characterization of Pixels in Ranges of Grayscale for the CT Images Obtained with the Alliant Scanner.

Range of Grayscale	Description of Pixels in Range
0 – 31	Air region
32 – 35	Air region, plastic edges
36 – 39	Air region, plastic edges, metal edges
40 – 63	Plastic edges, metal edges
64 – 83	Water region, plastic region, metal edges
84 – 131	Metal edges
132 +	Metal

present at values of grayscale as low as 36. In the range of grayscale between 48 and 51, shown in image (g), the pixels are all located along the boundary between two materials. This range is between the two peaks on the histogram. Another limited range is represented in image (h). The values represented by white pixels are in the range from 72 to 75. As seen in the histogram in Figure 4-20, the values in this range fall in the upper region of the water range and in the lower region of the plastic range. In addition, some of the pixels in this range represent metal pixels on the boundary between either air or water.

The histogram evaluation indicates that the identification of regions present in the images depends upon several factors. For the images presented, the identification of large regions of air or water is less complicated for the low-resolution images. The values of grayscale that represent the two regions do not overlap, as seen in the histograms. Thus, the level of noise in the reconstructed images is a consideration that must be made in addition to the trade-off between spatial and temporal resolution. If the regions do not contain a large fraction of edge pixels, and the level of noise is low, the use of a threshold value to distinguish between air and water is promising.

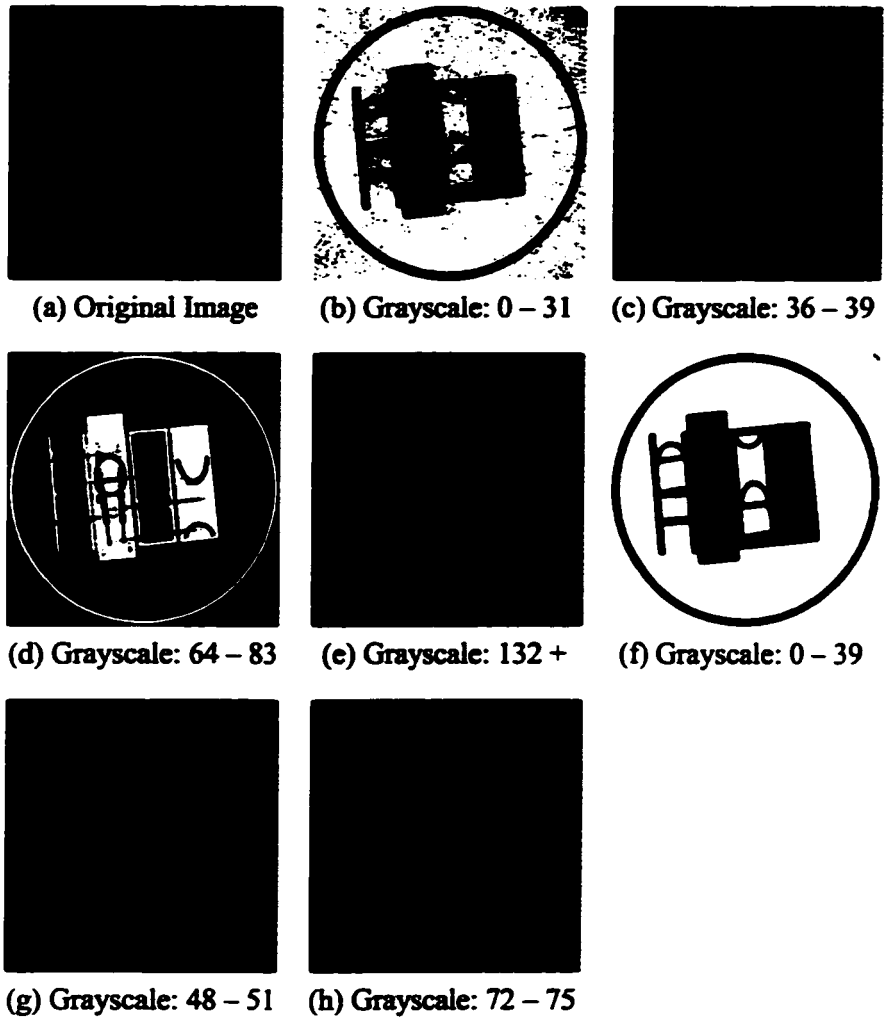

(a) Original Image (b) Grayscale: 0 – 31 (c) Grayscale: 36 – 39

(d) Grayscale: 64 – 83 (e) Grayscale: 132 + (f) Grayscale: 0 – 39

(g) Grayscale: 48 – 51 (h) Grayscale: 72 – 75

Figure 4-21. Image of the phantoms containing partial water obtained with the Alliant scanner. (a) Original image. (b)–(h) Images indicating pixels in various ranges of the grayscale.

However, edge pixels along the plastic and metal may not be classified correctly. Water pixels along an edge, such as those present as a film of water, are of great importance in determining the interfacial area within a vapor-liquid contactor. The

evaluation of the film-flow experiments will provide greater insights into the identification of thin regions of water.

4.1.4. Profiles Along Selected Lines

For select lines through the images of the phantoms, the values of grayscale encountered were determined. The lines were selected to pass perpendicularly to the stainless-steel surfaces. The lines selected through the images obtained with the 101B+ scanner were determined such that the profiles are observed through the same features at both high and low resolution. For these images, one line was selected through each phantom. For the images obtained with the Alliant scanner, the line profiles were determined along the same path for both the minimum- and maximum-water conditions. A total of four lines, each through a different phantom, were selected.

The lines specified through the high-resolution images of the phantoms, at an elevation of 126.7 mm, are depicted in Figure 4-22. The line number corresponds to the number of the phantom through which the line passed. Table 4-7 indicates the material along the path of each line in sequential order from left to right. The values of grayscale along each of these lines are shown in the four plots in Figure 4-22. The profile along Line 1 clearly shows five regions of air, three regions of water, and seven peaks for the metal surfaces. However, the difference between the various angles of the metal surfaces is not observable from the plot. Similarly, the regions of air and metal are observed for Line 2. The order of the metal surfaces along Line 3 is reverse of that for Line 2, and the air regions are replaced with water regions. The difference between water and metal is easily distinguished in the line profile. Along Line 4, the four regions of air and three regions of water are observable between the six peaks representing the metal surfaces. As was indicated by the histogram evaluation, there are values of grayscale that are located in both air and water regions. This can also be

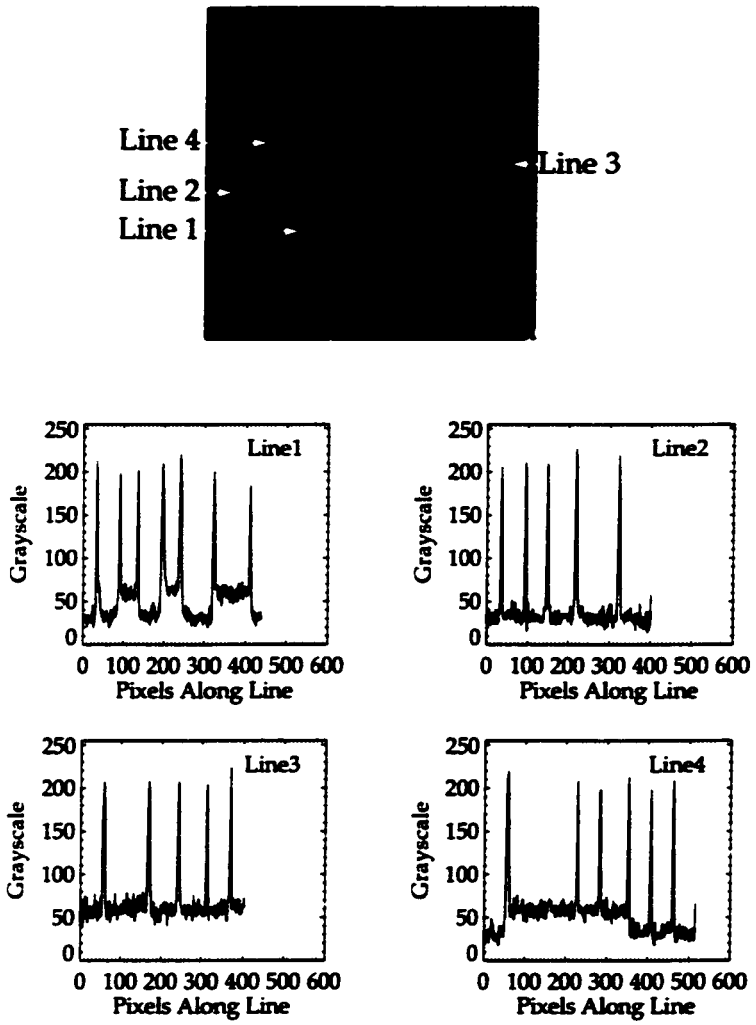

Figure 4-22. Lines specified through the high-resolution images of the phantoms and the values of grayscale along each line.

seen, for example, along Line 4. In the first air region, the values extend almost to 50, while in the first water region, values below 50 exist. This overlap does not inhibit the identification of the regions of water and air along the lines.

Table 4-7. Sequential Order of Material Along the Specified Lines Through Images of the Phantoms Obtained with the 101B+ Scanner.

Description	Materials (left to right)
Line 1	air, curved stainless steel at 90°, air, flat stainless steel at 90°, water, flat stainless steel at 60°, air, curved stainless steel at 0°, water, curved stainless steel at 0°, air, flat stainless steel at 45°, water, flat stainless steel at 90°, air
Line 2	air, flat stainless steel at 60°, air, curved stainless steel at 60°, air, flat stainless steel at 45°, air, flat stainless steel at 30°, air, curved stainless steel at 30°, air
Line 3	water, curved stainless steel at 30°, water, flat stainless steel at 30°, water, flat stainless steel at 45°, water, curved stainless steel at 60°, water, flat stainless steel at 60°, water
Line 4	air, curved stainless steel at 30°, water, flat stainless steel at 90°, water, curved stainless steel at 90°, water, curved stainless steel at 60°, air, flat stainless steel at 90°, air, curved stainless steel at 90°, air

The line profiles indicate that the size of the metal surfaces is on the order of the size of a pixel. The metal surface is represented by a sharp rise, and a subsequent sharp decline, in value of grayscale. In contrast to the water and air regions, the maximum value is reach for only one pixel as the line passes through the stainless-steel surfaces. The pixel size is 0.15 mm, thus the 0.38-mm-thick surface is expected to comprise three pixels. Two of the pixels that represent the surface are edge pixels, that represent both metal and one of the two fluids. The maximum value of the stainless-steel peak in the line profile may not represent the true attenuation coefficient for stainless steel, even in the high-resolution images.

The profiles of values along the corresponding lines through the low-resolution images were determined. The image at an elevation of 126.7 mm and the line profiles are shown in Figure 4-23. The materials along the lines are the same as for the high-

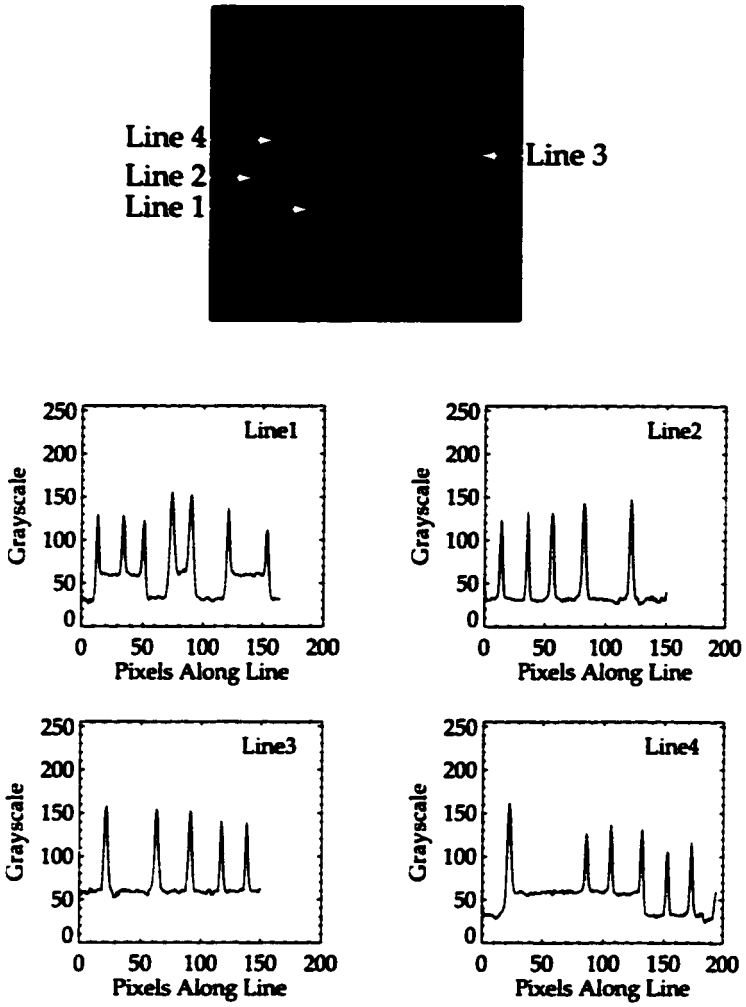

Figure 4-23. Low-resolution image of the phantoms with a line specified through each and plots of the values of grayscale along each of the lines.

resolution images, as described in Table 4-7. There is less fluctuation in the value of grayscale in the air and water regions, than there was in the high-resolution images. The narrower peaks in the histograms are also evidence of the lower level of noise

present in the low-resolution images. The overlap of values of grayscale between regions of air and water does not exist for the low-resolution images.

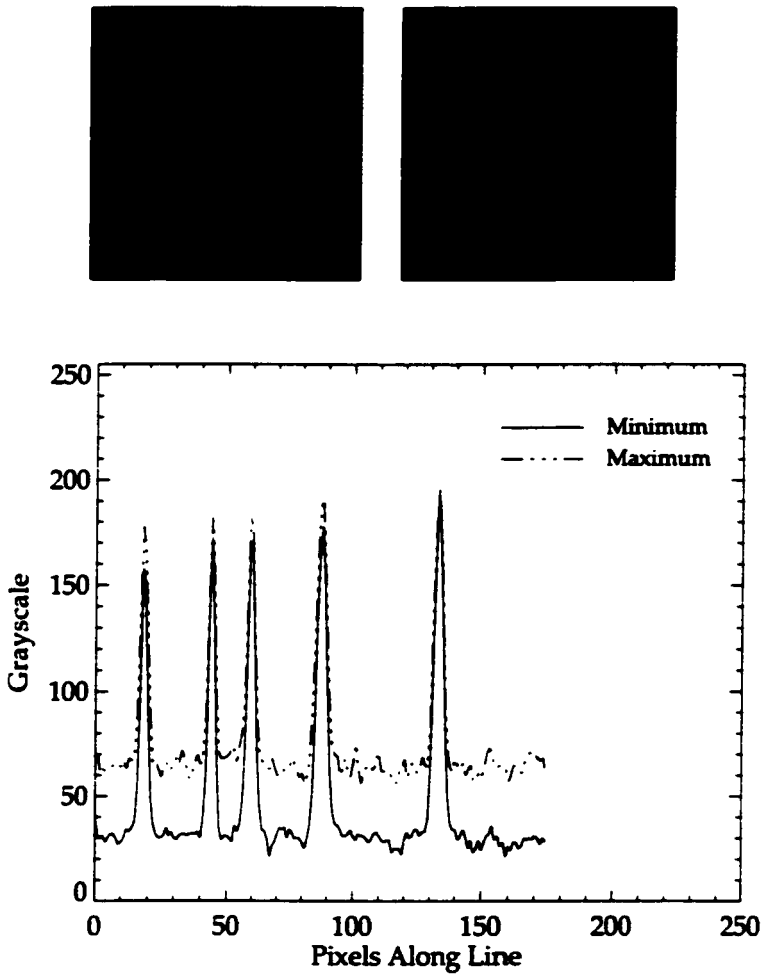

Figure 4-24. Line profile through Phantom 2 in the images at an elevation of 127.0 mm obtained with the Alliant scanner.

The peaks in the line profile that represent the metal regions are easily distinguished from the air and water regions. The maximum values for the steel are

less than in the profiles of the high-resolution images, as a result of the larger pixel size. This is consistent with the dimmer metal features observed in the CT images. For the low-resolution images, the pixel size is 0.4 mm, which is slightly larger than the 0.38-mm-thick metal surfaces. Thus, the region represented by a pixel is never completely filled with metal. Each metal feature is represented by more pixels than what would represent the true size. The true attenuation coefficient for the metal is not represented by the value of grayscale.

The lines specified for the Alliant scans at four different elevations are presented with the profiles along the line through the images of the minimum- and maximum- water conditions. For the scans with the Alliant scanner, the phantoms did not shift position between images. Thus, a direct comparison between water and air present in the same region of the phantoms, at different times, can be made. The features that are encountered along the lines are specified in Table 4-8.

Table 4-8. Sequential Order of Material Along the Lines Through the Images of the Phantoms Obtained with the Alliant Scanner.

Description	Stainless-Steel Surfaces (top to bottom)
Figure 4-24: Phantom 2, Elevation of 127.0 mm	flat at 60°, curved at 60°, flat at 45°, flat at 30°, curved at 30°
Figure 4-25: Phantom 1, Elevation of 129.0 mm	curved at 90°, flat at 90°, flat at 60°, curved at 0°, curved at 0°, flat at 45°, flat at 90°
Figure 4-26: Phantom 3, Elevation of 143.5 mm	flat at 0°, curved at 45°, curved at 60°
Figure 4-27: Phantom 4, Elevation of 145.5 mm	curved at 45°, flat at 90°, curved at 90°, parallel to curved at 0°

The images at an elevation of 127.0 mm, with a line specified through Phantom 2, and the profiles along the line are shown in Figure 4-24. The maximum value for each metal surface varies along the line. The air and water regions are

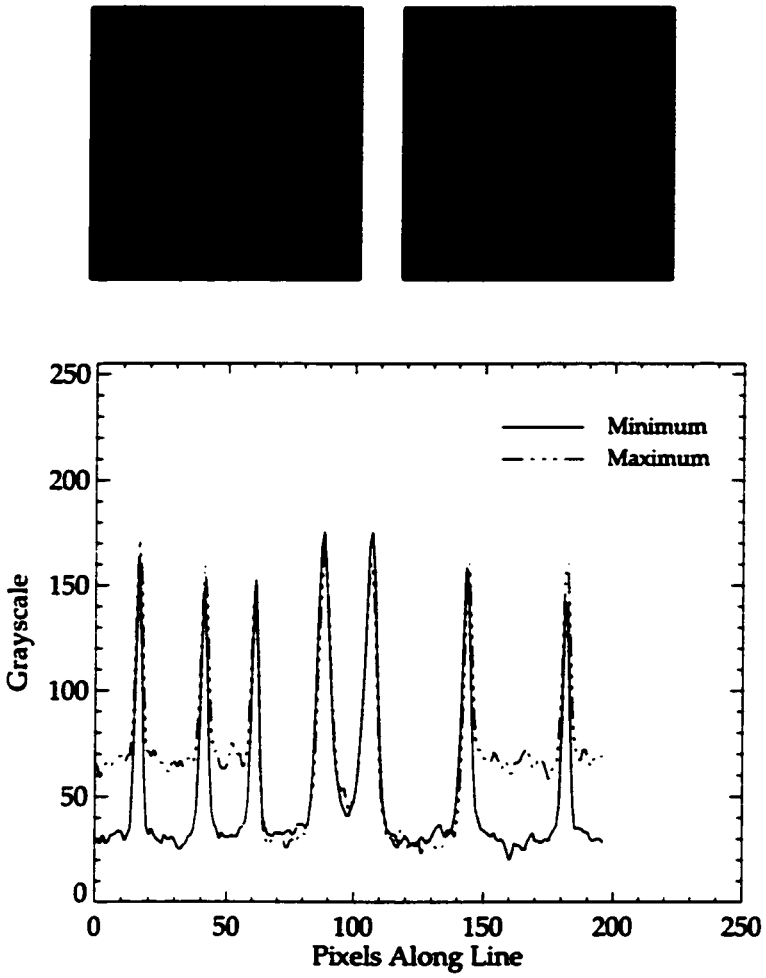

Figure 4-25. Line profile through Phantom 1 in the images at an elevation of 129.0 mm obtained with the Alliant scanner.

comprised of values in regions that do not overlap, as for the low-resolution images obtained with the 101B+ scanner.

Figure 4-25 represents line profiles through Phantom 1 at an elevation of 129.0 mm. Five regions along the line contained air for the minimum-water condition and water for the maximum-water condition. The difference between the values in these

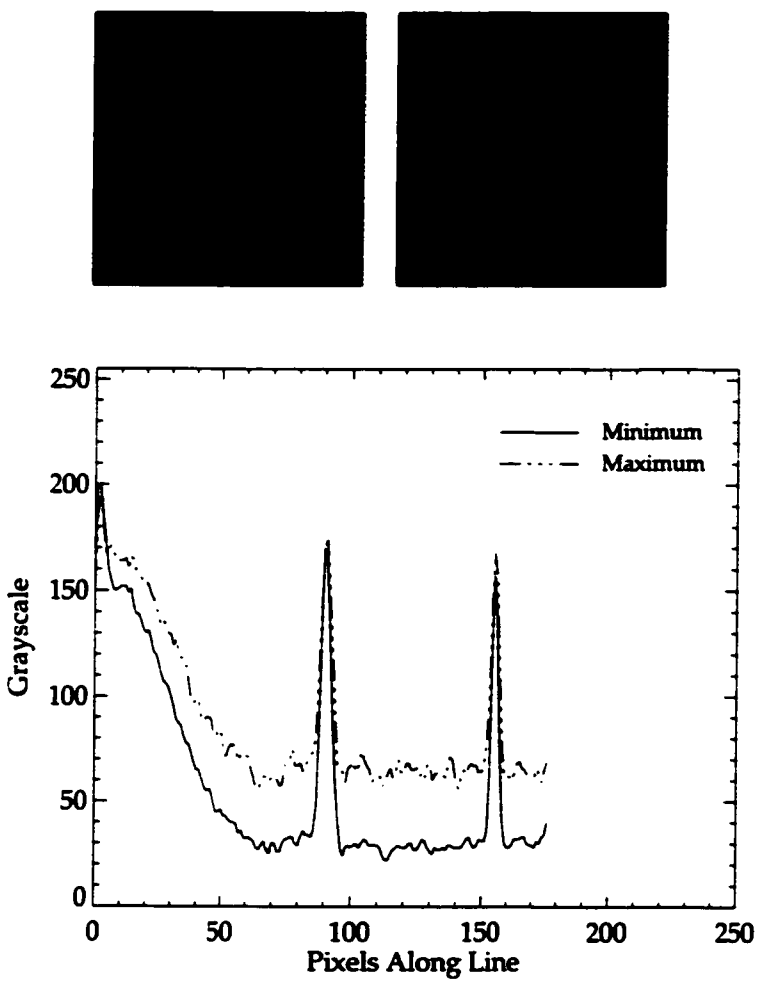

Figure 4-26. Line profile through Phantom 3 in the images at an elevation of 143.5 mm obtained with the Alliant scanner.

regions is observed in the line profile. At approximately 100 pixels along the line, the region of air between the horizontal curved surface is at a slightly higher value of grayscale than the other air regions. This indicates that if the metal surfaces were closer to each other, the air region would not be easily identified as such.

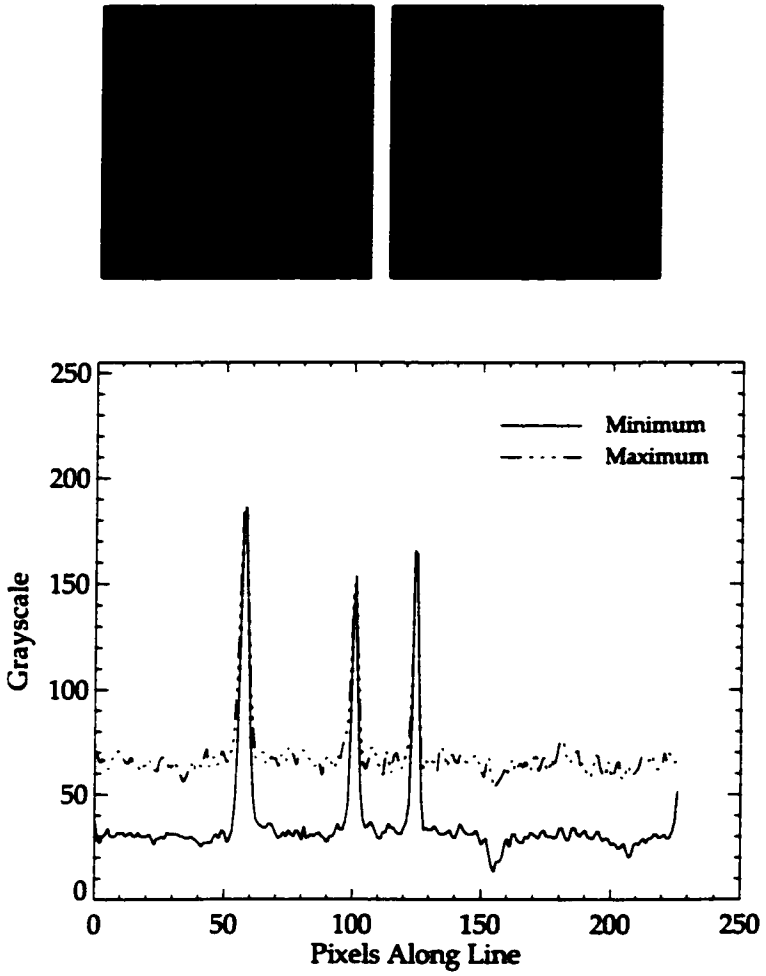

Figure 4-27. Line profile through Phantom 4 in the images at an elevation of 145.5 mm obtained with the Alliant scanner.

The third line along which the values of grayscale were determined was through Phantom 3 at an elevation of 143.5 mm, as shown in Figure 4-26. The image captures a nearly flat stainless-steel region. The slope of the value of grayscale corresponds to the slope of the metal surface. The value at the start of the line is comparable for the profiles of the dry and flooded images shown. However, along the

line the value of the maximum-water condition is consistently higher than that of the minimum-water condition. The metal surface does not comprise the entire region represented by the pixel. Therefore, the value in the pixel represents the combined attenuation coefficient of metal and the fluid that is present. This difference is more apparent in the line profile than in the CT image.

The final line specified for the Alliant scans is through Phantom 4, at an elevation of 145.5 mm, as seen in Figure 4-27. The line profile shown crosses one of the streak artifacts between 150 and 160 pixels along the line. The decrease in value due to the artifact is seen in both the air region and in the water region. The magnitude of the decrease is greater for the artifact in the air region.

The line profiles were used to obtain additional comparison of regions in one image or between two images. Differences that were observed in the line profiles were not always apparent in the images. The difference between the metal interfaces was not quantifiable at the relative size of a pixel and the metal features. However, the line profiles confirmed the presence of more noise in the high-resolution images than in the low-resolution images.

4.1.5. Calculation of Percent Water Using Sinograms

The sinograms corresponding to the high-resolution images at an elevation of 142.7 mm, shown in Figure 4-5, are shown in Figure 4-28. The sinogram in (a) represents the dry, or minimum-water, condition. The image shown in (c) represents the flooded, or maximum-water, condition. The image shown in (b) is the partial-water condition at the same elevation as the minimum- and maximum-water conditions. The brightest sinusoidal path that begins near the upper left corner of the sinogram represents the hose clamp that appeared in the images. The column walls are represented by the two nearly-linear parallel paths from the top to the bottom of the sinogram. Within the column region, the sinusoidal paths represent the phantoms.

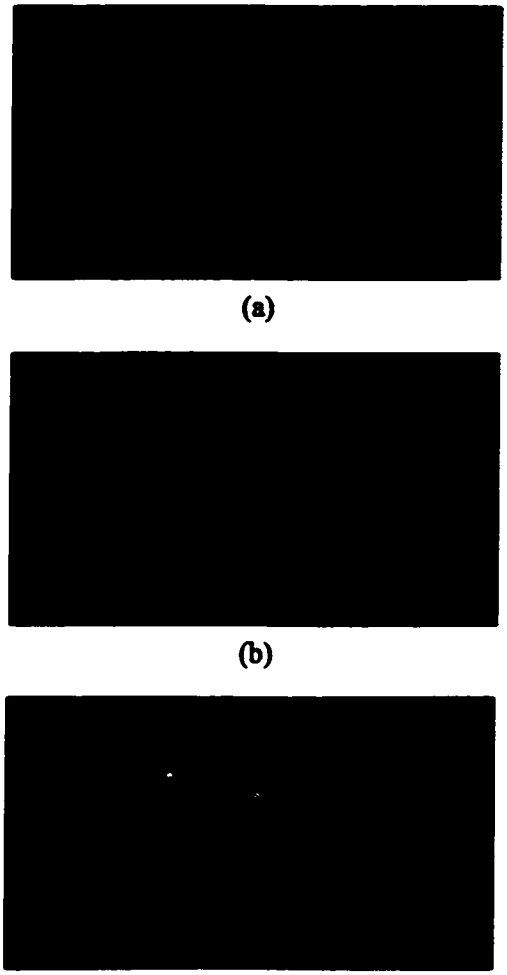

Figure 4-28. Sinograms corresponding to high-resolution CT scans of the phantoms with the 101B+ scanner at an elevation of 142.7 mm for (a) dry, (b) partially-filled, and (c) flooded conditions.

The sinograms of the dry, partially-filled, and flooded conditions at an elevation of 140.9 mm obtained with the 101B+ scanner using the low-resolution parameters are shown in Figure 4-29. The images that were reconstructed from these

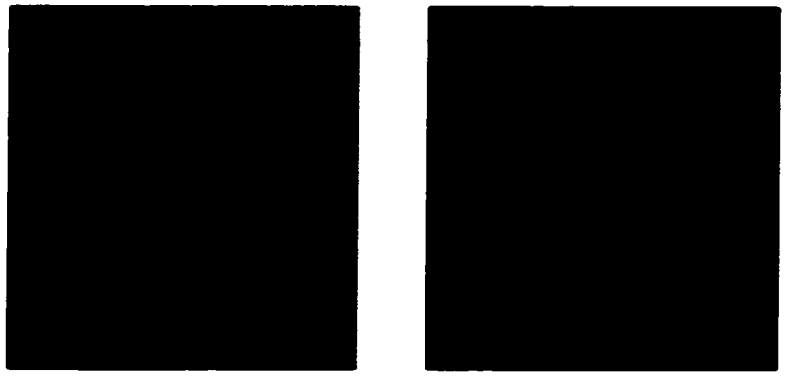

(a) (b)

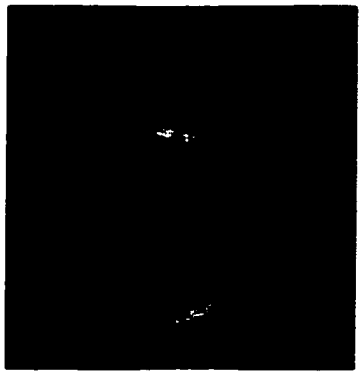

(c)

Figure 4-29. Sinograms corresponding to low-resolution CT scans of the phantoms with the 101B+ at an elevation of 140.9 mm for (a) dry, (b) partially-filled, and (c) flooded conditions.

sinograms were shown in Figure 4-6. The size of the sinograms is different from the sinograms for the high-resolution scans. The number of rows is now only 600 and the number of columns is 585, decreased from the values of 900 and 1638.

The sinograms from four of the scans with the Alliant scanner are shown in Figure 4-30. The features of the sinograms are similar to those in the sinograms obtained with the 101B+ scanner. The metal hose clamp was not located within the scan plane, and thus does not appear in the sinogram. Two sinusoidal paths, due to dry

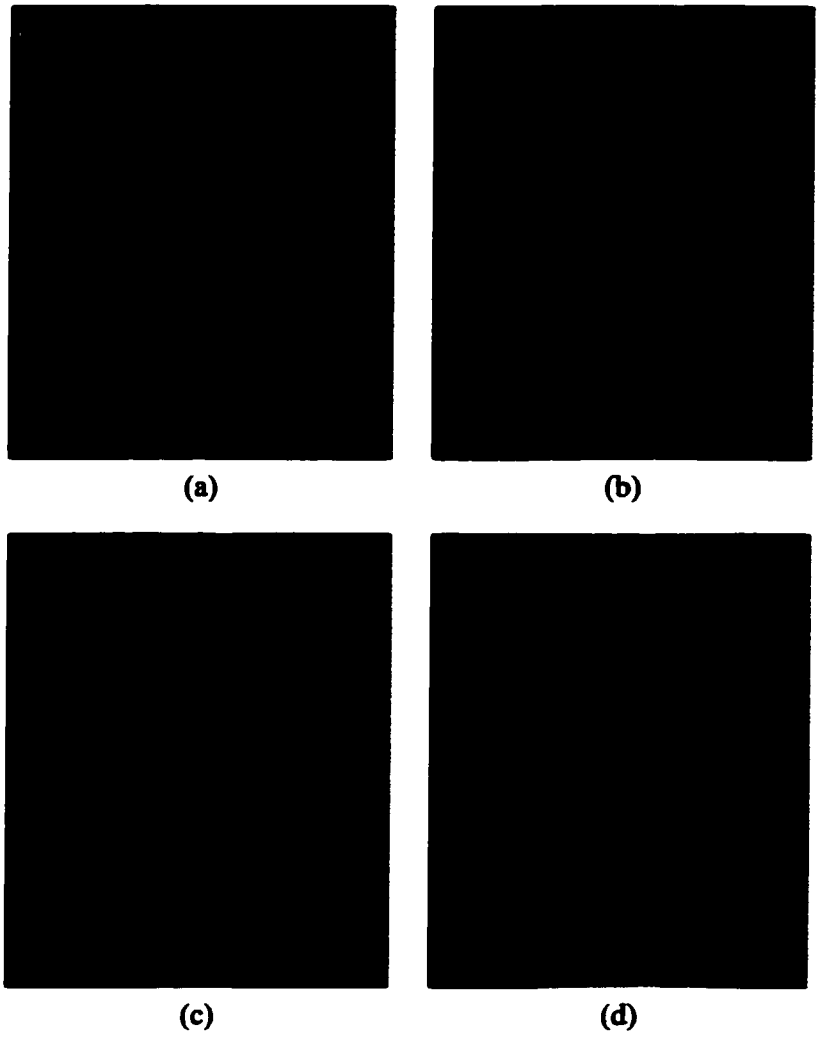

Figure 4-30. Sinograms corresponding to CT scans of the phantoms with the Alliant scanner at an elevation of 146.0 mm for (a) column and phantoms dry, (b) Phantom 4 filled, (c) Phantoms 2,3, and 4 filled, (d) entire column filled.

plastic tubes external to the column, are visible. In addition, the column walls follow sinusoidal paths in the sinogram, because the center of the column was not at the center of rotation for these scans.

The actual amount of water present in the phantoms at the time of scanning was calculated from the sinograms, which represent the transmission data that are used to reconstruct an image. The advantage of using the sinogram for this calculation is that the size of the region of water does not affect the identification of the water. The total amount of water present is represented by the sinogram. The calculation of percent water present using the averages of the sinograms for the minimum-, partial-, and maximum- water conditions was performed according to Equation 3-18. The values calculated from the sinograms will be referred to as the experimentally-determined sinogram values.

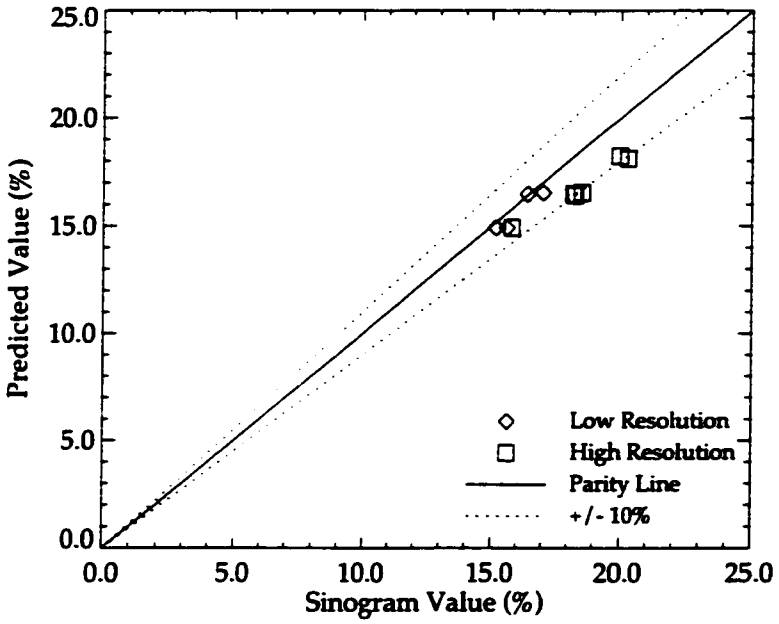

Figure 4-31. Parity plot of the expected vs. calculated percent water present in the phantoms, as determined using the sinogram data from the scans with the 101B+ scanner.

The amount of water present in the phantoms was calculated based upon the geometry of the phantoms. The details of this calculation are presented in Appendix A. The values calculated by this method will be referred to as the predicted value.

A parity plot of the predicted percent water versus the experimentally-determined sinogram percent water is shown in Figure 4-31 for the 101B+ scans. The data were calculated for both high- and low- resolution scans. On this plot, lines with ten percent variation from the parity line are shown. The data points in the plot fall within this region. The data points from the low-resolution scans are located closer to the parity line than those from the high-resolution scans.

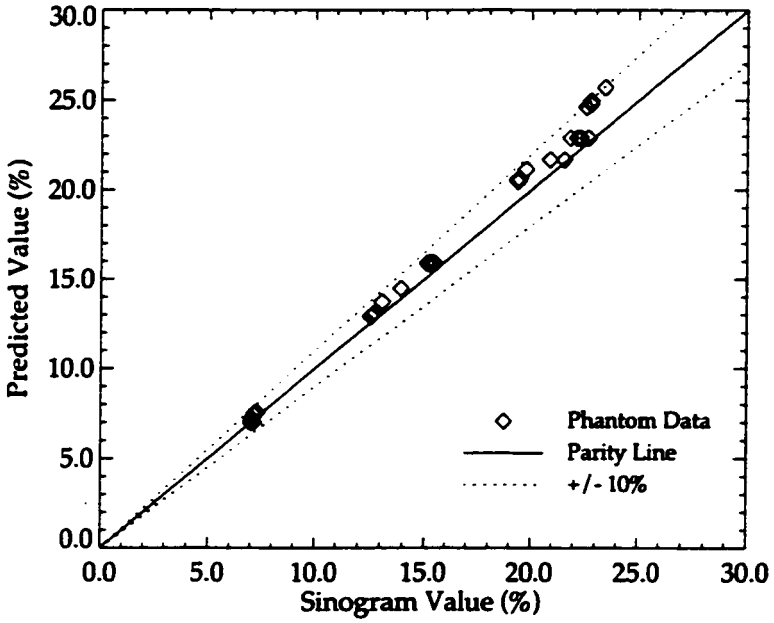

Figure 4-32. Parity plot of the expected vs. calculated percent water present in the phantoms. Calculations were performed using the sinogram data from the Alliant scans.

A comparison of the predicted and experimentally-determined percent water, determined for the Alliant scans, is shown in Figure 4-32. The range of predicted percent water was 7-25%, which is greater than that for the scans obtained with the 101B+ scanner. The values calculated from the sinograms for these scans all fell within plus or minus ten percent from the parity line. These calculations show that the sinograms can be used to calculate the amount of water present during a scan.

4.2. Film-Flow Imaging Experiments

4.2.1. Accuracy of the Metering Pump

The thickness of the film on the film-flow apparatus depends upon the volumetric flow rate of fluid to the column. The relationship between the pump drive setting of the metering pump and the actual flow rate was measured for the range of flow rates used experimentally. The results of these measurements are tabulated in Table 4-9, and depicted graphically in Figure 4-33. A variation in flow rate of five percent corresponds to a variation in film thickness of less than two percent, while a variation in flow rate of one percent corresponds to a variation in film thickness of less than half of a percent.

4.2.2. Radiograms

A radiogram of the film-flow apparatus within the acrylic column is shown in Figure 4-34. The scan elevation, which is approximately two inches from the top of the stainless-steel pipe, is labeled. In the radiogram, the inlet and outlet tubes are visible to the left and right of the column. The half-inch stainless-steel tube inside the column that is used to feed water to the center of the pipe is visible in the center of the image.

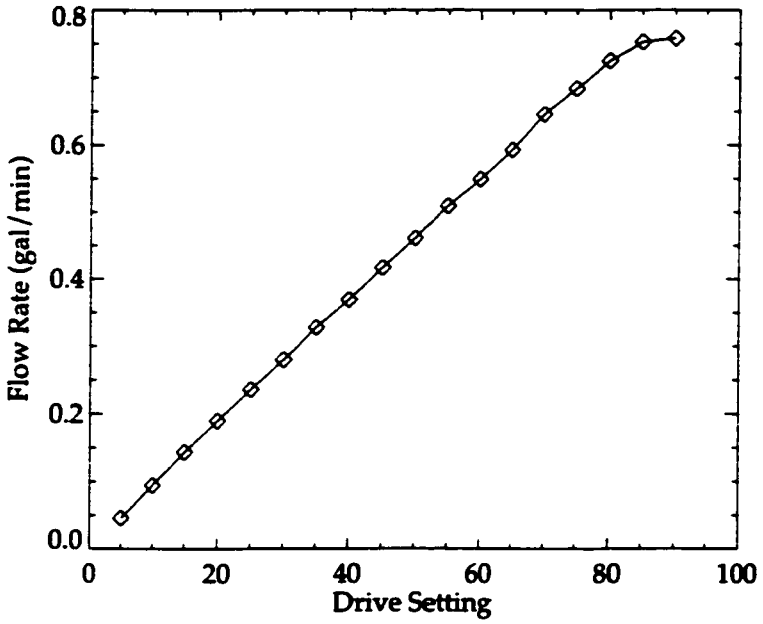

Figure 4-33. Relationship between volumetric flow rate of water at ambient conditions and the pump drive setting.

Table 4-9. Measured Flow Rates of the Metering Pump

Drive Setting	Flow Rate (gpm)	Maximum Percent Variation
20	0.19	0.6%
30	0.28	1.9%
40	0.37	1.6%
50	0.46	2.2%
65	0.59	0.8%
80	0.73	1.6%

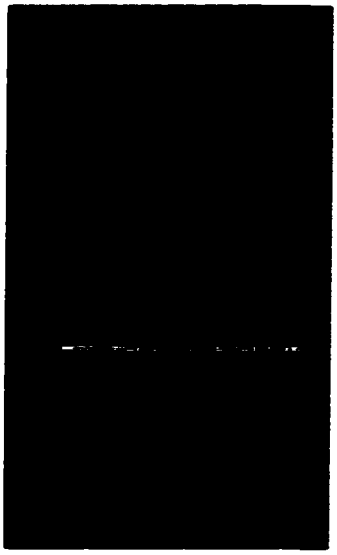

Figure 4-34. Radiogram of the film apparatus showing the 6-inch acrylic section and the stainless-steel wetted-wall surface. The elevation of the CT scans is indicated.

The film-flow apparatus was designed so that the water would overflow the central region of the pipe and form a thin film on the surface of the pipe. The levelness of the top of the pipe is thus important in obtaining a film with a consistent thickness on the entire surface. Radiograms were obtained from two orthogonal directions to determine how level the film apparatus was when placed on the Alliant scanner. Two radiograms obtained from the standard orientation are shown in Figure 4-35 and Figure 4-36, before and after adjustment, respectively. The region of the radiogram at the top of the pipe is shown in (a). Magnified regions of each side of the pipe are shown in (b). When the column was originally attached to the turntable of the Alliant scanner, the right edge of the pipe was measured to be one pixel lower than the left edge, as seen in Figure 4-35, which corresponds to a difference in height of 0.29 mm. The second radiogram from the standard orientation was obtained after shims were placed under the column to increase the height on the right edge. As shown in Figure

(a)

(b)

Figure 4-35. Radiogram of the top of the film apparatus from the standard perspective. (a) Entire column in view. (b) Magnified regions near the edges of the pipe with the top of the apparatus marked.

(a)

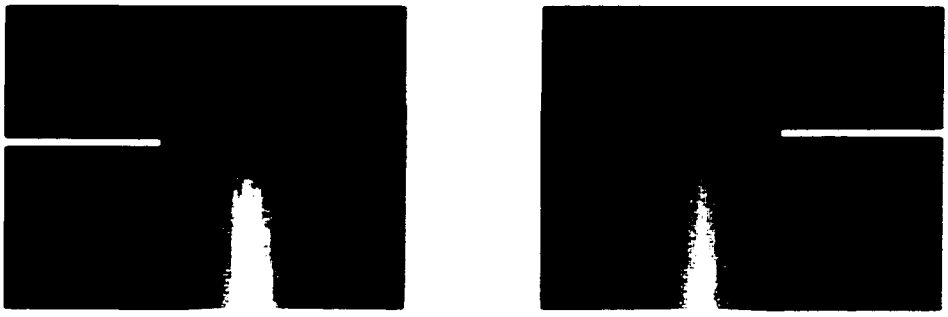

(b)

Figure 4-36. Radiogram of the top of the film apparatus from the standard perspective after adjustments. (a) Entire column in view (b) Magnified regions near the edges of the pipe.

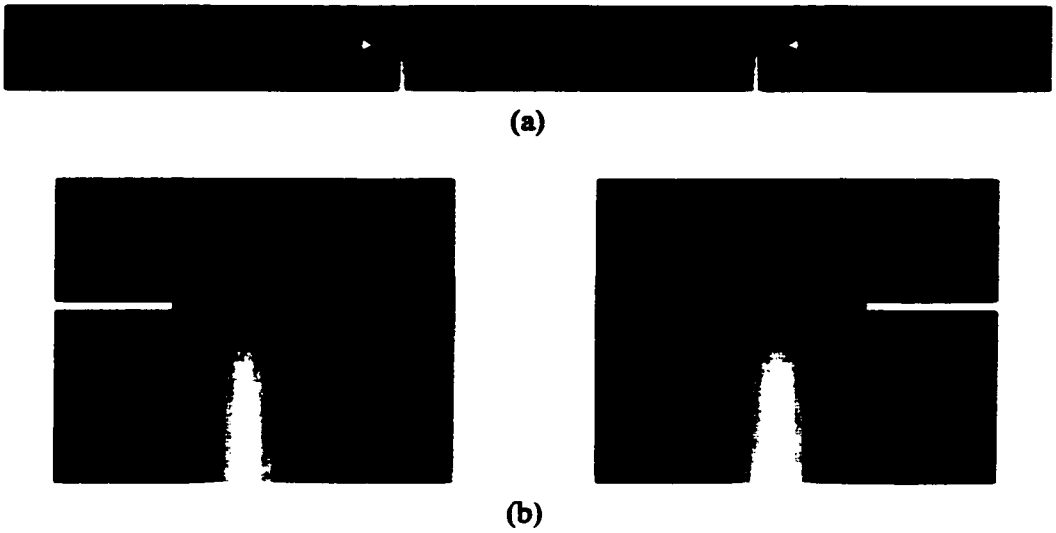

Figure 4-37. Radiogram of the film apparatus after adjustment of the levelness and a 90° rotation. (a) Entire width of the column. (b) Magnified sections of the radiogram.

4-36, the right edge was one pixel higher than the left after the adjustment. From this perspective, the angle of the top of the column with respect to the horizontal is less than a quarter of a degree. No finer adjustment was available to vary the position of the column. A radiogram of the apparatus was subsequently obtained after rotating the column 90°. At this orientation, both sides of the top of the pipe are at the same elevation, as seen in Figure 4-37. Thus, for the scans of the film-flow apparatus, the pipe was at an angle of less than 0.25° with the horizontal. The highest region of the apparatus will be located at the right side of each of the CT images.

4.2.3. CT Images

X-ray CT images were obtained of the film-flow apparatus under various conditions. Images representing four conditions are shown in Figure 4-38. Prior to the introduction of flow to the column, a scan at the desired elevation of 463.0 mm

was performed, and the resulting image is shown in (a). The second scan of the column was obtained with the center of the pipe filled with water, as shown in (b), to represent the minimum-water condition. The image shown in (c) represents a flow condition. The fourth image, (d), was obtained with the entire column filled with water and represents the maximum-water condition. As with the images of the phantoms, all CT images in this section are presented with consistent scaling, unless otherwise indicated.

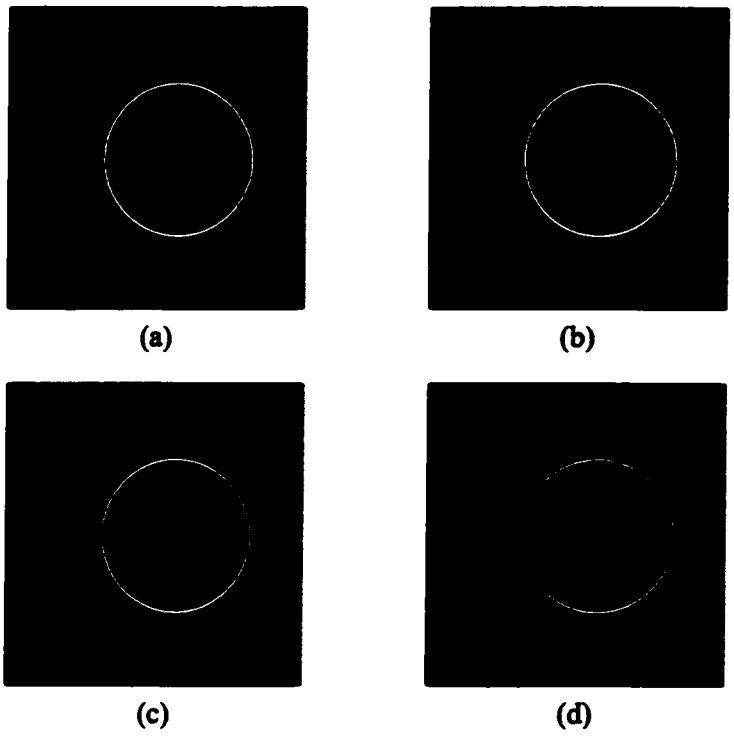

Figure 4-38. CT images of the film-flow apparatus. (a) Dry. (b) Stainless-steel pipe filled with water. (c) Thin film flowing on stainless-steel surface. (d) Entire column filled with water.

The film-flow apparatus was operated at the six flow rates listed previously in Table 4-9. The order in which the flow rates were run was determined randomly. Two sequential images were obtained of the film-flow apparatus at each rate. Each flow rate was repeated at least once; however, the 0.46 gal/min flow rate was used for three sets of scans. A total of 26 flow images were acquired. After each set of two scans, the flow on the metal surface was observed. At the lowest flow rate, a stable film was not present at the end of one set of images. For all other scans, the film remained stable for the duration of the scans.

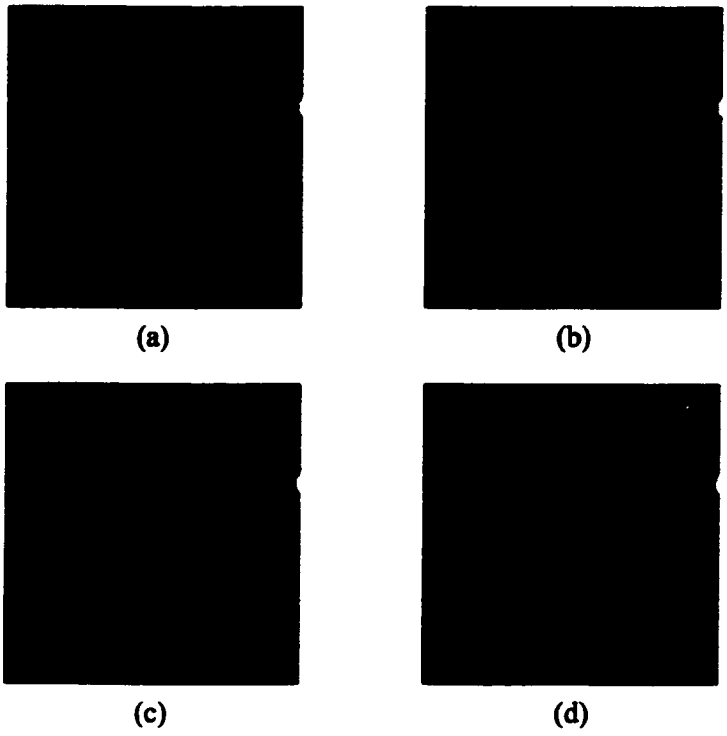

Figure 4-39. Images of the difference between flow images at various film thickness and the image with the pipe full of water. Flow rates (gpm): (a) 0.19 (b) 0.28 (c) 0.60 (d) 0.73

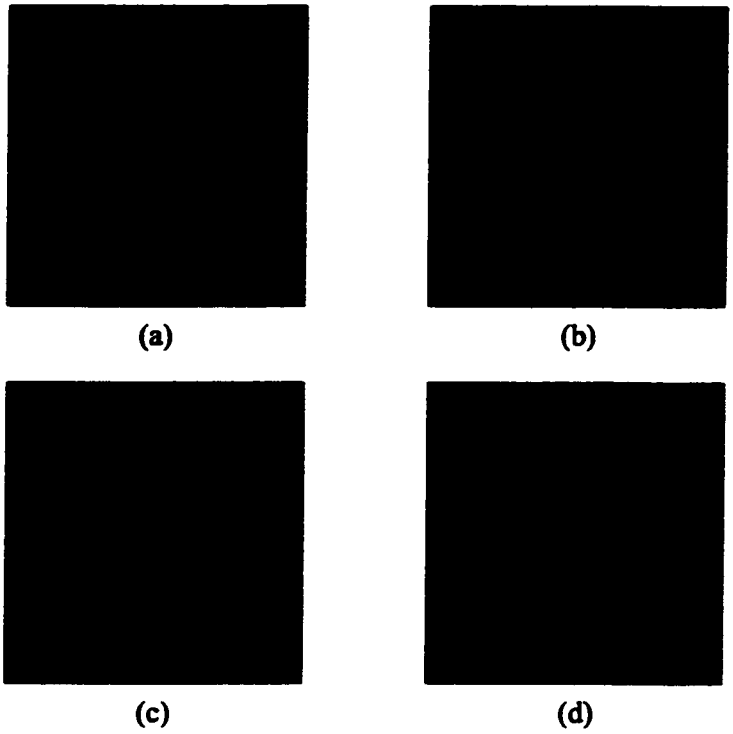

Figure 4-40. Images of the average film thickness, after processing in polar coordinates, corresponding to the images shown in Figure 4-39. Flow rates (gpm): (a) 0.19 (b) 0.28 (c) 0.60 (d) 0.73

To accentuate the differences between the flow images, the difference between each flow image and the pipe-full image was calculated. Difference images at four flow rates are shown in Figure 4-39. In each of the images, the thickness of the film appears comparable. However, the brightness of the circle that represents the water varies with flow rate. As with the stainless-steel surfaces in the images of the phantoms, the water film is comparable in size to the size of a pixel.

As described in Section 3.7.2, the polar-averaged image of the difference between the flow condition and the pipe-full condition was calculated to produce an

image representative of the average film of water. Examples of these images are shown in Figure 4-40 for the images that are shown in Figure 4-39.

4.2.4. Histograms and Line Profiles

The histograms for dry, pipe-full, and column-full conditions were determined for the images of the film-flow apparatus. A plot showing the three histograms is presented as Figure 4-41. The histograms were obtained for the circular region of the images within the column wall. Two large peaks are present in the plot, one at a value of approximately ten, and the other near a value of 35. Although barely visible in the full-scale histogram, there is an additional peak toward the upper end of the grayscale that is shown in the inset. The first two large peaks are representative of air and water, as in the scans of the phantoms. The histogram for the dry case does not have a peak for the region of water, while the histogram for the column-full case does not have a peak for the region of air. The additional peak represents the stainless-steel pipe, which contains more metal than was present in the phantoms. The metal pixels are still represented by a wide range of the grayscale. The peak due to the metal region has shifted to a lower value of attenuation coefficient for the image with the column full of water. In contrast to the images of the phantoms, there is no plastic region present within the column walls.

As with the phantoms, lines through the images were selected, and the profile of grayscale along the lines was determined. Figure 4-42 presents images of the film apparatus with the line of interest indicated in each image, (a)–(c). The three conditions shown are of the column with no water, at the minimum-water condition, and at the maximum-water condition. The plot in (d) shows the profile along the line through each of the images. At both edges of the profile, there is a region of air for both the dry and pipe-full conditions, but a region of water for the column-full condition. The metal is located at the same position for all of the scans. The

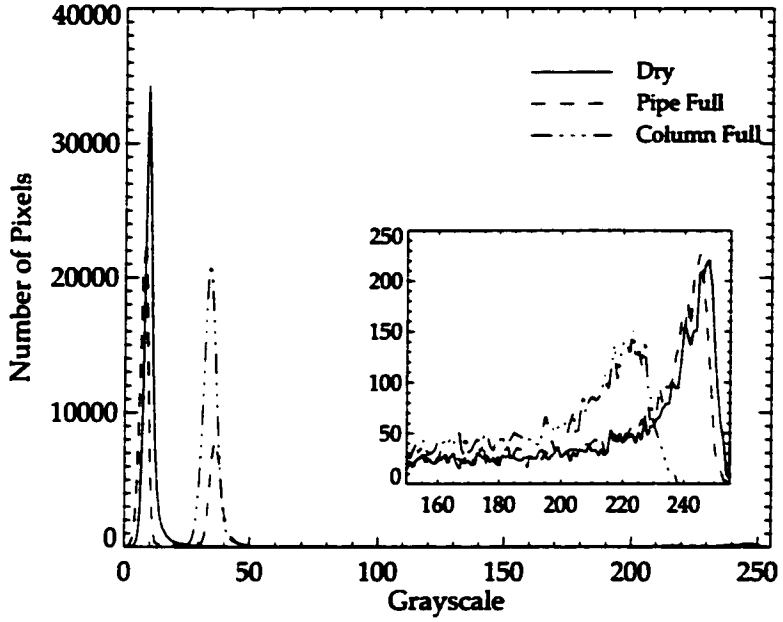

Figure 4-41. Histogram of the column region of the images of the film apparatus without water, with the pipe full of water, and with the column full of water.

maximum value along the line is higher for the dry and pipe-full cases than for the column-full condition. In the central region of the pipe, the line profile is similar for the pipe-full and column-full cases.

The profiles along a line through three polar-averaged difference images are shown in Figure 4-43. A sample image with the line of interest indicated is also shown. The profiles are shown for images at flow rates of 0.19, 0.37, and 0.60 gal/ min. The maximum value of grayscale is located in the region of the film, at 39 pixels along the line, and is greatest for the case with the highest flow rate. The maximum value decreases with decreasing film thickness, as expected. Also evident from the line profiles is the incomplete subtraction of the steel pipe. Small peaks corresponding

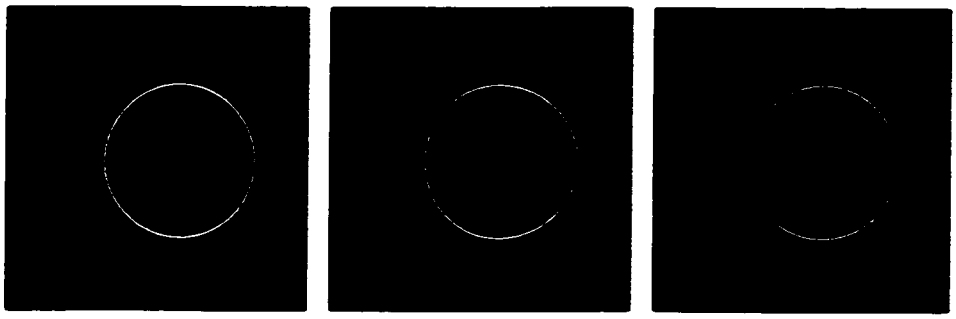

(a) (b) (c)

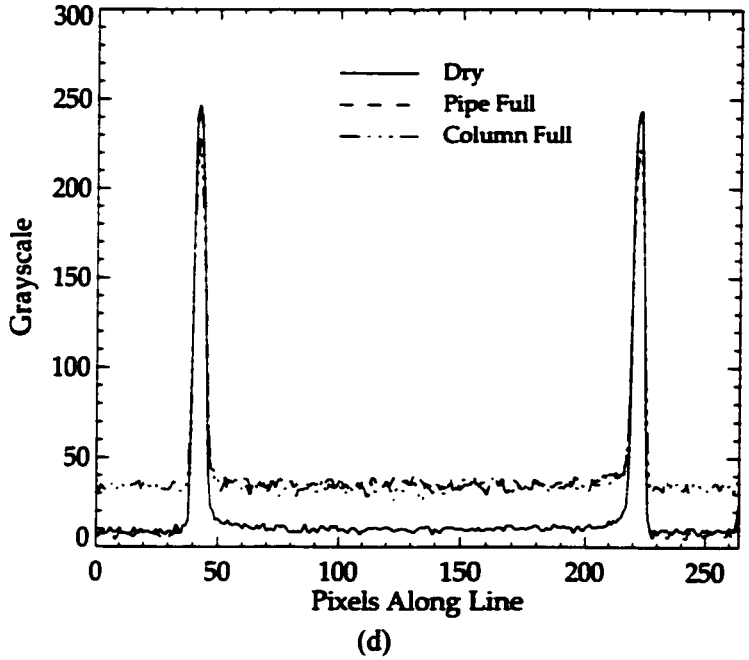

(d)

Figure 4-42. Values of grayscale along selected line through the images of the film apparatus. (a)–(c) Dry, pipe-full, and column-full images with lines drawn. (d) Line profile through each image

to the dark and bright regions in the difference image, in the region of the steel pipe, are present along the line profile.

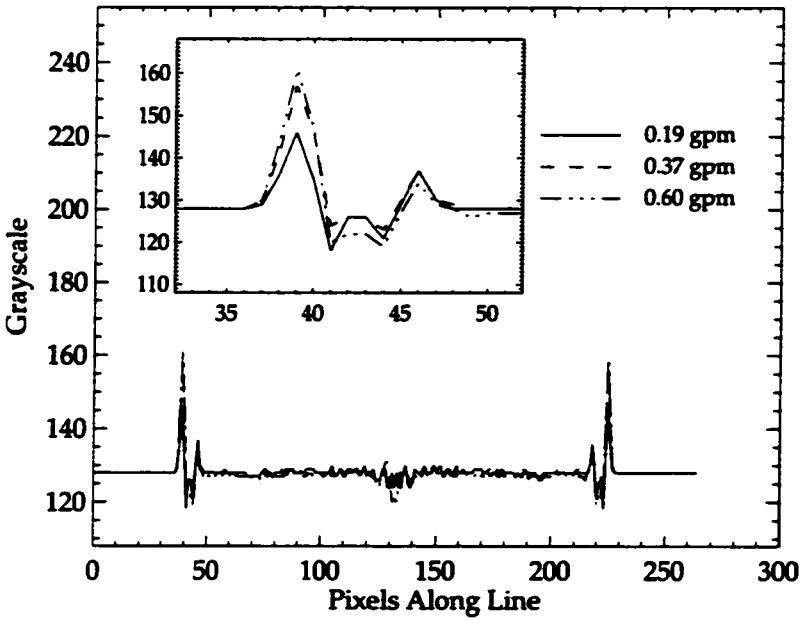

Figure 4-43. Line profiles through the polar-averaged images that represent average film thickness. Sample line along which profiles were obtained and line profiles.

4.2.5. Film-Thickness Calculations

The film thickness calculated, using two methods of image analysis, was compared to the value of film thickness expected from transport theory. The dependence of the thickness of a thin film flowing on a cylindrical surface on the

volumetric flow rate was derived from the Navier-Stokes equation, as shown in Appendix B. The film thickness based upon transport theory was calculated, for each of the six experimental flow rates, according to Equation 3-22 and Equation 3-23. These values will be referred to as the theory-predicted film thickness.

Two methods were used to calculate the film thickness from the CT images. The first method was a simple method that identified the maximum value located in the water region of the polar-averaged difference image, as represented by the maximum value of the peak in Figure 4-43. The maximum value for one flow image was used to determine the scaling between the film thickness and maximum value. The scaling determined was then applied to the maximum values in the polar-averaged difference images at all of the remaining flow rates. The parity plot for the maximum-value method is shown in Figure 4-44.

The parity plot shown in Figure 4-44 indicates that there are two data points that are not accurately predicted with the maximum-value method. These two data points correspond to two images obtained sequentially at the lowest flow rate. During these two scans of the film-flow apparatus, the film became unstable. When observed at the end of the imaging sequence, the film was not completely wetting the metal surface. The flow condition during the scans was not accurately known. Yet, it appears that the data points do not represent the intended condition. These two points will appear as outliers in all of the parity plots that include film-flow data.

With the elimination of the two outliers, the data points are located well within a variation of ten percent from the parity line. There is some variation in values of thickness calculated at each flow rate from the multiple images. A variation in film thickness between a half of a percent and two percent is expected, based upon the variation in flow rate measured and presented in Table 4-9.

The integration method was used to calculate an average film thickness for each of the 26 film-flow images. The calculations of film thickness are compared in

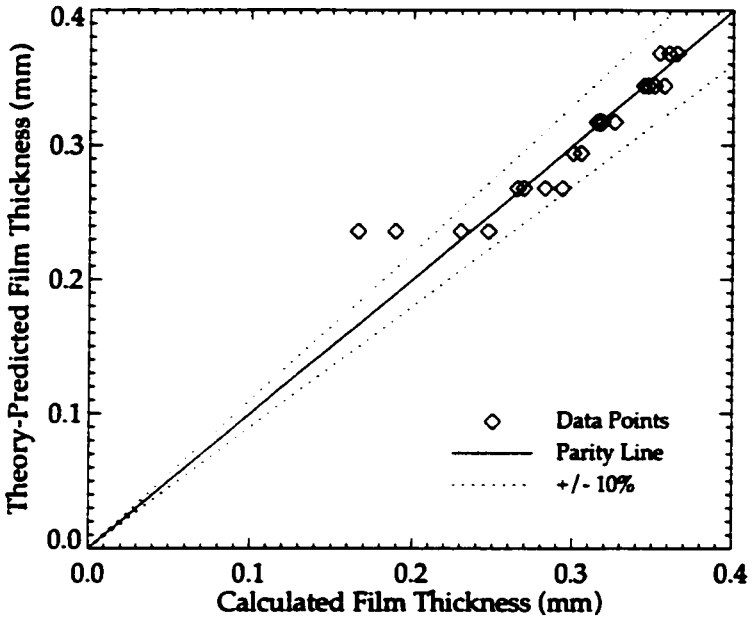

Figure 4-44. Parity plot for calculation of the film thickness with the maximum-value method compared with the theory-predicted values.

Figure 4-45. The parity plot for the values calculated using definition 1, which specified the region between the center of the pipe and a circle outside of the film, is represented in (a). The values calculated using this method were all less than the corresponding theory-predicted values. The inclusion of the dark region resulting from the subtraction of the metal region, likely contributed to this error. As expected, the use of definition 3, which specified the region between the locations in the film equal to half of the attenuation attributed to water, resulted in values less than the theory-predicted values. The parity plot for this definition is shown in (c). The region of integration specified by definition 2 was the most accurate, as shown in (b). The data points at the lowest two flow rates exhibited the greatest error when compared to the values predicted from transport theory. Disregarding the two outliers, two points

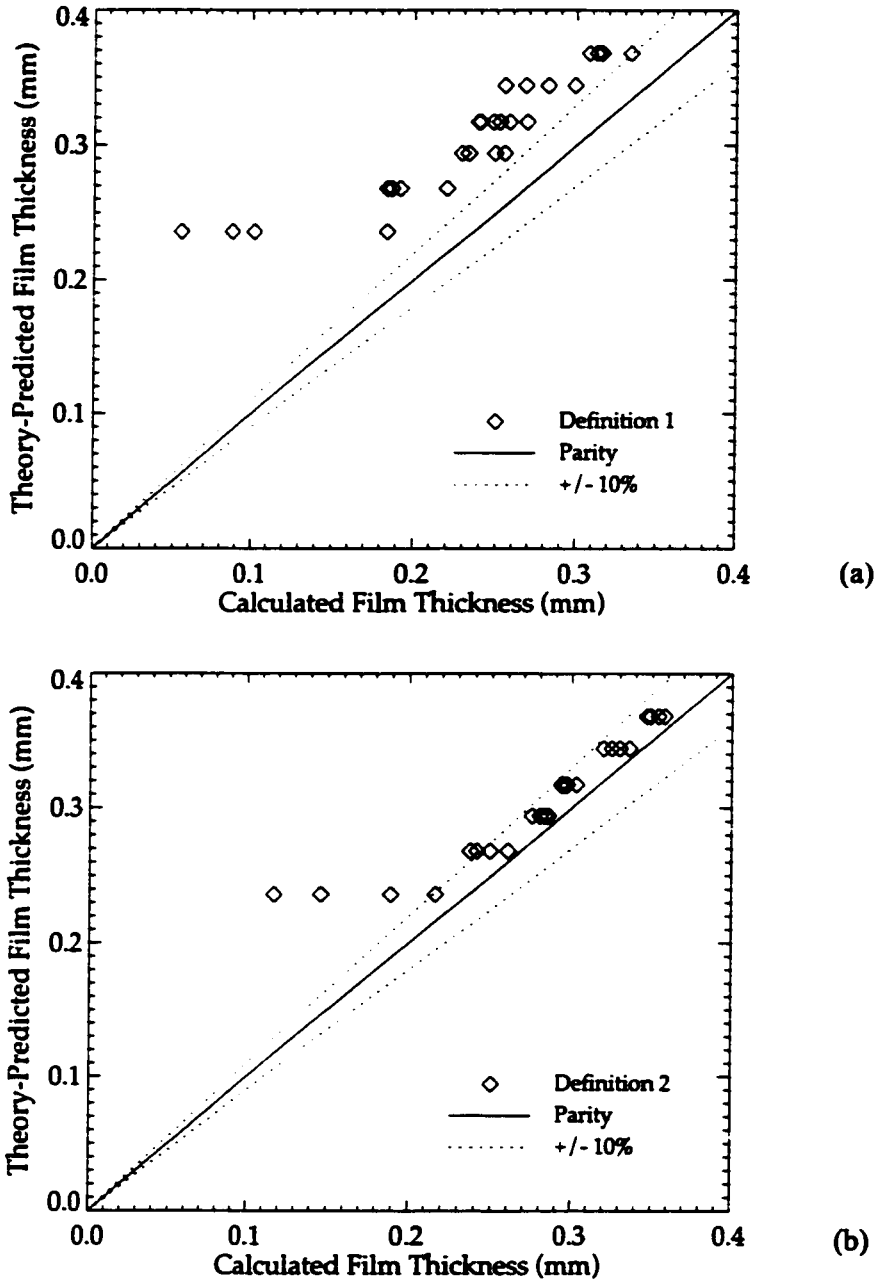

Figure 4-45. Parity plots for the integration method of calculating film thickness: (a) Definition 1, (b) Definition 2, (c) Definition 3

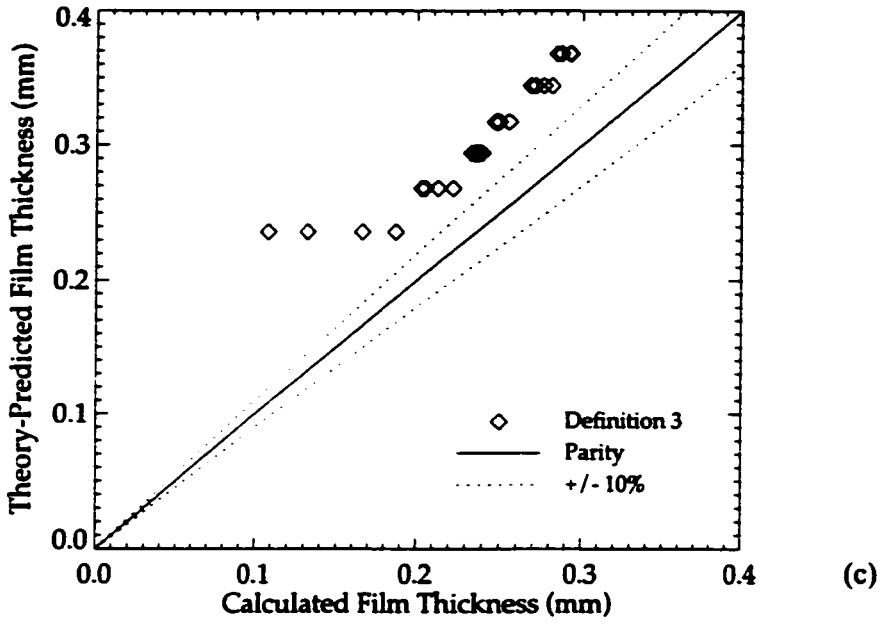

Figure 4-45 (cont.) Parity plots for the integration method of calculating film thickness: (a) Definition 1, (b) Definition 2, (c) Definition 3

were outside the region of ten percent variation from the parity line. The variation from the theory-predicted value was 11.5% and 20.0% for these two points.

Values of film thickness were calculated for each 5°-section around the circumference of the metal pipe with the integration method. Variation in the film thickness with respect to the angular position was evaluated. The values calculated using definition 2 to specify the integration region were used for this analysis.

The calculated film thickness varied around the circumference of the stainless-steel pipe. The angular variation in film thickness for two images obtained at a flow rate of 0.37 gal/min is shown in Figure 4-46. The images were not acquired sequentially. In the plot in (a), 72 values of film thickness calculated from each image are presented at increments of five degrees. The angular position is defined in the

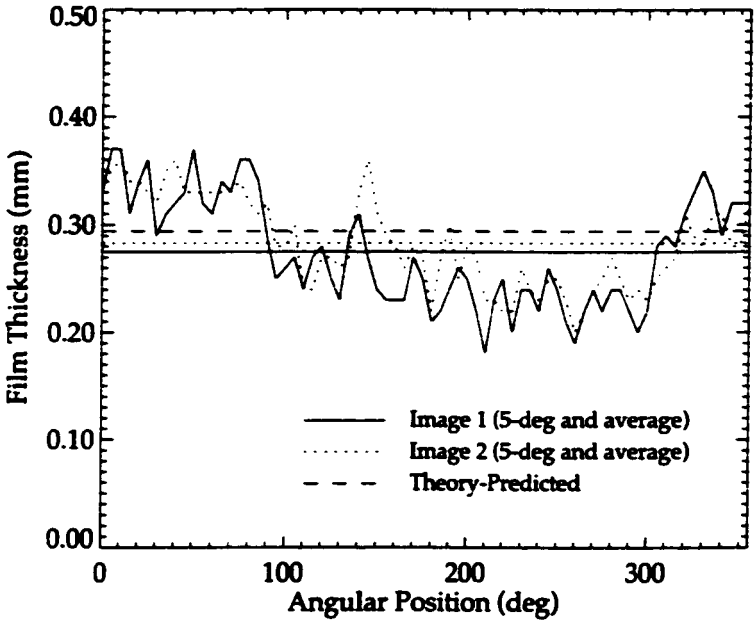

(a)

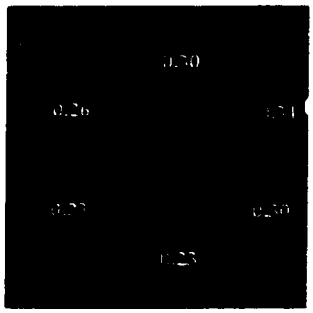

(b) Image 1

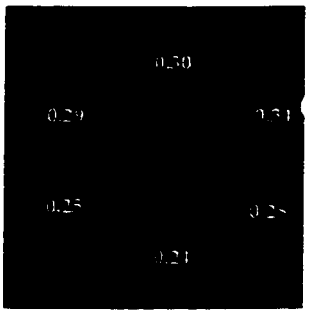

(c) Image 2

Figure 4-46. Angular variation in film thickness at a flow rate of 0.37 gpm. (a) Average values for 5° increments and the entire circumference are shown. (b)-(c) Location of angular variation is indicated for both images.

counter-clockwise direction from the positive x-axis. The theory-predicted value for this flow rate is indicated, as is the average value for the entire circumference of the

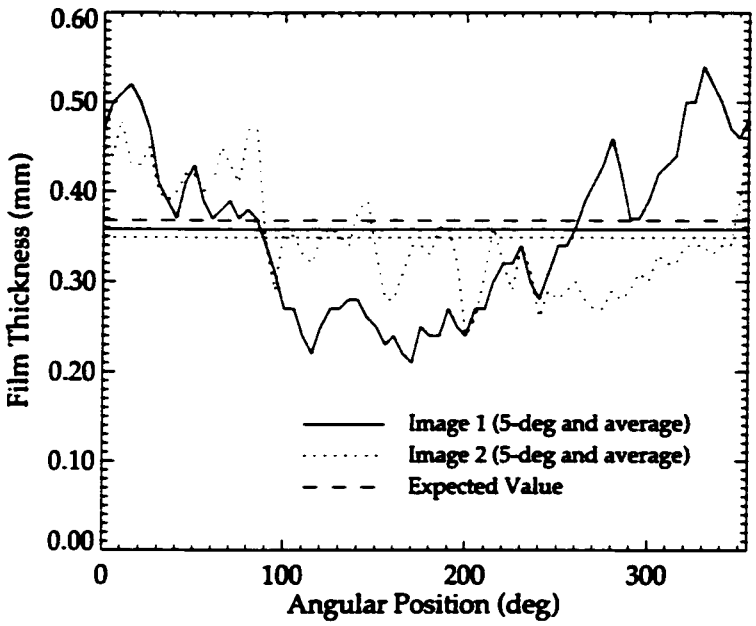

(a)

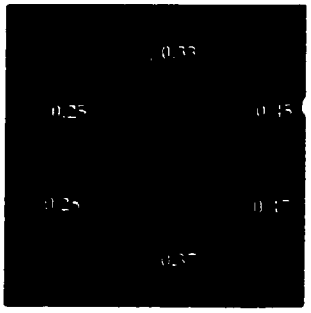

(b) Image 1

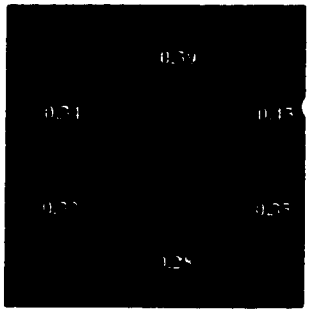

(c) Image 2

Figure 4-47. Angular variation in film thickness at a flow rate of 0.73 gpm. (a) Average values for 5° increments and the entire circumference are shown. (b)-(c) Location of angular variation is indicated for both images.

pipe for both images. The variation in flow rate for 30° segments around the pipe is depicted in (b) and (c), for each of the images. For these two flow conditions, the

variation in film thickness with respect to angular position was similar. The highest values of film thickness were calculated to be in the 0-60° segment of the pipe. In contrast, the analysis of the radiograms indicated that the pipe was higher on the right side of the CT image. However, experimentally, when the film became unstable and ceased to completely wet the surface, the break-up of the film consistently started in the region represented on the left side of the CT image. The pipe was nearly aligned with the scan plane defined by the Alliant scanner, but may not have been perfectly aligned with the direction of the gravitational force. Additional variation in the thickness of the film around the pipe may result from slight imperfections in the stainless-steel surface.

In Figure 4-47, the angular variation observed in two images at a different flow rate is presented. For these two non-sequential images at a flow rate of 0.73 gal/min, the variation in thickness does not follow the same pattern. The dependence of film thickness on the angular position is presented at 5° increments in (a). The average for each 60° section is indicated on the images shown in (b) and (c). In the region from 120° to 240°, the film in image 1 is thinner than the film in the region from 240° to 300°. The opposite trend is true for image 2.

4.2.6. Sinogram Analysis

The amount of water present in the column during a scan was calculated with use of the sinograms. Sinograms corresponding to the images presented in Figure 4-38 are shown in Figure 4-48. The four images represent the dry, pipe-full, flow, and column-full cases. The percent water was calculated as outlined in Section 3.6.2, using the pipe-full condition as the minimum condition and the column-full condition as the maximum condition. The film thickness was calculated from the percent water according to Equation 3-26. The values determined experimentally from the sinogram data were then compared to the theory-predicted values.

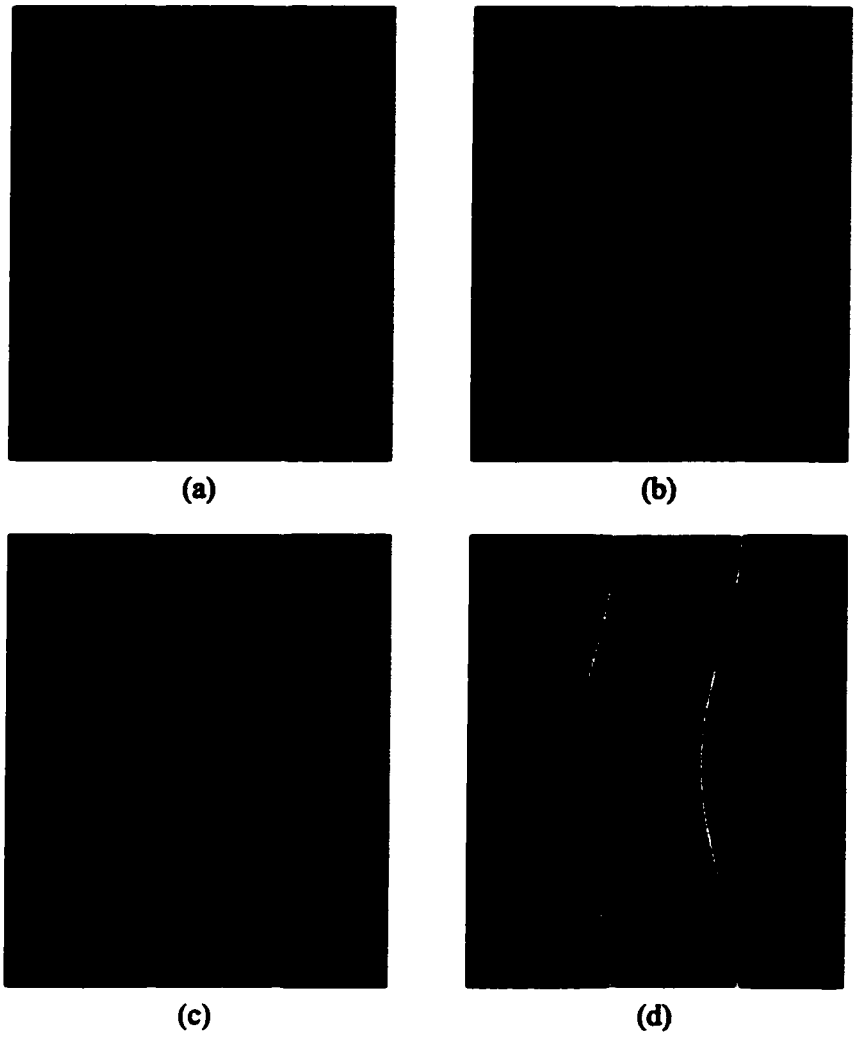

Figure 4-48. Sinograms for film-flow apparatus corresponding to the CT images shown in Figure 4-38. (a) No water present. (b) Stainless-steel pipe filled with water. (c) Thin film of water flowing on stainless-steel surface. (d) Entire column filled with water.

A parity plot of the theory-predicted values versus the experimental values of film thickness calculated from the sinogram is shown in Figure 4-49. The calculations presented in this plot are based upon the data in the entire sinogram. As seen, the

prediction from this set of data does not correlate well with the values predicted from transport theory. The two negative values of film thickness are for the same scans as the two outliers discussed previously. Two corrections to the data were incorporated to more accurately calculate the film thickness from the sinogram data.

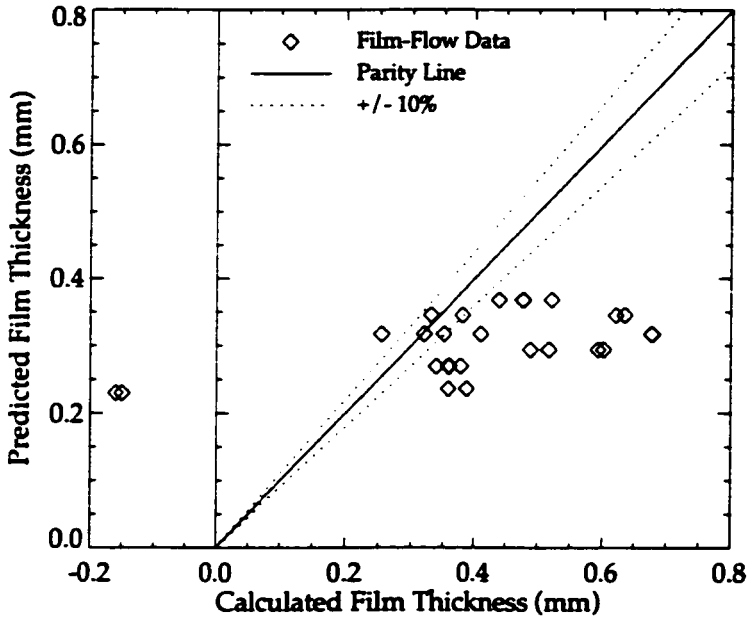

Figure 4-49. Parity plot of theory-predicted film thickness versus film thickness calculated using the entire region of the sinograms.

The first correction involved restricting the rows of the sinogram used for calculation. As can be seen in the difference images, the water outlet tube was dry during the pipe-full scan. This difference appears on the right edge of the images shown in Figure 4-39. This difference can also be seen when observing the sinograms in Figure 4-48. The inlet tube is represented by the sinusoidal path that begins at the top right of the image, outside of the column wall. In sinogram (b), this tube is empty,

while in sinogram (c) the tube is full. At the levels of water that are being measured for the film-flow apparatus, the amount of water in the tube is significant. Therefore, the region of the sinogram used to determine the mean value was restricted to rows in which the outlet tube was not within the column region. In addition, the region was restricted to the column region of the sinogram. To determine this region, a sine curve was fit to define the location of the inside column wall.

The second correction to the sinogram-based calculation of film thickness involved quantifying the drift in the response of the scanner over time. The region of the sinogram that is outside of the column should not change from one scan to the next. The mean of the sinogram in this region was calculated for the film-flow scans. The measurement of the time-dependent scanner drift is shown in Figure 4-50. There is a general upward trend in the mean within the air region of the sinogram, but the drift does not follow a predictable trend. To correct for the scanner drift, it was assumed that the drift measured in the air region was constant additive shift for all detectors. The column region of each sinogram was subsequently adjusted by the amount of shift in the air region, and the film thickness was calculated with the corrected sinogram.

A parity plot of the film thickness predicted after applying both corrections to the calculation of the sinogram is shown in Figure 4-51. The data, except for the two outliers, exhibit a high correlation between theoretical and experimental values. However, the film thickness calculated from the sinogram data is consistently approximately double the theory-predicted value. This variation is attributed to the hardening of the x-ray beam during these measurements.

As was mentioned in Chapter 3, when a polyenergetic x-ray source is used for CT imaging, the effects of beam-hardening are often noticeable. The underlying cause of beam hardening is the dependence of the attenuation coefficient on the energy of the x-ray beam. With a polyenergetic source, x rays of lower energy are preferentially

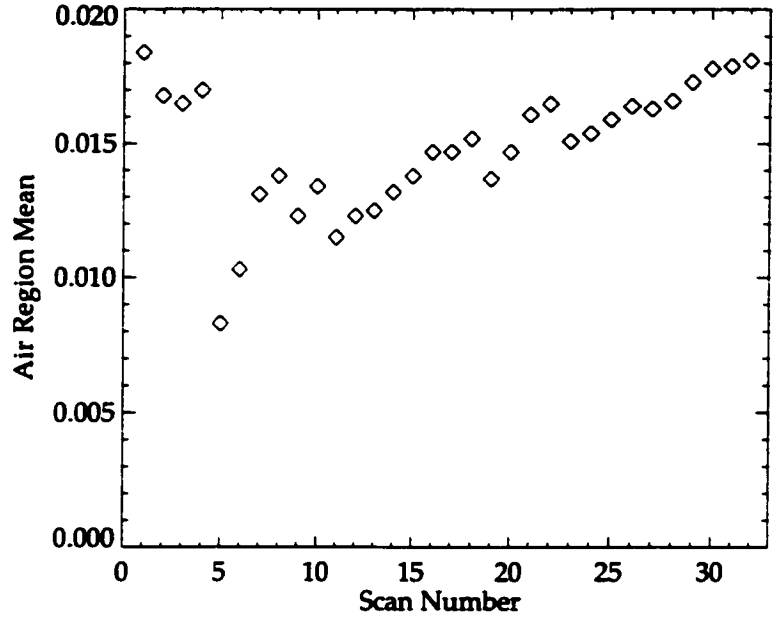

Figure 4-50. Variation with time in the air region of the sinogram for the film-flow experiments.

absorbed. As a result, the distribution of energy in the beam is altered, and the average energy of the beam increases along each path through the object. The image reconstruction algorithm that is applied to the transmission data does not account for the dependence of attenuation coefficient on the energy of the beam. Artifacts in the image, which do not represent the object accurately, are subsequently observed.

The beam-hardening artifacts present in the film-flow images are best described with the use of the histograms for the pipe-full and column-full images. The plot in the inset of Figure 4-41 indicates that the peak due to the stainless steel shifted to a lower value of grayscale for the column-full images. This shift is consistent with the steel having a lower apparent attenuation coefficient. The lower attenuation coefficient can be described by the beam-hardening effect. The average energy of the

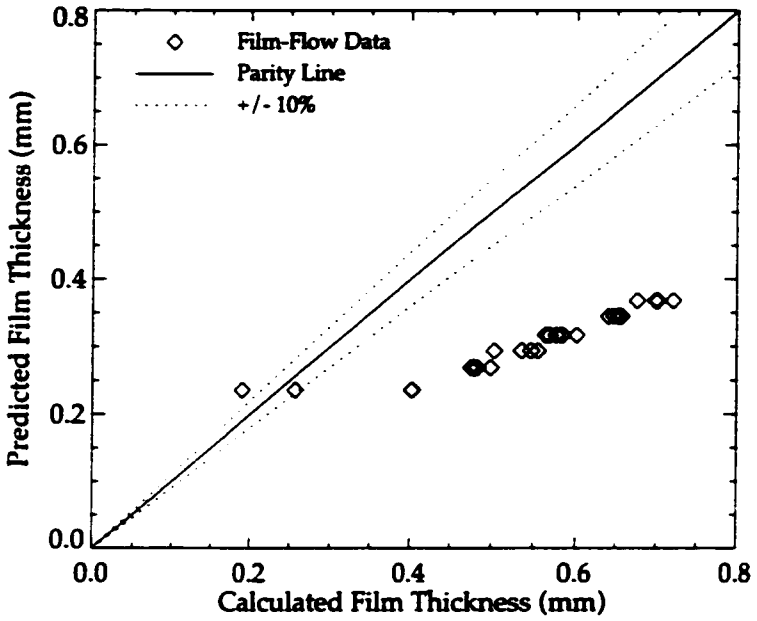

Figure 4-51. Parity plot of theory-predicted film thickness versus that calculated from the sinograms, after correcting for the scanner drift.

x-ray beam passing through the pipe was increased, as the lower-energy x rays were absorbed within the water as well as within the first portions of the stainless steel. The absorption of x rays in all of the steel regions was thus occurring at a higher average energy level, at which the attenuation coefficient is reduced.

The effect of the beam-hardening affected the calculation of film thickness from the sinograms. The calculation is based upon the principle that the attenuation coefficient of all non-water material is constant for the minimum-, partial-, and maximum- water conditions. However, in the case of the film-flow experiments, it is observed that the average attenuation coefficient is not consistent between the three conditions. In fact, for the maximum-water condition the attenuation coefficient for the metal is less than it is for the other conditions. This affects the sinogram

calculations because the calculated value of d_i^{max}, which appears in the denominator of Equation 3-21, is less than the true value. The denominator term is thus smaller than it should be, resulting in a calculated percent water that is larger than the true value. A higher percent water would result in a larger calculated film thickness, which is the trend seen in the parity plot in Figure 4-51.

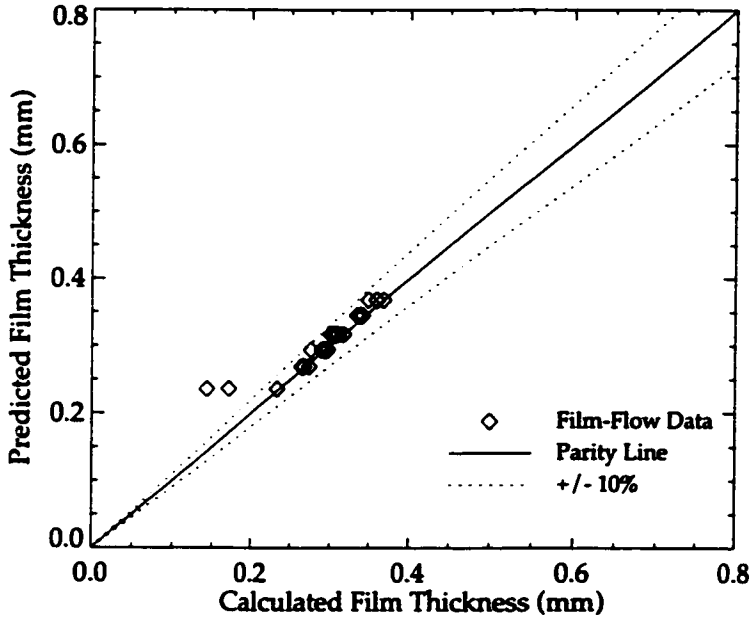

Figure 4-52. Parity plot of theory-predicted film thickness versus the scaled film thickness calculated from the sinograms.

The difference in the measured transmission values, as described by the sinogram, are still valuable in determining the amount of water present during the scan period. Rather than using the minimum- and maximum- water conditions to scale the sinogram data between 0 and 100% water, two flow sinograms were used. The

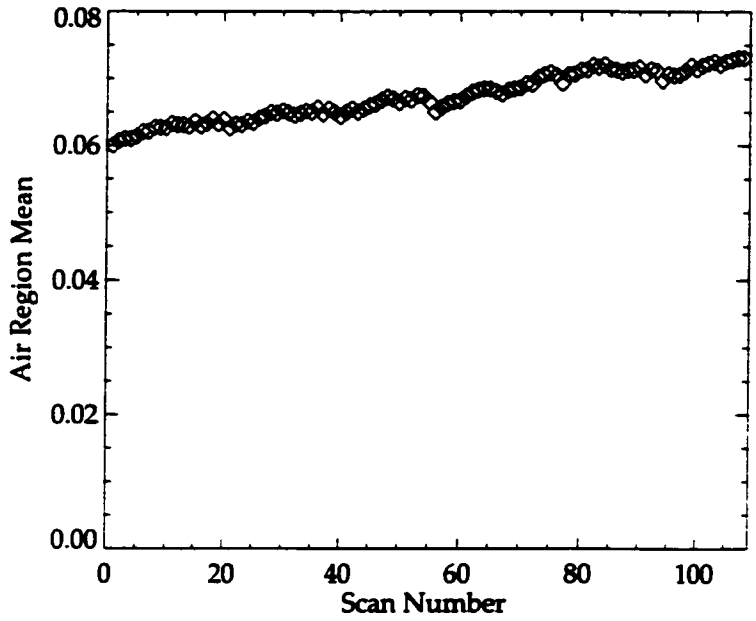

Figure 4-53. Variation with time in the air mean for the phantom scans with the Alliant scanner.

resulting parity plot, which shows less than 10% error for all flow rates excluding the previously explained outliers, is shown in Figure 4-52.

The drift in the response of the scanner over time was evaluated for the scans of the phantoms with the Alliant scanner. The variation of the mean in the air region of the sinogram over time is depicted in Figure 4-53. The general trend is again an upward drift in the response measured by the detectors. As seen in the adjusted values presented in Figure 4-54, the effect on the calculated percent water was not as large as for the film-flow experiments. The percent water is at a much higher level overall for the phantoms, with values in the range 7-25% rather than values below 0.5%. When measuring very small differences, as in the film studies, the values representing the scanner drift are a significant percentage of the difference between flow and

minimum, thus the percent water is affected significantly. The denominator term is not affected by large amounts in either case.

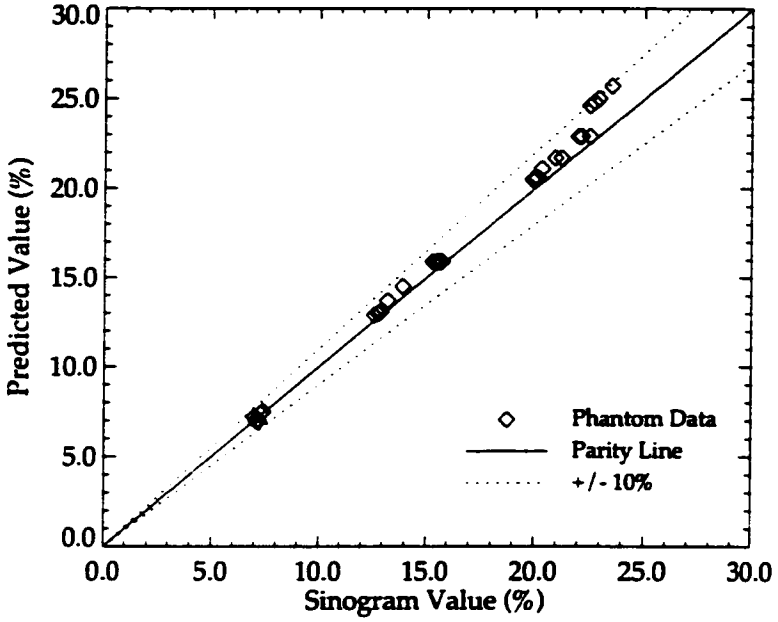

Figure 4-54. Percent water adjusted for the phantoms

4.3. Air-Water Contactor with Structured Packing

4.3.1. Radiograms

The air-water contactor was imaged with the 101B+ scanner at various operating conditions. A radiogram, as shown in Figure 4-55, was obtained of the entire packed bed section. The scan elevations for the CT images were determined from the radiogram and are annotated in the image. The lowest scan elevation, at 348.7 mm, is approximately two inches from the bottom of the packed bed. The highest scan elevation was the same distance from the top of the packed bed. The

remaining scan elevations were all located near the joint between the two elements of structured packing. Six of these elevations are annotated on the radiogram.

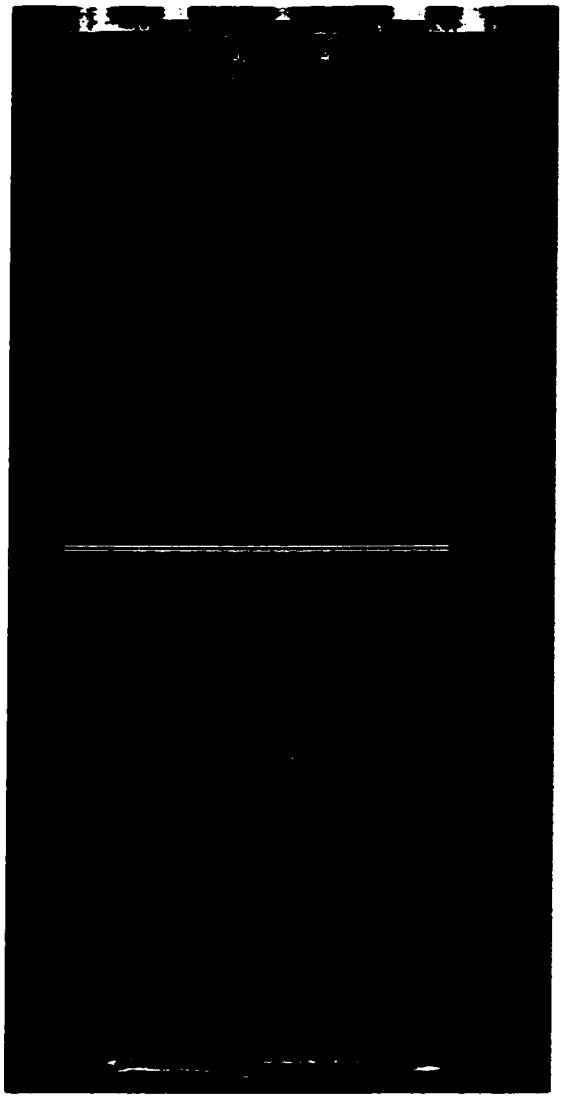

Figure 4-55. Radiogram of the air-water contactor containing structured packing with the scan elevations labeled.

4.3.2. CT Images

Horizontal cross-sectional images were obtained of the air-water contactor at various flow conditions and at different elevations. For each set of conditions, two successive scans were performed. The images of the packed bed in this section are all presented at a consistent pixel size, except when noted.

The materials present within the acrylic walls of the contactor during the scans were stainless steel, air, and water. The appearance of the phases of material in the CT images is similar to that observed in images of both the phantoms and the film-flow apparatus. The first image of the column, as shown in Figure 4-56, was acquired after allowing the column to dry for a period of 36 hours. The features that are present in the images of the Mellapak 500Y stainless-steel structured packing are labeled. The column wall is represented by the gray circle indicated by (1). Outside of the column, the water feed line is located in the upper right corner of the image, labeled (2). In the image shown, the tube is filled with air. In flow images, the region will contain water. The tube walls are not well-defined, as the tube changed position at least once during the scan. The four bright circles that are evenly spaced around the column, as indicated by (3), are the four stainless-steel supporting rods. Air regions, both in the interior and exterior of the column, are darker than the plastic column wall. In the interior of the column, the structured packing is represented by the bright curved lines labeled (4). In the image shown, the sheets of metal that comprise the packing are oriented parallel to a line from the lower left corner to the upper right corner of the image. The orientation of the corrugations is rotated 90° in the images of the upper packing element. The metal sheets contain perforations, such as those indicated by (5). The bright circle just inside the column wall, labeled as (6), represents the metal wiper band. The wiper band is used to hold the individual sheets of the stainless-steel packing together, and to reduce liquid flows along the column wall. The wiper band is not visible at all scan elevations. Although the column was allowed to dry for an

extended period of time, some water remained at this elevation, as shown by (7). The regions of water are of a value of grayscale similar to that of the plastic column wall.

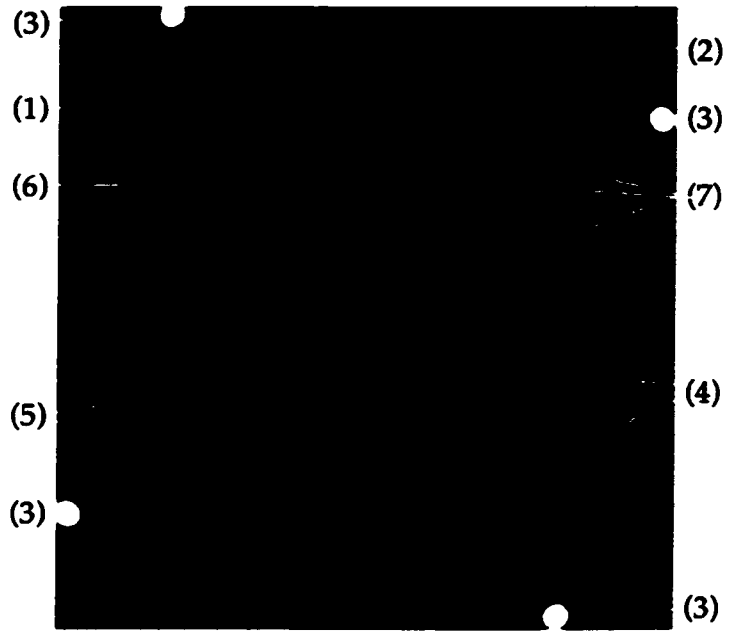

Figure 4-56. Image of dry structured packing with features of interest identified.

A set of images at an elevation of 348.7 mm is shown in Figure 4-57. The first condition represents the nearly-dry column, obtained after drying for over 36 hours. The image presented in (b) was obtained after shutting off the flows to the column for the flow condition represented in (c). The scan was obtained after water ceased draining from the bottom of the packed bed. The third condition represents a case with counter-current flow of air and water through the column. The water flow rate was 20 gpm/ft^2 and the air flow was at an F-factor of 0.14 $(ft/sec)(lb^{0.5}/ ft^{1.5})$. The image shown in (d) represents the column filled with water.

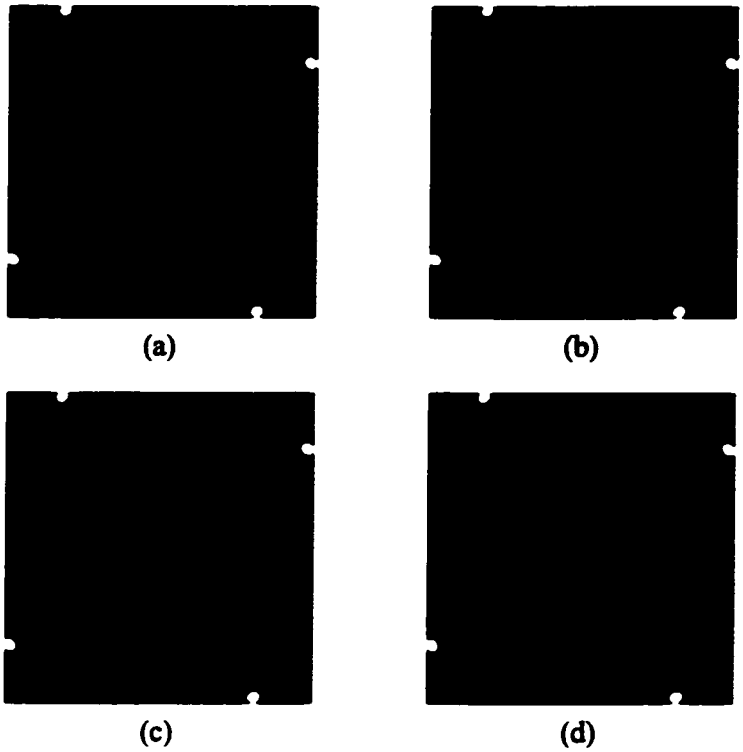

Figure 4-57. Four conditions at 348.7 mm represented: (a) almost dry, (b) static holdup only, (c) flow, and (d) flooded. (2x)

A feature is observed within the flow image that was not present in any of the images of the phantoms or the film-flow apparatus. Ring-like streaks that are concentric about the image center are present. The streaks do not represent the physical reality of the interior of the air-water contactor, thus can be classified as image artifacts. These artifacts are attributed to the dynamics of the flow through the contactor within the period of the scan. A magnified region of the column that contains these image artifacts is shown in Figure 4-58. The region is identified in (a) and shown magnified in (b). The corresponding region of the static holdup image is shown in (c). As the water flowing within the column is the only material that is

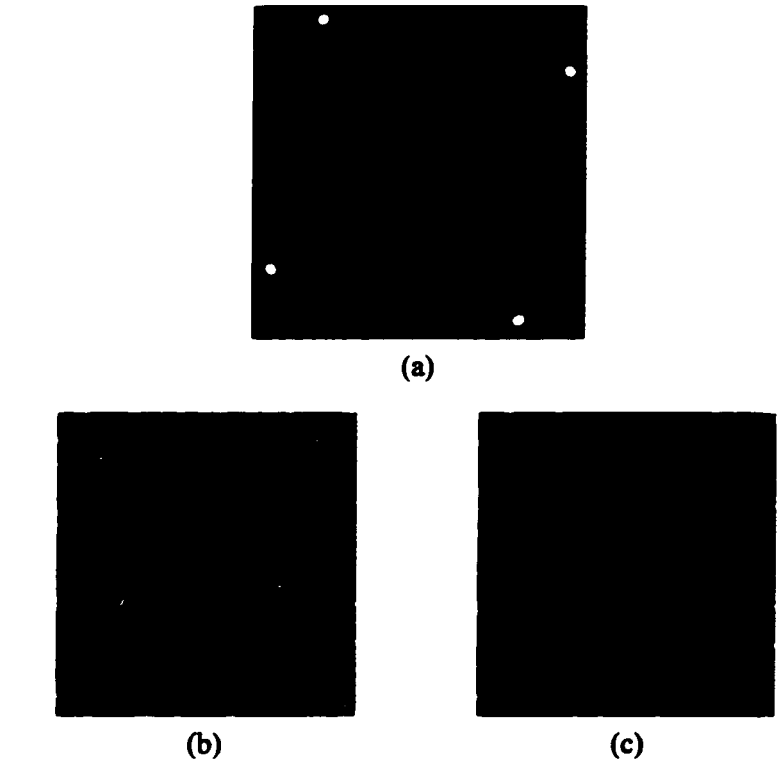

Figure 4-58. Ring-like artifacts observed in the flow images. (a) Region of magnification is identified. (2x) (b) Region of image with flow artifacts. (1/2x) (c) Region of corresponding static-holdup image. (1/2x)

changing position, it is hypothesized that the artifacts represent the water. The overall effect of the many artifacts is to make the image look blurry in certain regions.

An image artifact with a slightly different appearance was observed in the images for which no flows were introduced to the column. Two regions in each of the static-holdup images are identified in Figure 4-59 (a) and (b). The difference image, shown in (c), indicates that the regions containing water changed between scans. As shown enlarged in Figure 4-59(d)–(g), a region of water appears with bright and dark curved streaks. Comparison of the water region in (d) with the same region in (e)

indicates that the streaks are present in the first image only. However, in the lower region, shown in (f) and (g), regions of water both appear and disappear. The dark and light artifacts pass through the regions in which a change occurs between the two images. Potential causes of the artifacts are investigated further with the use of computer simulations in Chapter 5.

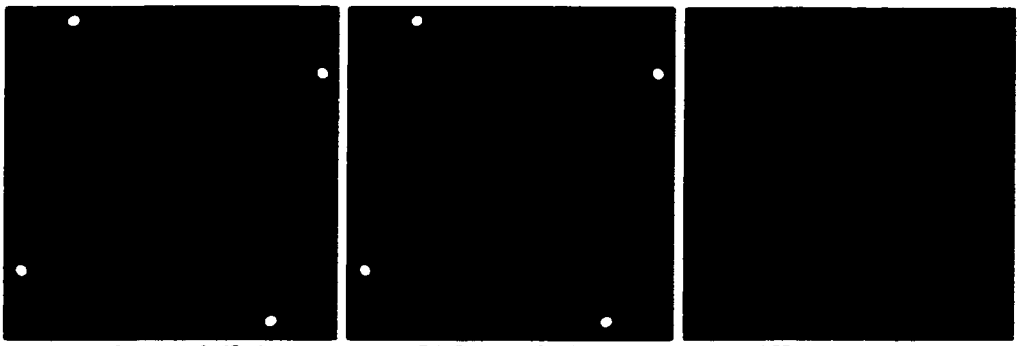

(a) Image 1 (2x) (b) Image 2 (2x) (c) Difference Image (2x)

(d) Upper region of image 1 (1/2x) (e) Upper region of image 2 (1/2x) (f) Lower region of image 1 (1/2x) (g) Lower region of image 2 (1/2x)

Figure 4-59. Images of the air-water contactor containing static holdup. The images in (a) and (b) were acquired sequentially. (c) Difference image. (d)–(g) Magnified regions indicate the presence of limited artifacts near regions of water.

The influence of the overlap correction applied prior to image reconstruction on the resulting images was evaluated. The overlap correction is used within the proprietary SMS software to account for variations in response between adjacent detectors. For scans of stationary objects, applying the correction reduces the

appearance of ring artifacts that are common in third-generation scanners. Prior to reconstruction, an adjustment is made to the transmission data so that the measurements along the same ray path with two detectors are consistent. However, for the scans of the operating air-water contactor, the difference in transmission that is measured with adjacent detectors can be attributed not only to detector differences, but also to differences in the distribution of the fluid.

Each sinogram was used to reconstruct images both with and without the overlap correction. The images representing the dry condition are shown in Figure 4-60 with and without the overlap correction. The image without correction exhibits wide rings throughout the image, which are characteristic of the ring artifacts observed with third-generation scanners. A variation in the darkness of the air region at evenly-spaced concentric rings is observed. The width of the rings correlates to the width of the beams that are measured at one detector. The image with the overlap correction prior to reconstruction does not exhibit this variation. The wide ring artifacts are not apparent in flow images that do not have the correction applied, as seen in Figure 4-61(a). In fact, comparison of (a) and (b) indicates that for the flow images, the differences between applying the correction and not are minor and are difficult to discern.

X-ray CT scans were also performed at the low-resolution set of scan parameters. The image shown in Figure 4-62 was acquired over a 1.4-minute period, compared to the 4.8 minutes required for the high-resolution images. However, in spite of the decreased scan time, the flow artifacts are still present. The remainder of the images presented in this section will be at high resolution.

Flow images were obtained at multiple scan elevations, as shown in Figure 4-63. Images are of conditions near the top and bottom of both elements of Mellapak 500Y. A difference in position of the structured packing surfaces at the four elevations is observable. The artifacts due to flow variation are present in each of the images.

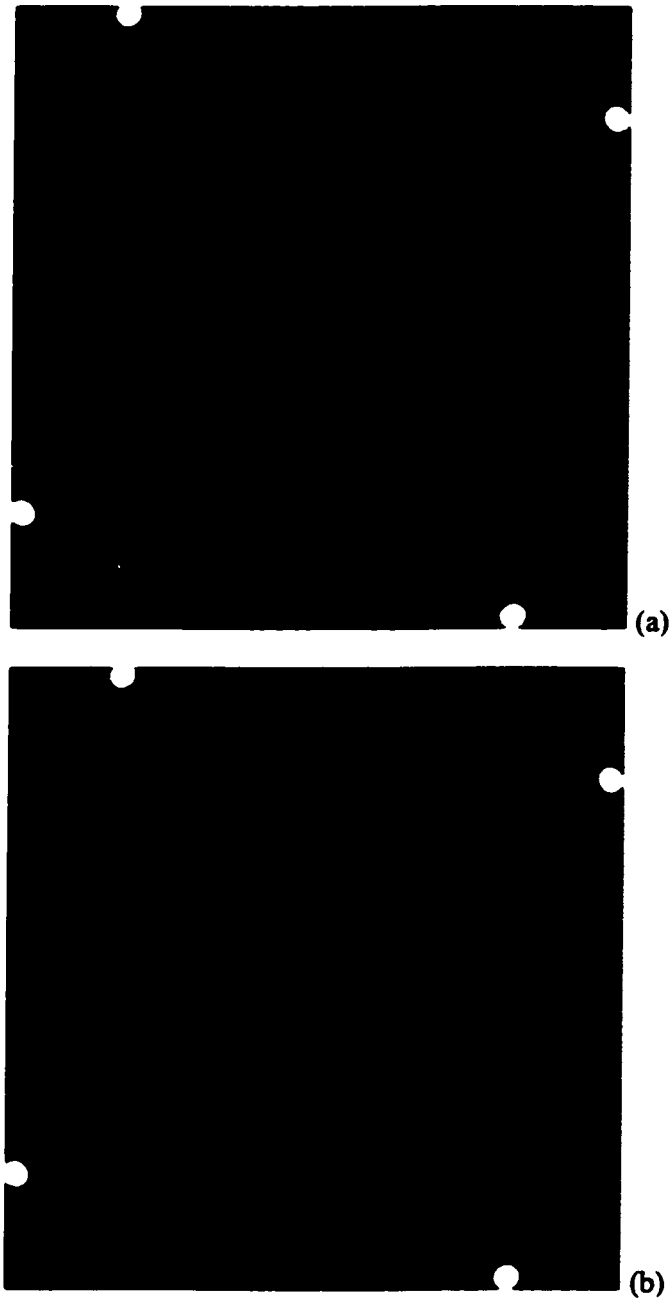

Figure 4-60. Image of structured packing without flows. (a) No overlap correction. (b) With overlap correction

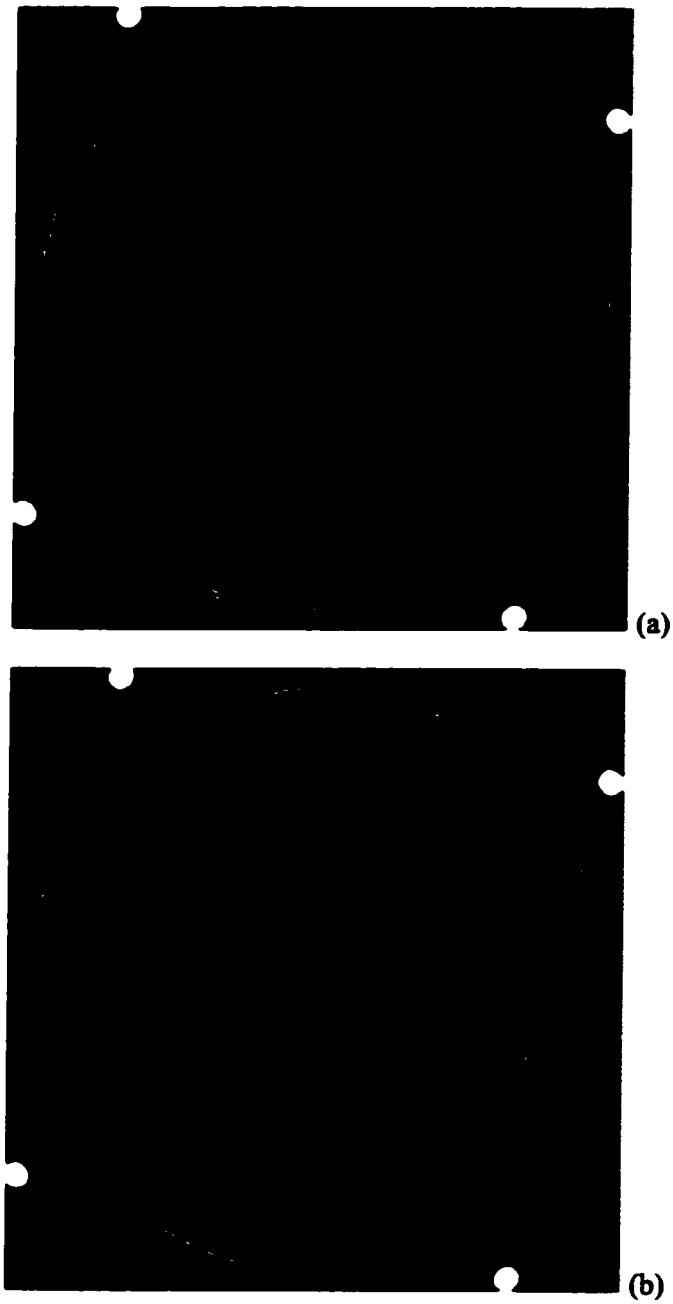

Figure 4-61. Flow image reconstructed (a) without the overlap correction and (b) with the overlap correction.

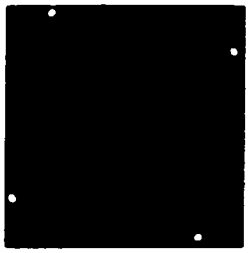

Figure 4-62. Image of a flow condition at low resolution

The metal wiper bands are visible in all images except at the highest elevation, shown in (d).

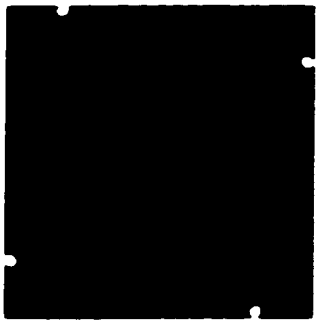

(a) Elevation = 348.7 mm

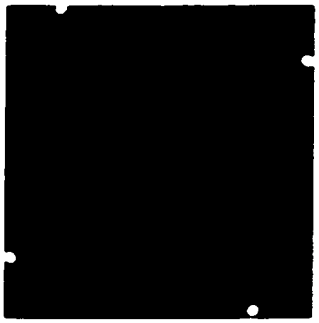

(b) Elevation = 485.35 mm

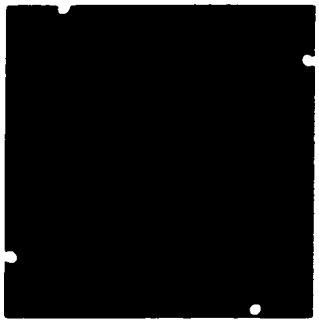

(c) Elevation = 512.25 mm

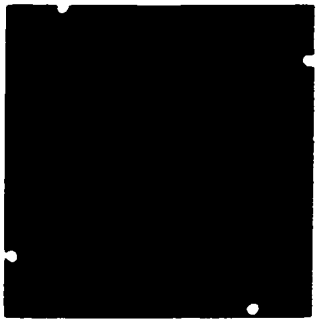

(d) Elevation = 645.2 mm

Figure 4-63. Images at different elevations. (2x)

One region of particular interest for structured packing is the joint between the two 8-inch-tall elements of packing. When structured packing is installed in a column, adjacent elements are rotated 90° with respect to each other. The flow patterns of the fluids are disrupted upon flowing from one element to the other. The liquid is redistributed onto the surfaces of the element below, and the vapor often must alter the direction of upward flow. Measurements of holdup for structured packing using gamma-ray measurements have shown that the holdup is higher at the joint between elements, than within each segment, when operated above the loading point; however, the liquid holdup is independent of elevation below the loading point [59]. As would be expected, when flooding occurs within the column, the joint region is often identified as the hydraulic limitation. Therefore, a series of CT scans was obtained in this region for flow conditions.

Eleven images, at increments of 0.3 mm, starting at an elevation of 497.6 mm and increasing to an elevation of 500.6 mm, are shown in Figure 4-64. This series of images begins at the top edge of the bottom element of packing. In the third image, the bottom of the upper element of packing is starting to appear in the lower region of the image. The sheets of the upper packing element become more visible as the scan elevation increases. In the sixth image, corrugations are observed in both directions. In the images without the surfaces of the upper element visible, there are still regions of water that are present but not located near the packing surface. As the images above the joint are viewed, it becomes apparent that these water regions are located just below the water that is forming in the channels above. In the final three images of the sequence, it can be seen that water is accumulating above the joint. The water selectively fills some channels and not others.

The column is operating below the loading point for the entire range of flow rates used in this study. According to the work of Suess and Spiegel [59], the loading point for stainless-steel Mellapak 500Y structured packing occurs at an F-factor of 1.8

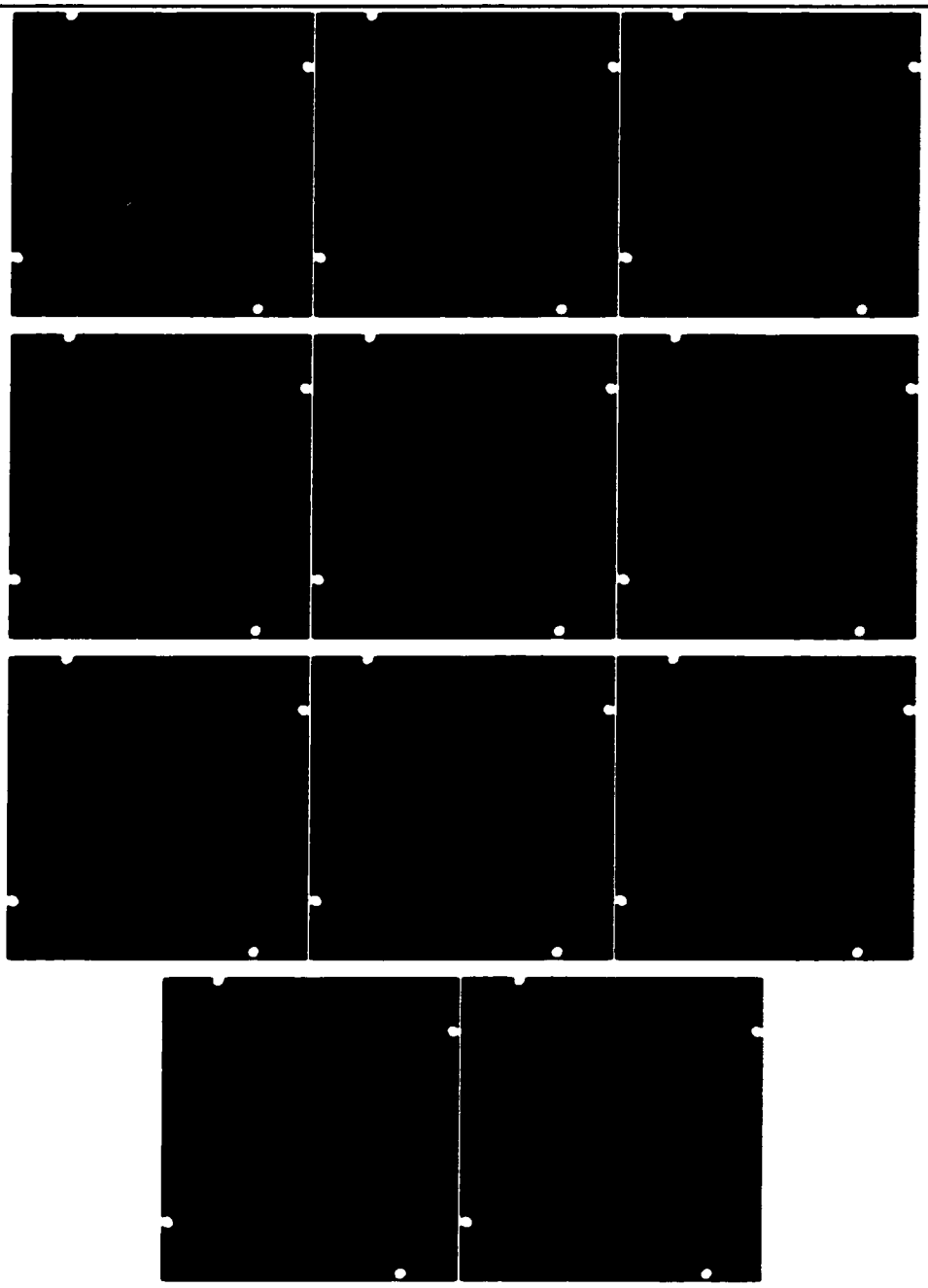

Figure 4-64. A series of CT images at the joint between elements of structured packing. The elevation change between images is 0.3 mm. Water flow=10.5 gpm/ft^2, F-factor=0.20 (ft/sec)(lb$^{0.5}$/ft$^{1.5}$). (2x)

$(m/sec)(kg^{0.5}/m^{1.5})$ (1.4 $(ft/sec)(lb^{0.5}/ ft^{1.5})$) at a liquid load of 50 m/h (2.7 ft/ min). The highest liquid rate used for the imaging studies was equivalent to a liquid velocity of 48.9 m/h. At lower liquid rates, the loading point occurs at a higher gas rate. The images presented in Figure 4-64 indicate that the holdup does, in fact, depend upon elevation below the loading point. However, the dependence observed is limited to a region of approximately 10 mm above the joint.

4.3.3. Image Histogram

A histogram was calculated for the column region of each of the images of structured packing. Figure 4-65 shows the histograms representing the four conditions that were depicted in Figure 4-57: dry, static, flow, and flooded. As with the images of the phantoms, the main peaks were centered at two values. The less attenuating region is centered at a value of grayscale of approximately 75. The more attenuating region, representing the water, is centered around a value of 110. The main peaks tend to trail off over a long range of values at the high end of the grayscale. There is not a well-defined peak for the metal, as the metal does not comprise a significant portion of the images.

The addition of water to the column for the flow images resulted in different behavior than was observed for the phantoms and for the film-flow apparatus. A second peak is not present in the histogram for the flow image. The peak that is present is much wider than that in the dry and static images; however, it is located in approximately the same position. The broadening of the peak is a result of the image artifacts in the flow images, which are both bright and dark.

4.3.4. Determination of Liquid Holdup

The liquid holdup within the air-water contactor containing structured packing was calculated using three different approaches. For each operating condition, a value

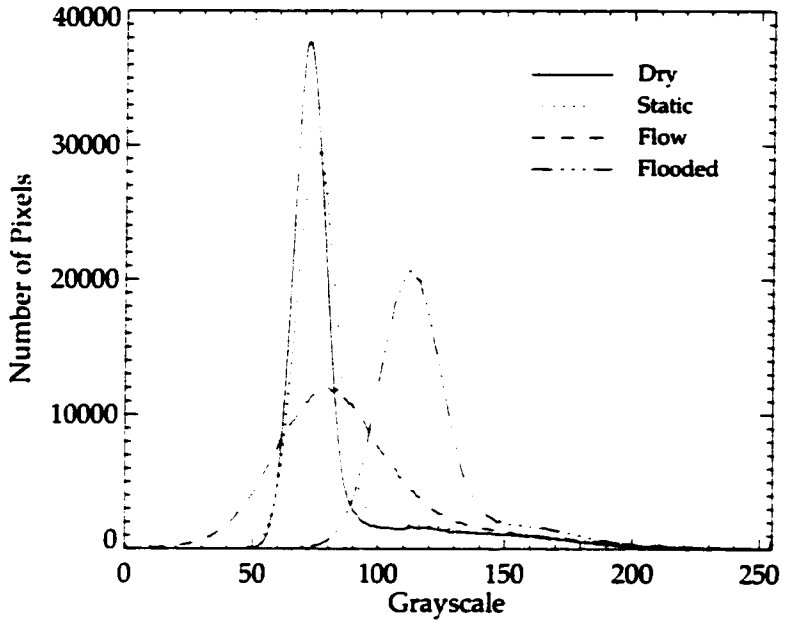

Figure 4-65. Histogram of four images representing different conditions for the structured packing.

of liquid holdup was predicted using the Rocha-Bravo-Fair model, according to Equation 2-1, which will be referred to as the model-predicted value. The liquid holdup was determined experimentally using two methods. The first method was to determine the holdup from the mean values of the sinograms. Sinograms are presented in Figure 4-66 for the images that were shown in Figure 4-57. The same methodology that was used for the phantom and film-flow sinograms was used to calculate the percent water for the scans of the structured packing under flow conditions. To convert from a percentage to liquid holdup, Equation 3-16 was applied using the vendor-specified void fraction of 0.975. The second experimental determination of liquid holdup was to measure the column-average liquid holdup as

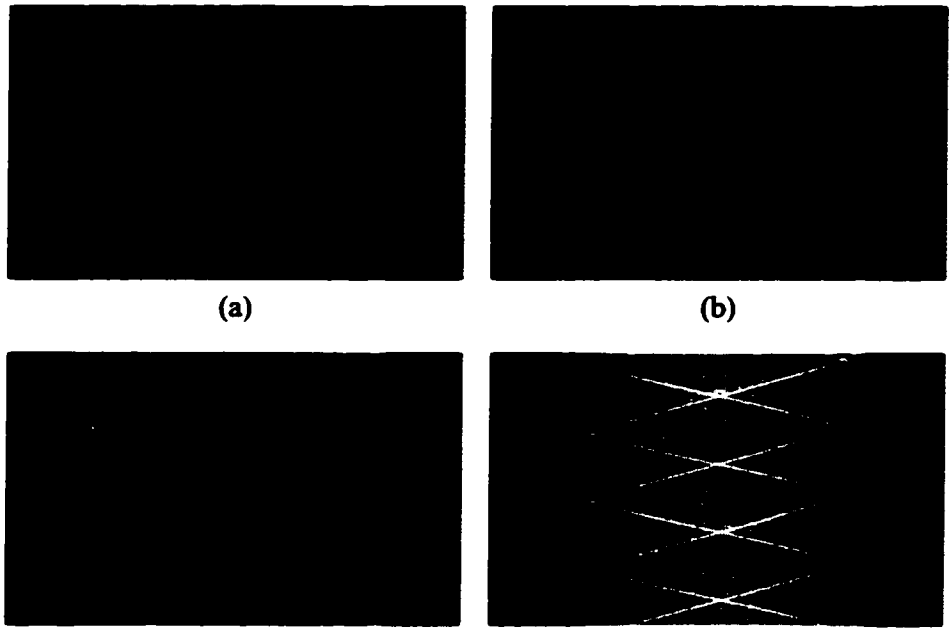

Figure 4-66. Sinograms for four conditions at 348.7 mm: (a) almost dry, (b) static holdup only, (c) flow, and (d) flooded.

described in Section 3.8. On the parity plots presented in this section, these methods will be described as experimental-sinogram and experimental-traditional, respectively.

Prior to calculation of holdup using the sinogram data, the scanner drift was evaluated in the air region. The mean values outside of the column region, for the flow cases at an elevation of 348.7 mm, are indicated in sequential order in Figure 4-67. There is an upward trend in the mean, until a large decrease in value occurred prior to the final set of two images. An adjustment for the scanner shift is performed when calculating the liquid holdup from the sinograms.

The first comparison is made between the two experimental methods of determining liquid holdup. A parity plot of the experimental data is shown in Figure 4-68. At the highest liquid flow rate, which corresponds to the largest holdup values,

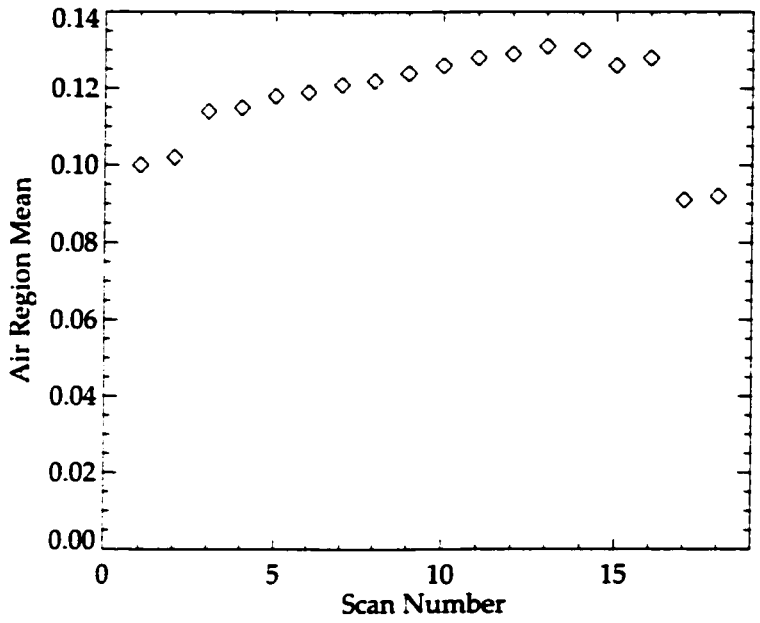

Figure 4-67. Scanner drift measured for the scans of the air-water contactor at an elevation of 348.7 mm.

the data points are all within less than 20 percent variation from the parity line. At the lowest liquid flow rate, the values obtained from the sinogram are more than twice the values obtained from the traditional method. In addition, at the intermediate value of liquid flow rate, the sinogram value is higher than the traditional value. The values determined by the traditional method are representative of the average holdup throughout the entire packed bed. In contrast, the values determined by the sinogram method represent the local holdup at one elevation. As seen qualitatively in the CT images, the liquid holdup depends upon elevation. However, the sinogram-method data are only available at the one elevation at which scans of the flooded column were performed. The weight limit of the scanner restricted measurement to this elevation.

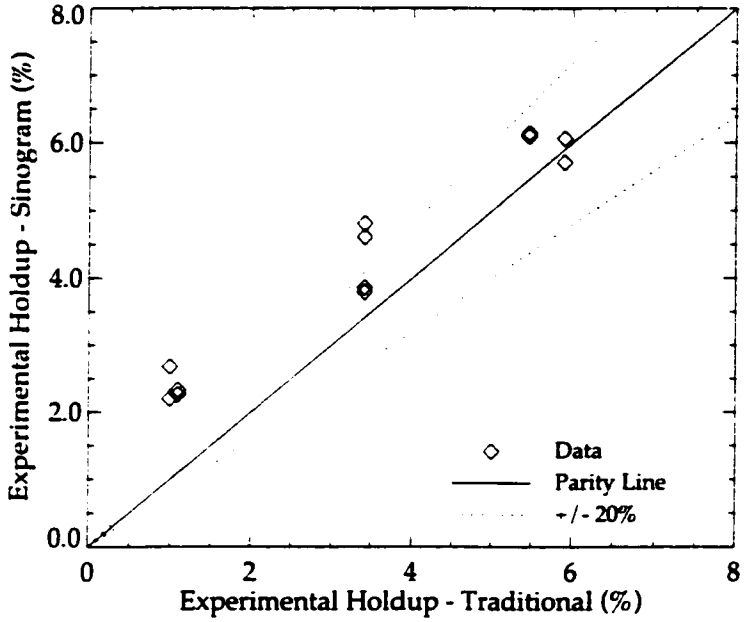

Figure 4-68. Comparison of the two experimental methods: sinogram vs. traditional method

The second parity plot presented compares the two sets of experimental data with the values of holdup predicted by the Rocha-Bravo-Fair model. The experimental-traditional values are consistently lower than the model-predicted values. At the lowest liquid rate, the absolute difference between the values is 0.8%. The absolute difference at the intermediate and high water rates is in the range of 1.0-1.4%. On a percentage basis, the experimental-traditional value is as much as 44%, and as little as 15%, less than the model-predicted value. At low liquid rates, the experimental-sinogram values are larger than the model-predicted values. However, the model-predicted value is larger at high liquid rates. All except three of the sinogram-based values are within 20 percent variation from the parity line. These three points are all at the lowest liquid rate, and two of the points are within 25 percent

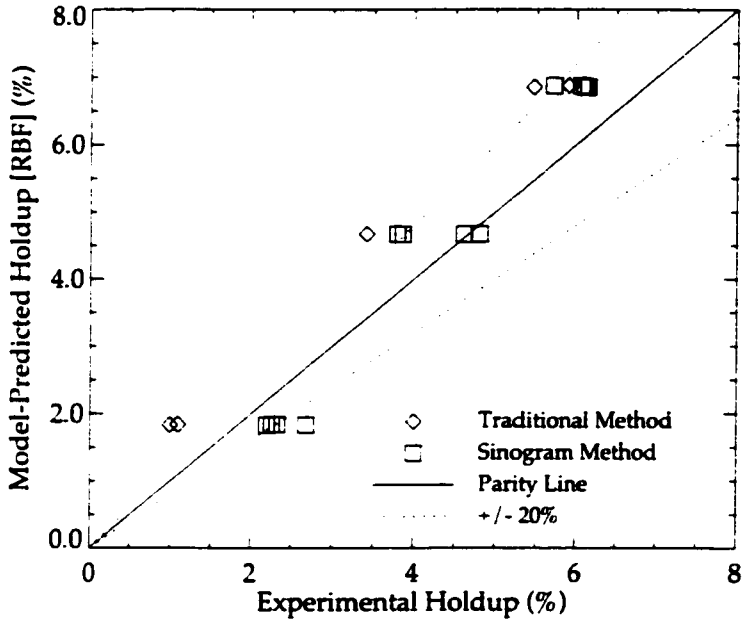

Figure 4-69. Parity plot comparing experimental methods of determining holdup with the model-predicted values.

variation from the parity line. The experimental-traditional and model-predicted values both represent the average holdup over the packed bed, while the experimental-sinogram values represent the local liquid holdup at a specific elevation.

4.3.5. Stationary Transmission Measurements

The transmission of x rays through the operating air-water contactor was measured along 117 fixed paths, with no rotation or translation of the column, for a five-minute period for various operating conditions. These measurements were obtained to provide an indication of the fluctuation in attenuation measured, due to both the variation in flow and the measurement error. The time period represented is the approximately the same as the time required to obtain a high-resolution image.

The air and water flow rates were varied for each set of transmission measurements. The data obtained are of the form shown in Equation 3-4, which is the same form as the data that are measured for a radiogram. The measurements corresponded to the row and columns of the sinogram indicated in Figure 4-70.

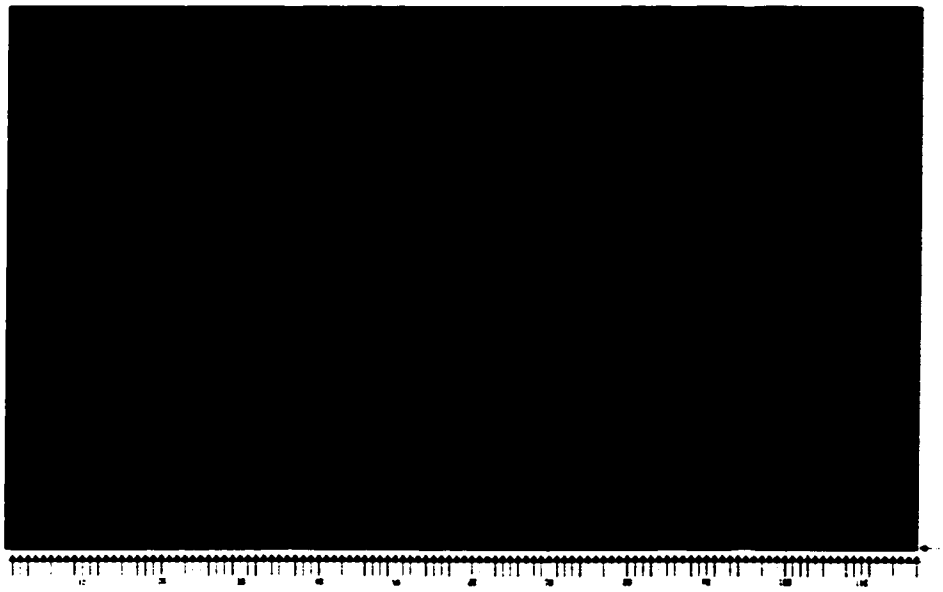

Figure 4-70. Sinogram with the row and columns that correspond to the paths of the stationary measurements marked.

The first set of data presented was obtained at an elevation of 348.7 mm, which is near the bottom of the packed bed section, with the aperture set at 0.3 mm x 0.3 mm. In Figure 4-71(a), the mean attenuation measured at all detectors over the five-minute period with air and water flow is shown. In addition, the range of the measured attenuation over the same period is shown. For comparison, the 117 data points from the flooded sinogram, which represents the maximum-water condition, at the same elevation are shown. The data from the sinogram represent one measurement at each detector. The four regions of high attenuation along the paths that pass through the

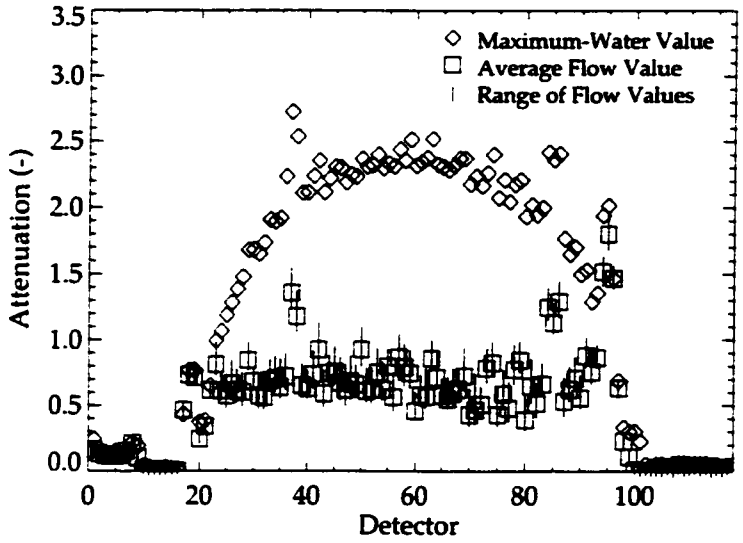

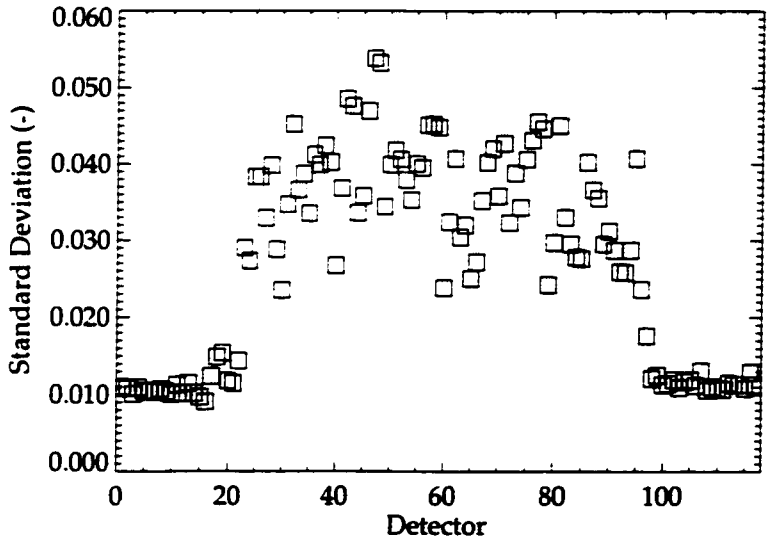

Figure 4-71. (a) Mean value and range of attenuation measured over a five-minute period for a water flow rate of 10.5 gpm/ft^2 and air flow rate of F-factor = 0.20 (ft/sec)(lb$^{0.5}$/ft$^{1.5}$). Maximum-water condition determined from the sinogram. (b) Standard deviation of attenuation at each detector.

stainless-steel support rods are measured by detectors: 17-19, 37-38, 84-86, and 94-96. The detectors that correspond to paths through the inside of the column are in the range 24-95. The curved shape of the maximum-water condition data in this range is indicative of the different amount of water that is present along each path. Through the center of the column, the total path length along the diameter of the column is greater than the path along a chord near the edge of the column. The amount of stainless-steel packing is not constant, nor in proportion to the amount of water, along the 117 measurement paths. The standard deviation of the set of measured attenuation values at each detector is shown in Figure 4-71(b). Within the column region, the standard deviation is 2–9% of the measured attenuation, while outside the column, the value is 5–9% of the measured attenuation. The absolute variation is larger in the interior of the column, where fluctuations due to the nature of the flow are a factor.

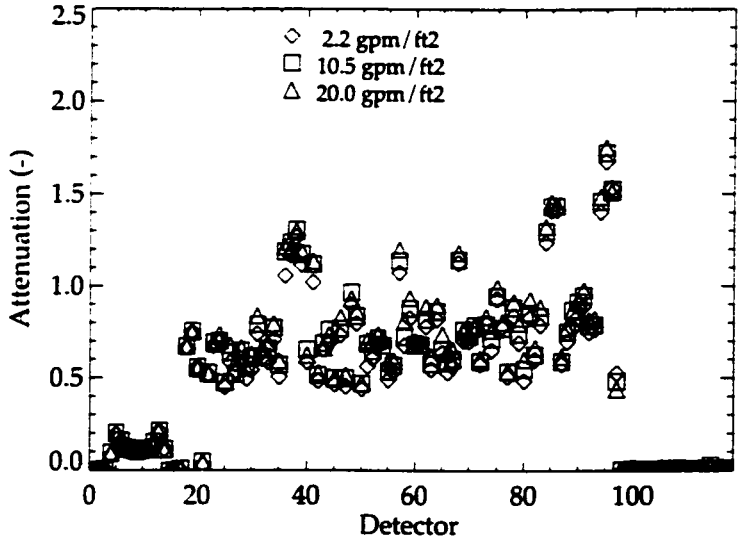

Figure 4-72. Mean attenuation values for three flow conditions

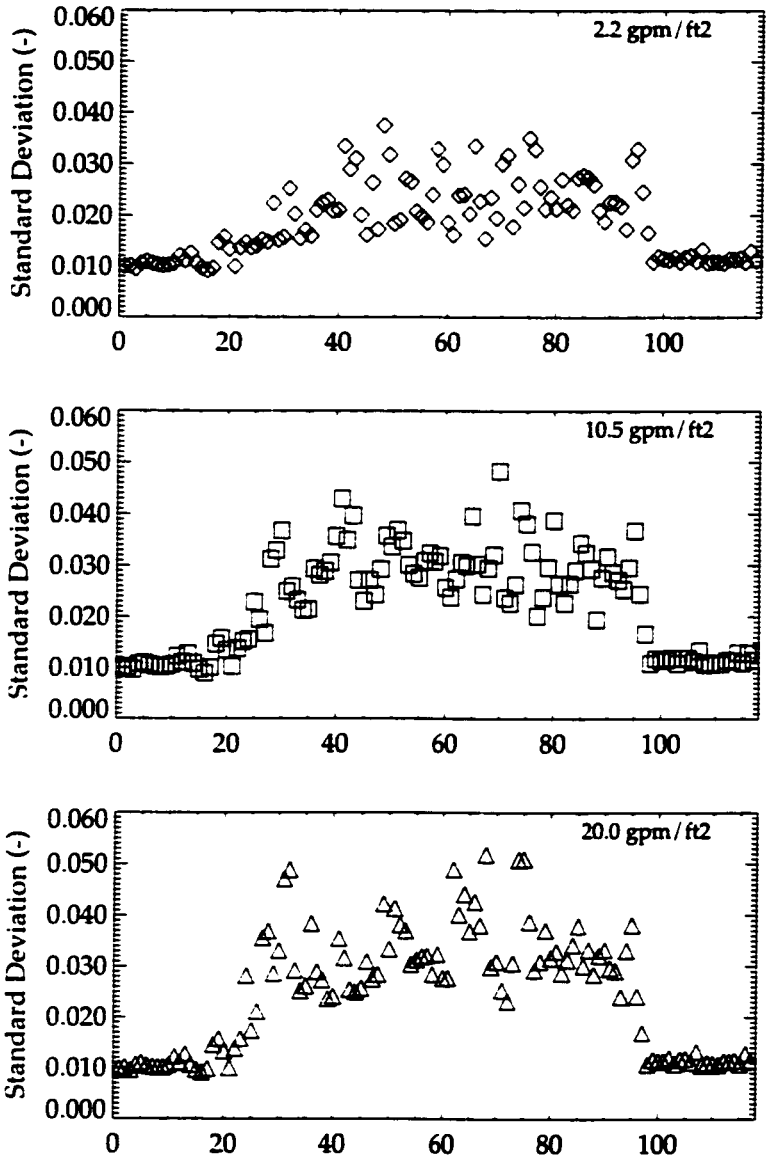

Figure 4-73. Standard deviation of attenuation values for the three flow conditions shown in Figure 4-72.

The region of data outside the column walls was used to determine a value that is indicative of the noise in measurement. As no change occurred in the material

present along the ray paths measured by these detectors, the variability is due to the measurement system. For the detectors at an aperture of 0.3 mm x 0.3 mm, the average standard deviation in the region outside the column was 0.010. Although not shown graphically, the standard deviation in the region outside the column with the detectors at 1.0 mm x1.0 mm aperture was $4.8x10^{-3}$, which is less than half that for the smaller aperture.

Three sets of mean attenuation value measured at each detector are shown in Figure 4-72. The values shown represent three water flow rates and were obtained at an elevation of 512.25 mm. The air flow was at an F-factor of 0.14, 0.20, and 0.27 $(ft/sec)(lb^{0.5}/ ft^{1.5})$, for the water flow rates of 2.2, 10.5, and 20.0 gpm/ft^2, respectively. The standard deviation for each of the flow conditions is shown in Figure 4-73. For most of the ray paths, the attenuation was greatest when the water flow rate was high, and least when the rate was low. However, there were detectors at which the attenuation at a flow rate of 10.5 gpm/ft^2 was greater than that at 20.0 gpm/ft^2. The attenuation measured at a detector was infrequently highest at the lowest flow rate, such as seen at detector 60. Three detectors, 31, 36, and 57, were selected to observe the variation of the attenuation measured over time.

The data presented in Figure 4-74 represent the attenuation measured at a detector over a five-minute period. When acquired, attenuation was measured at 0.015-second intervals. As shown, the attenuation is presented as an average of 100 points, or a period of 1.5 seconds. The mean value indicated for each set was presented as one data point in Figure 4-72. For all three plots, the mean attenuation value increases with the flow rate. The variation of two standard deviations around the mean is based upon the variation measured outside of the column, and is indicative of the measurement error, not the variation due to fluctuations in flow. The attenuation measured at detector 31, shown in Figure 4-74(a), was selected because the average values for the three flow rates were dissimilar. The standard deviation of the measured

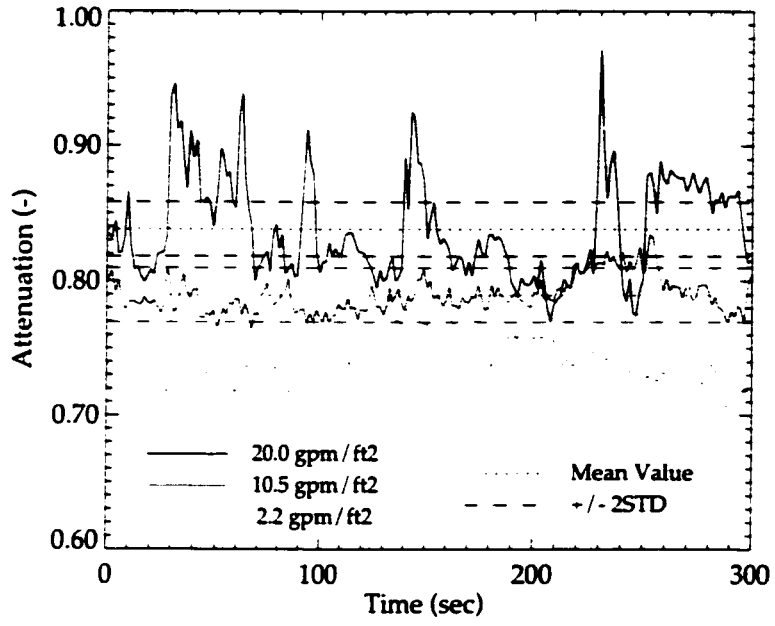

(a)

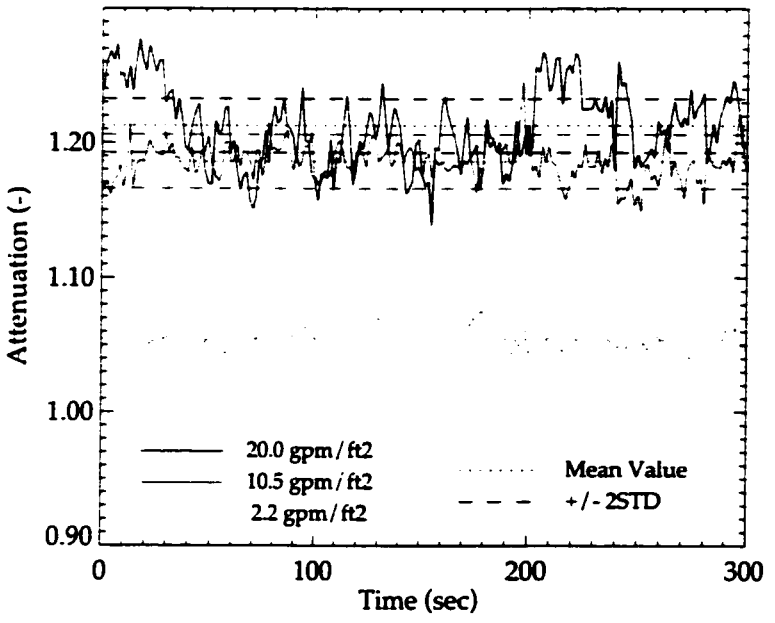

(b)

Figure 4-74. Variation in attenuation at detector: (a) 31, (b) 36, and (c) 57

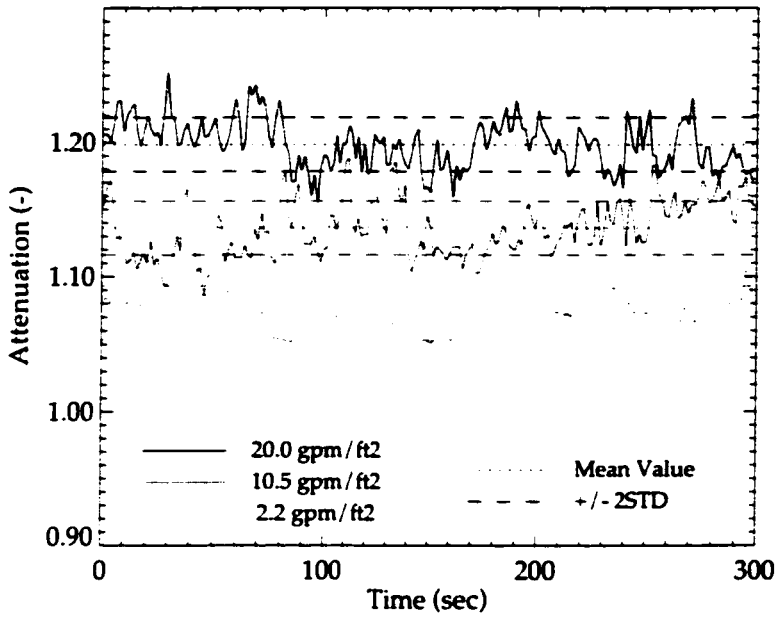

Figure 4-74 (cont.) Variation in attenuation at detector: (a) 31, (b) 36, and (c) 57

attenuation was comparable for the lower two flow rates, but nearly twice as large for the highest rate. The fluctuations in attenuation are significantly higher along this path through the column at the highest flow rate. Detector 36 was selected because the standard deviation at each flow rate was dissimilar. The three values of standard deviation corresponding to the responses shown in Figure 4-74(b) are 0.021, 0.029, and 0.038. The attenuation was nearly the same for the highest two flow rates. The measured attenuation at Detector 57, shown in Figure 4-74(c), for the three flow rates was characterized by a different mean for each flow rate. The standard deviation of the higher two flow rates was 33% larger than that for the lowest flow rate.

One set of stationary transmission data was acquired for the condition with no flows to or from the column. The majority of the data measured for this condition

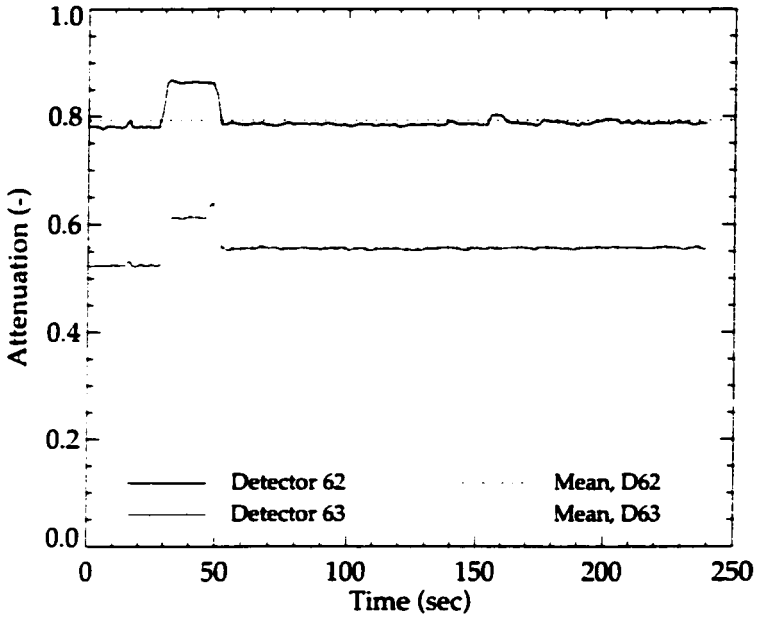

Figure 4-75. Variation in attenuation measured for a no-flow condition.

exhibited no variation in attenuation during the measurement period. However, the response at two detectors, as shown in Figure 4-75, indicated an increase and a subsequent decrease in the attenuation along the ray paths of the two adjacent detectors. As was shown in Figure 4-59, regions of water were not constant in the images with no flows to the column. The attenuation data for the case without flows indicate that for a 30-second period, a region of water was present in the scan plane along the path measured by detectors 62 and 63.

4.4. Summary

X-ray imaging techniques were applied to three experimental systems to evaluate the feasibility of obtaining hydraulic parameters of a vapor-liquid contactor. The systems were: (1) phantoms containing static regions of air, water, plastic, and stainless steel, (2) a film-flow apparatus designed to obtain a stable thin film of liquid on a stainless-steel surface, and (3) an air-water contactor containing structured packing.

The imaging studies involving the phantoms were valuable in comparing the characteristics of two different scanners, as well as evaluating image analysis techniques. The materials in the phantoms were classified by the value of grayscale, using the image histograms. A comparison of the images obtained at different scan parameters indicated that the noise associated with the transmission measurements will influence the capability to distinguish between air and water in a reconstructed image. The noise is an important factor when evaluating the trade-off between spatial and temporal resolution. In addition, the sinograms were used to calculate the amount of water present in the phantoms for the range of 7-25%.

The film-flow apparatus was imaged with the CT scanner, and the film thickness was calculated using both image- and sinogram- based calculations. Variation in the film thickness at the six flow rates was observed in the difference images that represented the films. The brightness of the circle representing water outside of the steel pipe was indicative of the thickness of the film, which varied with position around the stainless-steel surface. Prior to the scans, the film-flow apparatus was aligned to within an angle of 0.25° from the scan plane. The energy level of the Alliant scanner was not sufficient for the film-flow system, as beam hardening occurred. The effect of the beam hardening was observed in the images, the histogram, and the sinogram-based calculations.

Images of the air-water contactor were obtained at various elevations and operating conditions. Ring-like artifacts present in the images of flow through the column are attributed to changing flow patterns of the water. The artifacts were not observed in images obtained without flow, and the artifacts were not observed for the well-defined flow patterns on the film-flow apparatus. The overlap correction applied by 3DID did not significantly affect the appearance of the artifacts for the flow images. The artifacts were investigated further with the use of computer simulations, as discussed in Chapter 5. The variation of flow within the cross section during the period of a scan was confirmed with the use of stationary transmission measurements. The liquid holdup calculated from the sinograms deviated from values calculated from both the traditional experimental method and the model of Rocha, et al. [41]. However, the sinogram value represents a local measurement at one elevation, while the other two methods represent a column-average liquid holdup. Although not quantified, an accumulation of liquid at the region between the two packing elements was observed in the CT images.

CHAPTER 5: SIMULATION OF X-RAY CT

Computer simulations of the x-ray CT imaging procedure were performed to investigate the potential of applying the imaging technique to obtain hydraulic parameters of a vapor-liquid contactor. The simulations were focused on identifying and understanding the cause of the artifacts that were present in images of random packing obtained by Cartmel [8] and in images of structured packing shown in Chapter 4. Images of the operating air-water contactor obtained using x-ray CT exhibited ring artifacts. These artifacts were not prominent in images of the column without flow of air and water during the scanning period. The presence of the artifacts is attributed to the non-stationary nature of the fluid flow.

The artifacts observed in the CT images of the air-water contactor were shown in Figure 4-58 and in Figure 4-59. The first case of artifacts shown were in an image obtained with both air and water flowing to and from the column. The second type of artifacts was observed in the case when a droplet of water passed through the scan plane after the flows to the column had ceased. Both of these scenarios are investigated with the use of computer simulations.

5.1. Computer Simulation Procedures

The computer simulation involves the same main steps as the acquisition of a CT image from experiments. However, the process is idealized, and parameters and errors are controlled. Figure 5-1 presents a comparison of the experimental method with the technique for computer simulation. In the experimental system, the object is the air-water contactor, whereas in the simulation, the object is represented by a two-

dimensional array of values. The sinogram in the experimental system is obtained by measuring the transmission of x rays through the object. In the computer simulation, the sinogram is calculated by integrating the values in the object array along the defined ray paths. The calculation of attenuation in the simulation is for a monoenergetic source with no measurement error. The image reconstruction algorithm applied to the sinogram data is the same for both the simulated scans and the experimental scans.

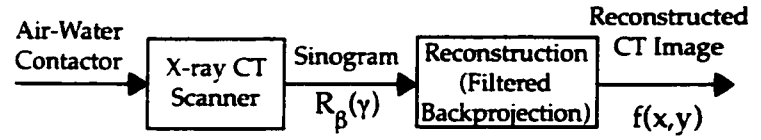

(a) Experiment

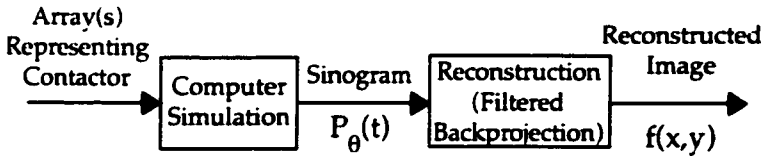

(b) Simulation

Figure 5-1. Comparison of the data acquisition and image reconstruction procedures for (a) experiments and (b) simulations.

The computer simulation of x-ray CT was written using IDL 5.4 from Research Systems, Inc. (Boulder, Colorado). The basic functions were adapted from code for the IDL demonstration of reconstruction. Additional code was written to simulate motion of objects during a scan.

The original IDL code is based upon the parallel-beam geometry, as described in Figure 3-5. The demonstration of reconstruction implemented by the IDL code, not

including the graphical interface, is depicted in Figure 5-2. The reconstruction algorithm applied was the filtered-backprojection technique, discussed in Section 3.3, which is the same method used by 3DID. The IDL demonstration included code for the four common filter functions: Ram-Lak, Shepp-Logan, Low-pass cosine, and Generalized Hamming. The projection data were calculated for each view of the object array to obtain the sinogram values. The filtered projection data were determined by calculating the convolution of the projection data and the calculated filter function. The final step in the original code was to calculate the reconstructed image using backprojection. The parameters that must be specified for the IDL demonstration are the number of views, the size of the filter function, the type of filter, and the method of interpolation used for calculation of ray sums and for backprojection.

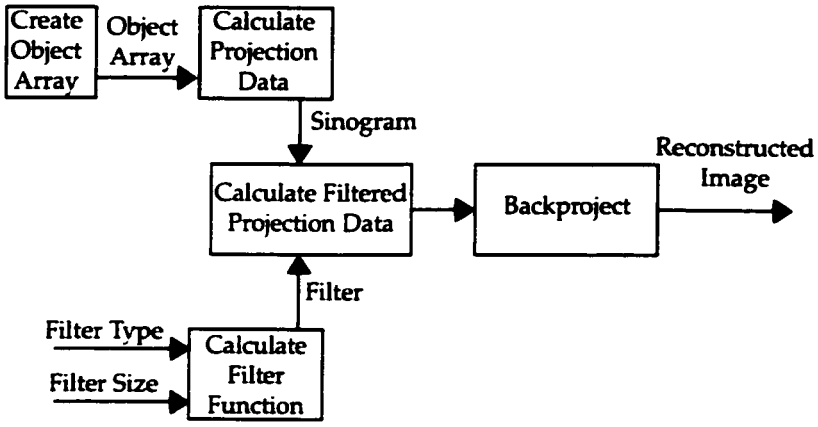

Figure 5-2. CT simulation process steps in the code for the IDL demonstration.

Motion that occurs during the period required to acquire the sinogram data is of interest for these simulation studies. The motion can be from one location in the scan plane to another, or can involve the disappearance of water from the scan plane,

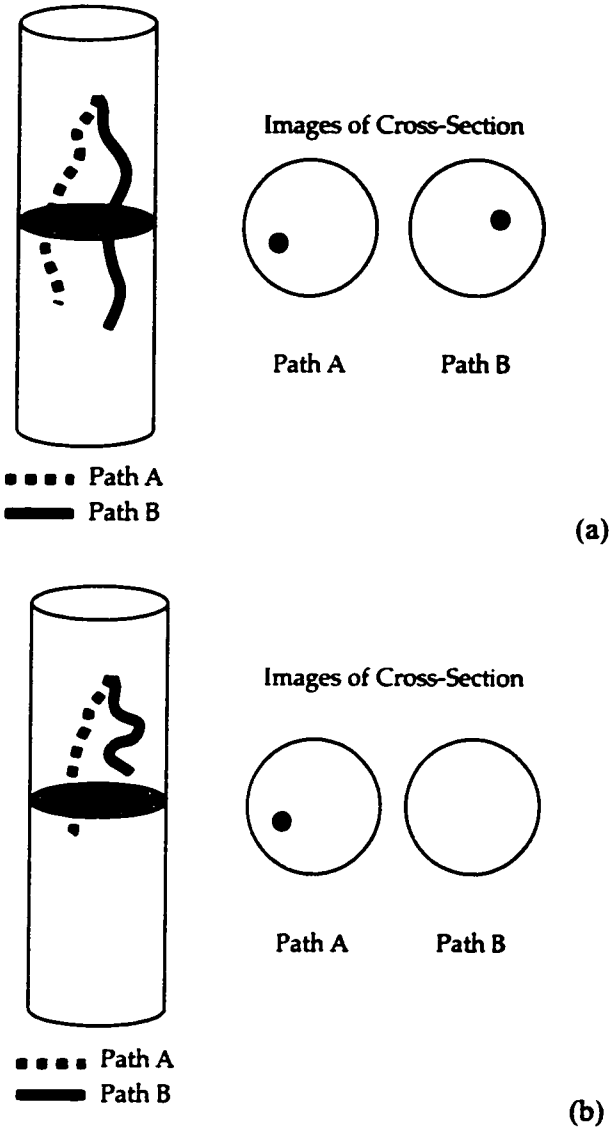

Figure 5-3. Two scenarios depicting variations in rivulet flow above the scan plane that affect the cross-sectional image. (a) The rivulet is in a different position in the scan plane. (b) The rivulet is no longer in the scan plane

as shown in Figure 5-3. When motion occurs during the scan of an object, some values in the sinogram represent one condition while other values represent another. Of the many values (up to 1.47×10^6) in a sinogram from the 3DID scans, a number of values equal to the number of detectors in use (up to 125) are obtained at the same time. The values acquired simultaneously are located in the same row of the sinogram. For the case of n subpositions, these values are in every n^{th} column.

The computer simulations were performed using programs written in the IDL language to simulate motion of features within the object array. Circles were used to simulate the position of a rivulet in the scan plane. The motion of the objects is limited in scope for the simulations. The variation is limited to three cases: (1) the positions of objects are dependent upon the view, or rotational position, of the object array, (2) the positions of objects are dependent upon the subposition, as defined for the pseudo-third-generation geometry, and (3) the positions of objects vary in a repeating pattern and depend upon both view and subposition. The first case indicates that the position of the object is constant for an entire row of the sinogram, but may vary from one row to the next. The second case indicates that the position of the object is the same for every n^{th} column of the sinogram, where n represents the number of subpositions. The only requirement in the third case is that within a particular row, every n^{th} column of the sinogram represents the same object position. The object is not necessarily in the same position for the entire column of the sinogram. The types of motion represented in the simulations include revolution of a circle around the center of the object array, motion along a straight line, and switching the object between two or more positions. The motion was defined by the position of objects in the specified object arrays and the manner in which the sinograms calculated for each object array were combined. The combined sinogram was reconstructed to obtain an image that represents a case with motion.

5.2. Simulation Scenarios Studied

The aim of the x-ray CT simulations was to reproduce the artifacts observed in the images of flow through the air-water contactor. The scenarios simulated were designed to verify the simulation code, to investigate the effect of a change in the object array on the artifacts, and to evaluate the influence of the pseudo-third-generation scan method on the appearance of artifacts. The parameters shown in Table 5-1 were determined by reconstructing a stationary circle, shown in Figure 5-4. The image was sharp and did not contain noticeable aliasing artifacts. The parameters were kept constant for all of the simulations. A summary of the simulation scenarios that will be discussed is presented in Table 5-2. The variables specified for each simulation are listed in Appendix C.

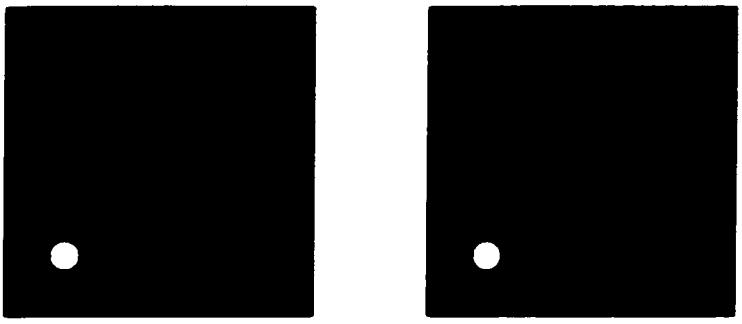

Figure 5-4. (a) Original array containing a circle. (b) Image representing the original array reconstructed from the computer simulation of x-ray CT.

5.2.1. Method Validation

The first set of computer simulations was performed to validate the simulation approach. The simulations of Sakamoto and Sato [45] were repeated using simulation programs written in IDL. The focus of these simulations was motion artifacts caused by a cylinder, represented in two dimensions as a circle, revolving around a point.

Table 5-1. Parameters Used for Computer Simulations

Parameter	Value
Object Array Size	512 x 512
Number of Ray Sums Per View	761
Number of Views	256
Type of Filter	Ram-Lak
Filter Size	33
Reconstructed Image Size	512 x 512
Method of Interpolation	linear

In the work of Sakamoto and Sato [45], simulations were performed with the parallel-beam CT configuration and the results were compared with data that were obtained with a fan-beam CT system. For the simulations, a circle revolved at a constant distance around the image origin. The adjustable parameters were the distance from the origin, the original object position, and the ratio of the speed of revolution of the object to that of the source and detectors. The filtered-backprojection reconstruction algorithm was used. According to the authors, the simulation results represented the experimentally observed data well. The reconstructed images for three sets of parameters were presented as examples of the results.

Simulation of motion artifacts resulting from the revolution of a circle around the center of the object array was performed to validate the results for the three cases reported. The original object position and the ratio of the speed of revolution of the object to that of the source and detectors were varied between the three cases. The motion of the circle in the object space is depicted in Figure 5-5. Each row of the sinogram was calculated with the circle in a different position along the path of motion. Thus, the path of the object in the sinogram is no longer sinusoidal, as shown in Figure 5-5(a) for Case R.1. Following the procedure outlined in Figure 5-2, the

Table 5-2. Summary of Simulation Scenarios Studied

Cases	Description	Variables	Purpose
R.1-3	revolution of a circle	original position revolution speed	validation of simulation method
L.1-4	linear motion of a circle	original position slope, length	investigation of alternate motion
F.1-3	position of circle dependent on view	flip cycle	evaluate appearance of artifacts when rivulet position is dependent on view
E.1-2	measurement error	position	introduce large measurement error in one subposition only
S1.1-4	position of one circle dependent on subposition	value of circle, frequency that position changes	evaluate dependence of artifacts on subposition, and observe disappearance of rivulet
S1.5-8	position of one circle dependent on subposition	frequency that position changes	evaluate artifacts when the motion between four and eight positions is around the center
S2.1-4	positions of two circles dependent on subposition	number of positions, frequency that position changes	evaluate artifacts for two circles when motion is around the center of the array
S2.5-7	positions of two circles dependent on subposition	number of positions, frequency that position changes	evaluate artifacts for two circles when motion is around other than the center of the array
S2.8-10	positions of two circles dependent on subposition	number of positions, frequency that position changes	evaluate artifacts for two circles when motion is between points on a rectangular grid
C.1-4	position dependent on subposition and view	with or without subpositions, flip cycle	direct comparison of use of subpositions

(a) Sinogram for Case R.1

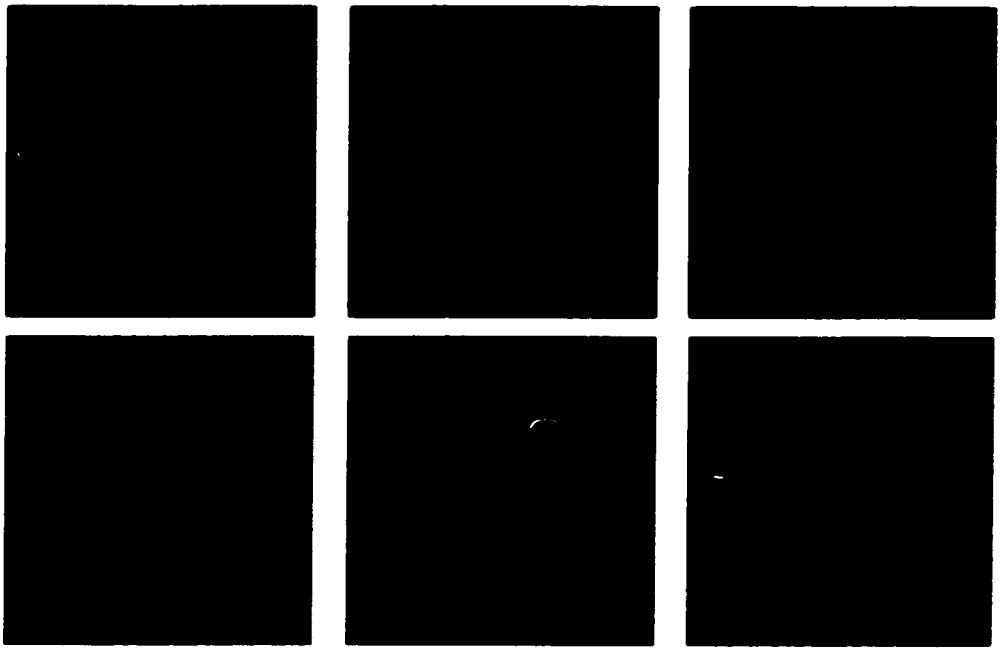

(b) Case R.1 (c) Case R.2 (d) Case R.3

Figure 5-5. (a) Sinogram obtained for simulation Case R.1. (b)-(d) Path of revolution of the circle and the reconstructed images for each of the three simulation cases. The circle labelled '1' represents the original position, the gray arc represents the continuous motion, and the circle labelled '2' represents the final position.

filter function, and subsequently the filtered projection, was calculated prior to backprojection of the data to form the reconstructed image.

The reconstructed images are shown in Figure 5-5, below the images indicating the paths of motion. The relative speed at which the revolution occurred varied, with the image presented in (b) moving the fastest and the image presented in

(c) moving the slowest. The circle in image (d) moved in the direction opposite the other two circles. The arcs in the reconstructed images are positioned close to the path of motion. For the two cases in which the relative speed of revolution was a positive value, the deviation was most significant toward the end of the scan. In all three of the reconstructed images, the artifact contains a bright region with a dark shadow. The reconstructed images closely matched those presented by Sakamoto and Sato [45].

5.2.2. Object Position Dependent Upon View

Two additional types of simulation were performed in which the object position was dependent upon the row in the sinogram. These motions included movement of a circle along a line in the object array and the flipping of a circle between two locations.

Linear motion of a circle in the object array was simulated in a manner similar to the revolution of a circle. The original object position was specified, along with the slope and length of the path of the object. The paths of the circle for three simulations are shown in Figure 5-6. Each row of the sinogram was calculated, the filter function was applied, and the reconstructed images, also shown in Figure 5-6, were determined.

The image artifacts for motion along a line are similar to those for revolution of the object. Although not shown, the sinograms for the cases of linear motion contained a non-sinusoidal bright streak, similar to the sinogram for the cases in which the circle revolved around a point. The features observable in the reconstructed images are in the same region of the array as the path of the circle. The features are curved, as in the simulations in which the circle travelled in a circular path, in spite of the fact that the circle travelled in a straight line path. The size of the features corresponds to the total distance travelled by the circle. The artifacts present in the reconstructed images are not ring-like and are not centered about the center of the image, as in the images of the air-water contactor.

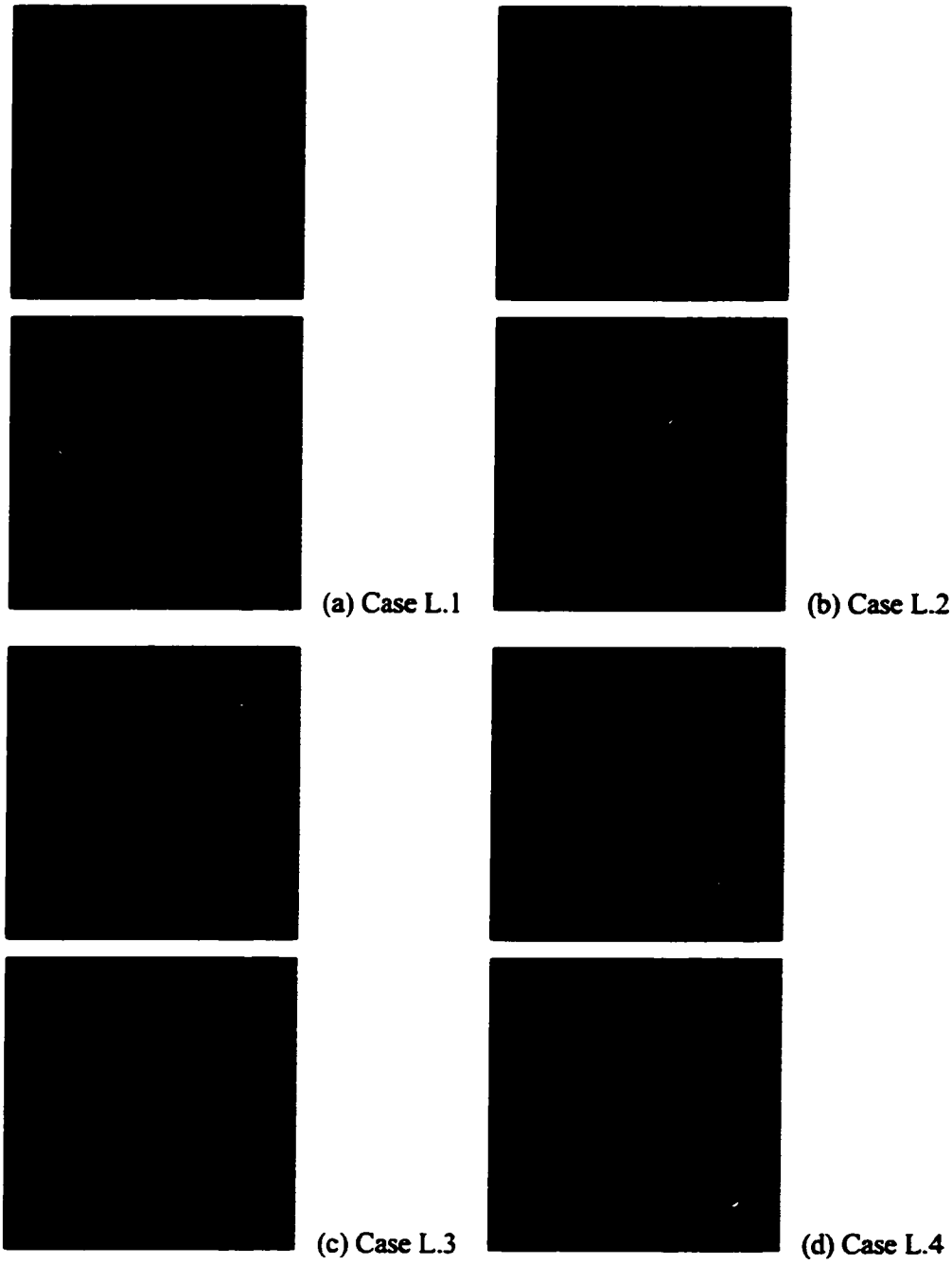

(a) Case L.1 (b) Case L.2

(c) Case L.3 (d) Case L.4

Figure 5-6. Motion of the circle along a line in the object array and the reconstructed image.

The motion of a rivulet switching between two distinct positions, as depicted in Figure 5-3, was investigated for cases in which the object position depended upon the rotational position of the simulated scanner. For these simulations, the flip cycle was specified to indicate the frequency of change between positions. The two positions at which the circle was located are shown in Figure 5-7(a). The circle remains in the first position for the period required to calculate a number of rows of the sinogram equal to the specified flip cycle. The circle is then in the second position for the same period. This cycle is repeated until all 256 rows of the sinogram are calculated. The sinogram for Case F.2 is shown in Figure 5-7(a). The sinogram consists of portions of two sinusoidal paths, switching after a number of rows equal to the flip cycle, which is 32 for the case shown. After the entire sinogram was calculated, the filter function was applied and the reconstructed image was determined. The reconstructed images for oscillation between two positions at three frequencies are shown in Figure 5-7.

The two positions at which the circle was located are apparent in the reconstructed images. The image shown in (c) represents the least amount of movement, with the circle changing position only once. The image shown in (e) represents the scenario in which the circle changed position after 8 rows of the sinogram, or 32 times total. The shape of the circle was elongated in the reconstructed images. The most severe change in shape was observed for the case in which the circle changed position only once. For this case, the circles in the reconstructed image are both elongated in directions perpendicular to each other. If the order of circle positions is reversed, the direction of elongation is also reversed. For the scenarios in which the position of the circle depends upon view, artifacts appear as linear streaks emanating from the centers of the circles. These artifacts are similar to aliasing artifacts that are present when the number of ray paths is insufficient. The streaks are thinner, but present in greater numbers, for the case in which the position of the circle varies more frequently.

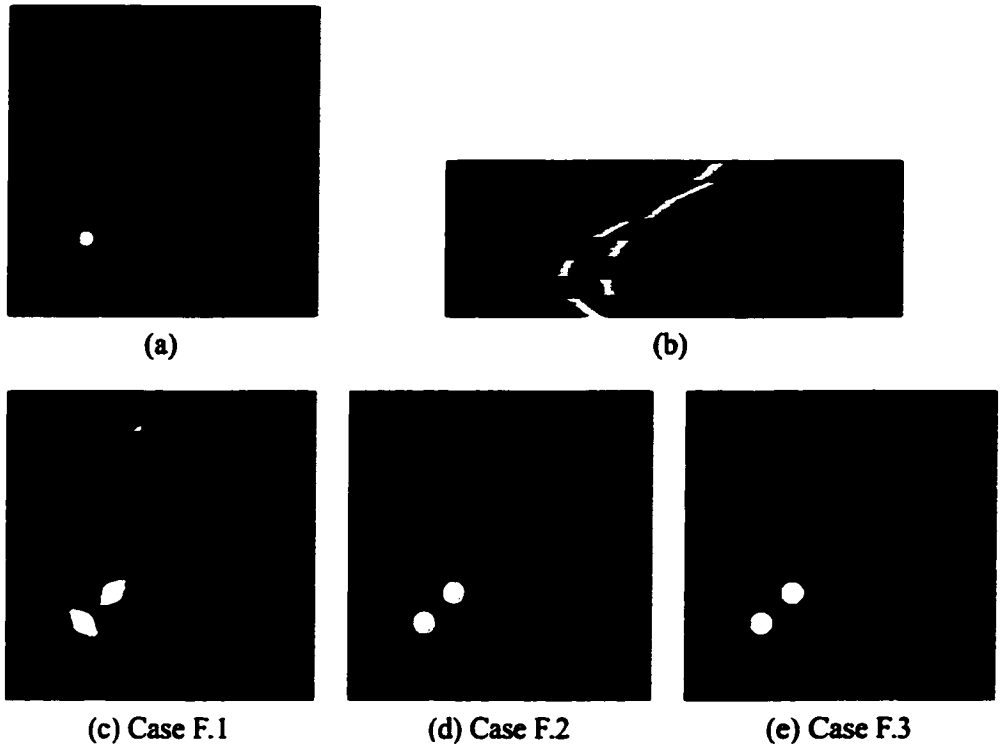

(a) (b)

(c) Case F.1 (d) Case F.2 (e) Case F.3

Figure 5-7. (a) The two object positions, as indicated by the white and gray circles. (b) Sinogram for Case F.2. Reconstructed images for flip cycles of (c) 128 (d) 32 and (e) 8.

5.2.3. Measurement Error at a Detector

The measurement error that was simulated is a system-wide error that occurred for one entire subposition. This error may be caused by a change in the output of the x-ray source, a change in responsiveness of the detectors, or other errors in the measurement system. To simulate a bad detector in the 3DID scan procedure, every eighth column in the sinogram was multiplied by 0.50. This is equivalent to a measurement error at the detector in which half of the attenuation is not recorded during one of eight subpositions. Two simulations were performed, one with a circle located in the corner of the image and one with a circle located at the image center.

The reconstructed images for two cases in which measurement error occurred are shown in Figure 5-8.

(a) Case E.1 (b) Case E.2

Figure 5-8. Reconstructed images representing measurement error during one subposition.

The pattern of the image artifacts is different for the two simulations of measurement error. When the circle was located at the center of the image array, the artifacts are limited to within the circle. In this case, concentric dark circles are present at equal distances from the center. The artifacts in the case with the circle positioned in the corner of the array are of two forms. Both types of artifacts are predominant on the circumference of a circle that passes through the center of the array and also through the position of the circle. The first type of artifacts occurs toward the exterior of the array, as thin arcs of alternating dark and light regions. The second type of artifacts can be described as rays extending from the position of the circle and is located near the center of the array. In general, the artifacts resulting from the simulation of measurement error during one subposition of a pseudo-third-generation scan are positioned relative to the center of the array.

5.2.4. Object Position Dependent Upon Subposition – One Circle

Additional simulations were performed in which the position of the object was dependent upon the subposition. This type of motion is feasible only for a pseudo-third-generation system, such as those at 3DID, as the true third-generation system does not acquire data at multiple subpositions. The subposition-dependent motions investigated are primarily of movement of rivulets of flow as depicted in Figure 5-3.

The simulations are of a scanner that requires the use of eight subpositions to acquire a complete sinogram. Any number of circles can be specified for the eight object arrays that each correspond to a subposition. A sinogram is calculated for each of the eight object positions. The sinogram that is used to reconstruct the image is formed from the eight sinograms and is the same size as each original sinogram. The sinograms are combined such that columns $8n + s$, where n is an integer (0,1,2,...) and s refers to the subposition (1,2,3,...,8), are all obtained from the sinogram of that subposition. The image is reconstructed using the filtered-backprojection algorithm. This process of simulation is depicted for four object positions, rather than the eight implemented, in Figure 5-9.

For the first set of four simulations, Cases S1.1–4, the circle was located at one of the two fixed positions in the lower left corner of the object array shown in Figure 5-10. The first scenario, Case S1.1, consisted of the position of the circle alternating between the two positions, with a change occurring after each subposition. The sinogram that results from this case is shown in Figure 5-11. The two paths are sinusoidal and contain dark vertical streaks. The dark streaks are present for the subpositions when object was not located in that position. Sinograms for other cases are similar in appearance. In Case S1.2, the second scenario, the circle disappeared in the odd-numbered subpositions, rather than appearing in a second position. Similarly, in Case S1.3, the circle disappeared during the even-numbered subpositions. The fourth scenario differed from the third by the frequency at which the position of the

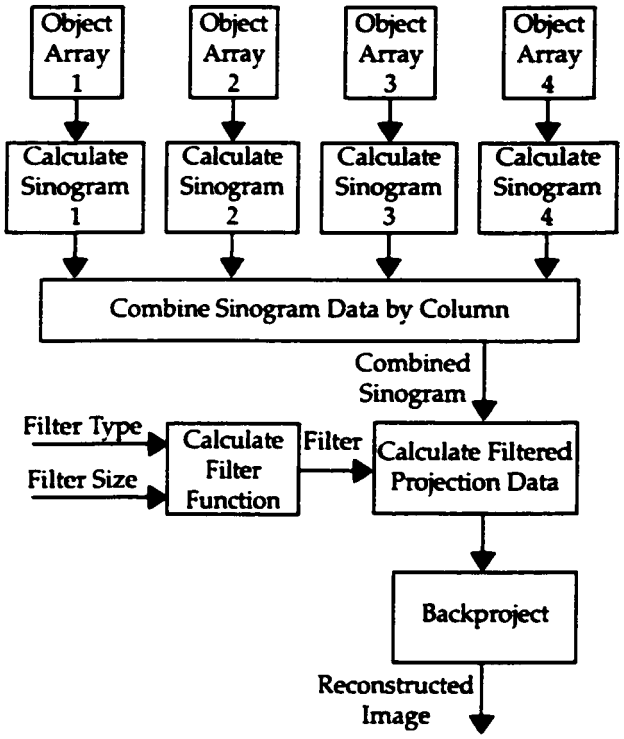

Figure 5-9. Process to simulate four subpositions by reconstructing an image from a composite sinogram created from sinograms calculated for four object arrays.

circle changed. Rather than alternating position after each subposition, the circle varied between being present and not every two subpositions for Case S1.4.

The reconstructed images for Cases S1.1–4, shown in Figure 5-12(a)-(d), all contain similar features. For the first scenario, in which the circle changed position for subsequent subpositions, artifacts are present along four main paths. The first two paths are similar to the path seen in Figure 5-8(a) which represented subposition-dependent measurement error. Each of the two paths pass through one object and the image center; the paths are nearly circular. The second two paths on which artifacts are present also pass through one object each. However, the paths are closed curves

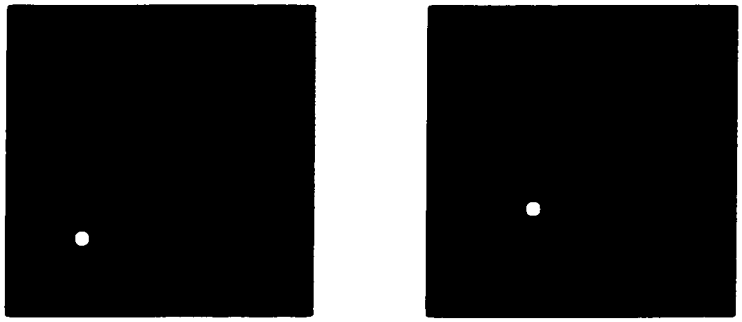

(a) [128,128] (b) [178,178]

Figure 5-10. Two fixed positions of the object for simulations involving subpositions, Cases S1.1–4.

Figure 5-11. Sinogram calculated for Case S1.1.

that include points in each of the four quadrants of the array. The artifacts in the reconstructed images from Case S1.2 and Case S1.3, shown in (b) and (c), are located on two paths for each case. The paths can be described in the same manner as those in (a). The sum of the reconstructed images (b) and (c) is nearly identical to the reconstructed image shown in (a). The difference image consists mainly of noise in the region around the two object positions. Thus, artifacts caused by this type of motion are additive and do not interact with each other. The difference between Case S1.4 and Case S1.3 was the frequency at which the circle disappeared. The

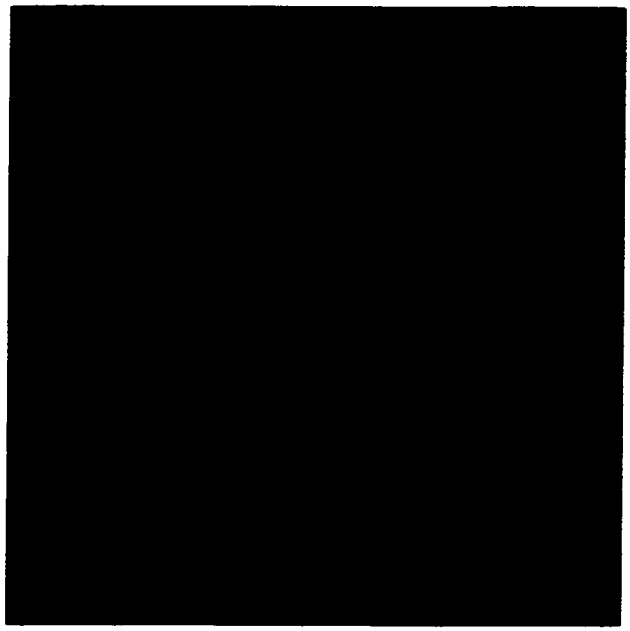

(a) Case S1.1

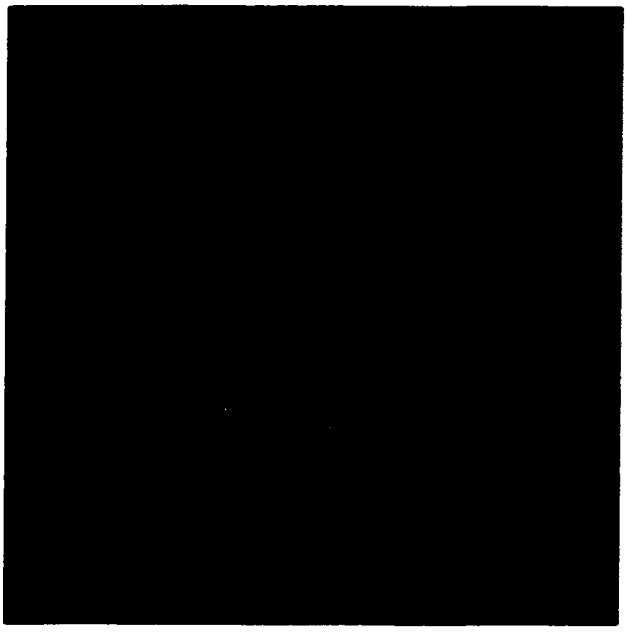

(b) Case S1.2

Figure 5-12. Simulation results of a scenario in which the position and value of the circle was dependent upon subposition, two fixed positions. (a)–(d) Cases S1.1–4.

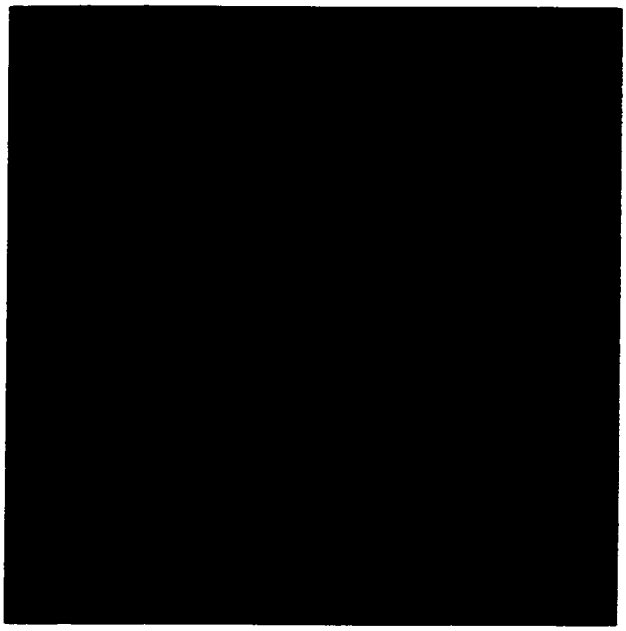

(c) Case S1.3

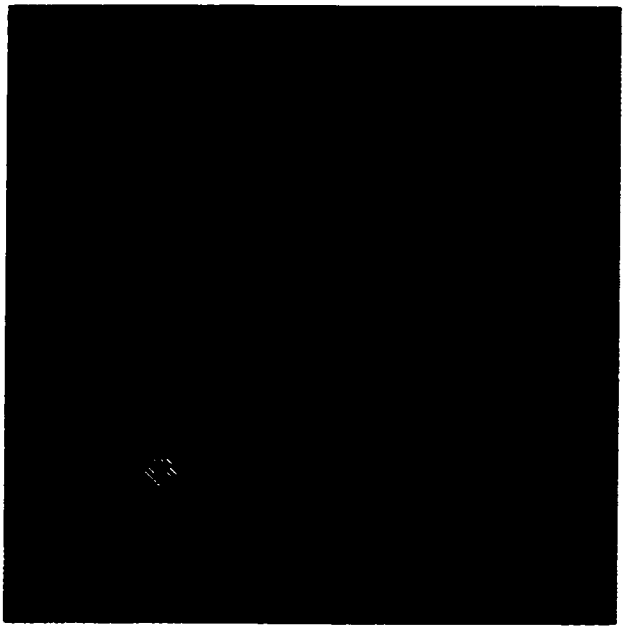

(d) Case S1.4

Figure 5-12 (cont.) Simulation results of a scenario in which the position and value of the circle was dependent upon subposition, two fixed positions. (a)–(d) Cases S1.1–4.

reconstructed image in (c) represents a change in the object array after every subposition. The reconstructed image for Case S1.4, shown in (d), represents a change after every two subpositions. This image is similar to the reconstructed image in the case of measurement error. The artifacts are present on one main closed path that passes through the center of the array and the center of the circle. The alternating dark and light streaks appear to be linear near the array center and curved near the position of the circle. In addition, streaks in the corners of the image are visible. This pattern of artifact is similar to that observed in the image of the air-water contactor containing static holdup.

The object was located in each of the four quadrants of the object array for the next set of four simulations. The four positions specified were equidistant from the center of the array, as shown in Figure 5-13(a). For simulation Case S1.5, the circle was positioned in the same location for two successive subpositions, while the position changed after each subposition in Case S1.6. For Case S1.7, a total of eight object positions, as shown in Figure 5-13(b), were included. The eight object positions used for Case S1.8 are all at the same distance from the center of the array, as shown in Figure 5-13(c). The reconstructed images are shown in Figure 5-14.

In all four of these simulations, ring-like artifacts are present in addition to other patterns. Near the center of the image, the artifacts from each of the circle positions are interfering with each other, resulting in a cross-hatched pattern. The primary differences between these four reconstructed images and those in the first set of four are the number of object positions represented and the distance between the bright streaks. The reconstructed image for Case S1.5 contains a pattern similar to that seen for Case S1.4. In the reconstructed images, the artifacts are located around the positions of the circles. However, the number of bright arcs passing through each circle is decreased by a factor of two from Figure 5-12(d). The object is located in each position for half the number of subpositions as in the image shown in Figure 5-

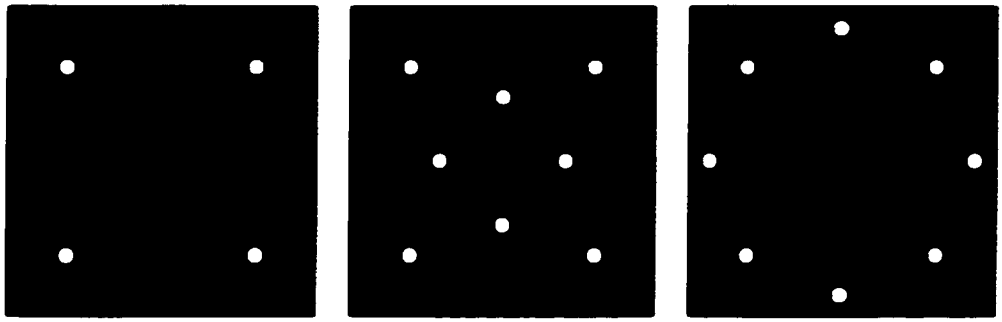

(a) four initial positions for Case S1.5 and S1.6

(b) eight positions for Case S1.7

(c) eight positions equidistant from the center for Case S1.8

Figure 5-13. Positions of the circle for the simulations in which one circle was present for each subposition, Cases S1.5–8.

14(a). Similarly, Case S1.6 exhibits a pattern parallel to that in Case S1.3. The analogous comparison between the number of bright arcs can be made. The artifacts that pass through the circles are more apparent in the case with four objects, as the distance between the arcs is greater. The circles are located nearer the edge of the array in Figure 5-14(b), than in Figure 5-12(c). As a result, the outer closed path extends beyond the reconstructed image. The circle was located in a different position for each subposition in the simulations shown in Figure 5-14(c) and (d). For both Case S1.7 and Case S1.8, the width of the arcs passing through the circles was the same as in Case S1.6 and the distance between the arcs was the same as in Case S1.5. For Case S1.7, the four additional positions of the circles were located closer to the center of the object array. The artifacts due to these positions are concentrated between the circle and the center of the array. In the case in which all positions were equidistant from the center, the arcs are located primarily at this distance. Some additional bright streaks are present in the center region, due to the interactions between the patterns from each circle.

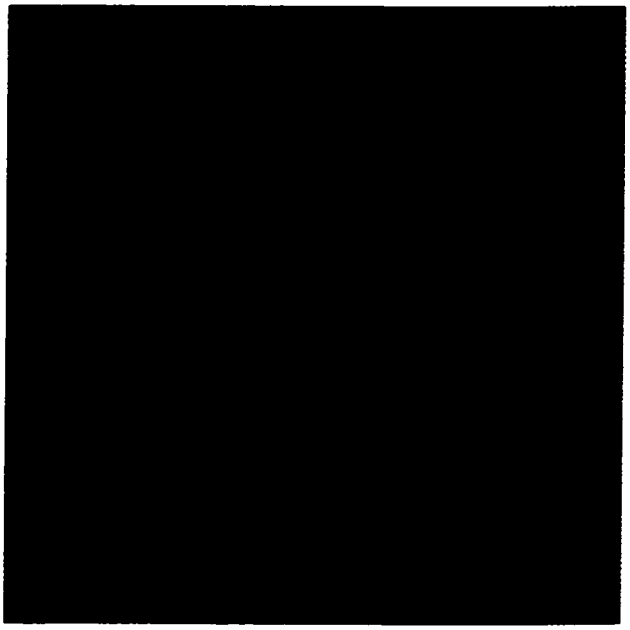

(a) Case S1.5

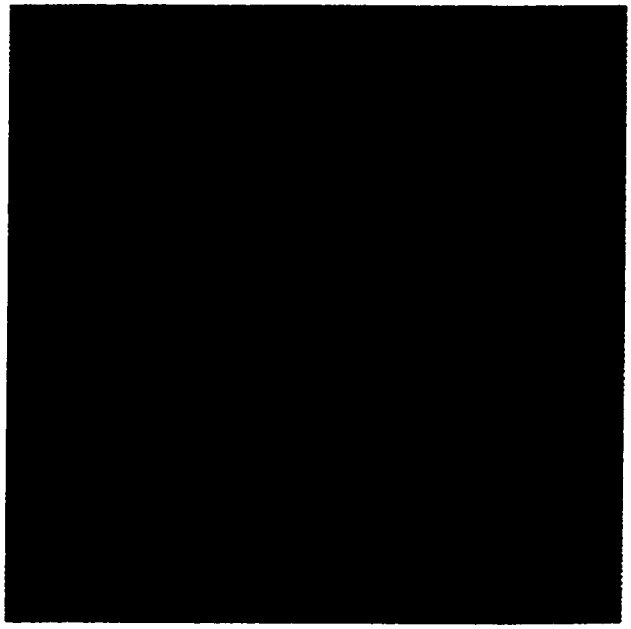

(b) Case S1.6

Figure 5-14. Simulation results of a scenario in which the position of the circle was dependent upon subposition. (a)–(d) Cases S1.5–8.

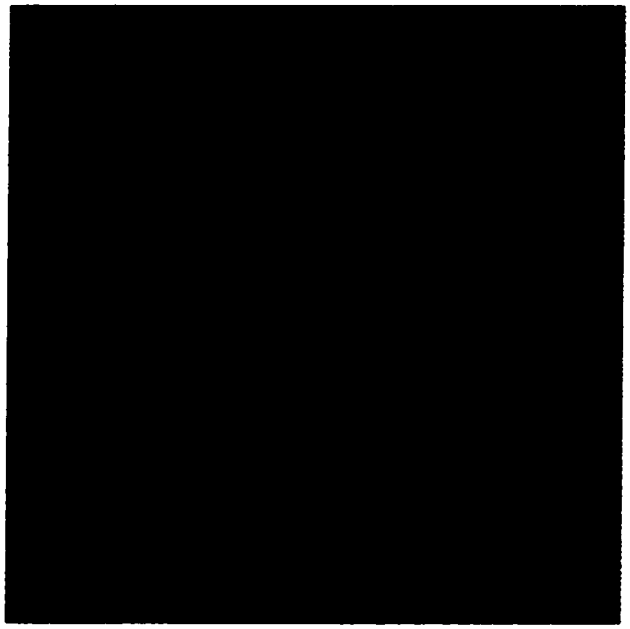

(c) Case S1.7

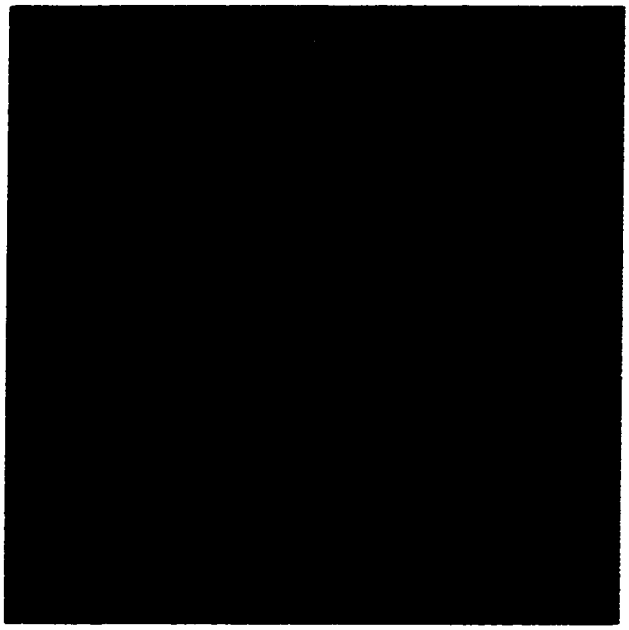

(d) Case S1.8

Figure 5-14 (cont.) Simulation results of a scenario in which the position of the circle was dependent upon subposition. (a)-(d) Cases S1.5–8.

5.2.5. Object Position Dependent Upon Subposition – Two Circles

The ten simulations in this section all involved two circles present in the array simultaneously. As with the preceding simulations, the positions of the circles were varied between subpositions. The scenarios included motion of circles around the center point of the array, motion of circles around a point other than the center of the array, and motion of circles between positions on a rectangular grid.

The first set of simulations performed with two objects parallels Cases S1.5–8, which were performed with one circle per array. As seen in Figure 5-15, the gray circles represent the positions of the second circle. For Case S2.1, the position of both circles changed after two subpositions. Thus, subpositions 1 and 2, 3 and 4, 5 and 6, and 7 and 8, were obtained of the same object array. In contrast, for Case S2.2, the location of the circles was varied after every subposition, and the cycle was repeated. Thus, subpositions 1 and 5, 2 and 6, 3 and 7, and 4 and 8 were calculated from the same object array. Case S2.3 and Case S2.4 involved circular motion of the two circles at different radii. Eight positions were specified for each circle, with the positions of the two circles shown in Figure 5-15(b) and (c). The difference between these two simulation cases is the distance from the center of the array to the outer circle. The reconstructed images for these four cases are shown in Figure 5-17.

The sinogram for Case S2.3 is shown in Figure 5-16 to illustrate a sinogram representing two circles present in each of eight arrays. Compared to the sinogram for Case S1.1, more sinusoidal paths are present. Each path corresponds to a position of a circle. The dark streaks along each sinusoidal path occur because the circle is not located in each position for all of the subpositions. The pattern of the bright regions and the location of the sinusoidal paths vary for each simulation case, although the overall appearance of the sinograms is similar to that shown.

The reconstructed images of the first four scenarios in which two circles are present at the same time exhibit concentric ring-like artifacts. The image in Figure 5-

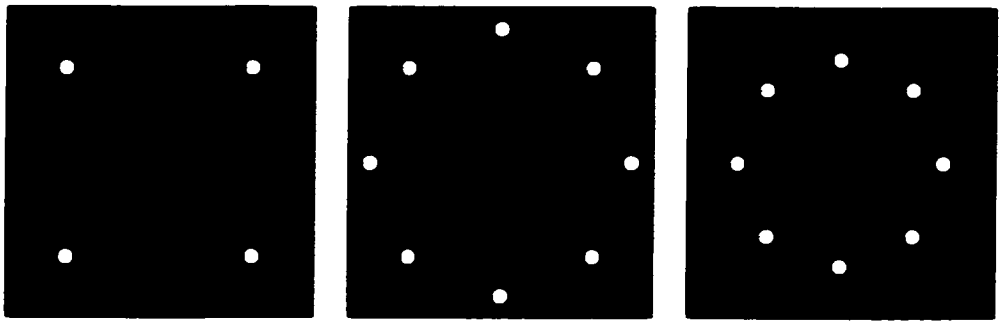

(a) positions of the circles for Cases S2.1 and S2.2 | (b) positions of the circles for Case S2.3 | (c) positions of the circles for Case S2.4

Figure 5-15. Positions of the circles for the simulations in which two circles were present for each subposition. Circle 1 positions are represented by white circles, and Circle 2 positions by gray circles. Cases S2.1–4.

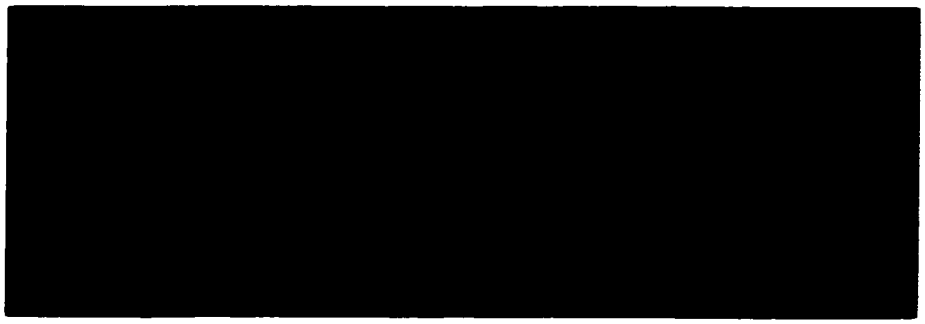

Figure 5-16. Sinogram calculated for Case S2.3.

17(a) is similar to the reconstructed image in Figure 5-14(c). The same object positions were used for both of the simulations. The reconstructed image in Figure 5-17(b) exhibits artifacts similar to those in (a); however, the distance between adjacent arcs is half that between arcs present in (a). The third and fourth simulation scenarios involved locating each of the two circles at a different position for each of the eight subpositions. The difference between the scenarios was the distance from the outer circles to the center of the array. As a result, the artifacts are not located as far from

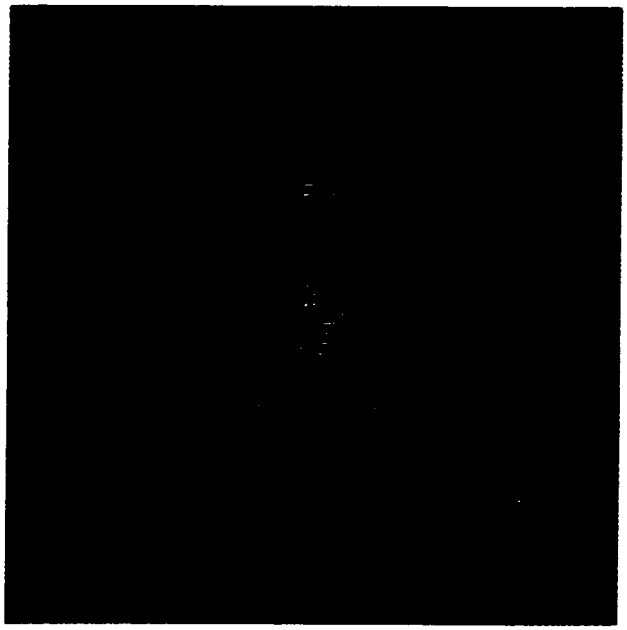

(a) Case S2.1

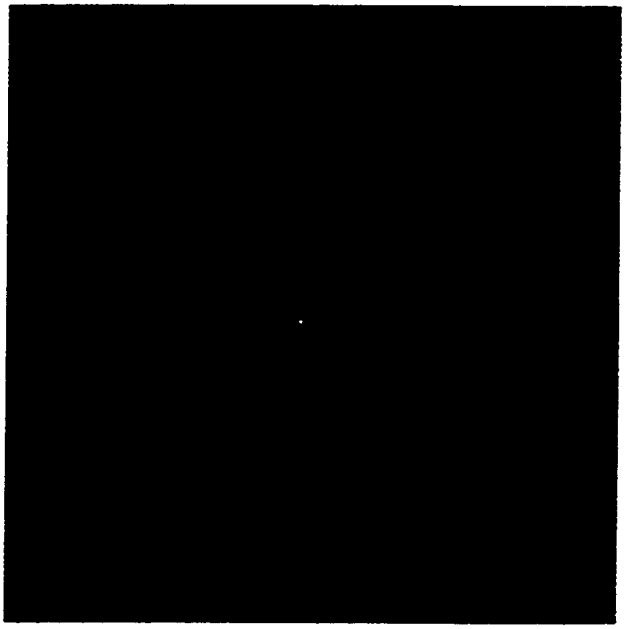

(b) Case S2.2

Figure 5-17. Simulation results of a scenario in which the position of two circles was dependent upon subposition. (a)-(d) Cases S2.1–4.

(c) Case S2.3

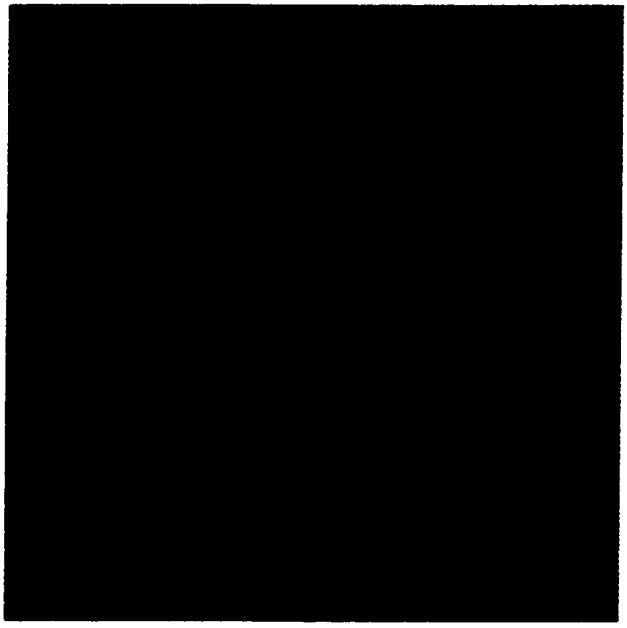

(d) Case S2.4

Figure 5-17 (cont.) Simulation results of a scenario in which the position of two circles was dependent upon subposition. (a)-(d) Cases S2.1–4.

the center in Figure 5-17(d) as in Figure 5-17(c). The ring-like nature of the artifacts in Figure 5-17(c) and (d) is more prominent than in previous simulations, and the linear appearance of artifacts near the center of the array is decreased. A comparison of the artifacts with those present in the images of the operating air-water contactor, as shown in Figure 4-58(b), indicates a similarity between the thin concentric streaks.

Simulations were performed in which the center of the rotation of the circles was not located at the center of the array. The resulting artifacts were evaluated to determine whether the artifacts are concentric around the center of the array or around the center of the object positions. The scenarios simulated in Cases S2.5–S2.7 involve the same pattern of motion as Cases S2.1, S2.2, and S2.4. However, the center of rotation for the circular paths is located 50 pixels left and 50 pixels down from the center of the array, as shown in Figure 5-18. The simulation case analogous to Case S2.3 would locate circles outside of the array, and thus, was not performed. The reconstructed images from these scenarios are shown in Figure 5-19.

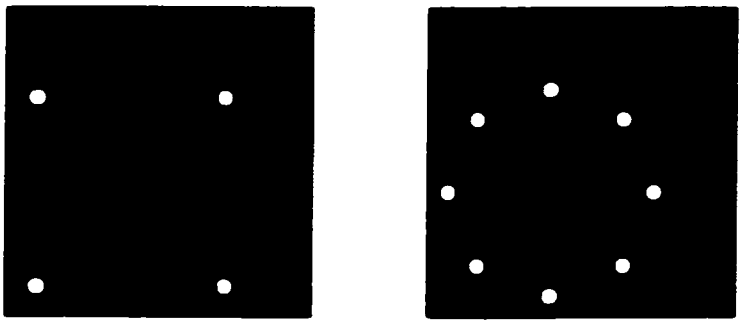

(a) four positions of the circles for Case S2.5 and Case S2.6

(b) eight positions for Case S2.7

Figure 5-18. Positions of the circles for the simulations in which two circles were present for each subposition. Circle 1 positions are represented by white circles, and Circle 2 positions by gray circles. Cases S2.5–7.

A comparison of Figure 5-19(a) with Figure 5-17(a), the analogous image containing centered motion, reveals that the artifacts passing through the circles are still centered around the center of the array. The simulation results represented in Figure 5-19(b) and (c) provide further support that the artifacts caused by the use of subpositions are concentric about the image center and are not caused by rotational motion of the circles. The artifact patterns in Figure 5-19(c) resemble those seen in the the images of flow through the air-water contactor.

A set of simulations in which the circle was positioned at points on a rectangular grid was performed. Two circles were located in different positions for each subposition. The positions for each subposition were determined randomly from the positions shown in Figure 5-20. For Case S2.8, sixteen evenly-spaced positions were used. For the second case, Case S2.9, only the four positions in the lower left quadrant of the array were used. Two circles were created in each of the eight object arrays, with each position used a total of four times. The circles were located at sixteen evenly-spaced points on a rectangular grid in the lower left quadrant for Case S2.10. As with Case S2.8, each of the sixteen positions was used only once and the order was determined randomly.

The reconstructed images for the simulations in which the circles were located at positions on a rectangular grid are shown in Figure 5-21. In the first reconstructed image, (a), the two circles were located at points throughout the entire object array. Ring-like artifacts, similar in appearance to those in the images of the operating air-water contactor, were also present throughout the entire object array. The second reconstructed image represents the circles located at only four different positions. The artifacts present in Figure 5-21(b) are similar to those that were seen in Figure 5-12(d) and in the region of artifacts in the image of static holdup in the air-water contactor. The distance between the arcs that pass through the circles provides an indication of when the circle was present at that location. The circle in the lower left has broad arcs

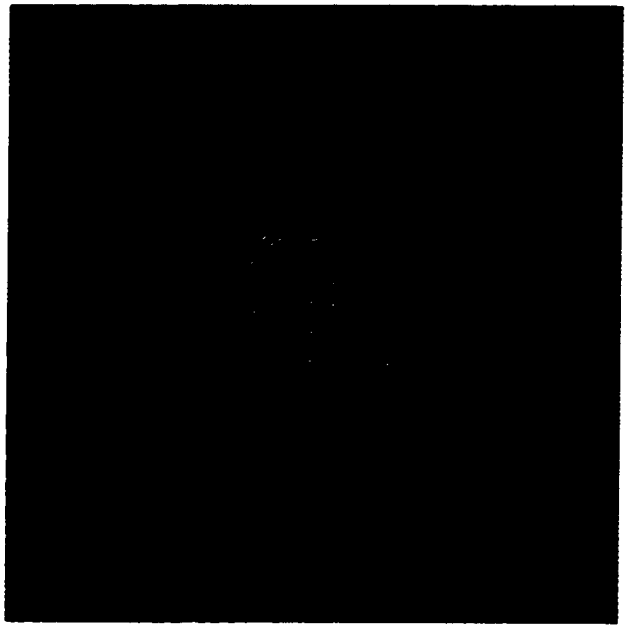

(a) Case S2.5

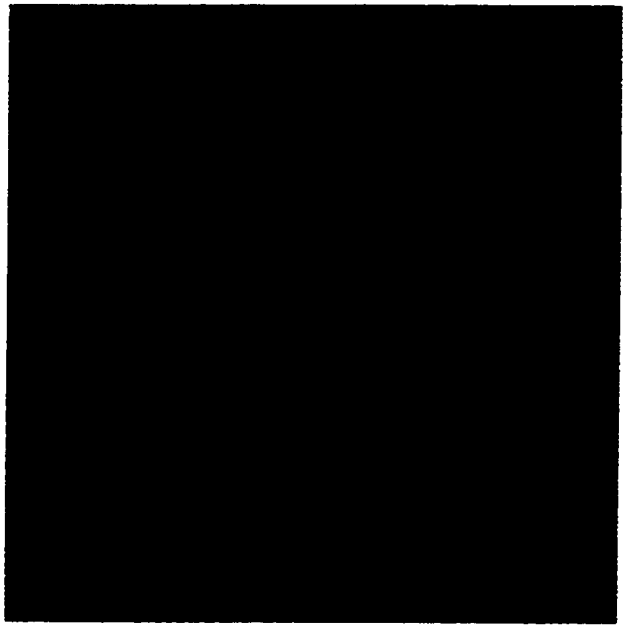

(b) Case S2.6

Figure 5-19. Simulation results of a scenario in which the position of two circles was dependent upon subposition. (a)-(c) Cases S2.5–7.

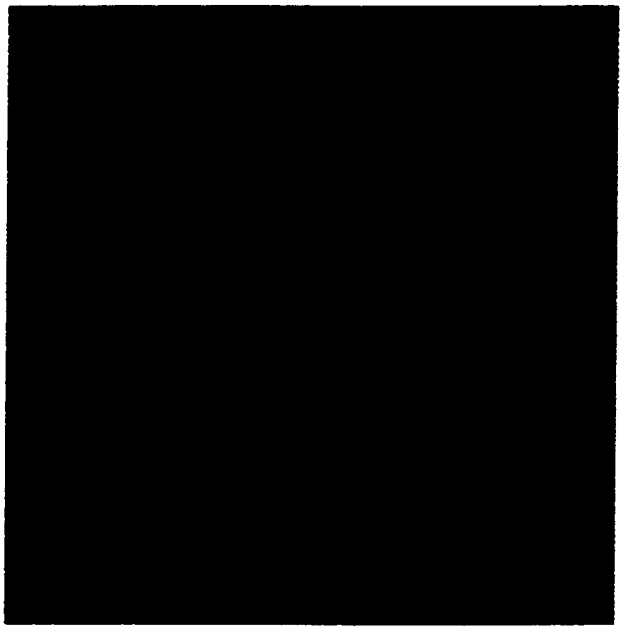

(c) Case S2.7

Figure 5-19 (cont.) Simulation results of a scenario in which the position of two circles was dependent upon subposition. (a)–(c) Cases S2.5–7.

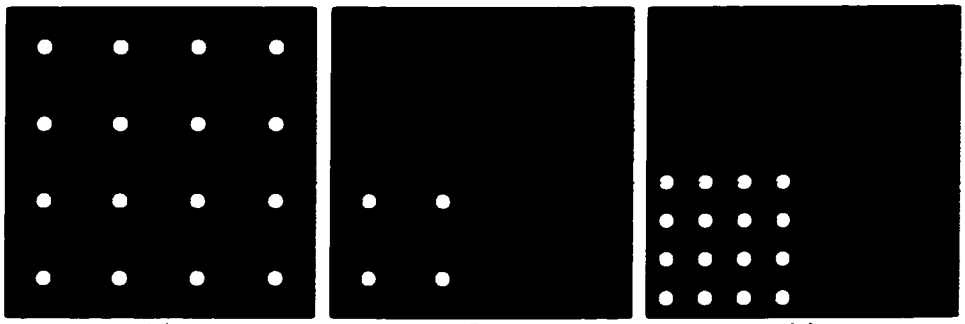

Figure 5-20. Rectangular grids on which circles are located for simulations of subposition. (a) Case S2.8. (b) Case S2.9. (c) Case S2.10.

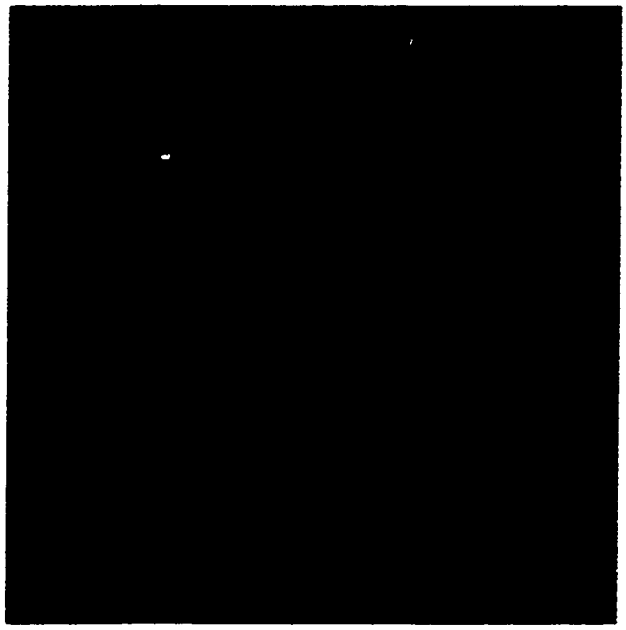

(a) Case S2.8

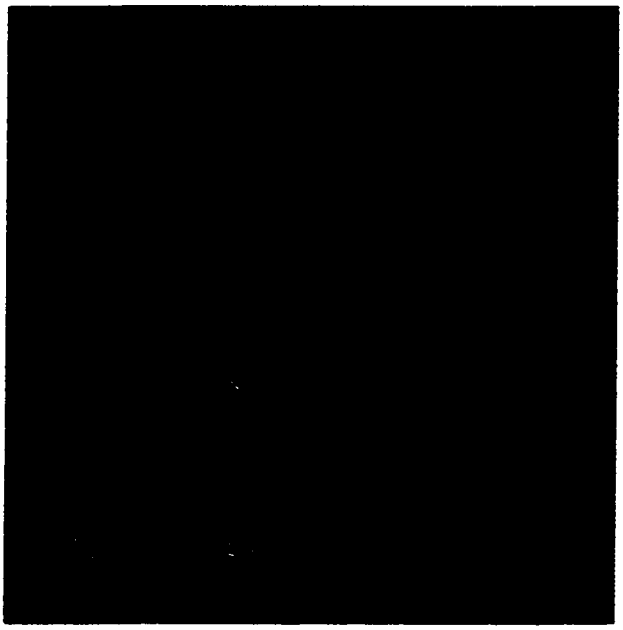

(b) Case S2.9

Figure 5-21. Simulation results of a scenario in which the position of two circles was dependent upon subposition. (a)-(c) Cases S2.8–10.

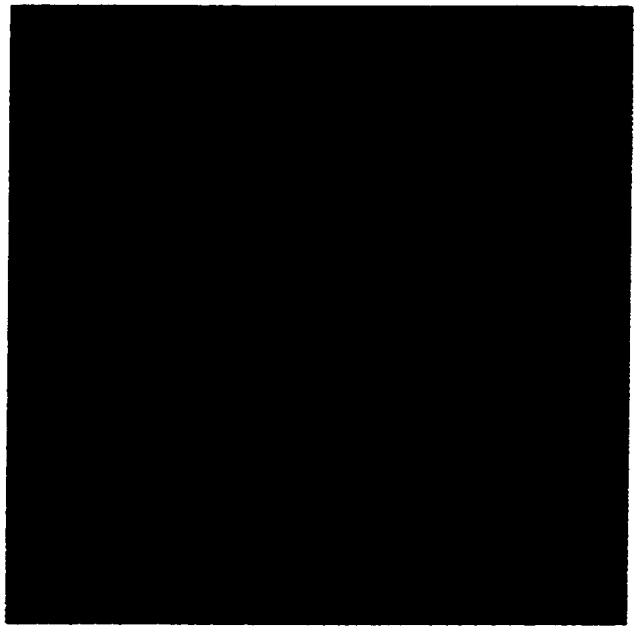

(c) Case S2.10

Figure 5-21 (cont.) Simulation results of a scenario in which the position of two circles was dependent upon subposition. (a)-(c) Cases S2.8–10.

equidistant from each other, indicative of the circle being present at that location for four successive subpositions. The circle in the upper left contains narrow equidistant arcs. This circle was present for two successive subpositions, rather than four. In contrast, the two circles positioned on the right have both broad and narrow arcs with a small distance between. This is due to the pattern of being present for one subposition, absent for two subpositions, present for three subpositions, and absent for two subpositions. The artifacts observed in Figure 5-21 are located primarily in the region in which the circles were located. For the images in (b) and (c), the artifacts extend slightly beyond the lower left quadrant. The arcs passing through the circles in Figure 5-21(c) are of the same width. In contrast to image (b), a circle was located in each position during only one subposition. The difference in the apparent distance between

the arcs is due to the difference in period of cycling between positions at the same distance from the center of the array. The artifacts observed in Figure 5-21 support the hypothesis that the artifacts in the images of the air-water contactor are caused by a combination of the fluctuations in flow pattern and the use of subpositions to acquire the set of transmission data.

5.2.6. Comparison of Scanners Requiring and Not Requiring Subpositions

Simulations were performed to compare the image artifacts obtained for the same flow pattern with two scanners. The first scenario implemented is a simulation of a scanner that is pseudo-third-generation and thus requires the use of subpositions. The scanner has 153 detectors spaced such that 5 subpositions are required. For the simulation cases, for which 256 views are used, a total of 1280 measurement periods are simulated. The second scenario is of a scanner that contains 761 detectors and does not require the use of subpositions. Thus, for 256 views, only 256 measurement periods are required. The size of the sinogram obtained with each scanner is the same, so that the resulting reconstructed image is of the same spatial resolution. The second scenario requires one fifth of the time of the first scanner to acquire the data for an image. Thus, only one fifth of the variation in position of the circles is represented in the sinograms. For the simulations with the first scanner, the positions of the circles depend upon both the row and column of the sinogram. For the simulations with the second scanner, the positions of the circles depend upon only the row of the sinogram. Ten positions for the circles are represented in Figure 5-22.

The reconstructed images from four simulation cases are shown in Figure 5-23. The effect of using subpositions and the effect of the frequency of the change of position of the circles were investigated using the scenarios simulated in Cases C.1–4. For all four cases, the motion of the circles was cyclical. The circles were located at one set of positions for a number of measurements equal to the specified flip cycle, as

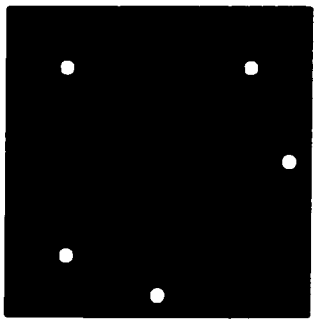

Figure 5-22. Position of two circles for simulations comparing cases with subpositions to cases without subpositions. Circle 1 positions are represented by white circles, and Circle 2 positions by gray circles. Cases C.1–4.

in simulation Cases F.1–3. The number of subpositions was five for the two cases, C.1 and C.3, that simulated the first scanner. The corresponding simulations that did not incorporate subpositions were Cases C.2 and C.4, respectively. The difference between Cases C.1 and C.3 was the frequency at which the circles changed positions.

The reconstructed images shown in Figure 5-23 all contain artifacts resulting from the motion of the circles. Two main types of artifacts are observed. In the images in (a) and (c), the artifacts are primarily dark and light arcs, or portions of concentric circles, that pass through the ten positions at which the circles were located. An interference pattern is also observed at the center of the image. The artifacts in images (b) and (d) are mainly streaks that emanate from the ten locations of the circles. For Case C.4, shown in (d), the shape of the circles is also affected. This case was one in which the flip cycle was larger, indicating that less fluctuation was captured during the simulated scan. This same effect was observed in simulation Cases F.1–3. A comparison of the four reconstructed images indicates that the circles are best represented by Case C.2. This scenario represents a scanner that does not require subpositions, but that has a scan time that is long enough to capture an average of the flow patterns.

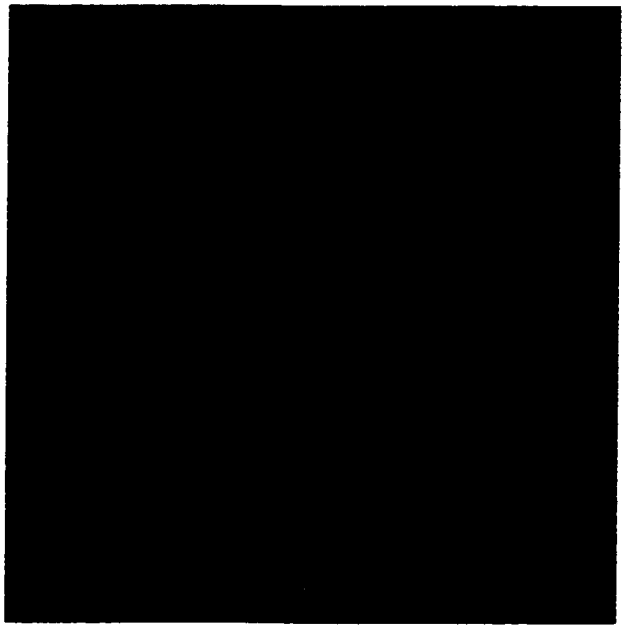

(a) Case C.1

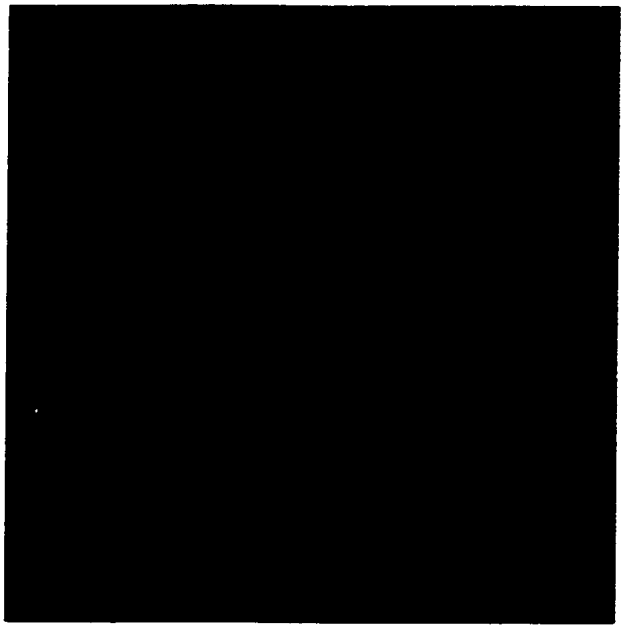

(b) Case C.2

Figure 5-23. Simulation results of scenarios to compare a scanner that requires subpositions, (a) and (c), with one that does not, (b) and (d).

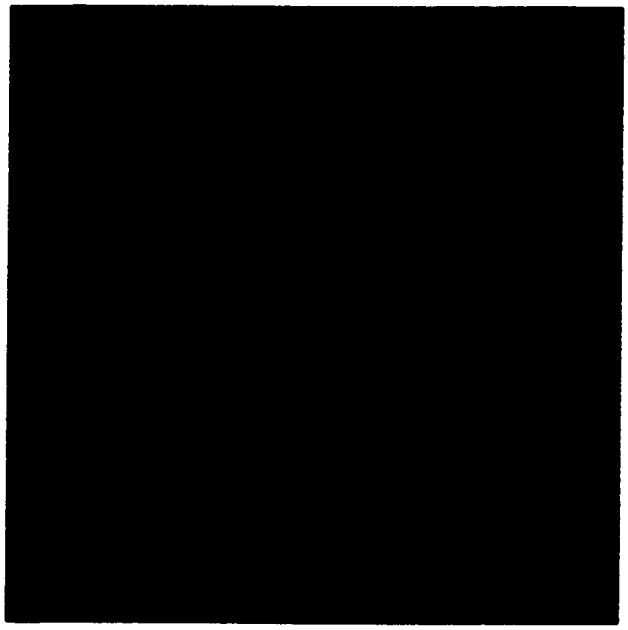

(c) Case C.3

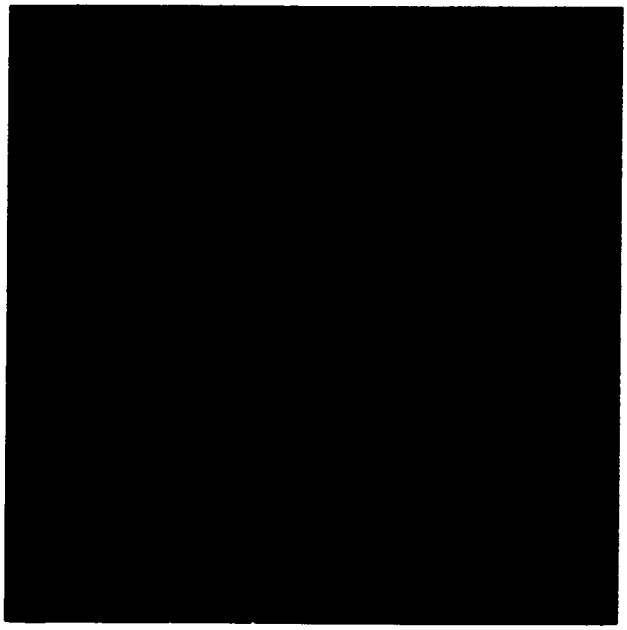

(d) Case C.4

Figure 5-23 (cont.) Simulation results of scenarios to compare a scanner that requires subpositions, (a) and (c), with one that does not, (b) and (d).

5.3. Summary

Artifacts similar to those observed in images of the air-water contactor were produced with the use of computer simulations of x-ray CT. Experimentally, artifacts were observed in images of flow through the column and in images in which a single droplet passed through the scan plane. Both types of artifacts were observed in images reconstructed from simulations in which the positions of circles in the object array depended upon subposition. The final simulations were performed to directly compare images obtained of cyclical motion using a pseudo-third-generation scanner with those obtained using a true-third-generation scanner. While motion artifacts are observed in both sets of images, the ring-like artifacts are present only in the images from the scanner that requires subpositions.

The simulations presented in this work provide support for the hypothesis that the ring-like artifacts in images of the air-water contactor are caused by a combination of the scanning method and the fluctuations due to flow through the column. In addition, the simulations indicate that the use of a true-third-generation scanner has promise for eliminating artifacts of this type.

CHAPTER 6: DISCUSSION OF RESULTS

The studies included in this work were performed to evaluate the potential of x-ray imaging techniques to investigate the hydraulic performance of a vapor-liquid contactor. Two x-ray CT scanners were used for the experimental work, and studies involving computer simulations were used to investigate further the experimental results. The objectives addressed were: (1) evaluation of x-ray imaging techniques for vapor-liquid contacting applications, (2) measurement of local properties of an air-water contactor, and (3) investigation of the cause of flow artifacts with the use of computer simulations.

The ideal imaging technique for use with a vapor-liquid contactor would acquire an instantaneous representation of the distribution of liquid within the entire column. A series of these three-dimensional descriptions of column behavior over time would provide the desired information about the time-varying flows throughout the packed bed. Parameters that are used to predict column behavior could be calculated based upon the distribution of fluid on the packing surfaces. The interfacial area between vapor and liquid, the liquid holdup throughout the bed, a measure of the quality of liquid distribution, and the fraction of the packing surface that is wetted are all parameters that are acknowledged as important factors in predicting the hydraulic and mass-transfer performance of a vapor-liquid contactor. The distribution of components in each of the two fluid phases will influence the mass-transfer efficiency. Evaluation of the flow and mass-transfer behaviors throughout the entire operating range of the column would eventually lead to a determination of the optimal operating point. Ideally, the evaluation would lead to an understanding of how operating parameters and physical properties of the system contribute to the desired behavior.

With this knowledge, the operation of columns could be optimized and the design of packing materials could be modified, resulting in a highly-efficient vapor-liquid contactor.

While process tomography has not yet advanced to exhibit this capability, progress is being made. Local measurements of process parameters that previously were not attainable, or that were attainable only with use of intrusive techniques, are possible. As x-ray CT scanner technology advances, and as the application of the technique is refined, experimental measurements of column behavior at a local level will continue to be increasingly valuable. Currently, a series of two-dimensional cross-sectional images of a vapor-liquid contactor can be acquired.

6.1. Evaluation of X-Ray Imaging

The advantages of x-ray imaging techniques continue to be the compatibility with the materials contained in a vapor-liquid contactor, the image resolution capabilities, and the linear nature of the measurements that results in standard reconstruction algorithms. However, the studies performed in this work have identified several disadvantages that must be overcome prior to widespread use of the technique for imaging operating vapor-liquid contactors to evaluate hydraulic behavior.

Experimental data from a vapor-liquid contactor that provide insights into the flows at a local scale are useful in developing and validating performance models. The hydraulic parameters of a vapor-liquid contactor that are included in existing models include the liquid holdup and interfacial area. However, the parameters are considered constant for the entire packed bed. Predictive models will become more robust if local effects are included. As mentioned in Chapter 2, CFD models that predict local behavior are being developed for distillation applications. Even though

the models predict local properties, the validity of the underlying closure models is not determined if experimental validation is performed with measurements representative of the behavior of the entire column. The continued development of more rigorous models depends upon experimental data to validate the behavior within the column. The identification of flow behavior within small regions throughout a column will lead to a more rigorous explanation of the transport phenomena involved. The resulting models will likely incorporate a dependence of performance on the radial or axial position within the column.

6.1.1. Requirements for CT Images

The primary objective for evaluating images of a vapor-liquid contactor is to identify the location of the liquid. With the liquid identified in an image, the liquid holdup, liquid distribution, and interfacial area can subsequently be calculated. The images of the phantoms were used to characterize the representation of the four materials typically present in a contactor, including water. The evaluation of the images of the film-flow apparatus provided additional insights into specifying a CT scanner for vapor-liquid contactor studies. Based upon the results presented in Chapter 4, the requirements for imaging a system containing air, water, and stainless steel have been refined.

A well-known trade-off for an x-ray CT scanner is that between the time required to obtain an image and the spatial resolution of the resulting image. The imaging experiments involving the phantoms identified the importance of also considering the level of noise in the transmission measurements. The evaluation of the histograms of the high- and low-resolution images identified the negative consequences that occur when the noise level is high. The high-resolution images obtained with the 101B+ scanner provide a more detailed representation of the phantoms. However, the ranges of grayscale that represent each material present in

the column are broader. As a result, the regions corresponding to air and water overlap. The ranges of values representing air and water do not overlap in the low-resolution images. Therefore, the identification of pixels in the low-resolution images is simplified. As seen in Table 4-3, in the low-resolution images of the phantoms with the 101B+ scanner, pixels with a value of 40 or above do not represent air, and pixels with a value of 47 or less do not represent water. Metal and plastic pixels are still present in both ranges, but the distinction between the location of the two fluids is made by applying a grayscale threshold.

The image analysis technique of applying a threshold will differentiate between air and water regions, when the noise level is low. However, additional techniques are required to classify pixels that contain two or more materials. As observed in the thresholded images in Figure 4-19, the knowledge of both the value and the location of a pixel can be used to determine the materials comprising the region of the pixel. In image (c), the pixels with values in the range 36-39 were located along edges between air and either plastic or steel. The pixels were not located near regions of water. The use of surrounding pixels to classify a pixel involves image analysis techniques that are classified as neighborhood-based algorithms.

Prior to the application of image analysis techniques to classify edge pixels, the location of the edge pixels can be determined with the combined use of a calculated image gradient and a histogram evaluation. The use of the image gradient to classify pixels as regions of metal was applied to images of the air-water contactor containing random packing by Cartmel [8]. For pixels such as those located on an inclined metal surface, as seen in Figure 4-26, the pixels would all be identified as edge pixels using the image gradient approach. Again, the neighborhood-based image analysis will be valuable in classifying regions of edge pixels as slanted surfaces. However, the ability to differentiate between the air-steel and water-steel edge pixels will indicate the effectiveness of the image analysis.

For images that contain distinct regions of water and air, neighborhood-based image analysis will be useful to classify the edge pixels. The neighbors of a pixel are typically defined as four or eight pixels. The three common definitions are depicted in Figure 6-1 [17]. Using a neighborhood-based approach, the classifications of the neighbor pixels are evaluated to determine the classification for a given pixel. If the pixel is surrounded by pixels of one classification, it is likely the pixel is also of this classification. In this case, the pixel represented noise within a distinct region and was not located along an edge. If the pixels are of one classification in one direction and a second classification in the second direction, the pixel is likely on the edge between the two classifications. The histogram evaluation of the phantom images provides visual evidence that this approach has promise for further classifying the materials present in an image of an air-water contactor. One challenge with the use of neighborhood-based analysis is identifying films of liquid on a solid surface that are on the order of a pixel thick.

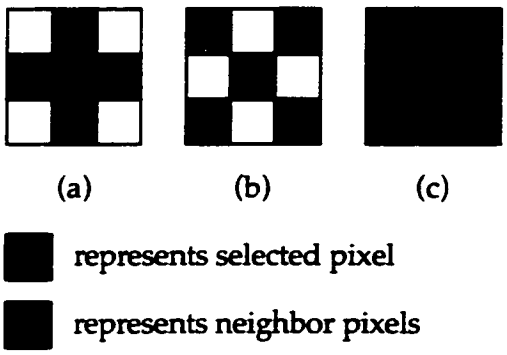

Figure 6-1. Three common definitions of neighbor pixels: (a) four, (b) four diagonal, and (c) eight.

The analysis of the images of the film-flow apparatus resulted in the calculation of the thickness of films as thin as 0.27 mm (0.011 in) with less than 12 percent variation from theory-predicted values. At a theory-predicted film thickness

of 0.24 mm (0.009 in), the calculated value was within 20 percent. For vapor-liquid contacting applications, measurement of the interfacial area is important for evaluating the mass-transfer performance. Thin films contribute significantly to this area, thus the identification of the location of films is important. The technique used to identify the film thickness on the steel surface of the film-flow apparatus is applicable to the controlled scenario that existed.

The thin films observed on the film-flow apparatus were primarily of thicknesses smaller than the size of a pixel. The film was observed in the difference image calculated between the flow condition and the pipe-full condition. The geometry of the steel surface of the film-flow apparatus was well defined. Although the surfaces of structured packing are ordered in a manner that repeats, the texturing of the surface and the location of holes in the stainless steel sheets makes the definition of the location of the surface more complex. The image analysis techniques that were used successfully for the film-flow apparatus may not be as accurate for the less-well-defined surface. However, if a film was thicker than a pixel in the image, the identification of the region of water could be performed with the above described neighborhood-based techniques.

The presence of the flow artifacts in the images of the air-water contactor complicate the analysis of the images. Thus, to measure films on the structured packing surfaces, the flow artifacts in the images first must be removed. Srinivas and Costa [57] and Chiu and Yau [11] have both proposed methods of compensating for motion when performing image reconstruction. Unfortunately, both proposed techniques assume motion of either slow variations or motion that can be defined prior to reconstruction. The stochastic behavior of the flows within an air-water contactor does not classify as motion of either type. The artifacts, and factors that contribute to the appearance of the artifacts, will be discussed in Section 6.2.1.

6.1.2. Use of Sinograms

One common aim of the three experimental studies was to determine the accuracy of calculating the amount of water present in the cross section of the column from the transmission data. In the work of Cartmel [8], one challenge was identifying water directly from the CT images. Fortunately, calculation of liquid holdup from the sinogram data resulted in improved agreement with values obtained using the traditional experimental method and predicted using the model of Stichlmair et al. [58]. The calculation method involved determining a scaling factor by matching the sinogram average for one experimental condition with the model-predicted value. In the calculations based upon the sinograms in this work, the sinograms were scaled using a minimum- and maximum-water condition to determine the 0% and 100% ends of the scale.

The prediction of percent water in the phantoms using the mean values of the sinograms resulted in less than 10 percent variation from the expected value. The conditions of the phantoms ranged from 7 to 25 percent water. The precision of the calculations with the Alliant scanner was better than that with the 101B+ scanner. However, this may be due in part to the greater complexity of the geometry defining the regions with water in the 101B+ scans. The water-filled regions for the images obtained with the Alliant scanner were simple rectangles. In contrast, the water-filled regions for the images obtained with the 101B+ scanner were bounded by portions of ellipses and other curved shapes.

The accuracy of correlating the film thickness with the sinogram data for the film-flow studies was remarkable. However, the precision of the calculations was affected by the beam-hardening effect observed. After the data were scaled using two flow conditions, as shown in Figure 4-52, only the two data points classified as outliers exhibited more than 10 percent variation from the theory-predicted values. Differences between six films with thicknesses in the range 0.24 – 0.37 mm (0.009 –

0.15 in) were identified. These values correspond to water present in 0.3 – 0.5% of the void space.

As the amount of water present in the cross section imaged decreases, the influence that the measurement errors of the scanner have on the calculations of the amount of liquid present increases. The scanner drift measured between images of the film-flow apparatus contributed to the significant error in calculation of film thickness that was presented in Figure 4-49. However, at the higher amounts of total water that were present in the phantoms, a similar scanner drift did not significantly impact the sinogram-based calculations, as was shown in Figure 4-54.

An advantage of the sinogram-based calculations is that the calculation of the total amount of liquid present does not depend upon identifying small regions, or thin films, of liquid. The values of liquid holdup calculated from the sinograms can thus be used to assist with the development of image-based calculations. If the amount of liquid present is determined accurately from the sinograms, insights can be gained when performing the image analysis. If regions of liquid are identified in an image, the remaining amount of liquid present as films, or small regions, can be calculated.

The values of liquid holdup calculated for the air-water contactor from the sinograms did not compare as favorably to values determined with other methods. However, the liquid holdup from the sinogram represents the condition at one elevation of the packed bed, while the methods to which the data were compared are representative of the entire packed bed. Measurements of liquid holdup at equally-spaced intervals throughout the packed bed would provide a set of data that, when averaged, could be compared to the column-average holdup obtained with other methods. Such data would confirm whether the dependence of holdup on elevation is contributing to the variation between holdup determined with other techniques. The use of additional scaling data, as described below, would provide a direct calculation of the variation in both holdup and void fraction over the length of the packed bed.

For the three studies presented, the sinograms were used to calculate the percentage of the void space that contained liquid. However, with additional scaling measurements, a direct calculation of both the void fraction and the liquid holdup from sinogram data is feasible. For vapor-liquid contacting applications, liquid holdup is defined as the volume of liquid per total volume of the packed bed. To directly calculate liquid holdup at a select scan elevation, the column must be imaged empty, full, and with dry packing. The empty-column condition is defined as the column without any material present inside, i.e. with no packing material. The measurement of attenuation along a path for this condition is described by Equation 6-1. The notation is consistent with that presented in Section 3.6. The portion of the path that will contain the stainless steel is comprised of air for this measurement, as is the void space. Therefore, a measurement of the attenuation due to the plastic column wall is obtained. The full-column condition is defined as containing water, but no packing, as shown by Equation 6-2.

[6-1] $$d_i^{empty} = \mu_a L_i^v + \mu_p L_i^p + \mu_a L_i^s = \mu_p L_i^p$$

[6-2] $$d_i^{full} = \mu_w L_i^v + \mu_p L_i^p + \mu_w L_i^s$$

The liquid holdup is the total amount of liquid per the total column volume. Thus, as shown in Equation 6-3, the holdup is the length of water along a path divided by the sum of the lengths of void and stainless steel. The minimum-water condition consists of the column with the dry packing inserted. The use of this equation allows direct calculation of the liquid holdup without the need to use a calculated value, or the vendor-specified value, for void fraction.

[6-3] $$\text{holdup} = \frac{L_i^w}{L_i^s + L_i^v} = \frac{d_i - d_i^{min}}{d_i^{full} - d_i^{empty}}$$

The measurement of void fraction can be made from the sinogram data if the column is imaged at four non-flow conditions. As shown in Equation 6-4, the local void fraction is the ratio of the length of void to the sum of the lengths of steel and void. The maximum-water condition is defined as the column containing the packing material, with the void space filled with water. The variation in void fraction throughout the packed bed can thus be compared with the variation in liquid holdup.

$$[6\text{-}4) \qquad \varepsilon_i = \frac{L_i^v}{L_i^s + L_i^v} = \frac{d_i^{max} - d_i^{min}}{d_i^{full} - d_i^{empty}}$$

6.2. Evaluation of the Air-Water Contactor

The air-water contactor was imaged using the 101B+ scanner. In addition to standard CT images and radiograms, transmission measurements through the operating contactor were obtained over time. The methods of imaging using the x-ray CT scanner provided insights into the flow behavior within the column. In addition to the experimental work, an investigation into the artifacts present in the CT images was performed. Additional requirements for using the x-ray imaging techniques for vapor-liquid contacting applications, based upon these studies, will be discussed in the final section of this chapter. In spite of the image artifacts, use of the 101B+ scanner resulted in valuable observations of the column performance.

6.2.1. Investigation of Image Artifacts

Ring-like artifacts present in the CT images obtained of the operating air-water contactor were investigated with the use of computer simulations. The artifacts were not observed in images of the phantoms or images of the film-flow apparatus. In addition, the artifacts were not observed in images of the air-water contactor prior to

the introduction of fluid flow. Thus, the hypothesis was made that the artifacts were caused by a change in position of water within the slice plane during the acquisition of an image.

The simulation of image artifacts included three main scenarios. Initial simulations focused on scenarios in which the object position depended upon the view, or rotational position, of the object. The scenarios in this category are feasible for the pseudo-third-generation geometry that is used by 3DID, as well as for the true-third-generation geometry. However, for the scenarios to occur with the pseudo-third-generation geometry, the motion of the fluid within the column must be periodic and synchronized with the period required for a subposition. For the second type of scenario, the object position depended upon the subposition. The scenarios of this type are not feasible for the true-third-generation geometry. The object position depended upon both view and subposition in the final category of scenarios.

The variations in the motion of fluid within the scan plane are expected to be random. The position of water is not anticipated to follow a line, or a curve, throughout the period of a scan. Therefore, the scenarios in which the object is located at one or more distinct positions are the focus of this discussion of image artifacts.

Two distinct types of artifacts were observed in the air-water contactor images, both exhibiting the ring-like behavior. The first artifacts were observed in images that contained static holdup, but no flow to or from the packed bed section. In the region of the artifacts, water was observed to appear or disappear in sequentially obtained images. The stationary transmission measurements confirmed that water did move into and out of the scan plane during measurements of a static-holdup condition in the contactor. The second type of artifacts were observed in the images of flow conditions. The artifacts were located within the entire region of the column and obscured the liquid flow regions in the images. Artifacts similar to both types were obtained from the simulations.

The artifacts observed in the image representing static holdup were presented in Figure 4-59. Similar artifacts appear in simulation case S1.4, shown in Figure 5-12(d), in which the position of one circle was dependent upon the subposition. Alternating streaks of bright and dark regions pass through the object position in both the CT image and the simulated image. The reproduction of the image artifact is support for the hypothesis that the change in position of the water causes the artifacts. The appearance of the artifact in a simulation in which the position depends upon subposition lends support to a hypothesis that the artifacts result from the combined effect of water movement and scanning method.

As the number of objects, and the number of positions of the objects, in the simulations increased, the pattern of concentric ring-like artifacts became more similar to the patterns observed in the CT images of the air-water contactor. In particular, the images from simulation Cases S2.3, S2.4, S2.7, and S2.8 resemble the ring-like artifacts presented in Figure 4-58. Although the streaks in the flow image are more numerous, the patterns are similar. Both bright and dark streaks are observed. In the flow images, the artifacts pass through regions that are brighter than the value attributed to the air region. Similarly, in the images from the simulations, the regions where the object was positioned during portions of the scan are brighter than the background.

The image artifacts in the simulations are located near the region in which the object was present. For example, in Case S2.4 shown in Figure 5-17(d), the artifacts only extended to a radius from the image center equal to the farthest circle. The circles were not located in the upper right corner of the image space for Case S2.7, and the artifacts do not extend into this region, as seen in Figure 5-19(c). The position of the objects was restricted to the third quadrant of the image for Case S2.10. Even though the artifacts extend slightly beyond the bounds of the quadrant, as seen in Figure 5-21(c), the artifacts are primarily contained within the section of the image in which the

circles were located. Based upon the observation that the location of artifacts correlates with the positions of the object, the water within the air-water contactor was located throughout the entire cross-sectional area.

Simulations in which the object position depended upon subposition resulted in the replication of both of the distinct types of artifacts observed in the air-water contactor images. With the stochastic nature of the flows within the column, the recommended approach to reducing the appearance of artifacts is by modifying the experimental method. The simulations performed in Cases C.1–4 provide support that the elimination of the use of subpositions, as required for the pseudo-third-generation geometry, results in the elimination of the ring-like artifacts. However, as the variation in flow pattern will still exist, artifacts due to the dependence on view are still observed. The artifacts of this type are characterized by linear streaks emanating from the position of the circle. However, artifacts of this type are not as dominant in the reconstructed image. As the object changes position more frequently during the acquisition of a scan, the artifacts become less apparent in the resulting image. Thus, for flow images obtained with a true-third-generation scanner, the possibility that water is present at each location for only a portion of the scan period must be considered, even in the absence of noticeable image artifacts.

6.2.2. Variability of Liquid Flow

The ordered nature of structured packing indicates that for well-distributed liquid, the flow is expected to be in the form of relatively stable films on the surface of the packing. In comparison to contactors containing random packing, less variation in the location of the liquid throughout the column is expected. However, variations in flow through a select cross section were measured in the air-water contactor.

The applications of x-ray CT to image a packed column at the University of Hannover [40][48][49][50] were performed at flow rates selected such that the liquid

flow was classified by the authors as stationary. The maximum liquid flow rate for the imaging studies reported was 30 m^3/m^2h, which corresponds to 12.3 gpm/ft^2 for the 200-mm-diameter column. No mention of image artifacts is made, which supports the hypothesis that the artifacts observed in this work would be eliminated if a true-third-generation scanner was used. However, based upon the variability of flow observed in this study within the range of flow rates used, the flows observed may not have been stationary during the 15-minute scan period at the University of Hannover.

Fluctuations in flow along select paths through the column at similar flow rates was observed in the stationary transmission measurements presented in this work. As observed in Figure 4-74, the attenuation was measured for a flow rate of 10.5 gpm/ft^2 along a fixed path over a period of five minutes, which is shorter than the time required to obtain the images at the University of Hannover. The measurements shown at three detectors are representative of fluctuations that are observed at each detector measuring attenuation through the column region.

As mentioned in the discussion of image artifacts, caution must be taken when interpreting flow images. The simulations indicated that all regions where the object was located are brighter than the background. Thus, a difference image may indicate the various positions of the liquid, but not necessarily the fraction of time spent in each position. Schmitz et al. [43, 44] report that a film was found over all surfaces of the metal structured packing. However, in consideration of the results from simulations, it is possible that the regions identified as water contained water for only a portion of the time required to acquire the image. Use of the sinograms to calculate holdup and validate the value obtained from the image would be beneficial. If the values do not match, further analysis may be required to determine whether the time-variant flow patterns are being accurately identified. In addition, further evaluation of scenarios in which water is present at known locations for portions of the scan period would

provide insight into accurately interpreting the CT images for non-stationary flow scenarios.

A shorter scan time will reduce the amount of variation in the position of the flows that occurs during a scan. As noted by Kantzas [24], images obtained from a three-second scan were time-averaged representations of the flow in a trickle bed and a fluidized bed. The images from the simulations shown in Figure 5-23(b) and (d) represent cyclical motion of the circles, at two different frequencies. The image in (d) captured fewer changes in position, thus represents a shorter scan time. However, the positions of the circles were not accurately represented. Therefore, for some patterns of motion, a shorter scan time may distort the shapes of the region of water.

6.2.3. Observation of Liquid Flow Patterns

The region of the packed bed between elements of structured packing has received increased attention in recent years. High-capacity packings that have modified surfaces at the bottom of each element have been introduced by packing vendors. The intent of the modified surface is to improve the distribution of the liquid to the element below and to reduce the accumulation of liquid at the joint between elements. The focus of the improvements is at flow conditions above the loading point, for which the liquid holdup has been measured to be higher at the bottom of each packing element.

The liquid distribution at the region of contact between the two elements of Mellapak 500Y structured packing was observed in this study. Even at the low air rates, which are characterized as below the loading point, a region of liquid was observed at the joint, but not at other elevations. Although the image artifacts were still present, water appeared to be present in the channels formed by the surfaces of the structured packing for a portion of the scan period, and perhaps for the entire period. The amount of the liquid was not quantified.

The accumulation of liquid in the bottom portion of the upper packing element was observed with the x-ray imaging technique, but likely would not have been observable with the use of gamma rays. The gamma-ray imaging techniques, such as that used in the work of Suess and Spiegel [59], involve the use of detectors that capture a slice with a thickness on the order of a centimeter. To measure an accumulation of liquid, the height of the liquid needs to be comparable to the size of the detector. In the x-ray CT images, the liquid was observed to fill the channels only within a fraction of a centimeter from the bottom of the packing element. The higher resolution attainable with x-ray CT due to the smaller detectors was required to observe this particular effect.

A combination of x-ray imaging techniques could be applied to observe flow behaviors of interest. One particular behavior of interest is the hydraulic flooding of a vapor-liquid contactor. The onset of flood typically begins at one location within the column, which could be monitored using the stationary transmission measurements. Often, the hydraulic limitation of the column is at the bottom of a packing element. The stationary transmission measurements provide a measure of the amount of liquid present, without requiring the reconstruction of an image. Such measurements can be used to monitor one elevation of the column, as flow rates are adjusted. At various stages on the approach to flood, as identified from the stationary transmission measurements, CT images could be obtained. The images would provide additional insights into the pattern of accumulation.

6.3. Requirements for the Imaging System

In spite of the challenges that must be overcome with the use of x-ray CT, the technique continues to be the most promising for quantifying parameters of an operating vapor-liquid contactor such as liquid holdup, liquid distribution, and

interfacial area. The spatial resolution of x-ray CT is in the range required to observe film flow in an image that contains few artifacts. In comparison to electrical capacitance tomography (ECT), the imaging system is more flexible. The imaging plane can be varied without repositioning sensors that are attached to the column. The cross section represented in an image can be varied in the axial direction by increments of 0.1 mm or smaller. Thus, variations in flow can be observed in both the axial and radial directions, with the acquisition of images of adjacent sections.

The quality of images obtained of an operating air-water contactor can potentially be improved with changes in the x-ray imaging technique. While some improvements are feasible with the existing x-ray CT systems operated by 3DID, other requirements are only possible if an alternate scanner is used. The imaging studies performed indicate characteristics desired for the x-ray source and detectors and for the method of acquiring transmission data.

The comparison of images of the phantoms obtained with the 101B+ scanner at the two different sets of scan parameters indicate that it is important to have a low level of noise in the images so that the air and water pixels can be distinguished. A reduction in the noise in the transmission measurements will result in a decrease in the level of noise in the images. The noise in each measurement is dependent upon the total number of x rays that are measured. When a larger number of x rays is incident on a detector, the noise level is decreased. Thus, the noise level depends upon both the time of each measurement, which is described by the snapshot time, and the effective area of the detector, which is described by the aperture. The level of noise was not optimized for any of the imaging studies performed in this work.

A quantitative comparison in measurement noise was made with the stationary transmission measurements of the air-water contactor using the 101B+ scanner. The measurements through the air region provided an indication of the noise resulting from both the source output and the detector response. The average standard deviation in

this region was $1.0x10^{-2}$ with the aperture set at 0.3 mm x 0.3 mm and $4.8x10^{-3}$ with the aperture set at 1.0 mm x 1.0 mm. The output of x rays from the source is assumed to be consistent as the energy level and x-ray filter were unchanged. The level of noise appeared to be comparable for the low-resolution images obtained with both scanners, as evidenced by the width of the peaks in the histograms. The aperture of the two scanners was the same; however, the snapshot time for the 101B+ scanner was more than twice that of the Alliant scanner. Without knowledge of the output of x rays from the source of each scanner, the noise levels can not be quantified.

A reduction in the measurement noise can be made without adjusting the pixel size in a reconstructed image from the 101B+ scanner by increasing the vertical aperture of the detectors. The aperture of the detectors is adjustable in both the vertical and horizontal directions, independent of each other, as was shown in Figure 3-2. An increase in the vertical aperture would increase the number of x rays incident on the detectors, thus decreasing the level of noise. The scan time would not change, if the horizontal aperture and snapshot time were not varied. However, an image would represent a larger vertical slice of the object. Other options to reduce the measurement noise include altering the snapshot time, which will influence the time required to obtain an image, and adjusting the horizontal aperture, which will influence the spatial resolution.

A high-energy source, such as that of the 101B+ scanner, must be used to reduce the effect of beam hardening on quantitative analysis of the conditions within the column. A significant difference between the two CT scanners used for the experimental studies is the energy level of the x rays. A negative consequence of using the Alliant scanner, which contains the 320kV source, was the appearance of beam-hardening effects in the scans of the film apparatus completely filled with water. The effect on the images was primarily within the metal pipe, and thus the calculation of the film thickness from the images was not adversely affected. However, the

calculations based upon the sinograms did not accurately predict the amount of water present in the column as a result of the beam hardening. For the calculations from the sinogram to accurately represent liquid holdup or void fraction, the x-ray beam must not be significantly hardened after passing through the column filled with water and the packing material.

The rotation of the column, rather than the source and detectors, during a scan should be eliminated if the option exists. The current sequence of motion during a scan influences both the scan time and possibly the flow patterns. The time required to obtain an image is increased when the tubing through which the liquid and air flow is connected to the column. The unwind sequence is incorporated to prevent the tubing from becoming entwined. Thus, the scan time is increased by the total amount of time that is required to rotate the column in the negative direction. Visual observations of the flows in the column during the movement sequence required for a scan indicated that the change in rotational direction did not affect the flows at the wall. However, if the column were kept stationary, no question would exist regarding potential effects on the flow patterns within the column that are observed in the x-ray CT images.

Eliminating the need for subpositions by using a scanner with a continuous detector array will result in images that can be analyzed more accurately. The results of the computer simulations indicate that the use of subpositions with the pseudo-third-generation scanner geometry contributes significantly to the appearance of the ring-like image artifacts. The artifacts observed in images reconstructed for scenarios in which the object position depended on view contain streak artifacts. However, the streak artifacts do not obscure the regions of the objects as significantly as the ring-like artifacts do.

CHAPTER 7: CONCLUSIONS AND RECOMMENDATIONS

7.1. Summary of Conclusions

Experimental studies and computer simulations were performed to evaluate the potential of x-ray imaging to quantify the hydraulic characteristics of a vapor-liquid contactor. To predict the performance of a column, the parameters of interest in this study were liquid holdup, interfacial area, and liquid distribution. These three variables affect both the hydraulic and mass-transfer performance of vapor-liquid contactors, such as those used in distillation applications. The identification of liquid in images of the column is instrumental in quantifying the parameters, which can be subsequently used to develop more rigorous predictive models. The conclusions from these studies can be categorized as: (1) requirements for the CT scanner, (2) comments on methods of evaluation, and (3) observations of flow behavior.

The characteristics desirable of an x-ray CT scanner were further refined based upon the results of the imaging studies. Two x-ray CT scanners were used for the experimental studies involving the phantoms, the film-flow apparatus, and the air-water contactor. The method of acquiring data to reconstruct an image was the same for the two scanners, although the characteristics of the source and detectors were different. The difference in energy level between the two scanners was observed to be significant. The use of two apertures for the detectors on the 101B+ scanner led to an important observation regarding measurement noise. Conclusions that pertain to the x-ray scanner are:

- The level of the noise in the transmission measurements must be considered in addition to spatial and temporal resolution. Accurate

differentiation between regions of air and water in the reconstructed image is not feasible with a high level of noise.

- The energy level of the x-ray source must be higher than 320kV when passing through the material equivalent to a 0.12"-thick 3.5"-diameter stainless-steel pipe filled with water. The beam hardening observed with the 320kV x-ray source of the Alliant scanner affected the precision of the measurement of film thickness.
- The use of subpositions must be eliminated to remove the ring-like artifacts observed in images of time-variant flow. The artifacts obscured the regions of water in the images of flow through the air-water contactor. The computer simulations were used to reproduce the artifacts and to show an improvement when the subpositions were not required.
- A decrease in the scan time will still result in a time-averaged image; however, less variation in the position of flow will be captured.

The first two characteristics can be achieved with the existing 101B+ scanner operated by 3DID. However, a scanner with a continuous detector array would be required to obtain a CT image without the use of subpositions. Eliminating the need for subpositions would decrease scan time, but additional advances in CT systems could result in further reductions in scan time.

The objectives of the studies performed included evaluating methods to analyze the data from the CT scans. The local amount of liquid present at a specified elevation was calculated directly from the transmission measurements, rather than from the reconstructed image, for images of the three experimental systems. The sinograms were used to calculate the percent water present with less than ten percent variation from expected values for conditions of as little as 0.3% water and as much as 25% water. The computer simulations performed indicate that if an object is present in

two locations during the period of a scan, both regions are represented in the CT image. The CT images of time-variant flow conditions contained artifacts that interfered with further analysis. However, the presence of regions of values between those of air and water does not necessarily imply that water was present in those regions for the entire period. Regarding methods of interpreting scan data, it can be concluded that:

- the liquid holdup can be calculated from the sinogram data with less than 10% error for liquid present as large regions or as thin films, and
- identification of regions of water that were present for portions of a scan must be further investigated.

The observations related to the identification of the location of water for the flow studies were performed with transmission measurements and CT images. The focus of the film-flow apparatus studies was to determine how thin a film could be identified. In spite of the image artifacts present in images of the air-water contactor, a qualitative evaluation of the region near the joint between two elements of structured packing was feasible. The major conclusions from these studies are:

- films with thicknesses in the range 0.24–0.37 mm were measured and identified in CT images of the film-flow apparatus that had a pixel size of 0.34 mm,
- the distribution of liquid along various paths through the contactor was observed at all flow rates, even those previously classified as stationary, and
- images of the air-water contactor indicate that accumulation of liquid occurs at the joint between elements at flow rates below the loading point.

7.2. Recommendations for Future Study

The use of x-ray imaging techniques continues to have promise of measuring hydraulic parameters important in predicting the performance of a vapor-liquid contactor at a local scale. The recommendations for future study fall into two categories: the studies that can be performed with the existing scanner, and the studies that require the use of an alternate scanner.

7.2.1. Studies With the Scanner at 3DID

The use of the 3DID scanner for time-variant flows is limited to the evaluation of transmission data. The transmission data can be either that obtained from a stationary position or that obtained in the form of a sinogram. When using sinograms for other than the purpose of calculating a reconstructed image, the size of the sinogram is not limited by requirements that exist when the purpose is to reconstruct a quality CT image. The studies that are recommended include:

- Measurement of both the void fraction and the liquid holdup at multiple elevations with the use of sinogram data, and subsequent comparison of the average of the local holdup values to the column-average holdup.
- Operation of the air-water contactor at rates up to the flood point, while monitoring operation with the stationary transmission measurements and periodically calculating the liquid holdup throughout the packed bed.
- Comparison of flow behavior, including the local liquid holdup, between a column containing structured packing with and without modifications intended to increase the hydraulic capacity.

7.2.2. Studies That Require the Use of an Alternate Scanner

The major limitation of the scanners used in this study was the use of subpositions as required for the pseudo-third-generation scan geometry. The use of an alternate scanner that does not require subpositions has the potential of identifying films of liquid on the surface of the packing. The prominence of image artifacts must be reduced if the film thickness on packing surfaces is to be identified, and subsequently quantified.

In addition to the studies recommended with the existing scanner, the studies recommended with a new scanner include:

- Evaluation of images that include regions of water for a portion of a scan, with the use of controlled time-variant flows through the column.
- Varying the physical properties of the fluids, e.g. decrease surface tension, to determine the dependence of hydraulic parameters on fluid properties.

APPENDIX A: GEOMETRY OF PHANTOMS AND CALCULATION OF PERCENT WATER

A.1. Geometry of Phantoms

The side view of each of the phantoms is shown in Figure A-1. The actual measurements of the length of metal surfaces and the angles between surfaces are annotated on the sketches. Phantoms 2 and 3 were designed to be identical. However, as the measurements indicate there are some minor differences. The design width of each phantom was 5/8-inch plus the two 1/8-inch thick acrylic walls. The actual dimensions of each acrylic section is listed in Table A-1. Figure A-2 represents how the walls were constructed and identifies the dimensions specified.

Table A-1: Length and Area of the Acrylic Walls of the Phantoms*

Object	Front (in)	Back (in)	Right (in)	Left (in)	Area (in^2)
Phantom 1	2.67	2.66	n/a	n/a	0.64
Phantom 2	2.38	2.39	0.91	0.91	0.79
Phantom 3	2.39	2.38	0.92	0.91	0.79
Phantom 4	3.06	3.06	0.89	0.90	0.95

* The width of all acrylic sections is 0.12 inches.

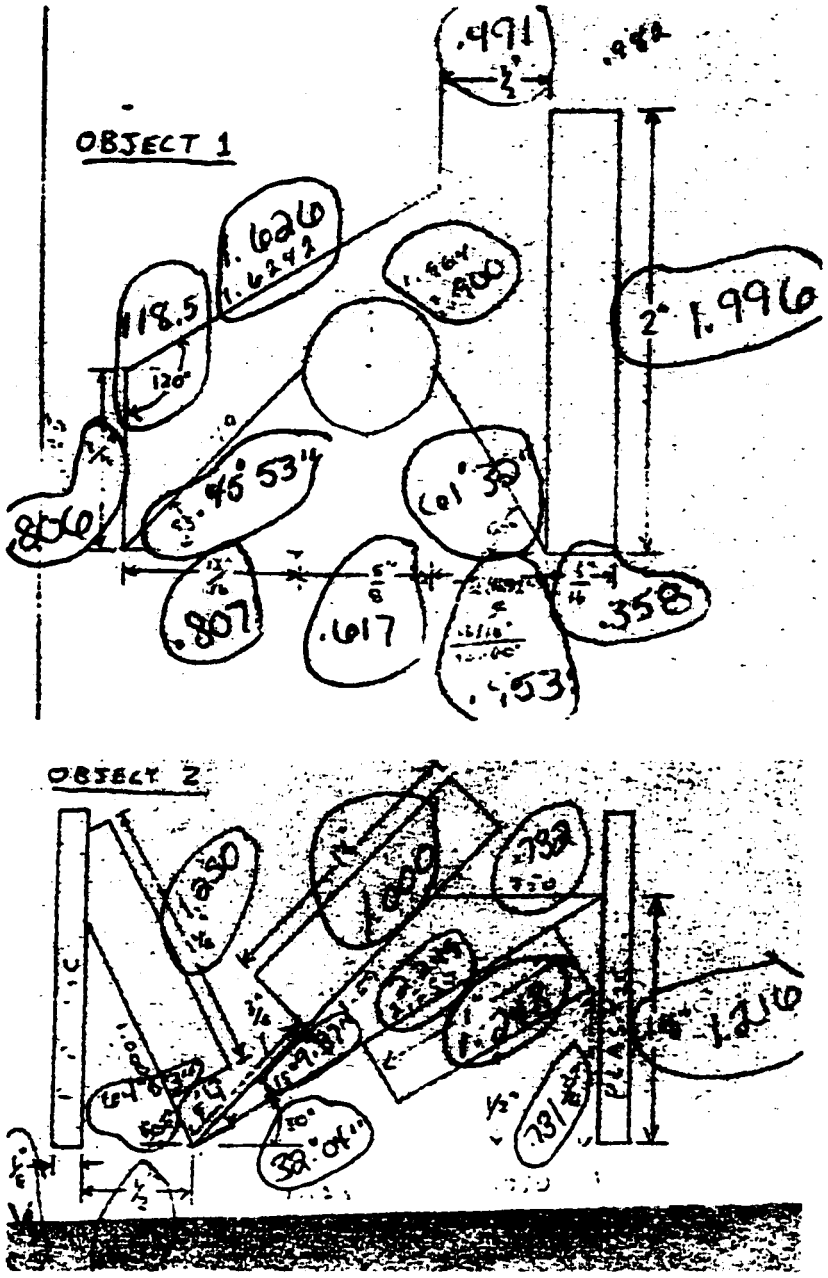

Figure A-1. Actual dimensions of the phantoms.

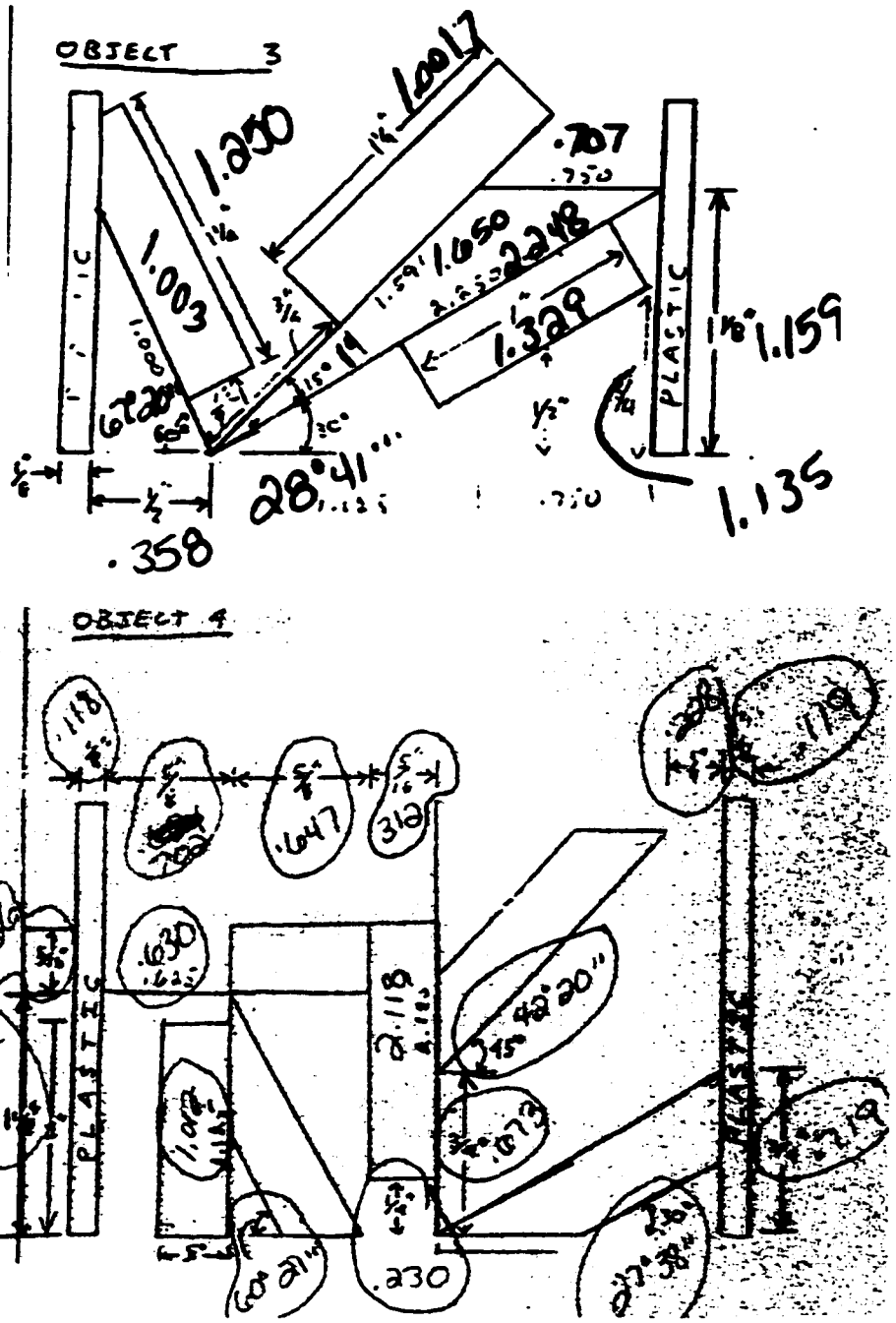

Figure A-1 (cont.) Actual dimensions of the phantoms.

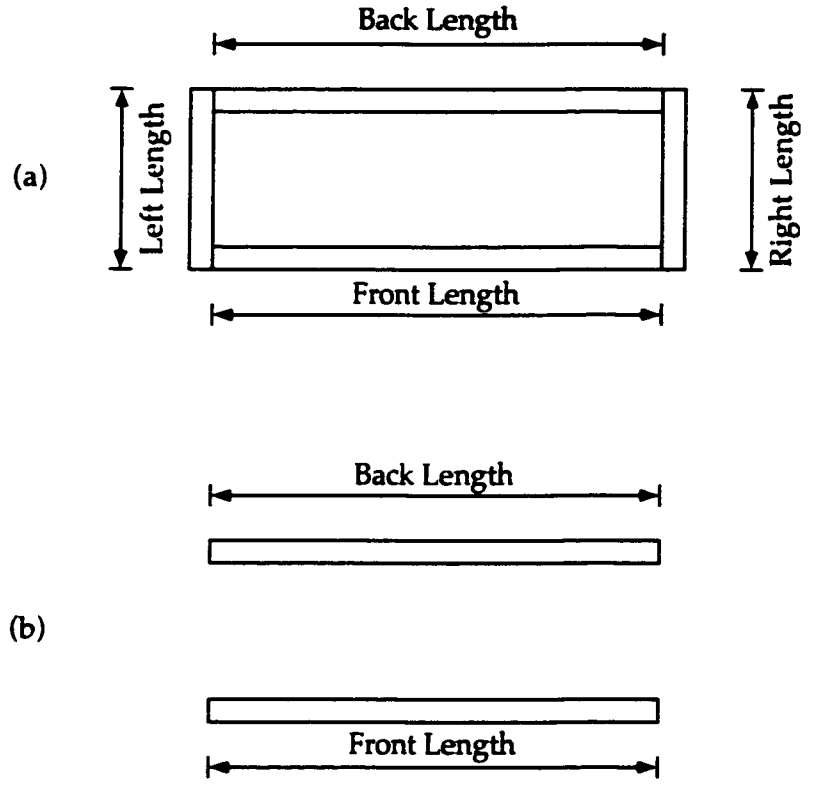

Figure A-2. Top view of the phantoms indicating the layout of the acrylic walls with dimensions labelled. (a) walls for Phantoms 2, 3, 4. (b) walls for Phantom 1.

A.2. Calculation of Expected Water for 101B+ Scans

The phantoms contained water in selected regions during the CT scans on the 101B+ scanner. When the thin metal surface was located within a region of water, the volume of it was neglected when calculating the volume of the water. In addition to scans of the phantoms with water in the desired regions, scans were performed with

the phantoms dry and with both the phantoms and column flooded. The dry and flooded scans represent the minimum- and maximum-water conditions, respectively.

A.2.1. Calculation of Void Volume at 101B+ Scan Elevations

The void volume was calculated for each of the elevations at which dry and flooded scans were obtained. For these calculations, the void volume is assumed to be constant over the small thickness of the scan. Thus, the measurements are discussed in terms of area, which is consistent with the two-dimensional nature of the images. The total area within the column is calculated using the known inner diameter of 5.75 inches, resulting in an area of $\pi((5.75 \text{ in})/2)^2$ or 26.0 in^2. The area of the acrylic walls was then subtracted from this total area to obtain a value for the total possible void area. Finally, regions of the maximum-water condition scans that did not contain water were subtracted from the total area. These regions existed at elevations of 140.3 and 140.9 mm, as shown in Figure A-3. A small region containing an air bubble was neglected.

The contribution of each of the dry regions to the reduction in void area is calculated from the known geometry of the phantoms. The region of Phantom 4 that is always dry is a rectangular region. The length of the region is 0.63 in and the width of the region is 0.625 in. The resulting area of 0.394 in^2 is subtracted from the total area. The region of Phantom 3 that is never full of water has a length of 0.707 in and a width of 0.625 in. The area of this region is 0.442 in^2. At the elevation 140.9 mm, half of this region is filled with stainless steel, thus only half never contains water. The region of Phantom 1 that always is comprised of air is the segment under the curved surface that is horizontal. The geometry of this section is described in Figure A-4. The expression used to calculate the area is shown by Equation A-1. The elevation of the scan is represented by z. The elevation of the center of the circle, z_c, was determined

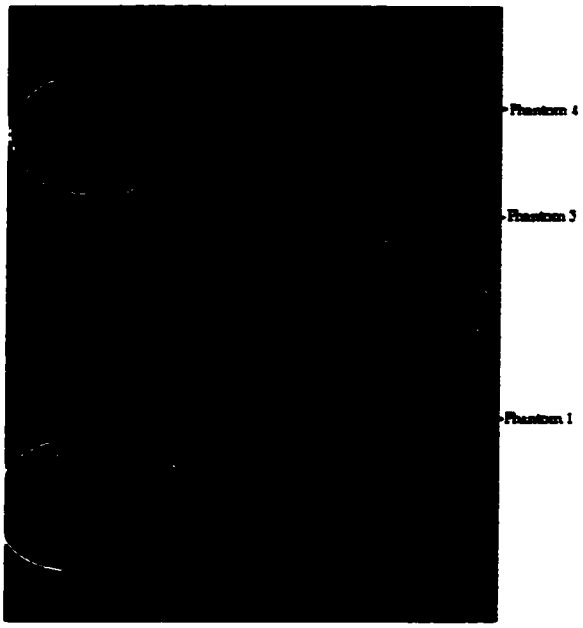

Figure A-3. Regions of the 101B+ scans that did not contain water. Section of the image obtained at 140.3 mm elevation is shown.

to be 133.6 mm from the radiogram. The calculated void areas are shown in Table A-2.

[A-1] $$A = WL_c = (0.625\text{in})\left(2\sqrt{(0.309\text{in})^2 - \left[\frac{z - z_c}{25.4\text{mm/in}}\right]^2}\right)$$

A.2.2. Calculation of Percent Water Present

The percent of the void area that is filled with water is calculated for each elevation. The calculations are performed for both the high- and low- resolution scans. The area of water is calculated from the known geometry of the phantoms,

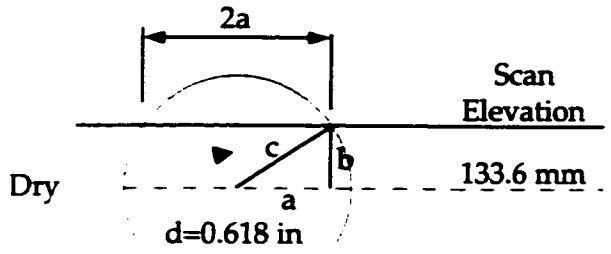

$c = 0.309$ in

$b = (\text{Scan Elevation}) - 133.6$ mm

$a = (c^2-b^2)^{0.5}$

Figure A-4. Geometry of the region of Phantom 1 that does not contain water with elevations defined for the 101B+ scans.

Table A-2: Void Areas of the Phantoms Calculated for the 101B+ Scans

Scan Elevation (mm)	Void Area (in^2)
140.3	21.8
140.9	22.0
141.5	22.8
142.1	22.8
142.7	22.8
144.5	22.8

similar to the calculation of void area. For the 101B+ scans, the phantoms were scanned with one partial water condition.

At the elevations of interest, water was present in Phantoms 1, 3 and 4. The water in Phantom 3 was determined from the length and width of the region created by the acrylic walls. The presence of the thin stainless steel within this region was

neglected. This area is calculated as 1.49 in^2. Similarly, the water in Phantom 4 was in rectangular sections. Based upon the measured geometry of the phantoms, the length of the water section was 2.36 inches for elevations 141.5 mm or less and 3.06 inches for elevations greater. The resulting areas are 1.47 and 1.91 in^2, respectively. Water was present in Phantom 1 for the scans that were below an elevation of 143.3 mm for the high-resolution scans and 141.5 mm for the low-resolution scans. The variation was due to leakage of water from the phantom during scanning. The region of water was calculated from the geometry described in Figure A-5. For the elevations that contained air regions, the area calculated above was subtracted from the water area. The area of the water calculated at each scan elevation is listed in Table A-3.

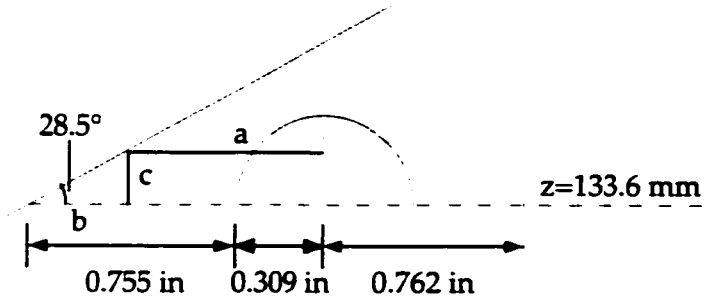

$$c = (\text{Scan Elevation}) - 133.6 \text{ mm}$$

$$b = c \,/\, \tan(28.5°) = 1.84\, c$$

$$a = 1.064 - b$$

Figure A-5. Geometry used to calculate the region of water present in Phantom 1 at some elevations.

A.3. Calculation of Expected Water for Alliant Scans

For the CT scans performed with the Alliant Scanner, the phantoms either were completely full of water or contained no water. The volume of the thin metal surfaces

Table A-3: Volume of Water Calculated at Scan Elevations of 101B+ Scans

Scan Elevation (mm)	Water Area – High Resolution (in^2)	Water Area – Low Resolution (in^2)
140.3	3.6	3.6
140.9	3.6	3.6
141.5	3.7	3.4
142.1	4.2	3.4
142.7	4.1	3.4
144.5	3.4	3.4

was neglected when calculating the water volume. The first set of scans was performed with no water in any of the phantoms, and will be used as the measure of the minimum-water condition. The second set of scans was performed with Phantom 2 filled with water. Both Phantom 2 and Phantom 4 were filled with water for the third set of scans. Prior to the fourth set of scans, water was added to Phantom 3. The scans at the upper elevations in the fifth set of scans were identical to those in the fourth set. However, the scans at the lower elevations contained water in Phantom 1 in addition to the water present in the fourth set. The final set of scans contained water in all regions of the phantoms and the column that was defined as void. There are several regions that are sealed and thus can not be filled with water.

A.3.1. Calculation of Void Volume at Each Elevation

The void volume was calculated for each of the 18 scan elevations. These calculations are discussed in terms of the area of the cross section. The void area for each elevation is listed in Table A-4. The absolute elevation measurements do not correspond to the same elevation of the phantoms as for the 101B+ scans, as a result of

differences in the scanners. The total area within the column is calculated using the known inner diameter of 5.75 inches. Thus, the area is $\pi((5.75\text{ in})/2)^2$ or 26.0 in^2. The area of the acrylic walls of the four phantoms was then subtracted from this total area to obtain a value for the total possible void area. For nine of the elevations, additional adjustment to the void volume was required. At these elevations, there were regions that did not contain water in the scan of the maximum-water condition.

Table A-4: Void Area Calculated for Scan Elevations of the Alliant Scans

Scan Elevation (mm)	Void Area (in^2)
127.0	21.3
127.5	21.3
128.0	21.3
129.5	21.5
142.0	22.2
142.5	22.2
143.0	22.2
143.5	22.8
144.0	22.8
144.5	22.8
145.0	22.8
145.5	22.8
146.0	22.8
146.5	22.8
147.0	22.8
147.5	22.8

At scan elevations 142.0, 142.5, and 143.0 mm, there is a region in Phantom 1 and a region in Phantom 4 that never contain water. A section of the CT scan showing these regions without water is shown in Figure A-6. The area of the region in Phantom 4 is a rectangular region with a length of 0.63 inches and a width of 0.625 inches, for a total area of 0.394 in^2. The area of the region in Phantom 1 depends upon the length of a chord through a circular segment. Figure A-7 depicts the geometry of this region. The elevation of the center of the circle was determined to be 136.0 mm from the radiogram. The expression used to calculate the region that is always dry was previously represented by Equation A-1, with z representing the scan elevation.

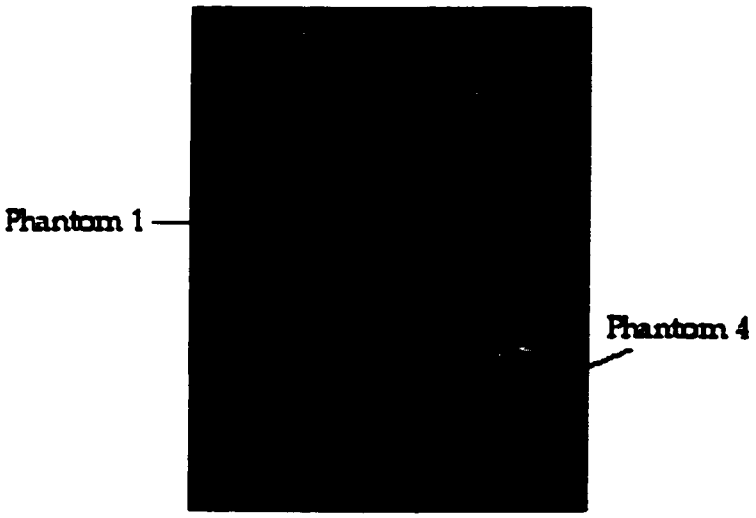

Figure A-6. Region of CT image at 142.5 mm elevation depicting the regions of Phantoms 1 and 4 that never contain water.

At the lower scan elevations (127-129.5 mm), regions in which there is always air exist in Phantoms 1 and 4. A CT scan showing these regions without water is presented in Figure A-8. The calculation of the entire area is comprised of three

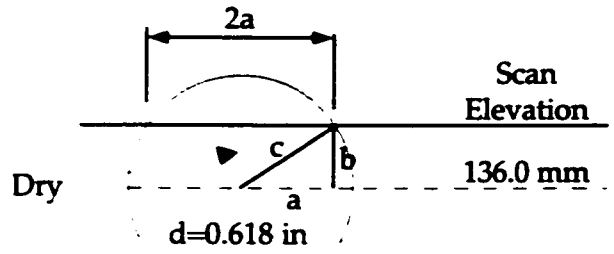

$c = 0.309$ in
$b = (\text{Scan Elevation}) - 136.0$ mm
$a = (c^2 - b^2)^{0.5}$

Figure A-7. Geometry of the region of Phantom 1 at elevations 142.0, 142.5, and 143.0 that is always dry.

separate regions. The first region is the region of Phantom 4 consisting of a rectangle and a half circle. This area is calculated by Equation A-2. The second region is comprised of a rectangle in Phantom 1 for which the length depends upon the scan elevation. The geometry associated with this calculation is shown in Figure A-9. The elevation of the base of the triangles was determined to be 114.6 mm from the radiogram. The calculation of the area of this region is specified by Equation A-3, with z again representing the scan elevation. The quantity of metal within this region was not negligible for elevations 128.5 and 129.0 mm, thus the total void area was not calculated. The remaining region of Phantom 4 was calculated for the segment of the ellipse that does not contain water. The geometry of the ellipse is defined in Figure A-10. The area of a segment of an ellipse is given by Equation A-4. The value for h was estimated for each elevation from the CT image.

[A-2] $$A = (0.625\text{in})(0.63\text{in}) + \pi(0.313\text{in})^2$$

[A-3] $$A = (0.625\text{in})[1.04(0.776\text{in} - z') + 0.617\text{in} + 0.542(0.835\text{in} - z')]$$

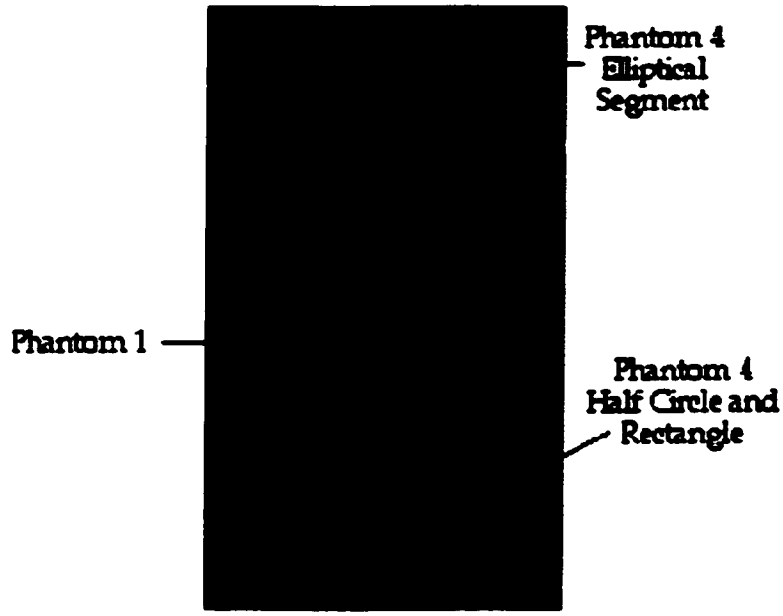

Figure A-8. Regions of Phantoms 1 and 4 at the lower elevations that always contain air. CT scan at 127 mm is shown.

$$\text{where } z' = \frac{z - 114.6\text{mm}}{25.4\text{mm/in}}$$

[A-4] $$A = \frac{a}{b}\left(h\sqrt{b^2 - h^2} + b^2 \operatorname{asin}\frac{h}{|b|} + \frac{\pi}{2}b^2\right)$$

A.3.2. Calculation of Percent Water at Each Elevation

The percent water present at each elevation was determined by dividing the area of the water by the void area. The volume of water at each elevation is calculated using the known geometry of the phantoms. Again, these calculations are discussed in terms of the area of the cross section. Calculations are required for each of the four

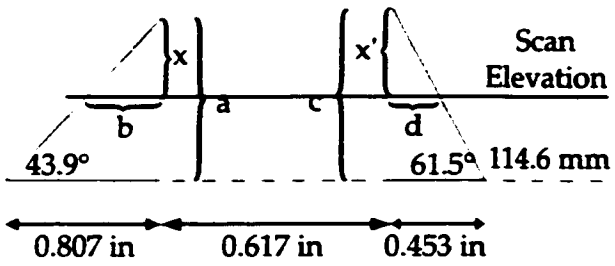

$a = 0.807in * \tan(43.9°) = 0.776$ in

$x = a - [(\text{Scan Elevation}) - 114.6\text{ mm}]$

$b = x/(\tan 43.9°) = 1.04\,x$

$c = 0.453in * \tan(61.5°) = 0.835$ in

$x' = c - [(\text{Scan Elevation}) - 114.6mm]$

$d = x'/(\tan 61.5°) = 0.542\,x'$

Figure A-9. Geometry defining length of the rectangular region of Phantom 1.

sets of images that were obtained. A summary of the volume of water at each elevation under the four conditions is provided in Table A-5.

The first region of water that was filled was the entire region of Phantom 2. The area of this region is that of a rectangle, still assuming the volume of the metal in the region to be small in comparison to the entire region. Based upon the measurements of the acrylic walls shown in Table A-1, the area of this region is 1.60 in^2.

Phantom 4 was next filled with water which increased the total water present. In the upper range of elevations, the region filled was a rectangle. For elevations 142.0 mm through 144.0 mm, the area of the region was 1.60 in^2. For the other elevations in the upper range, the area was 2.02 in^2. For the lower range of elevations,

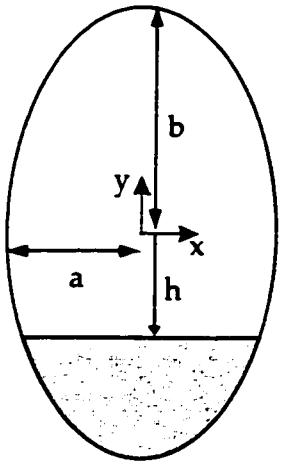

Ellipse: $x^2/a^2 + y^2/b^2 = 1$

$a = 0.625$ in

$b = 0.625 \sin(27.6°) = 1.35$ in

Figure A-10. Geometry defining segment of the elliptical region of Phantom 4.

this total area of 2.02 in^2 was reduced by the area that never contains water that was calculated previously.

The volume of water present in Phantom 3 was constant for all elevations. The amount is calculated with the use of the dimensions of the acrylic walls. The area of the region is identical to that of Phantom 2, 1.60 in^2.

For the fourth set of scans, water was added only to the lower region of the Phantom 1. Thus, the conditions of the phantoms at the upper elevations were the same as for the third set of scans. The water present at the lower elevations was calculated based upon the large rectangular region and the small half circle. The area of the region that never contains water was subtracted.

Table A-5: Volume of Water in the Scan Plane for Each Set of Scans

Elevation (mm)	Set 1 (in^2)	Set 2 (in^2)	Set 3 (in^2)	Set 4 (in^2)
127.0	1.60	2.74	4.34	5.23
127.5	1.60	2.77	4.37	5.28
128.0	1.60	2.80	4.40	5.32
129.5	1.60	2.95	4.55	5.54
142.0	1.60	3.21	4.81	4.81
142.5	1.60	3.21	4.81	4.81
143.0	1.60	3.21	4.81	4.81
143.5	1.60	3.21	4.81	4.81
144.0	1.60	3.21	4.81	4.81
144.5	1.60	3.62	5.22	5.22
145.0	1.60	3.62	5.22	5.22
145.5	1.60	3.62	5.22	5.22
146.0	1.60	3.62	5.22	5.22
146.5	1.60	3.62	5.22	5.22
147.0	1.60	3.62	5.22	5.22
147.5	1.60	3.62	5.22	5.22

APPENDIX B: DERIVATION OF EXPECTED FILM THICKNESS

The film-flow apparatus and the coordinate system used for development of the expression to relate film thickness and volumetric flow rate is shown in Figure B-1.

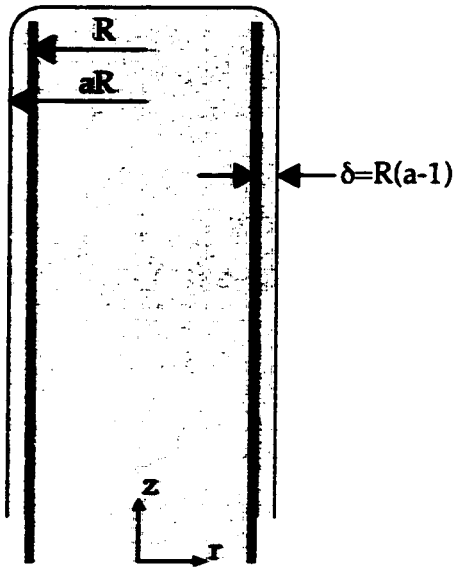

Figure B-1. Coordinate system for film apparatus

The first step in the calculation of the expected film thickness is to determine the velocity of the fluid within the film. The momentum balance is described by the Navier-Stokes equation as expressed in Equation B-1. The boundary conditions for the system shown in Figure B-1 are described by Equation B-2 and Equation B-3. The

use of the second boundary condition involves the assumption of Newtonian flow in the system.

[B-1] $$\rho\frac{Dv}{Dt} = -\nabla p + \mu\nabla^2 v + \rho g$$

[B-2] B.C. 1: $v_z = 0$ at $r = R$

[B-3] B.C. 2: $\tau_{rz} = -\mu\dfrac{dv_z}{dr} = 0$ at $r = aR$

The z-component of Equation B-1 is simplified and expressed in cylindrical coordinates in Equation B-4. The left side of the equation is reduced to zero with three assumptions. The first is that steady state flow occurs. The second assumption is that the flow velocity is zero in both the radial (r) and azimuthal (θ) directions. The final assumption is that the velocity in the axial direction can be expressed as a function of r only, as described by Equation B-5. The right side of the equation is simplified with the aforementioned assumptions and the lack of a pressure gradient in the axial direction. The momentum balances in the radial and azimuthal directions reduce to $0 = 0$.

[B-4] $$0 = \frac{\mu}{r}\frac{d}{dr}\left(r\frac{dv_z}{dr}\right) + \rho g_z$$

[B-5] $$v_z = v_z(r)$$

Integration of Equation B-4 with respect to r twice results in Equation B-7 which contains two unknowns, C_1 and C_2. These unknowns are determined by applying the two boundary conditions, as shown, resulting in the velocity profile expressed in Equation B-9.

$$d\left(r\frac{dv_z}{dr}\right) = -\frac{\rho}{\mu}g_z\, r dr$$

$$r\frac{dv_z}{dr} = -\frac{\rho g_z}{2\mu}r^2 + C_1$$

[B-6] $$\frac{dv_z}{dr} = -\frac{\rho g_z}{2\mu}r + \frac{C_1}{r}$$

[B-7] $$v_z = -\frac{\rho g_z}{4\mu}r^2 + C_1 \ln r + C_2$$

Applying B.C. 2 to Equation B-6:

$$0 = -\frac{\rho g_z}{2\mu}aR + \frac{C_1}{aR}$$

[B-8] $$C_1 = \frac{\rho g_z}{2\mu}a^2R^2$$

The value of the second constant, C_2, is determined by substituting the value of C_1, expressed in Equation B-8, and applying the second boundary condition. The velocity profile for the film flowing down the exterior surface is then expressed as shown in Equation B-9.

$$0 = -\frac{\rho g_z}{4\mu}R^2 + \frac{\rho g_z}{2\mu}a^2R^2 \ln R + C_2$$

$$C_2 = \frac{\rho g_z}{2\mu} R^2 \left(\frac{1}{2} - a^2 \ln R \right)$$

[B-9] $$v_z = \frac{\rho g_z R^2}{4\mu} \left(1 - \left(\frac{r}{R} \right)^2 + 2a^2 \ln \frac{r}{R} \right)$$

Integration of the velocity profile determined for the exterior surface is equivalent to the volumetric flow rate, as expressed in Equation B-10. The final expression relating theory-predicted film thickness to the volumetric flow rate and properties of the fluid is shown in Equation B-12.

[B-10] $$Q = \int_0^{2\pi aR} \int_R v_z(r) r dr d\theta$$

$$Q = \int_0^{2\pi aR} \int_R \left[\frac{\rho g_z R^2}{4\mu} \left(1 - \left(\frac{r}{R} \right)^2 + 2a^2 \ln \frac{r}{R} \right) \right] r dr d\theta$$

$$Q = \frac{\pi \rho g_z R^2 aR}{2\mu} \int_R \left(r - \frac{1}{R^2} r^3 + 2a^2 r \ln \frac{r}{R} \right) dr$$

$$Q = \frac{\pi \rho g_z R^2}{2\mu} \left(\frac{1}{2} a^2 R^2 - \frac{1}{2} R^2 - \frac{a^4 R^4}{4R^2} + \frac{R^4}{4R^2} + 2a^2 \int_R^{aR} r \ln \frac{r}{R} dr \right)$$

[B-11] $$Q = \frac{\pi \rho g_z R^2}{2\mu} \left(\frac{a^2 R^2}{2} - \frac{R^2}{4} - \frac{a^4 R^2}{4} + 2a^2 \int_R^{aR} r \ln \frac{r}{R} dr \right)$$

The integral remaining in Equation B-11 can be evaluated using the integration by parts method, as shown below. Simplification of the resulting expressions results in the expression in Equation B-12.

$$\int_R^{aR} r \ln\frac{r}{R} dr = \left(\frac{1}{2} r^2 \ln\frac{r}{R}\right)\Bigg|_R^{aR} - \frac{1}{2}\int_R^{aR} r\,dr$$

$$\int_R^{aR} r \ln\frac{r}{R} dr = \frac{1}{2}a^2R^2 \ln\frac{aR}{R} - \frac{1}{2}R^2 \ln\frac{R}{R} - \frac{1}{4}a^2R^2 + \frac{1}{4}R^2$$

$$\int_R^{aR} r \ln\frac{r}{R} dr = \frac{1}{2}a^2R^2 \ln a - \frac{1}{4}a^2R^2 + \frac{1}{4}R^2$$

$$Q = \frac{\pi\rho g_z R^2}{2\mu}\left(\frac{a^2R^2}{2} - \frac{R^2}{4} - \frac{a^4R^2}{4} + 2a^2\left(\frac{1}{2}a^2R^2 \ln a - \frac{1}{4}a^2R^2 + \frac{1}{4}R^2\right)\right)$$

[B-12] $$Q = \frac{\pi\rho g_z R^4}{2\mu}\left(-\frac{3a^4}{4} + a^2 - \frac{1}{4} + a^4 \ln a\right)$$

APPENDIX C: VARIABLES SPECIFIED FOR COMPUTER SIMULATIONS OF X-RAY CT

Table C-1. Parameters Specified for the Simulations of a Revolving Circle

Parameter	Case R.1	Case R.2	Case R.3
Original Center of Circle	[405.,256.]	[378.,341.]	[127.,182.]
Relative Revolution Speed	2./3.	7./36.	-4./9
Radius of Circle	5	5	5
Value Within Circle	225	225	225

Table C-2. Parameters Specified for the Simulations of Motion Along a Line

Parameter	Case L.1	Case L.2	Case L.3	Case L.4
Original Center of Circle	[96, 163]	[163, 400]	[412, 412]	[400, 100]
Slope of Line	1.	-1.	1./2	-1.
Length of Line	300	200	-200	50
Radius of Circle	5	5	5	5
Value Within Circle	225	225	225	225

Table C-3. Parameters Specified for the Simulations of Flipping Object Position

Parameter	Case F.1	Case F.2	Case F.3
Centers of Circles	[128, 128], [178, 178]	[128, 128], [178, 178]	[128, 128], [178, 178]
Flip Cycle	128	32	8
Radius of Circle	20	20	20
Value Within Circle	225	225	225

Table C-4. Parameters Specified for the Simulations of a Bad Detector

Parameter	Case E.1	Case E.2
Centers of Circle	[128, 128]	[256, 256]
Fractional Error	0.5	0.5
Spacing of Error	8	8
Radius of Circle	20	20
Value Within Circle	225	225

Table C-5. Simulations with One Circle Per Subposition, Two Fixed Positions

Parameter	Case S1.1	Case S1.2	Case S1.3	Case S1.4
Array 1: Position Radius, Value	[128, 128] 15, 150	[128, 128] 15, 0	[128, 128] 15, 150	[128, 128] 15, 150
Array 2: Position Radius, Value	[178, 178] 15, 150	[178, 178] 15, 150	[178, 178] 15, 0	[128, 128] 15, 150
Array 3: Position Radius, Value	[128, 128] 15, 150	[128, 128] 15, 0	[128, 128] 15, 150	[178, 178] 15, 0
Array 4: Position Radius, Value	[178, 178] 15, 150	[178, 178] 15, 150	[178, 178] 15, 0	[178, 178] 15, 0
Array 5: Position Radius, Value	[128, 128] 15, 150	[128, 128] 15, 0	[128, 128] 15, 150	[128, 128] 15, 150
Array 6: Position Radius, Value	[178, 178] 15, 150	[178, 178] 15, 150	[178, 178] 15, 0	[128, 128] 15, 150
Array 7: Position Radius, Value	[128, 128] 15, 150	[128, 128] 15, 0	[128, 128] 15, 150	[178, 178] 15, 0
Array 8: Position Radius, Value	[178, 178] 15, 150	[178, 178] 15, 150	[178, 178] 15, 0	[178, 178] 15, 0

Table C-6. Simulations with One Circle Per Subposition, Motion Centered

Parameter	Case S1.5	Case S1.6	Case S1.7	Case S1.8
Array 1: Position Radius, Value	[100, 412] 15, 150	[100, 412] 15, 150	[100, 412] 15, 150	[100, 412] 15, 150
Array 2: Position Radius, Value	[100, 412] 15, 150	[100, 100] 15, 150	[100, 100] 15, 150	[35, 256] 15, 150
Array 3: Position Radius, Value	[100, 100] 15, 150	[412, 100] 15, 150	[412, 100] 15, 150	[100, 100] 15, 150
Array 4: Position Radius, Value	[100, 100] 15, 150	[412, 412] 15, 150	[412, 412] 15, 150	[256, 35] 15, 150
Array 5: Position Radius, Value	[412, 100] 15, 150	[100, 412] 15, 150	[256, 362] 15, 150	[412, 100] 15, 150
Array 6: Position Radius, Value	[412, 100] 15, 150	[100, 100] 15, 150	[150, 256] 15, 150	[477, 256] 15, 150
Array 7: Position Radius, Value	[412, 412] 15, 150	[412, 100] 15, 150	[256, 150] 15, 150	[412, 412] 15, 150
Array 8: Position Radius, Value	[412, 412] 15, 150	[412, 412] 15, 150	[362, 256] 15, 150	[256, 477] 15, 150

Table C-7. Positions of Two Circles Per Subposition, Cases S2.1–S2.4

Parameter	Case S2.1	Case S2.2	Case S2.3	Case S2.4
Array 1: Circle 1	[100, 412]	[100, 412]	[100, 412]	[135, 377]
Circle 2	[256, 362]	[256, 362]	[331, 181]	[331, 181]
Array 2: Circle 1	[100, 412]	[100, 100]	[35, 256]	[85, 256]
Circle 2	[256, 362]	[256, 150]	[362, 256]	[362, 256]
Array 3: Circle 1	[100, 100]	[412, 100]	[100, 100]	[135, 135]
Circle 2	[256, 150]	[362,256]	[331, 331]	[331, 331]
Array 4: Circle 1	[100, 100]	[412, 412]	[256, 35]	[256, 85]
Circle 2	[256, 150]	[150, 256]	[256, 362]	[256, 362]
Array 5: Circle 1	[412, 100]	[100, 412]	[412, 100]	[377, 135]
Circle 2	[362,256]	[256, 362]	[181,331]	[181,331]
Array 6: Circle 1	[412, 100]	[100, 100]	[477, 256]	[427, 256]
Circle 2	[362,256]	[256, 150]	[150, 256]	[150, 256]
Array 7: Circle 1	[412, 412]	[412, 100]	[412, 412]	[377, 377]
Circle 2	[150, 256]	[362,256]	[181, 181]	[181, 181]
Array 8: Circle 1	[412, 412]	[412, 412]	[256, 477]	[256, 427]
Circle 2	[150, 256]	[150, 256]	[256, 150]	[256, 150]

Table C-8. Positions of Two Circles Per Subposition, Cases S2.5–S2.7

Parameter	Case S2.5	Case S2.6	Case S2.7
Array 1: Circle 1	[50, 362]	[50, 362]	[85, 327]
Circle 2	[206, 312]	[206, 312]	[281, 131]
Array 2: Circle 1	[50, 362]	[50, 50]	[35, 206]
Circle 2	[206, 312]	[206, 100]	[312, 206]
Array 3: Circle 1	[50, 50]	[362, 50]	[85, 85]
Circle 2	[206, 100]	[312, 206]	[281, 281]
Array 4: Circle 1	[50, 50]	[362, 362]	[206, 35]
Circle 2	[206, 100]	[100, 206]	[206, 312]
Array 5: Circle 1	[362, 50]	[50, 362]	[327, 85]
Circle 2	[312, 206]	[206, 312]	[131, 281]
Array 6: Circle 1	[362, 50]	[50, 50]	[377, 206]
Circle 2	[312, 206]	[206, 100]	[100, 206]
Array 7: Circle 1	[362, 362]	[362, 50]	[327, 327]
Circle 2	[100, 206]	[312, 206]	[131, 131]
Array 8: Circle 1	[362, 362]	[362, 362]	[206, 377]
Circle 2	[100, 206]	[100, 206]	[206, 100]

Table C-9. Positions of Two Circles on a Rectangular Grid, Cases S2.8–S2.10

Parameter	Case S2.8	Case S2.9	Case S2.10
Array 1: Circle 1	[64, 64]	[64, 64]	[224, 96]
Circle 2	[320, 64]	[64, 192]	[224, 32]
Array 2: Circle 1	[64, 320]	[192, 64]	[96, 224]
Circle 2	[448, 320]	[64, 192]	[224, 160]
Array 3: Circle 1	[192, 64]	[192, 64]	[32, 160]
Circle 2	[192, 192]	[192, 192]	[96, 96]
Array 4: Circle 1	[192, 448]	[192, 64]	[32, 224]
Circle 2	[64, 192]	[192, 192]	[32, 32]
Array 5: Circle 1	[320, 448]	[192, 192]	[32, 96]
Circle 2	[320, 320]	[64, 192]	[160, 96]
Array 6: Circle 1	[448, 448]	[64, 64]	[160, 160]
Circle 2	[64, 448]	[64, 192]	[224, 224]
Array 7: Circle 1	[330, 192]	[64, 64]	[160, 32]
Circle 2	[448, 64]	[192, 64]	[96, 32]
Array 8: Circle 1	[448, 192]	[64, 64]	[160, 224]
Circle 2	[192, 320]	[192, 192]	[96, 160]

Table C-10. Positions of Two Circles, Cases C.1–C.4

Parameter	Case C.1	Case C.2	Case C.3	Case C.4
Array 1: Circle 1	[100, 412]	[100, 412]	[100, 412]	[100, 412]
Circle 2	[331, 181]	[331, 181]	[331, 181]	[331, 181]
Array 2: Circle 1	[100, 100]	[100, 100]	[100, 100]	[100, 100]
Circle 2	[331, 331]	[331, 331]	[331, 331]	[331, 331]
Array 3: Circle 1	[256, 35]	[256, 35]	[256, 35]	[256, 35]
Circle 2	[256, 362]	[256, 362]	[256, 362]	[256, 362]
Array 4: Circle 1	[477, 256]	[477, 256]	[477, 256]	[477, 256]
Circle 2	[150, 256]	[150, 256]	[150, 256]	[150, 256]
Array 5: Circle 1	[412, 412]	[412, 412]	[412, 412]	[412, 412]
Circle 2	[181, 181]	[181, 181]	[181, 181]	[181, 181]
Flip Cycle	32	32	8	8
Subpositions	Yes	No	Yes	No

BIBLIOGRAPHY

[1] American Society for Testing and Materials. ASTM E1441-97: Standard Guide for Computed Tomography (CT) Imaging (1997).

[2] Anderson, S.; Bothe, M.; Walter, R.E.; Zaczepinski, S. Koch East Plant Flexicracking Unit Feed Injection System Replacement Project. Presented at the 1997 NPRA Annual Meeting; San Antonio, Texas; March 1997.

[3] Azzi, M.; Turlier, P.; Bernard, J.R.; Garnero, L. Mapping Solid Concentration in a Circulating Fluid Bed Using Gammametry. *Powder Technology* 1991, 67, 27-36.

[4] Banholzer, W.F.; Spiro, C.L.; Kosky, P.G.; Maylotte, D.H. Direct Imaging of Time-Averaged Flow Patterns in a Fluidized Reactor Using X-Ray Computed Tomography. *Ind. Eng. Chem. Res.* 1987, 26, 763-767.

[5] Bartholomew, R.N.; Casagrande, R.M. Measuring Solids Concentration in Fluidized Systems by Gamma-Ray Absorption. *Ind Eng. Chem.* 1957, 49, 428-431.

[6] Bowman, J.D. Use Column Scanning for Predictive Maintenance. *Chem. Eng. Prog.* 1991, 87 (2), 25-31.

[7] Bowman, J.D. Troubleshoot Packed Towers with Radioisotopes. *Chem. Eng. Prog.* 1993, 89 (9), 34-41.

[8] Cartmel, D.B. *Investigation of Local Scale Phenomena in Vapor Liquid Contactors Using X-Ray Tomography.* M.S.E. Thesis, The University of Texas at Austin, 1999.

[9] Chaouki, J.; Larachi, F.; Dudukovic, M.P. Noninvasive Tomographic and Velocimetric Monitoring of Multiphase Flows. *Ind. Eng. Chem. Res.* 1997, 36, 4476-4503.

[10] Chen, J.; Gupta, P.; Degaleesan, S.; Al-Dahhan, M.H.; Dudukovic, M.P.; Toseland, B. A. Gas Holdup Distributions in Large-Diameter Bubble Columns Measured by Computed Tomography. *Flow Meas. and Inst.* 1998, 9, 91-101.

[11] Chiu, Y.J.; Yau, S.F. Tomographic Reconstruction of Time-Varying Object from Linear Time-Sequential Sampled Projections. IEEE Proceedings of International Conference on Acoustics, Speech, and Signal Processing; April 1994; V309-V312.

[12] Copley, D.C.; Eberhard, J.W.; Mohr, G. A. Computed Tomography Part I: Introduction and Industrial Applications. *JOM* 1994, 46 (1), 14-26.

[13] Deshusses, M.A.; Cox, H.H.J.; Miller, D.W. The Use of CAT Scanning to Characterize Bioreactors for Waste Air Treatment. Presented at the Air & Waste Management Association's 91st Annual Meeting & Exhibition; San Diego, California; June 1998.

[14] Edwards, W.M. Section 14. Mass Transfer and Gas Absorption. In: Perry, R.H.; Green, D.W.; Maloney, J.O.; Eds. *Perry's Chemical Engineers' Handbook* Sixth Edition. McGraw-Hill Book Company: New York, 1984, 14-14.

[15] Fair, J.R.; Seibert, A.F.; Behrens, M.; Saraber, P.P.; Olujic, Z. Structured Packing Performance – Experimental Evaluation of Two Predictive Models. *Ind. Eng. Chem. Res.* 2000, 39, 1788-1796.

[16] Gladden, L.F.; Alexander, P. Applications of Nuclear Magnetic Resonance Imaging in Process Engineering. *Meas. Sci. Technol.* 1996, 7, 423-435.

[17] Gonzalez, R.C.; Woods, R.E. *Digital Image Processing.* Addison-Wesley Publishing Company: Reading, Massachusetts, 1993, 40-41.

[18] Grassler, T.; Wirth, K.-E. X-Ray Computer Tomography – Potential and Limitations for the Measurement of Local Solids Distribution in Circulating Fluidized Beds. Presented at 1st World Congress on Industrial Process Tomography; Buxton, England; April 1999; 402-409.

[19] Herman, G.T. *Image Reconstruction from Projections: The Fundamentals of Computerized Tomography.* Academic Press: New York, 1980.

[20] Hines, A.L.; Maddox, R. N. *Mass Transfer: Fundamentals and Applications.* Prentice Hall, Inc.: Englewood Cliffs, New Jersey, 1985, 148-149 and 151-160.

[21] Humphrey, J.L.; Keller, G.E. *Separation Process Technology.* McGraw-Hill Book Company: New York, 1997.

[22] Jain, A.K. *Fundamentals of Digital Image Processing.* Prentice Hall, Inc.: Englewood Cliffs, New Jersey, 1989, 431-475.

[23] Johns, M.L.; Sederman, A.J.; Bramley, A.S.; Gladden, L.F.; Alexander, P. Local Transitions in Flow Phenomena through Packed Beds Identified by MRI. *AIChE J.* 2000, 46, 2151-2161.

[24] Kantzas, A. Computation of Holdups in Fluidized and Trickle Beds by Computer-Assisted Tomography. *AIChE J.* 1994, 40, 1254-1261.

[25] Kantzas, A.; Kalogerakis, N. Monitoring the Fluidization Characteristics of Polyolefin Resins Using X-Ray Computer Assisted Tomography Scanning. *Chem. Eng. Sci.* 1996, 51, 1979-1990.

[26] Kantzas, A.; Wright, I.; Kalogerakis, N. Quantification of Channelling in Polyethylene Resin Fluid Beds Using X-Ray Computer Assisted Tomography (CAT), *Chem Eng. Sci.* 1997, 52, 2023-2035.

[27] Kumar, S.B.; Dudukovic, M.P. Computer Assisted Gamma and X-Ray Tomography: Applications to Multiphase Flow Systems. In: Chaouki, J.; Larachi, F.; Dudukovic, M.P.; Eds. *Non-Invasive Monitoring of Multiphase Flows.* Elsevier: Amsterdam, The Netherlands, 1997, 47-104.

[28] Kumar, S.B.; Moslemian, D.; Dudukovic, M.P. A Gamma-ray Tomographic Scanner for Imaging Voidage Distribution in Two-Phase Flow Systems. *Flow Meas. and Instr.* 1995, 6, 61-73.

[29] Kumar, S.B.; Moslemian, D.; Dudukovic, M.P. Gas-Holdup Measurements in Bubble Columns Using Computed Tomography. *AIChE J.* 1997, 43, 1414-1425.

[30] Lockett, M.J. Easily Predict Structured-Packing HETP. *Chem. Eng. Prog.* 1998, 94, 60-66.

[31] Loser, T.; Petritsch, G.; Mewes, D. Investigation of the Two-Phase Countercurrent Flow In Structured Packings Using Capacitance Tomography. Presented at 1st World Congress on Industrial Process Tomography; Buxton, England; April 1999: 354-361.

[32] Lutran, P.G.; Ng, K.M.; Delikat, E.P. Liquid Distribution in Trickle Beds. An Experiment Using Computer-Assisted Tomography. *Ind. Eng. Chem. Res.* 1991, 30, 1270-1280.

[33] Marchot, P.; Toye, D.; Crine, M.; Pelsser, A-M.; L'Homme, G. Investigation of Liquid Maldistribution in Packed Columns by X-Ray Tomography. *Trans IChemE* 1999, 77, 511-518.

[34] Mewes, D.; Loser, T.; Millies, M. Modelling of Two-Phase Flow in Packings and Monoliths. *Chem. Eng. Sci.* 1999, 54, 4729-4747.

[35] Pilling, M. Sulzer ChemTech, Personal Communication, July 2001.

[36] Pollock, G.S.; Eldridge, R.B. Neural Network Modeling of Structured Packing Height Equivalent to a Theoretical Plate. *Ind. Eng. Chem. Res.* 2000, 39, 1520-1525.

[37] Potthoff, R. *Maldistribution in Füllkörperkolonnen.* Ph.D. Dissertation. University of Essen, 1992.

[38] Reinecke, N.; Mewes, D. Tomographic Imaging of Trickle-Bed Reactors. *Chem. Eng. Sci.* 1996, 51, 2131-2138.

[39] Reinecke, N; Mewes, D. Investigation of the Two-Phase Flow in Trickle-Bed Reactors Using Capacitance Tomography. *Chem. Eng. Sci.* 1997, 52, 2111-2127.

[40] Reinecke, N.; Petritsch, G.; Schmitz, D.; Mewes, D. Tomographic Measurement Techniques – Visualization of Multiphase Flows. *Chem Eng. Technol.* 1998, 21, 7-18.

[41] Rocha, J.A.; Bravo, J.L.; Fair, J.R. Distillation Columns Containing Structured Packings: A Comprehensive Model for Their Performance. 1. Hydraulic Models. *Ind. Eng. Chem. Res.* 1993, 32, 641-651.

[42] Rocha, J.A.; Bravo, J.L.; Fair, J.R. Distillation Columns Containing Structured Packings: A Comprehensive Model for Their Performance. 2. Mass-Transfer Model. *Ind. Eng. Chem. Res.* 1996, 35, 1660-1667.

[43] Rosenfeld, A.; Kak, A.C. *Digital Picture Processing* Second Edition, Volume 1. Academic Press: San Diego, 1982.

[44] Roy, S.; Chen, J.; Kumar, S.B.; Al-Dahhan, M.H.; Dudukovic, M.P. Tomographic and Particle Tracking Studies in a Liquid-Solid Riser. *Ind. Eng. Chem. Res.* 1997, 36, 4666-4669.

[45] Sakamoto, T.; Sato, S. Motion Artifacts in the X-Ray CT Image of a Revolving Point Object. *Systems and Computers in Japan* 1994, 25 (11), 49-57.

[46] Schmit, C.E.; Cartmel, D.; Eldridge, R.B. Process Tomography: An Option for the Enhancement of Packed Vapor-Liquid Contactor Model Development. *Ind. Eng. Chem. Res.* 2000, 39, 1546-1553.

[47] Schmit, C.E.; Cartmel, D.B.; Eldridge, R.B. The Experimental Application of X-ray Tomography to a Vapor-Liquid Contactor. *Chem. Eng. Sci.* 2001, 56, 3431-3441.

[48] Schmitz, D.; Petritsch, G.; Mewes, D.; Moser, F. Tomographic Measurement of the Liquid Hold-up in a Structured Packing. *Proc. ASME Heat Transfer Division* 1998, Vol. 361-5, 371-378.

[49] Schmitz, D.; Reinecke, N.; Petritsch, G.; Mewes, D. X-Ray Computed Tomography for Stationary Multiphase Flow in Random and Structured Packings. Presented at Frontiers in Industrial Process Tomography II, Delft, April 1997, 103-108.

[50] Schmitz, D.; Reinecke, N.; Petritsch, G.; Mewes, D. High Resolution X-Ray Tomography for Stationary Multiphase Flows. Presented at OECD/CSNI Specialist Meeting on Advanced Instrumentation and Measurement Techniques; Santa Barbara, California; March 1997.

[51] Seader, J.D.; Henley, E. J. *Separation Process Principles*. John Wiley & Sons, Inc.: New York, 1998.

[52] Sederman, A.J.; Johns, M.L.; Bramley, A.S.; Alexander, P.; Gladden, L.F. Magnetic Resonance Imaging of Liquid Flow and Pore Structure within Packed Beds. *Chem. Eng. Sci.* 1997, 52, 2239-2250.

[53] Separation Technologies for the Industries of the Future. Report of the Panel on Separation Technology for Industrial Reuse and Recycling. Committee on Industrial Technology Assessment, National Research Council; National Academy Press, Washington, D.C.; 1998.

[54] Severance, W.A.N. Advances in Radiation Scanning of Distillation Columns. *Chem. Eng. Prog.* 1981, 77 (9), 38-41.

[55] Shi, M.G.; Mersmann, A. Effective Interfacial Area in Packed Columns. *Ger. Chem. Eng.* 1985, 8, 87-96.

[56] Smith, G.B.; Gamblin, B.R.; Newton, D. X-Ray Imaging of Slurry Bubble Column Reactors: The Effects of System Pressure and Scale. *Trans. IChemE* 1995, 73, 632-636.

[57] Srinivas, C.; Costa, M.H.M. Motion-Compensated CT Image Reconstruction. Presented at IEEE International Conference on Image Processing, November 1994, 849-853.

[58] Stichlmair, J.; Bravo, J.L.; Fair, J.R. General Model for Prediction of Pressure Drop and Capacity of Countercurrent Gas/Liquid Packed Columns. *Gas Sep. Purif.* 1989, 3, 19-28.

[59] Suess, P.; Spiegel, L. Hold-up of Mellapak Structured Packings. *Chem. Eng. Proc.* 1992, 31, 119-124.

[60] Toye, D.; Marchot, P.; Crine, M.; L'Homme, G. The Use of Large Scale Computer Assisted Tomography for the Study of Hydrodynamics in Trickling Filters. *Chem. Eng. Sci.* 1994, 49, 5271-5280.

[61] Toye, D.; Marchot, P.; Crine, M.; L'Homme, G. Modelling of Multiphase Flow in Packed Beds by Computer-Assisted X-Ray Tomography. *Meas. Sci. Technol.* 1996, 7, 436-443.

[62] Toye, D.; Crine, M.; Marchot, P.; L'Homme, G. Modeling of the Liquid Distribution in a Packed Column Based Upon X-Ray Tomography Images. Presented at Frontiers in Industrial Process Tomography II, Delft, April 1997, 337-342.

[63] Toye, D; Marchot, P.; Crine, M.; Pelsser, A.-M.; L'Homme, G. Local Measurements of Void Fraction and Liquid Holdup in Packed Columns Using X-Ray Computed Tomography. *Chem. Eng. and Proc.* 1998, 37, 511-520.

[64] Wagner, I.; Stichlmair, J.; Fair, J.R. Mass Transfer in Beds of Modern, High-Efficiency Random Packings. *Ind. Eng. Chem. Res.* 1997, 36, 227-237.

[65] Whaley, A.K.; Bode, C.A.; Ghosh, J.; Eldridge, R.B. HETP and Pressure Drop Prediction for Structured Packing Distillation Columns Using a Neural Network Model. *Ind. Eng. Chem. Res.* 1999, 38, 1736-1739.

[66] Xu, S.X.; Kennedy, G. Gamma-Ray Computer-Aided Tomography of Industrial Packed Columns. Presented at AIChE 1999 Spring National Meeting; Houston, Texas; March 1999; Paper 2d.

[67] Yin, F.H.; Sun, C.G.; Afacan, A.; Nandakumar, K.; Chuang, K.T. CFD Modeling of Mass-Transfer Processes in Randomly Packed Distillation Columns. *Ind. Eng. Chem. Res.* 2000, 39, 1369-1380.

[68] Zarabi, T.; Kantzas, A. Predictions on Bubble and Solids Movement in Laboratory Polyethylene Fluid Beds as Visualized by X-ray Computer Assisted Tomography (CAT) Scanning. *Can. J. Chem. Eng.* 1998, 76, 853-865.

VITA

Carolyn Elizabeth Schmit was born on 12 August 1974 in Syracuse, New York, the daughter of Daniel E. and Elizabeth H. Schnipp. She married Geoffrey Schmit in 1999.

Carolyn graduated from Cicero-North Syracuse High School in Cicero, New York in June 1992. She attended Case Western Reserve University in Cleveland, Ohio from 1992-1997. During the same period she had co-op jobs with Quantum Chemical Company in Cincinnati, Ohio and Hoechst Celanese Corporation in Narrows, Virginia. In the summer of 1995, she attended the Chemical Engineering Summer Course at University College London in London, England. She received a Bachelor of Science degree with a major in Chemical Engineering, summa cum laude, in May 1997. After serving as a visiting scholar at University College London in the summer of 1997, she entered graduate school at The University of Texas at Austin in August 1997. During the summer of 1998, she worked for Equilon Enterprises, LLC in Houston, Texas. She received a Master of Science in Engineering, majoring in Chemical Engineering, from The University of Texas at Austin in August 2000. Upon graduation, she plans to begin work with BP Chemicals located in Naperville, Illinois.

Permanent Address: ces10@alumni.cwru.edu

This dissertation was typed by the author.